



ΠΑΝΕΠΙΣΤΗΜΙΟ ΠΕΙΡΑΙΩΣ
Τμήμα Ψηφιακών Συστημάτων

ΜΟΝΤΕΛΟΠΟΙΗΣΗ ΡΑΔΙΟΔΙΑΥΛΟΥ
ΠΟΛΛΑΠΛΩΝ-ΕΙΣΟΔΩΝ ΠΟΛΛΑΠΛΩΝ-ΕΞΟΔΩΝ
ΓΙΑ ΑΣΥΡΜΑΤΑ ΕΥΡΥΖΩΝΙΚΑ ΣΥΣΤΗΜΑΤΑ
ΣΤΡΑΤΟΣΦΑΙΡΙΚΩΝ ΕΠΙΚΟΙΝΩΝΙΩΝ

ΔΙΔΑΚΤΟΡΙΚΗ ΔΙΑΤΡΙΒΗ
ΤΟΥ
ΕΜΜΑΝΟΥΗΛ Θ. ΜΙΧΑΗΛΙΔΗ

Πειραιάς, Μάιος 2011



ΠΑΝΕΠΙΣΤΗΜΙΟ ΠΕΙΡΑΙΩΣ
Τμήμα Ψηφιακών Συστημάτων

ΜΟΝΤΕΛΟΠΟΙΗΣΗ ΡΑΔΙΟΔΙΑΥΛΟΥ
ΠΟΛΛΑΠΛΩΝ-ΕΙΣΟΔΩΝ ΠΟΛΛΑΠΛΩΝ-ΕΞΟΔΩΝ
ΓΙΑ ΑΣΥΡΜΑΤΑ ΕΥΡΥΖΩΝΙΚΑ ΣΥΣΤΗΜΑΤΑ
ΣΤΡΑΤΟΣΦΑΙΡΙΚΩΝ ΕΠΙΚΟΙΝΩΝΙΩΝ

ΔΙΔΑΚΤΟΡΙΚΗ ΔΙΑΤΡΙΒΗ
του
ΕΜΜΑΝΟΥΗΛ Θ. ΜΙΧΑΗΛΙΔΗ

Η διατριβή υποβάλλεται για την μερική κάλυψη των απαιτήσεων
με στόχο την απόκτηση του Διδακτορικού Διπλώματος

Πειραιάς, Μάιος 2011



UNIVERSITY OF PIRAEUS
Department of Digital Systems

MULTIPLE-INPUT MULTIPLE-OUTPUT
RADIO CHANNEL MODELING FOR BROADBAND WIRELESS
STRATOSPHERIC COMMUNICATIONS SYSTEMS

A Thesis
Presented to
The Academic Faculty

by

EMMANOUEL T. MICHAILIDIS

In Partial Fulfillment
of the Requirements for the Degree
Doctor of Philosophy

Piraeus, Greece, May 2011

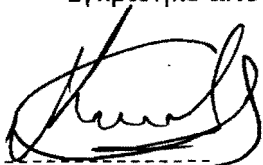
ΠΑΝΕΠΙΣΤΗΜΙΟ ΠΕΙΡΑΙΩΣ
Τμήμα Ψηφιακών Συστημάτων

ΜΟΝΤΕΛΟΠΟΙΗΣΗ ΡΑΔΙΟΔΙΑΥΛΟΥ
ΠΟΛΛΑΠΛΩΝ-ΕΙΣΟΔΩΝ ΠΟΛΛΑΠΛΩΝ-ΕΞΟΔΩΝ
ΓΙΑ ΑΣΥΡΜΑΤΑ ΕΥΡΥΖΩΝΙΚΑ ΣΥΣΤΗΜΑΤΑ
ΣΤΡΑΤΟΣΦΑΙΡΙΚΩΝ ΕΠΙΚΟΙΝΩΝΙΩΝ

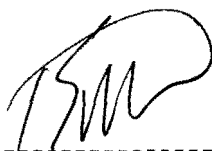
ΔΙΔΑΚΤΟΡΙΚΗ ΔΙΑΤΡΙΒΗ
ΤΟΥ
ΕΜΜΑΝΟΥΗΛ Θ. ΜΙΧΑΗΛΙΔΗ

Συμβουλευτική Επιτροπή: Αθανάσιος Γ. Κανάτας
Γεώργιος Ευθύμογλου
Φίλιππος Κωνσταντίνου

Εγκρίθηκε από την επταμελή εξεταστική επιτροπή την 9^η Μαΐου 2011.



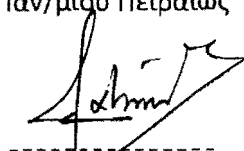
Α. Γ. Κανάτας
Αναπλ. Καθηγητής
Παν/μίου Πειραιώς



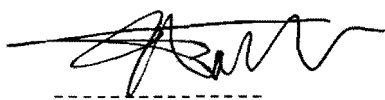
Γ. Ευθύμογλου
Επικ. Καθηγητής
Παν/μίου Πειραιώς



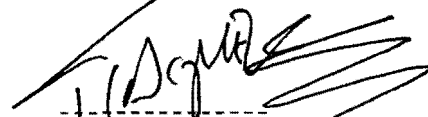
Φ. Κωνσταντίνου
Καθηγητής
Ε.Μ.Π.



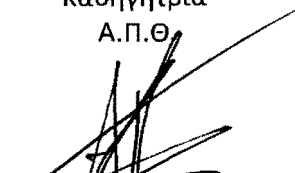
Σ. Κ. Κάτσικας
Καθηγητής
Παν/μίου Πειραιώς



Φ.-Ν. Παυλίδου
Καθηγήτρια
Α.Π.Θ.



Π. Δεμέστιχας
Αναπλ. Καθηγητής
Παν/μίου Πειραιώς



Α. Δ. Παναγόπουλος
Λέκτορας
Ε.Μ.Π.



Εμμανουήλ Θ. Μιχαηλίδης

Διδάκτωρ Πανεπιστημίου Πειραιώς

Copyright© 2011 – Εμμανουήλ Θ. Μιχαηλίδης

Με επιφύλαξη παντός δικαιώματος.

Απαγορεύεται η αντιγραφή, αποθήκευση και διανομή της παρούσας εργασίας, εξ ολοκλήρου ή τμήματος αυτής, για εμπορικό σκοπό. Επιτρέπεται η ανατύπωση, αποθήκευση και διανομή για σκοπό μη κερδοσκοπικό, εκπαιδευτικής ή ερευνητικής φύσης, υπό την προϋπόθεση να αναφέρεται η πηγή προέλευσης και να διατηρείται το παρόν μήνυμα. Ερωτήματα που αφορούν τη χρήση της εργασίας για κερδοσκοπικό σκοπό πρέπει να απευθύνονται προς τον συγγραφέα. Οι απόψεις και τα συμπεράσματα που περιέχονται σε αυτό το έγγραφο εκφράζουν τον συγγραφέα και δεν πρέπει να ερμηνευθεί ότι αντιπροσωπεύουν τις επίσημες θέσεις του Πανεπιστημίου Πειραιώς.

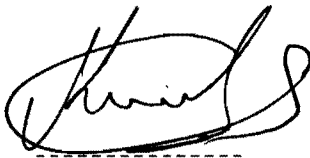
UNIVERSITY OF PIRAEUS
Department of Digital Systems

MULTIPLE-INPUT MULTIPLE-OUTPUT
RADIO CHANNEL MODELING FOR BROADBAND WIRELESS
STRATOSPHERIC COMMUNICATIONS SYSTEMS

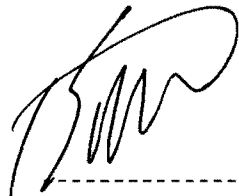
Doctor of Philosophy Thesis

EMMANOUEL T. MICHAILIDIS

Approved by:



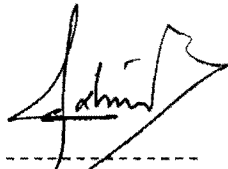
A. G. Kanatas, Supervisor
Assoc. Professor
University of Piraeus



G. Efthymoglou, Advisor
Assist. Professor
University of Piraeus



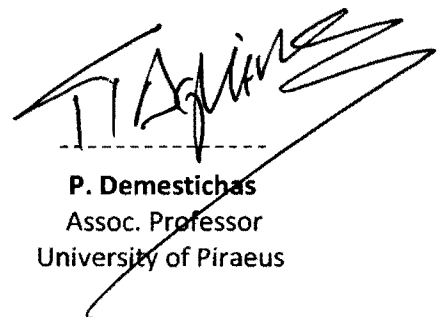
P. Constantinou, Advisor
Professor
N.T.U.A.



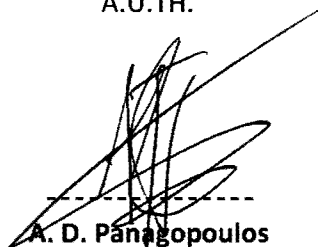
S. K. Katsikas
Professor
University of Piraeus



F.-N. Pavlidou
Professor
A.U.TH.



P. Demestichas
Assoc. Professor
University of Piraeus



A. D. Panagopoulos
Lecturer
N.T.U.A.

Date Approved: May 9th 2011



Dr. Emmanouel T. Michailidis

Copyright© 2011 – Emmanouel T. Michailidis

All rights reserved.

Copying, storing or distributing of this thesis, as part or as a whole, for commercial purposes is prohibited. Copying, storing or distributing this thesis for non-profit, educational or research purposes is allowed, provided the source is explicitly mentioned and the nonce-text is preserved. Questions concerning the non-profit use of this thesis will have to be addressed to the author. The concepts and conclusions included in this work express the author's personal opinion and should not be interpreted that they represent University of Piraeus official concepts.

ΠΑΝΕΠΙΣΤΗΜΙΟ ΠΕΡΔΙΑ

*στους γονείς μου
Θεόδωρο και Πέρσα,
και στον αδερφό μου Σπύρο...*

*to my parents
Theodoros and Persa,
and my brother Spiros...*

ΕΥΧΑΡΙΣΤΙΕΣ

Η πορεία μας στη ζωή βασίζεται στις ευκαιρίες που θα βρεθούν στο δρόμο μας και στις αποφάσεις μας αν θα τις εκμεταλλευτούμε ή όχι. Η παρούσα Διδακτορική Διατριβή ξεκίνησε ως μια ευκαιρία για την κατάκτηση της γνώσης και αποτελεί το επιστέγασμα μιας δύσκολης, επίπονης και αδιάλειπτης προσωπικής προσπάθειας, η οποία απαίτησε όχι μόνο κόπο και χρόνο, αλλά και ψυχική δύναμη. Εντούτοις, η ολοκλήρωση της Διατριβής αυτής θα ήταν αδύνατη χωρίς την αμέριστη συμπαράσταση και ουσιαστική συμβολή κάποιων ατόμων, τα οποία αισθάνομαι την ανάγκη να ευχαριστήσω.

Καταρχάς, θα ήθελα να ευχαριστήσω θερμά τον Αναπληρωτή Καθηγητή του Πανεπιστημίου Πειραιά και επιβλέποντα της Διδακτορικής μου Διατριβής Δρ. Αθανάσιο Κανάτα για την εμπιστοσύνη που έδειξε στις δυνατότητες μου, για την άριστη συνεργασία μας, για την υποδειγματική ερευνητική καθοδήγηση και για την αδιάκοπη στήριξη, βοήθεια, επιμονή και υπομονή του. Με την εμπειρία του και τις υψηλές επιστημονικές του αξίες αποτέλεσε σύμμαχο σε κάθε ερευνητική μου δραστηριότητα. Του εύχομαι καλή συνέχεια στο εκπαιδευτικό και ερευνητικό του έργο, καθώς και προσωπική και οικογενειακή ευτυχία.

Τις ελικρινείς μου ευχαριστίες θα ήθελα επίσης να εκφράσω προς τον Επίκουρο Καθηγητή του Πανεπιστημίου Πειραιά και μέλος της τριμελούς συμβουλευτικής μου επιτροπής Δρ. Γεώργιο Ευθύμογλου για τις πολύτιμες συμβουλές του στις μεταξύ μας συνεργασίες και τη συνεχή ενθάρρυνση που μου παρείχε.

Επίσης, θα ήθελα να ευχαριστήσω μερικούς συναδέλφους, με τους οποίους μοιραζόμαστε τα ίδια όνειρα και προσπάθειες, για την άψογη συνεργασία σε διάφορες εκπαιδευτικές και ερευνητικές δραστηριότητες, για τις εποικοδομητικές συζητήσεις και για την αλληλοσυμπάρσταση στην κοινή μας πορεία. Συγκεκριμένα, θα ήθελα να ευχαριστήσω τους Βλάση Μπαρούση, Δρ. Παναγιώτη Θεοφιλάκο, Δρ. Χρήστο Σπηλιωτόπουλο, Δρ. Γεώργιο Μπράβο, Κώστα Κυρίτση και

Δρ. Άγγελο Σαατσάκη. Τους εύχομαι από καρδιάς καλή σταδιοδρομία και πολλές επαγγελματικές και προσωπικές επιτυχίες.

Επιπλέον, θα ήθελα να ευχαριστήσω το νονό μου και Αναπληρωτή Καθηγητή της Οικονομικής Επιστήμης του Πανεπιστημίου *Mid-Sweden University* της Σουηδίας Δρ. Νικία Σαράφογλου για τις χρήσιμες υποδείξεις, παρατηρήσεις και συμβουλές του.

Δεν παραλείπω να ευχαριστήσω ιδιαίτερα τους φίλους μου για τη συνεχή και υπομονετική στήριξή τους και τις ευχάριστες και ξένοιαστες στιγμές που περνάμε μαζί εδώ και χρόνια. Θα ήθελα αρχικά να ευχαριστήσω τον αδερφικό μου φίλο και Μηχανολόγο Μηχανικό ΕΜΠ Σπύρο Καπαγερίδη για τη φιλία, το ήθος και τη συμπαράσταση του στα εύκολα και τα δύσκολα από τις πρώτες τάξεις του Λυκείου μέχρι σήμερα. Επίσης, ευχαριστώ από καρδιάς για τη φιλία τους τον Κώστα Κουφόγλου, τη Νεκταρία Χουλιαρά, το Γιώργο Παπαδόπουλο, τη Δώρα Μπέλλου, τον Τάκη Αλεφραγκή, το Γιώργο Αγιοργιωτάκη, τον Παναγιώτη Ιασωνίδη, το Νεκτάριο Φαρασσόπουλο, το Θανάση Τσαγκάρη, το Σωτήρη Τραχιώτη, το Γιώργο Ολυμπίου, το Γιάννη Θωμαΐδη, το Στέφανο Κόκλα, τη Μαριάνθη Καραγιάννη και την αγαπημένη μου Έλενα Τριανταφυλλίδη.

Τέλος, θα ήθελα να ευχαριστήσω ολόψυχα την οικογένειά μου, τον πατέρα μου Θεόδωρο, τη μητέρα μου Πέρσα και τον αδερφό μου Σπύρο για την παντοτινή τους αγάπη, την κατανόηση και την αδιάκοπη ηθική και υλική στήριξη που μου παρέχουν απλόχερα από τη στιγμή που γεννήθηκα. Ως μικρή ένδειξη ευγνωμοσύνης και αγάπης, τους αφιερώνω το πιο ξεχωριστό μου επίτευγμα, τη Διδακτορική μου Διατριβή...

Εμμανουήλ Θ. Μιχαηλίδης
Πειραιάς, Μάιος 2011

ACKNOWLEDGEMENTS

We are defined by opportunities, even the ones we miss. This doctoral thesis started as an opportunity for the conquest of knowledge and stands for the outcome of a difficult, painful, and uninterrupted struggle, which not only required exertion and time, but also inward power. Nevertheless, this thesis would not have been completed without the unreserved solidarity and substantial contribution of some persons, for which I truly feel gratitude.

To begin with, I would like to warmly thank Dr. Athanasios Kanatas, supervisor of my doctoral thesis and Associate Professor at the University of Piraeus, for his trust and faith to my capabilities and potential, for our excellent cooperation, his exemplary guidance to my research, and his continuous support, help, persistence, and forbearance, which all strongly and successfully raised my research activity. I wish him to effectually continue his educational and research tasks and have personal happiness and family prosperity.

In addition, I would like to truthfully thank Dr. George Efthymoglou, Assistant Professor at the University of Piraeus and advisor of my thesis, for his continuous provision with valuable advices and encouragement.

Furthermore, I would also like to thank my colleagues for our excellent cooperation, constructive discussions, mutual understanding and support in our common course, with whom I perfectly collaborated in various educational and research activities and we share the same dreams and endeavors. In particular, I would like to thank Vlasios Barousis, Dr. Panagiotis Theofilakos, Dr. Christos Spiliotopoulos, Dr. George Bravos, Kostas Kyritsis, and Dr. Aggelos Saatsakis. I heartily wish them to have a brilliant career and many successful achievements.

I would also like to thank my godfather Dr. Nikias Sarafoglou, Associate Professor of Economics at the Mid-Sweden University for his useful advices and comments.

I would not omit to especially thank my friends for their constant and patient reliance and the joyful and carefree moments we have shared together for many

years. I would initially like to thank my brotherly friend Spiros Kapageridis, Mechanical Engineer, NTUA, for his friendship, his morality, and his solidarity in both good and tough moments, since the first grades of high school. I would also like to sincerely thank Kostas Koufoglou, Nektaria Houliara, George Papadopoulos, Dora Bellou, Takis Alefragis, George Agiorgiotakis, Panagiotis Iasonidis, Nektarios Farassopoulos, Thanasis Tsagaris, Sotiris Trahiotis, George Olymbiou, John Thomaidis, Steve Koklas, Marianthi Karagianni, and my beloved Elena Triantafillidi for their friendship.

Finally, I would like to express my deepest thankfulness to my family, my father Theodoros, my mother Persa, and my brother Spiros for their everlasting love, their encouragement, and their incessant moral and material support, since the day I was born. As the least token of gratitude and love, I dedicate to them my most especial achievement, this doctoral thesis...

*Emmanouel T. Michailidis
Piraeus, Greece, May 2011*

ΠΕΡΙΛΗΨΗ

Οι στρατοσφαιρικές πλατφόρμες (high altitude platforms – HAPs) αποτελούν μία από τις πολλά υποσχόμενες εναλλακτικές τεχνολογίες για τη δημιουργία ασύρματων δικτύων υψηλών ταχυτήτων νέας γενιάς. Οι επιτακτικές ανάγκες για αποδοτικότερη εκμετάλλευση του φάσματος συχνοτήτων, για αύξηση του ρυθμού μετάδοσης πληροφορίας και χωρητικότητας του διαύλου, καθώς και για βελτίωση της αξιοπιστίας της ασύρματης ζεύξης έχουν οδηγήσει στην ραγδαία ανάπτυξη της αρχιτεκτονικής πολλαπλών-εισόδων πολλαπλών-εξόδων (multiple-input multiple-output – MIMO). Η αρχιτεκτονική αυτή έχει χαρακτηριστεί ως η βασική τεχνολογία φυσικού στρώματος για τα μελλοντικά ευρυζωνικά συστήματα επικοινωνιών. Εντούτοις, η επιτυχής εφαρμογή πολλαπλών κεραιών και στα δύο άκρα της ασύρματης ζεύξης προϋποθέτει κατάλληλο χαρακτηρισμό και μοντελοποίηση του διαύλου επικοινωνίας. Η παρούσα διδακτορική διατριβή πραγματεύεται την ανάπτυξη και αξιολόγηση μοντέλων διαύλου τεχνολογίας MIMO για ευρυζωνικά ασύρματα συστήματα επικοινωνιών βασισμένα σε HAPs.

Συγκεκριμένα, αναπτύσσονται καινοτόμα θεωρητικά γεωμετρικά μοντέλα τριών-διαστάσεων για διαύλους Ricean HAP-MIMO στενής και ευρείας ζώνης στις εκχωρημένες για κινητές επικοινωνίες μέσω HAPs ζώνες συχνοτήτων L και S. Με χρήση των προτεινόμενων μοντέλων χαρακτηρίζεται λεπτομερώς η πολυδιαδρομική διάδοση και μελετώνται διεξοδικά οι στατιστικές ιδιότητες και η απόδοση της χωρητικότητας του διαύλου, λαμβάνοντας υπόψη διάφορες παραμέτρους, όπως η γωνία ανύψωσης της πλατφόρμας, η διάταξη των στοιχειοκεραιών, η διασπορά Doppler, η διασπορά καθυστέρησης και η τριών-διαστάσεων μη-ισοτροπική κατανομή των τοπικών σκεδαστών που περιβάλλουν τον επίγειο σταθμό. Επιπρόσθετα, τα προτεινόμενα μοντέλα επιτρέπουν την εκτίμηση της απαιτούμενης απόστασης των στοιχείων της κεραίας των HAPs, ώστε να εξασφαλίζονται ασυσχέτιστες αποκρίσεις στον πίνακα MIMO του διαύλου.

Επιπλέον, αναπτύσσονται καινοτόμα ντετερμινιστικά και στατιστικά μοντέλα προσομοίωσης τριών διαστάσεων για διαύλους HAP-MIMO, τα οποία βασίζονται

στα προαναφερθέντα θεωρητικά μοντέλα στενής και ευρείας ζώνης. Για την ανάπτυξη των μοντέλων προσομοίωσης χρησιμοποιείται η μέθοδος αθροίσματος ημιτόνων (sum-of-sinusoids – SoS), η οποία έχει γίνει αποδεκτή ευρέως στον ακαδημαϊκό χώρο και στη βιομηχανία. Η αποδοτικότητα, η ακρίβεια και η πολυπλοκότητα των προτεινόμενων μοντέλων προσομοίωσης διερευνάται με γνώμονα τις στατιστικές ιδιότητες. Τα αποτελέσματα επιβεβαιώνουν την υψηλή επίδοση των μοντέλων αυτών.

Τέλος, προτείνεται μια καινοτόμος γεωμετρική σχεδιαστική μέθοδος μεγιστοποίησης της χωρητικότητας του διαύλου HAP-MIMO σε συστήματα επικοινωνιών σταθερής ασύρματης πρόσβασης στις εκχωρημένες ζώνες συχνοτήτων K_a και V για σταθερές επικοινωνίες μέσω HAPs. Σε αυτές τις χιλιοστομετρικές συχνότητες η παρουσία ισχυρής απευθείας συνιστώσας είναι απαραίτητη και η βροχή επηρεάζει σημαντικά την ποιότητα της ζεύξης. Το ενδεχόμενο αυξημένο κέρδος χωρητικότητας του διαύλου της προτεινόμενης βελτιστοποιημένης αρχιτεκτονικής διερευνάται, υπό συνθήκες καθαρού ουρανού και βροχής.

Τα προτεινόμενα μοντέλα διαύλου HAP-MIMO παρέχουν σε άλλους ερευνητές τις κατάλληλες κατευθυντήριες γραμμές για τον χαρακτηρισμό, την ανάλυση, την αξιολόγηση και την σχεδίαση μελλοντικών συστημάτων κινητών και σταθερών επικοινωνιών τεχνολογίας HAP-MIMO.

Λέξεις Κλειδιά: Διαλείψεις Ricean, δίαυλος πολλαπλών-εισόδων πολλαπλών-εξόδων (MIMO), επίδραση βροχής, μοντέλο προσομοίωσης, στρατοσφαιρικές πλατφόρμες (HAPs), συσχέτιση, τριών διαστάσεων (3-D) σκέδαση, χωρητικότητα.

ABSTRACT

High altitude platforms (HAPs) are one of the most promising alternative infrastructures for realizing next generation high data-rate wireless communications networks. Considering the continuous demand for enhanced spectral efficiency, increased channel capacity, and improved link reliability, multiple-input multiple-output (MIMO) technology is the leading candidate for future communications systems. The development of MIMO-based communications networks depends on a proper characterization and modeling of the propagation channel. To enable the successful design and performance evaluation of broadband wireless HAP-MIMO systems, this doctoral thesis focuses on modeling of HAP-MIMO channels.

Novel three-dimensional (3-D) geometry-based reference models for Ricean fading channels are proposed that encompass narrowband and wideband HAP-MIMO channel scenarios with line-of-sight (LoS) and non-line-of-sight (NLoS) connections at L and S frequency bands licensed for mobile communications through HAPs. From these models, the statistical properties and the capacity performance are analytically and thoroughly studied in terms of various parameters, such as the elevation angle of the platform, the antenna array configuration, the Doppler and delay spread, and the 3-D non-isotropic distribution of the local scatterers. Using the theoretical expressions one can easily evaluate numerically the HAP antenna inter-element spacing required to achieve uncorrelated responses in the HAP-MIMO channel matrix.

Moreover, novel 3-D deterministic and statistical simulation models for HAP-MIMO channels based on the reference narrowband and wideband models are developed by using the sum-of-sinusoids (SoS) method, which has been widely accepted by academia and industry. The efficiency, the accuracy, and the complexity of these models are thoroughly investigated with respect to the statistical properties. The results indicate that the proposed simulation models

yield high-performance and satisfactorily approximate the statistical properties of the reference models.

Finally, a novel geometrical design approach to construct high-capacity HAP-MIMO communications systems in LoS propagation environments is proposed, considering the Ka and V frequency bands licensed for fixed broadband communications through HAPs. In these mm-wave frequencies, the rain has a significant effect on the quality of the link. The potential channel capacity gain of the optimized LoS-HAP-MIMO architecture is investigated, under clear sky and rain conditions.

The proposed models for HAP-MIMO channels would provide other researchers a convenient framework and guidelines for the characterization, analysis, test, and design of future mobile and fixed HAP-MIMO communications systems.

Keywords: Capacity, correlation, high-altitude platforms (HAPs), multiple-input multiple-output (MIMO) channel, rain effects, Ricean fading, simulation model, three-dimensional (3-D) scattering.

TABLE OF CONTENTS

ΕΥΧΑΡΙΣΤΙΕΣ	i
ACKNOWLEDGEMENTS	iii
ΠΕΡΙΛΗΨΗ	v
ABSTRACT	vii
TABLE OF CONTENTS	ix
LIST OF TABLES	xiii
LIST OF FIGURES	xv
ABBREVIATIONS	xxi
1 INTRODUCTION	1
1.1 High-Altitude Platforms for Wireless Communications.....	1
1.1.1 Structures.....	3
1.1.2 Advantages.....	5
1.1.3 Spectrum Allocation and Licensed Frequency Bands.....	5
1.1.4 Applications and Services.....	9
1.1.4.1 Broadband Fixed Wireless Access.....	10
1.1.4.2 High-Speed Mobile Services.....	10
1.2 Future Trends in Wireless Communications.....	11
1.3 Thesis Motivation and Objectives.....	14
1.4 Research Contributions and Author’s Publications.....	16
1.5 Thesis Outline.....	18
2 OVERVIEW ON PROPAGATION MECHANISMS, MIMO PRINCIPLE, AND CHANNEL MODELING	19
2.1 Introduction.....	19
2.2 The Wireless Propagation Channel.....	19
2.2.1 Path Loss.....	21
2.2.2 Rain Effects.....	22
2.2.3 Shadow Fading.....	25
2.2.4 Multipath Fading.....	26

2.2.5 Time, Frequency, and Space Selectivity.....	27
2.2.6 The Diversity Concept.....	29
2.3 The MIMO Technology.....	31
2.3.1 Benefits.....	32
2.3.2 Channel Statistics.....	33
2.4 The Earth-Stratosphere Channel: From SISO to MIMO Modeling.....	36
2.4.1 Survey of HAP-SISO Channels.....	36
2.4.1.1 Switched-Channel Models.....	37
2.4.1.2 Empirical Channel Models.....	38
2.4.1.3 Geometry-based Channel Models.....	39
2.4.2 Classification of MIMO Channel Models.....	41
2.4.3 Recent Advances in Satellite/HAP MIMO Channel Modeling.....	42
2.4.3.1 Physical-Statistical Modeling.....	43
2.4.3.2 Analytical Modeling.....	44
2.4.3.3 Polarized Satellite/HAP MIMO Channels.....	45
2.4.4 Potential Application of MIMO Technology over Single HAPs.....	45
3 THREE-DIMENSIONAL MODELING OF SPACE-TIME CORRELATED HAP-MIMO CHANNELS.....	47
3.1 Introduction.....	47
3.2 The HAP-MIMO System Model.....	49
3.3 A Reference Model for HAP-MIMO Channels.....	50
3.3.1 Channel Impulse Response.....	56
3.4 Space-Time Correlation Function.....	59
3.4.1 Investigation of Space-Time Correlation of HAP-MIMO Channels...	66
3.4.1.1 Effect of HAP Antenna Displacement.....	77
3.5 Analysis of HAP-MIMO Channel Capacity.....	79
3.5.1 Definition of HAP-MIMO Channel Capacity.....	79
3.5.2 Numerical Results.....	82
3.6 Summary.....	87

4	THREE-DIMENSIONAL SIMULATION OF HAP-MIMO CHANNELS.....	89
4.1	Introduction.....	89
4.2	The Stochastic Simulation Model.....	91
4.3	The Deterministic Simulation Model.....	94
4.3.1	The Deterministic Simulation Model Based on Set Partitioning.....	98
4.4	The Statistical Simulation Model.....	101
4.5	Simulation Results.....	103
4.6	Summary.....	111
5	THREE-DIMENSIONAL MODELING AND SIMULATION OF WIDEBAND HAP-MIMO CHANNELS.....	113
5.1	Introduction.....	113
5.2	The Wideband HAP-MIMO System Model.....	115
5.3	A Reference Model for Wideband HAP-MIMO Channels.....	116
5.3.1	Input Delay-Spread and Time-Variant Transfer Functions.....	120
5.4	Statistical Properties of Wideband HAP-MIMO Channels.....	123
5.4.1	Space-Time-Frequency Correlation Function.....	123
5.4.2	Space-Doppler Power Spectrum.....	126
5.4.3	Power Space-Delay Spectrum.....	130
5.4.4	Numerical Results.....	133
5.5	Simulation Models for Wideband HAP-MIMO Channels.....	137
5.5.1	Simulation Results.....	140
5.6	Summary.....	141
6	MODELING OF LINE-OF-SIGHT HAP-MIMO CHANNELS.....	143
6.1	Introduction.....	143
6.2	The LoS-HAP-MIMO System Model.....	145
6.2.1	A Geometrical Model for LoS-HAP-MIMO Channels.....	147
6.3	Capacity Optimization Techniques.....	148
6.3.1	Practical Considerations.....	150
6.4	Numerical Results.....	151
6.4.1	Sensitivity Study.....	155

6.5 Summary.....	158
7 CONCLUSIONS AND FUTURE RESEARCH DIRECTIONS.....	159
7.1 Conclusions.....	159
7.2 Future Research Directions.....	161
APPENDIX A.....	165
APPENDIX B.....	169
REFERENCES.....	173
ΣΥΝΤΟΜΟ ΒΙΟΓΡΑΦΙΚΟ ΣΗΜΕΙΩΜΑ.....	187
VITA.....	189

LIST OF TABLES

1	Radio frequency bands.....	7
2	Microwave frequency bands.....	7
3	Frequency spectrum available for HAP-based applications.....	8
4	Regression coefficients for estimating specific rain attenuation.....	24
5	Definition of the parameters used in the reference model.....	54
6	The complexity of the simulation models.....	102
7	Performance valuation of the deterministic simulation model (A).....	104
8	Performance valuation of the deterministic simulation model (B).....	105
9	Accuracy evaluation of the statistical simulation model.....	110
10	Efficiency evaluation of the statistical simulation model.....	110
11	Definition of the parameters used in the reference wideband model.....	119
12	Link budget parameters.....	154

РАНЕЕЗНАМО ТЕРРА

LIST OF FIGURES

1	The troposphere, stratosphere, and mesosphere layers of the atmosphere.....	2
2	The average wind velocity for different altitude above the Earth's surface.....	3
3	The HAP and UAV structures: (a) solar-powered unmanned aircraft, (b) manned aircraft, (c) unmanned aerial vehicle, and (d) solar-powered unmanned airship.....	4
4	The ITU region map.....	6
5	Visualization of an integrated satellite-HAP-terrestrial 4G wireless communications system providing fixed and mobile broadband services.....	12
6	High level view of the future 4G wireless reconfigurable radio systems...	13
7	Architecture of a generic wireless communications system.....	21
8	The specific rain attenuation as a function of the rain rate for different carrier frequency.....	24
9	Rain attenuation path geometry.....	25
10	Visualization of a multipath propagation environment.....	27
11	The relationships of the time, frequency, and space domains.....	29
12	Basic representation of SISO, SIMO, MISO, MIMO, and MU-MIMO systems.....	31
13	Visualization of the MIMO radio channel.....	34
14	The typical geometry of a HAP-based system.....	39
15	The ellipsoid geometrical model for HAP-SISO channels.....	40
16	The circular cone geometrical model for HAP-SISO channels.....	40
17	Visualization of isotropic scattering conditions in an open area.....	48
18	Visualization of non-isotropic scattering conditions in a narrow street....	48
19	Basic concept of a HAP-based communication system and a cylindrical scattering region inside the coverage area.....	51
20	The LoS paths of the 3-D geometrical model for a 2×2 HAP-MIMO channel.....	52
21	The LoS paths of the projection of the 3-D geometrical model for a 2×2 HAP-MIMO channel.....	52
22	The NLoS paths of the 3-D geometrical model for a 2×2 HAP-MIMO channel.....	53
23	The NLoS paths of the projection of the 3-D geometrical model for a 2×2 HAP-MIMO channel.....	53

24	The probability density for the distribution of the angle of arrival of the scattered waves for different degree of scattering.....	62
25	The probability density for the distribution of the distance between TMS and the scatterers for different values of the parameter a	63
26	The mean distance between the TMS and the scatterers for different values of the parameter a	64
27	The probability density for the distribution of the building heights in London (U.K.) and Guildford (U.K.).....	65
28	3-D building distribution in a typical urban propagation environment.....	67
29	The absolute correlation of HAP-MIMO channels for various values of the Ricean factor.....	67
30	The transmit SCF of a 2×2 HAP-MIMO Rayleigh channel for various elevation angles of the SBS, in isotropic ($k = 0$) and non-isotropic ($k = 3$) scattering environments.....	68
31	The transmit (a) and receive (b) SCF of a 2×2 HAP-MIMO Rayleigh channel for different orientation of the SBS and TMS antenna array, respectively.....	70
32	The transmit (a) and receive (b) SCF of a 2×2 HAP-MIMO Rayleigh channel for different degree of local scattering at the TMS.....	70
33	The transmit (a) and receive (b) SCF of a 2×2 HAP-MIMO Rayleigh channel for different spread of the scatterers around the TMS.....	70
34	The transmit (a) and receive (b) SCF of a 2×2 HAP-MIMO Rayleigh channel for different maximum distance between the projections to the x - y plane of the TMS and an effective scatterer.....	71
35	The receive SCF of a 2×2 HAP-MIMO Rayleigh channel with horizontally ($\psi_R = 0^\circ$) or vertically ($\psi_R = 90^\circ$) placed TMS antennas, for various mean values of the scatterer height.....	71
36	The SCF of a 2×2 HAP-MIMO (a) Rayleigh and (b) Ricean channel.....	72
37	The TCF of a HAP-SISO Rayleigh channel for different different degree of local scattering at the TMS.....	73
38	The TCF of a HAP-SISO Rayleigh channel for different spread of the scatterers around the TMS and different maximum distance between the projections to the x - y plane of TMS and an effective scatterer.....	74
39	The TCF of a HAP-SISO Rayleigh channel for various mean values of the scatterer height.....	74
40	The TCF of a HAP-SISO Rayleigh channel for different maximum Doppler frequency and different moving direction at the TMS.....	75
41	The TCF of a HAP-SISO Ricean channel for different HAP structures.....	75

42	The transmit STCF of a 2×2 HAP-MIMO (a) Rayleigh and (b) Ricean channel.....	76
43	The receive STCF of a 2×2 HAP-MIMO (a) Rayleigh and (b) Ricean channel.....	76
44	Geometrical representation of roll, pitch, and yaw effects.....	77
45	The transmit SCF of a 2×2 HAP-MIMO Rayleigh channel for different directions of HAP displacement due to stratospheric winds.....	78
46	The transmit SCF of a 2×2 HAP-MIMO Rayleigh channel for different elevation angle of the p^{th} SBS antenna element (pitch effect).....	79
47	Comparison of the ergodic channel capacities obtained using a 2×2 HAP-MIMO architecture and a HAP-SISO architecture as a function of the received SNR for different Ricean factor.....	83
48	Comparison of the ergodic channel capacities obtained using a 2×2 HAP-MIMO architecture and a HAP-SISO architecture as a function of the Ricean factor for different received SNR.....	83
49	The ergodic capacity of a 2×2 HAP-MIMO channel as a function of the spacing between the SBS antenna elements for different SBS elevation angle.....	84
50	The complementary cumulative distribution function of the capacity of 2×2 HAP-MIMO channel for different antenna array orientation at the SBS.....	85
51	The complementary cumulative distribution function of the capacity of 2×2 HAP-MIMO channel for different degree of scattering, spread of the scatterers around TMS, and maximum distance between the TMS and the scatterers.....	85
52	The complementary cumulative distribution function of the capacity of 2×2 HAP-MIMO channel for horizontally or vertically placed TMS antennas and different mean of the scatterer height.....	86
53	The complementary cumulative distribution function of the capacity of 2×2 HAP-MIMO channel for different normalized Doppler frequency and different moving direction at the TMS.....	87
54	The cumulative distribution of the angle of arrival of the scattered waves for different degree of scattering.....	92
55	The cumulative distribution of the distance between TMS and the scatterers for different values of the parameter a	93
56	The cumulative distribution of the building heights in London (U.K.) and Guildford (U.K.).....	94
57	Visualization of the three scatterer sub-regions, each consisting of N_1 , N_2 , and N_3 coordinates (“•”) of scattering points, respectively.....	95

58	The set partitioning of three scatterer constellations into V_1 , V_2 , and V_3 sub-constellations, each consisting of 3 coordinates (“•”) of relevant scattering points.....	99
59	Comparison between the TCFs of the reference model and the deterministic simulation model.....	105
60	The absolute error between the SCFs of the reference model and the deterministic simulation model.....	106
61	Comparison between the TCFs of the reference model and the deterministic SP simulation model.....	107
62	The absolute error between the SCFs of the reference model and the deterministic SP simulation model.....	107
63	Comparison between the TCFs of the reference model and the statistical simulation model.....	109
64	The absolute error between the SCFs of the reference model and the statistical simulation model.....	109
65	Comparison of the ergodic capacities obtained using the reference model and the simulation models.....	111
66	The LoS paths of the 3-D geometrical wideband model for a 2×2 HAP-MIMO channel.....	117
67	The LoS paths of the projection of the 3-D geometrical wideband model for a 2×2 HAP-MIMO channel.....	117
68	The NLoS paths of the 3-D geometrical wideband model for a 2×2 HAP-MIMO channel.....	118
69	The NLoS paths of the projection of the 3-D geometrical wideband model for a 2×2 HAP-MIMO channel.....	118
70	The relative maximum propagation delay for different maximum scatterer height and different maximum distance in the azimuth domain between the TMS and the scatterers.....	122
71	The FCF of a HAP-SISO Rayleigh channel for different elevation angles of the SBS.....	134
72	The transmit SFCF of a 2×2 HAP-MIMO (a) Rayleigh and (b) Ricean channel.....	134
73	The receive SFCF of a 2×2 HAP-MIMO (a) Rayleigh and (b) Ricean channel.....	135
74	The TFCF of a HAP-SISO (a) Rayleigh and (b) Ricean channel.....	135
75	The SDPS of a HAP-SISO and a 2×2 HAP-MIMO Rayleigh channel.....	136
76	The relative PSDS of a HAP-SISO and a 2×2 HAP-MIMO Rayleigh channel.....	137
77	Comparison between the STFCFs of the reference and the simulation models.....	141

78	A geometrical model for a 2×2 LoS-HAP-MIMO channel.....	148
79	Comparison of the channel ergodic capacities obtained using the full-rank and rank-one 2×2 LoS-HAP-MIMO, LoS-HAP-SISO, and the Rayleigh i.i.d. 2×2 MIMO architectures, under clear sky conditions.....	153
80	The complementary cumulative distribution function of the channel capacity achieved with the full-rank and rank-one 2×2 LoS-HAP-MIMO architectures for different rain rates.....	154
81	The ergodic capacity obtained using the full-rank 2×2 LoS-HAP-MIMO architecture as a function of the rain rate for different carrier frequency.	155
82	The normalized capacity obtained using the full-rank 2×2 LoS-HAP-MIMO architecture as a function of the deviation factor.....	156
83	The normalized capacity obtained using the full-rank 2×2 LoS-HAP-MIMO architecture for different orientation of the SBS antenna array.....	157
84	The normalized capacity obtained using the full-rank 2×2 LoS-HAP-MIMO architecture as a function of the antenna array shifting from the optimal point.....	158

РАНЕЕЗНАМО ПЕРПАА

ABBREVIATIONS

2-D	Two-Dimensional
3-D	Three-Dimensional
3G	Third Generation
3GPP	Third Generation Partnership Project
4G	Fourth Generation
ΕΜΠ	Εθνικό Μετσόβιο Πολυτεχνείο
ΕΤΣ	Εργαστήριο Τηλεπικοινωνιακών Συστημάτων
ΜΔΕ	Μεταπτυχιακό Δίπλωμα Ειδίκευσης
NTUA	National Technical University of Athens
TE	Τεχνολογική Εκπαίδευση
TEI	Τεχνολογικό Εκπαιδευτικό Ίδρυμα
ACE	Antenna Centre of Excellence
AESP	Antenna Elements Spacing Product
AFD	Average Fade Duration
ΑοΑ	Angle of Arrival
ΑοD	Angle of Departure
AWGN	Additive White Gaussian Noise
BAN	Body Area Network
BER	Bit Error Rate
BFWA	Broadband FWA
CCDF	Complementary Cumulative Distribution Function
CDF	Cumulative Density Function
CNES	Centre National d'Etudes Spatiales
COST	European COoperation in Science and Technology
CSI	Channel State Information
DAB	Digital Audio Broadcasting
dB	Decibel
DoF	Degrees of Freedom

DSP	Digital Signal Processor
DVB	Digital Video Broadcasting
EHF	Extra High Frequency
EM	Electromagnetic
ESA	European Space Agency
FCC	Federal Communications Commission
FCF	Frequency Correlation Function
FSL	Free-Space Loss
FT	Fourier Transform
FWA	Fixed Wireless Access
Gbps	Gigabits per second
GBSB	Geometry-Based Single-Bounce
HAP	High-Altitude Platform
HDTV	High-Definition Television
HSDPA	High-speed Downlink Packet Access
HSPA	High-Speed Packet Access
IEEE	Institute of Electrical and Electronics Engineers
IFT	Inverse Fourier Transform
i.i.d.	Independent and identically distributed
IMT	International Mobile Telecommunications
IP	Internet Protocol
IST	Information Society Technologies
ITU	International Telecommunication Union
Kbps	Kilobits per second
LAN	Local Area Network
LCR	Level Crossing Rate
LMDS	Local Multipoint Distribution Services
LMS	Land Mobile Satellite
LoS	Line-of-Sight
LPNM	L_p -norm method

LTE	Long Term Evolution
MAN	Metropolitan Area Network
MBMS	Multimedia Broadcast and Multicast Services
Mbps	Megabits per second
MCM	Management Committing Meeting
MD	Maximal Deviation
MIMO	Multiple-Input Multiple-Output
MISO	Multiple-Input Single-Output
MU-MIMO	Multi-user MIMO
NLoS	Non-Line-of-Sight
NTUA	National Technical University of Athens
OECD	Organization for Economic Cooperation and Development
OFDMA	Orthogonal Frequency Division Multiple Access
PAN	Personal Area Network
PC	Personal Computer
PDA	Personal Digital Assistant
PDF	Probability density function
PSD	Power Spectral Density
PSDS	Power Space-Delay Spectrum
QoS	Quality of Service
RMSE	Root Mean Square Error
SAA	Spherical Antenna Array
SBS	Stratospheric Base Station
SCF	Spatial Correlation Function
SDMA	Space-Division Multiple Access
SDPS	Space-Doppler Power Spectrum
SFCF	Space-Frequency Correlation Function
SHF	Super High Frequency
SIMO	Single-Input Multiple-Output
SISO	Single-Input Single-Output

SNR	Signal-to-Noise Ratio
SoS	Sum-of-Sinusoids
SP	Set Partitioning
STCF	Space-Time Correlation Function
STFCF	Space-Time-Frequency Correlation Function
SU	Subscriber Unit
SU-MIMO	Single-user MIMO
TCF	Temporal Correlation Function
TDL	Tapped Delay Line
TFCF	Time-Frequency Correlation Function
TFS	Terrestrial Fixed Station
TMS	Terrestrial Mobile Station
TSL	Telecommunications Systems Laboratory
UAV	Unmanned Aerial Vehicle
UCA	Uniform Circular Array
UHF	Ultra High Frequency
ULA	Uniform Linear Array
UMB	Ultra Mobile Broadband
UMTS	Universal Mobile Telephone System
UPA	Uniform Planar Array
V-MIMO	Virtual MIMO
WAN	Wide Area Network
WiMAX	Worldwide Interoperability for Microwave Access
WRC	World Radiocommunications Conference
WSSUS	Wide-Sense Stationary Uncorrelated Scattering

Chapter 1

Introduction

1.1 High-Altitude Platforms for Wireless Communications

For several years, the wireless communications sector [1], [2] has definitely been the fastest growing market segment in communications around the world with dazzling new applications and products emerging on an almost daily basis. Wireless communications have changed the way people communicate and have directly and significantly influenced our everyday life by offering nomadicity, i.e., the ability to connect to a network from different locations via different base stations, portability, i.e., the ability to readily transport from one location to another, and mobility, i.e., the ability to keep ongoing connections active while moving at vehicular speeds. Strongly supported by the advances in semiconductor and signal processing technologies, new communications architectures are being envisioned to improve as well as complement current networks to meet future needs.

Wireless communications networks enable the provision of both mobile and fixed services to serve a variety of commercial and business applications and services. Nowadays, third generation (3G) mobile cellular systems [3]-[5] have enabled access to advanced services, such as video communications, multimedia, and high-speed internet access. Typical example of 3G standards is the Universal Mobile Telephone System (UMTS) [3]-[5], especially supplemented with High-speed Downlink Packet Access (HSDPA) [6], [7]. In addition, Fixed Wireless Access (FWA) [8]-[10] communications systems attempt to provide a set of reliable, cost-effective and secure communications services in case where existing wired infrastructure is impractical, expensive or temporary. In general, FWA can serve two main categories of services, Internet access for the public and businesses and private high-speed data communications for small, medium, and large businesses.

Wireless communications services are traditionally provided by terrestrial and satellite systems. Terrestrial links are widely used to provide services in areas with complex propagation conditions, while satellite links are usually used to provide high-speed connections, where terrestrial infrastructure is not available. These systems represent two well established infrastructures that have been dominant in the telecommunications arena for years. In recent years, a new alternative wireless communications technology has emerged known as *high-altitude platforms* (HAPs) [11]-[17] and has attracted attention worldwide [18]-[23]. The term HAPs defines aerial platforms flying at an altitude between 17 and 22 km above the Earth's surface, in the stratosphere [11]-[17].

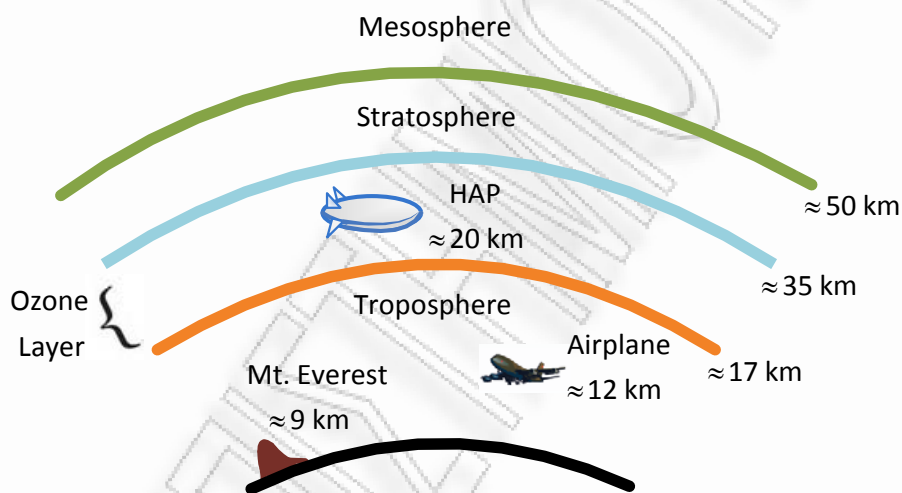


Figure 1: The troposphere, stratosphere, and mesosphere layers of the atmosphere.

As shown in Fig. 1, the stratosphere is the second major layer of Earth's atmosphere, just above the troposphere, and below the mesosphere. This operating altitude was chosen because it represents a layer of relatively mild wind and turbulence in most regions of the world. At this altitude, HAPs can succeed in maintaining station-keeping and flying against the wind without excessive power demands. Fig. 2 illustrates the average wind velocities for different altitudes obtained from worldwide measurements [12], [13]. Although this wind profile may considerably vary with latitude, season and location, it generally follows this rough distribution. The proposed range in altitude is above commercial air-traffic heights

(the maximum altitude of airplane lanes is about 12 km), which would otherwise prove a potentially prohibitive constraint. However, as the altitude increases the air density is reduced, rendering the placement of the HAPs very difficult. For example, considering 12 km altitude, the density is about 25% compared to that at the sea level, while at 24 km the density is only about 3.6% [12].

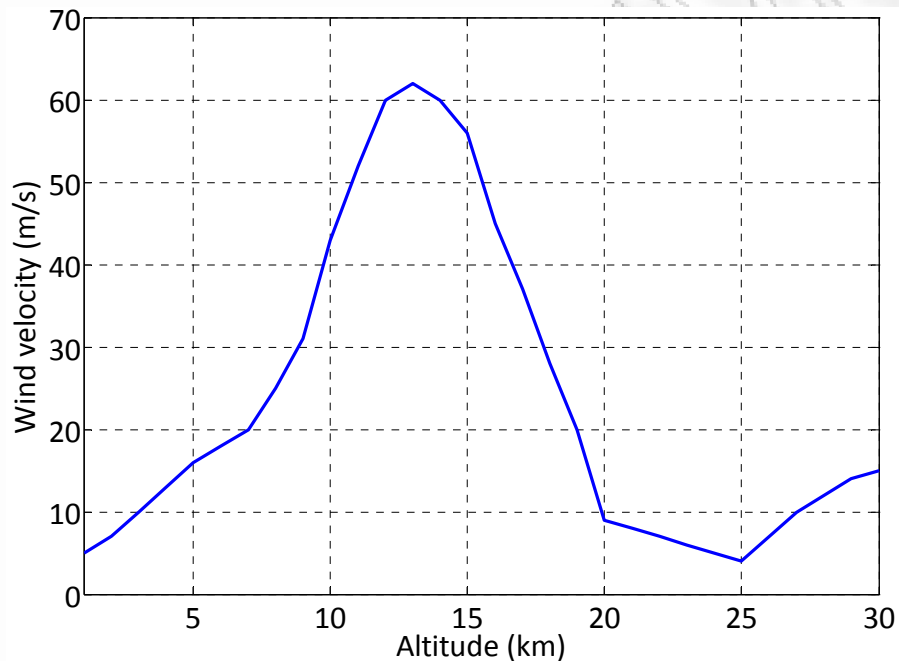


Figure 2: The average wind velocity for different altitude above the Earth's surface.

1.1.1 Structures

Two major HAP structures are considered in the literature, the circling aircrafts (approximately 30 m in length or with wingspan of about 35-70 m) and the lighter-than-air quasi-stationary airships (of about 150-200 m in length) [11]-[17]. The aircrafts fly in a roughly circular tight path (about 2 km radius or more) and can be either solar-powered and unmanned with continuous flight duration in the order of months or manned with average flight duration of some hours due to the fuel constraints and human factors. The unmanned aerial vehicles (UAVs) are another type of small fuelled unmanned aircraft employed only for military short time surveillance (up to 40 hours) at modest altitudes. The airships use very large semi-

rigid or non-rigid helium-filled containers and electric motors and propellers for station-keeping. Prime power required for propulsion and station-keeping as well as for the payload and applications is provided from lightweight solar cells in the form of large flexible sheets. The achievable mission duration for airships is hoped to be 5 years at least. HAP stability problems and displacements due to the winds or pressure variations of the stratosphere are a problem to be faced for both aircrafts and airships [24]-[26]. Although, it is easier for airships than for aircrafts to remain quasi-stationary, it is rather difficult to remotely control the airship's position. Recently, advances in composite materials, computers, navigation systems, aerodynamics, and propulsions systems, have made station keeping more realizable and hence HAP-based systems more achievable.



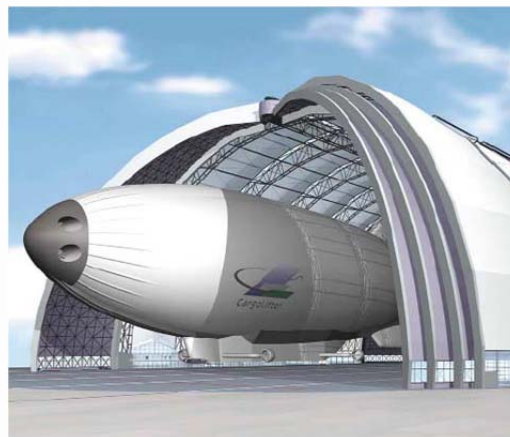
(a)



(b)



(c)



(d)

Figure 3: The HAP and UAV structures: (a) solar-powered unmanned aircraft, (b) manned aircraft, (c) unmanned aerial vehicle, and (d) solar-powered unmanned airship.

1.1.2 Advantages

HAPs preserve some of the best characteristics of terrestrial and satellite communication systems, while avoiding many of their drawbacks [11]-[17]. In comparison to terrestrial wireless technologies, HAPs require considerably less communications infrastructure and they can serve potentially large coverage areas. When compared to satellite communication systems, HAPs provide lower propagation delays (a serious issue for voice communications over satellite links) and less free space loss, as well as easy maintenance and upgrading of the payload during the lifetime of the platform. In addition, the cost for the development of satellite systems is much greater (the eventual cost of HAPs is expected to be about 10% of that of a satellite) and it may be economically more efficient to cover a large area with many HAPs rather than with many terrestrial base stations or with a satellite system. Hence, HAPs represent an economically attractive technology. HAPs are also well-suited for temporary provision of basic or additional communications services due to their rapid deployment and movable on demand, providing network flexibility and adaptability. Finally, HAPs can use most of conventional base station technology and terminal equipment, while solar-powered HAPs are non-pollutant and environmentally friendly. Although HAPs provide substantial advantages over terrestrial and satellite systems, their successful deployment requires integration of available and emerging technologies to make long-term operation feasible and profitable. Specifically, some issues on communications systems need to be addressed and are of fundamental importance, such as the design and implementation of the onboard antennas, the channel characterization and modeling, the resource management, and the coordination and inter-operability between different systems.

1.1.3 Spectrum Allocation and Licensed Frequency Bands

Radio transmission involves the use of part of the electromagnetic spectrum and different parts of the radio spectrum are used for different radio transmission

technologies, services and applications. The tasks of internationally coordinating the use of radio spectrum and setting global standards are undertaken by the International Telecommunication Union (ITU) [27]. The ITU divided the world into three regions for the purposes of managing the global radio spectrum and each region has its own set of frequency allocations. As shown in Fig. 4, Region 1 comprises Europe, Africa, Russia and Middle East, Region 2 comprises North and South America, and Region 3 comprises Asia, Oceania and Pacific Countries.

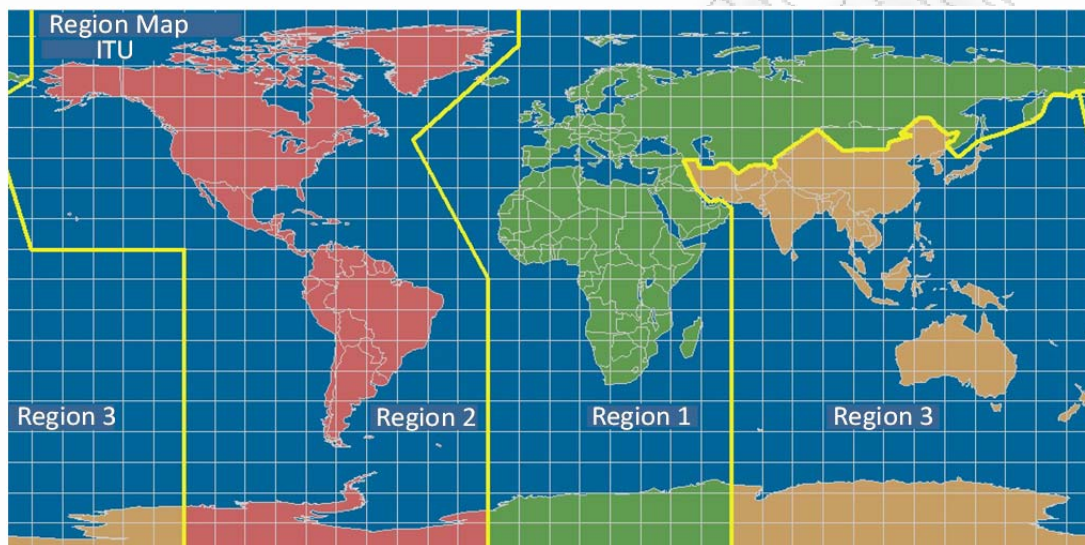


Figure 4: The ITU region map.

According to Table 1, the radio frequency spectrum involves electromagnetic (EM) radiation with frequencies between 3 Hz and 300 GHz [28]. As the demand for new and different communication services increases, more radio spectrum space at higher frequencies is required. Hence, the utilization of the Ultra High Frequency (UHF), Super High Frequency (SHF), and Extra High Frequency (EHF) bands has emerged. The common microwave band designations are summarized in Table 2. The properties of the EM energy depend on the frequency. Hence, different frequencies have different properties, and propagation at high frequencies is dominated by different mechanisms as compared to propagation at low frequencies (these mechanisms will be analytically studied in the next chapter). In particular, high rain attenuation and atmospheric losses at millimeter-wave

frequencies make communications difficult and unreliable [29]. Therefore, frequency bands less susceptible to path loss, absorption and noise should be chosen to minimize the cost of the transmission and maximize its information carrying rate.

TABLE 1
RADIO FREQUENCY BANDS

BAND	NOMENCLATURE	FREQUENCY	WAVELENGTH
ELF	Extra low frequency	3 – 30 Hz	100,000 – 10,000 km
SLF	Super low frequency	30 – 300 Hz	10,000 – 1,000 km
ULF	Ultra low frequency	300 – 3,000 Hz	1,000 – 100 km
VLF	Very low frequency	3 – 30 KHz	100 – 10 km
LF	Low frequency	30 – 300 KHz	10 – 1 km
MF	Medium frequency	300 – 3,000 KHz	1000 – 100 m
HF	High frequency	3 – 30 MHz	100 – 10 m
VHF	Very high frequency	30 – 300 MHz	10 – 1 m
UHF	Ultra high frequency	300 – 3,000 MHz	1 – 0.1 m
SHF	Super high frequency	3 – 30 GHz	10 – 1 cm
EHF	Extra high frequency	30 – 300 GHz	10 – 1 mm

TABLE 2
MICROWAVE FREQUENCY BANDS

BAND NAME	FREQUENCY	WAVELENGTH
L-band	1 – 2 GHz	30 – 15 cm
S-band	2 – 4 GHz	15 – 7.5 cm
C-band	4 – 8 GHz	7.5 – 3.75 cm
X-band	8 – 12 GHz	3.75 – 2.5 cm
Ku-band	12 – 18 GHz	2.5 – 1.67 cm
K-band	18 – 27 GHz	1.67 – 1.11 cm
Ka-band	27 – 40 GHz	11.1 – 7.5 mm
V-band	40 – 75 GHz	7.5 – 4 mm
W-band	75 – 110 GHz	4 – 2.7 mm

TABLE 3
FREQUENCY SPECTRUM AVAILABLE FOR HAP-BASED APPLICATIONS

FREQUENCY BAND	MICROWAVE FREQUENCY BAND	AREA/COUNTRY	TYPE OF SERVICE
47.9 – 48.2 GHz	V	Global	Fixed (uplink)
47.2 – 47.5 GHz	V	Global	Fixed (downlink)
31.0 – 31.3 GHz	Ka	40 countries	Fixed (uplink)
27.5 – 28.35 GHz	Ka	40 countries	Fixed (downlink)
2.160 – 2.170 GHz	S	Regions 1 and 3	Mobile
2.110 – 2.160 GHz	S	Global	Mobile
2.010 – 2.025 GHz	S	Regions 1 and 3	Mobile
1.885 – 1.985 GHz	L	Global	Mobile

Several frequency bands (see Table 3) have been licensed for communications through HAPs on a global, regional or national basis and for each frequency band appropriate regulatory provisions have been established based on technical and operational studies [30]. The choice of the frequency bands at which HAPs can operate is mainly determined by the frequency sharing and compatibility with other existing services provided by terrestrial/satellite systems, which would cause interference problems if spectrum allocation is not carefully controlled [31], [32].

At the ITU World Radiocommunications Conference in 1997 (WRC-97) the concept of HAPs was formally introduced into the radio regulations as a separate category of the communications infrastructures and was decided that HAPs can provide fixed wireless services. Specifically, the bands 47.2-47.5 GHz (downlink) and 47.9-48.2 (uplink) were regulated for use by HAPs on a global basis. Use of these bands is subject to the provisions of Resolution 122, which was revised at WRC-07 [33]. At WRC-00, a need for a lower frequency band for fixed wireless services was expressed due to the severe rain attenuation occurring at 47/48 GHz bands. Hence, the bands 27.5-28.35 GHz (downlink) and the band 31.0-31.3 GHz (uplink) were regulated for use by HAPs in several countries located mainly at Region 3. The WRC-03 increased the number of countries with access to the HAPs allocations including Region 2. Use of these bands is subject to the provisions of Resolution 145, which was revised at WRC-07 [34]. Hence, HAPs can serve as base

stations of FWA networks at 47/48 and 28/31 GHz bands providing data, voice, and video services with a total bandwidth of up to 300 MHz in each direction shared on a non-harmful interference, non-protection basis with fixed satellite and terrestrial services.

The WRC-00 also decided that HAPs may be used as base stations within the terrestrial component of the International Mobile Telecommunications 2000 (IMT-2000) system. This alternative way of delivering the IMT-2000 services by HAPs on a co-primary basis was regulated in the frequency ranges 1885-1980, 2010-2025 and 2110-2170 MHz in Region 1 and Region 3, and 1885-1980 and 2110-2160 MHz in Region 2. Such use of the bands above is subject to the provisions of Resolution 221, which was revised at WRC-07 [35]. Hence, HAPs can serve as base stations of 3G cellular networks providing mobile data/voice/video services with a total bandwidth of up to 50/60 MHz (amount of bandwidth varies slightly with region) worldwide.

Finally, spectrum identification in the range between 5,850-7,075 MHz to facilitate gateway links to and from HAPs has been also envisioned, since WRC-07 agenda, Resolution 734 [36].

1.1.4 Applications and Services

An application can be considered as the end product offered to public and businesses over which services are accessed. The major wireless communications applications intend to be facilitated by HAPs can be divided technologically into two types, the broadband FWA (BFWA) [12], [15], [19], [37] and the provision of mobile services [38]-[40]. These types of applications are briefly described in the following subsections. Note that the flexibility of HAP-based communications systems allows not only for carrying wireless communications payloads but also for serving other applications, such as navigation and positioning [41], monitoring, remote sensing, and surveillance [42], disaster management and relief [43], [44], telemedicine [45], and military applications [46].

1.1.4.1 Broadband Fixed Wireless Access

As mentioned above, HAPs have already been accepted by the ITU as alternative base stations of serving BFWA at the 47/48 GHz (V band) and 28/31 GHz (Ka band). BFWA communications provide in general high rate of data transmission. The ITU has defined broadband as a transmission capacity that is faster than 1.5-2 megabits per second (Mbps) [47], while the Federal Communications Commission (FCC) definition of broadband is 768 kilobits per second (Kbps). The Organization for Economic Cooperation and Development (OECD) has defined broadband as 256 Kbps in at least one direction and this bit rate is the most common baseline that is marketed as "broadband" around the world. High-speed broadband services include but are not limited to conversational services (voice/video telephony, high resolution video conferencing), streaming and broadcast services (real-time radio and television, video on demand), local multipoint distribution services (LMDS), interactive data access (broadband internet access, web browsing), and large file transfers. In addition, HAPs could potentially be used as an alternative solution for the provision of Digital Video Broadcasting (DVB) and Digital Audio Broadcasting (DAB). A feasibility study of HAPs-DVB/DAB has been conducted by European Space Agency (ESA) under STRATOS project [22]. Although these services are offered mainly to fixed terminals, their application could be extended to mobile scenarios in order to benefit from existing air interfaces and accelerate the development of new applications, such as the provision of high-speed Internet access, audio and video on demand and file transfer to cars, trains, airplanes, boats, etc. [48].

1.1.4.2 High-Speed Mobile Services

In addition to BFWA, ITU has also endorsed the use of HAPs in the IMT-2000 spectrum for the provision of 3G/UMTS mobile services, as well as enhanced HSDPA services offering data transfer speeds up to 14 Mbps on the downlink. These services are expected to have the same functionality and meeting the same service and operational requirements as traditional terrestrial tower-based

systems. HAPs can be designed to serve as the sole station in a stand-alone infrastructure (essentially, replacing the tower base station network with a “base station network in the sky”) [38]-[40]. In particular, a single HAP can replace a large number of terrestrial base stations and their backhaul infrastructure (microwave or optical links) and can serve a large city, a suburban area, a rural region [49], or even a whole state. Moreover, HAPs could be able to deliver Worldwide Interoperability for Microwave Access (WiMAX) [50], [51] mobile services based on the IEEE 802.16e standard (the most popular implementation of the IEEE 802.16 standard) at frequencies between 2-6 GHz [52]-[53]. WiMAX adopts Orthogonal Frequency Division Multiple Access (OFDMA) and enables wireless transmission of data using a variety of transmission modes at speeds up to 40 Mbps [52]-[53].

1.2 Future Trends in Wireless Communications

The growing demand for greater bandwidth, higher data rates, improved quality of service (QoS) and ubiquitous access have prompted the development of next-generation wireless communications systems, which can by far surpass the capabilities of existing systems and attempt to bring broadband applications to new experience scenarios. Fourth generation (4G) communications systems will employ a comprehensive and secure all-Internet-Protocol (IP) network and will support fixed and mobile ultra-broadband (gigabit speed) access and multi-carrier transmission [54]-[57]. New broadband applications are expected to thrive with the advent of 4G, such as multimedia broadcast and multicast services (MBMS), IP telephony, high-quality voice, high-definition television (HDTV), mobile television, ultra-broadband Internet access, gaming services, and high-quality streamed multimedia. The available data rates of 3G/HSDPA cellular networks will further be increased with the Evolved High-Speed Packet Access (HSPA+) technology [7], [8], which intends to provide theoretical data rates up to 84 Mbps on the downlink. The high performance Third Generation Partnership Project (3GPP) Long Term Evolution (LTE) technology [58], [59] will bring 3G cellular networks a step toward

to the 4G providing data rates of at least 320 Mbps on the downlink, while LTE Advanced technology will fully support the 4G requirements offering data rates up to 1 gigabit per second (Gbps) [60]. Moreover, next generation Mobile WiMAX based on the IEEE 802.16m [61] standard will support at least 100 Mbps at mobile and 1 Gbps at fixed-nomadic services, and hence will be compliant with 4G next generation mobile networks.

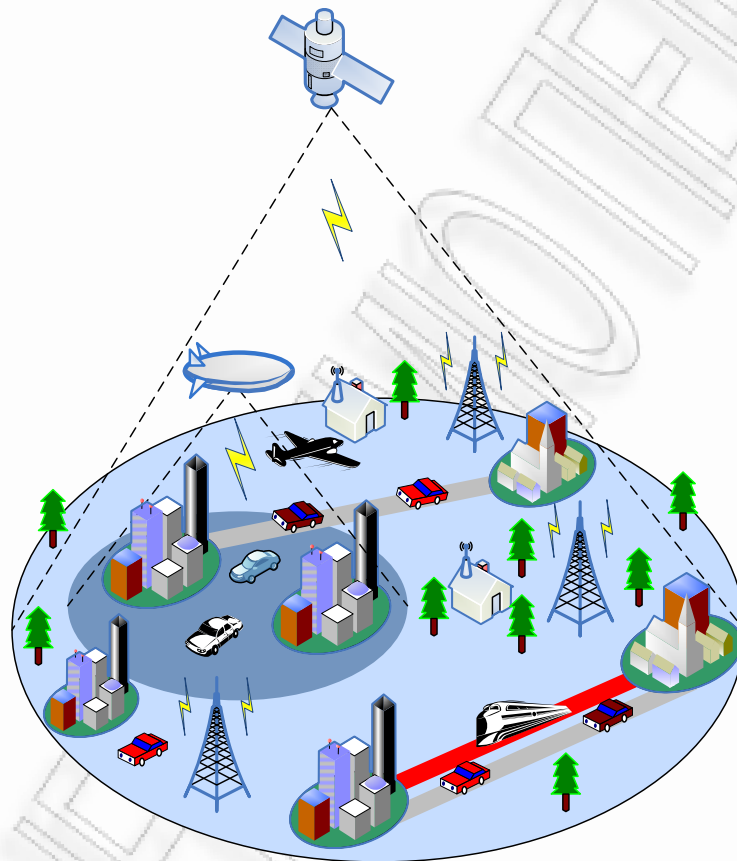


Figure 5: Visualization of an integrated satellite-HAP-terrestrial 4G wireless communications system providing fixed and mobile broadband services.

Indeed, the term 4G is widely used to include several types of broadband fixed and mobile wireless communications systems. As shown in Figs. 5 and 6, 4G systems will seamlessly integrate the entire communications infrastructure (terrestrial base stations, satellites, and HAPs), the modern communications terminals (mobile phones, personal digital assistants (PDAs), tablet computers, laptops, etc.), the transportation vehicles (cars, trains, airplanes, boats, etc.), the

available networks (body area networks-BANs, personal area networks-PANs, local area networks-LANs, metropolitan area networks-MANs, and wide area networks-WANs), and the next generation applications (as mentioned above) to satisfy increasing user demands [54]-[57]. Hence, complex network topologies of heterogeneous nature will be deployed. Each network has different capabilities, in terms of capacity, coverage, mobility support, cost, and is best suited for handling certain situations. However, these different networks will have to co-exist, and be complementarily and efficiently exploited. This can be achieved by introducing the reconfigurability concept [62], [63], which offers service differentiation, customization, and personalization according to the environment requirements. In particular, reconfigurability dynamically tackles the changeable behavior of wireless networks and associated equipment, specifically in the fields of radio spectrum, radio access technologies, protocol stacks, and application services.

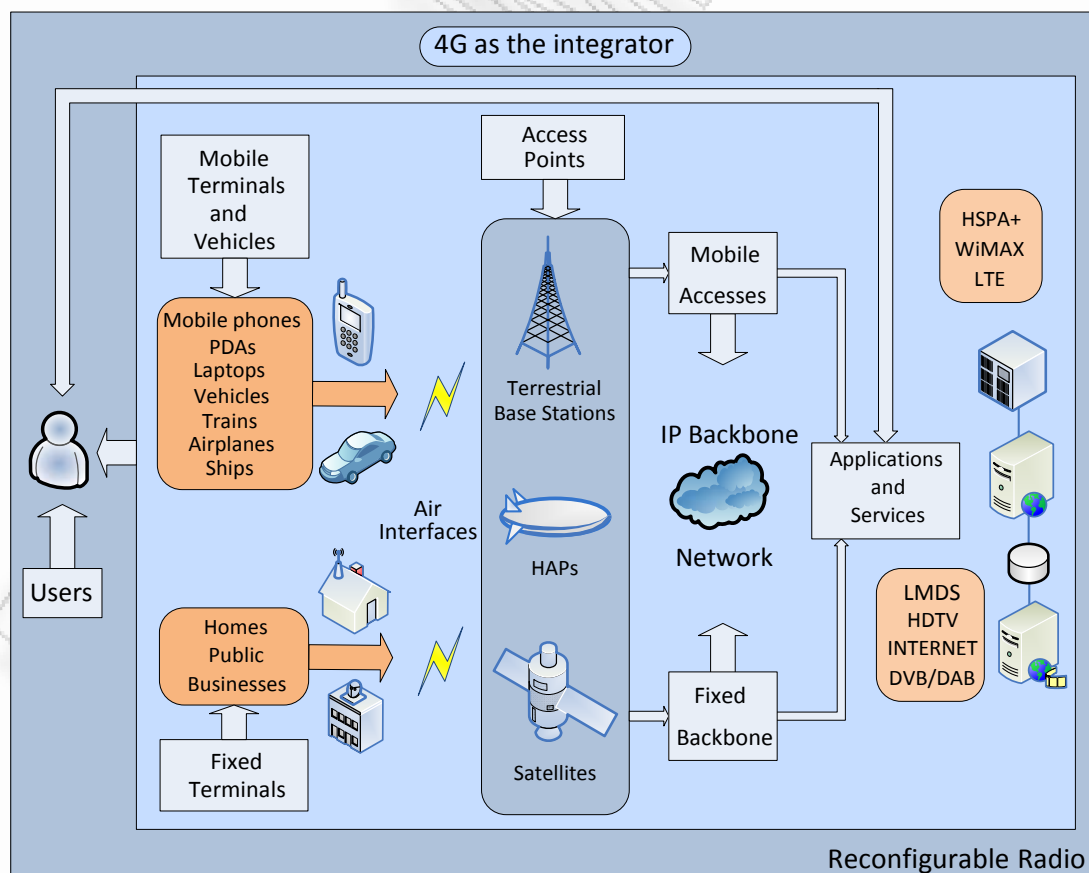


Figure 6: High level view of the future 4G wireless reconfigurable radio systems.

1.3 Thesis Motivation and Objectives

As new requirements for access to wireless networks are emerged within the communications society, HAPs can play an important role in the evolution of current and future communications systems [64]-[67]. In particular, HAPs are expected to alternatively or complementary fulfill the vision of optimal connectivity anywhere providing high data throughputs in virtually every possible scenario at low cost. However, wireless systems designers are facing a number of challenges. These include the limited availability of the radio frequency spectrum and a complex space-time varying wireless environment [68]. In addition, next generation wireless communications services will require increased network coverage, higher data rates, enhanced capacity, enriched QoS, and improved efficiency. Thus, new technologies have to continuously be under development in order to meet these growing demands.

In recent years, the multiple-input multiple-output (MIMO) technology has emerged as the most promising technology in these measures due to its powerful performance-enhancing capabilities [69]. The MIMO communications systems can be defined intuitively by considering that multiple antennas are used at both the transmitting and the receiving end. The core idea behind MIMO is the use of space-time processing in which time (the natural dimension of digital communication signals) is complemented with the spatial dimension inherent in the use of multiple spatially distributed antennas. Then, the signals sampled in the spatial domain at both ends are combined in such a way that they either create effective multiple parallel spatial data pipes (therefore increasing the data rate), and/or add diversity to improve the quality, i.e., the bit-error-rate (BER) of the communication link. This can in turn significantly improve spectral efficiency and enduringly preserve the QoS for the range of services offered. Different aspects of MIMO technology are being planned or have already been incorporated in wireless standards, such as the IEEE 802.11n, 802.16e, 802.16m, 802.20, 802.22, 3GPP Releases 7, 8, and 9, 3GPP2 ultra mobile broadband (UMB), DVB-T2 among others. Thus, MIMO technology is

seen as an ideal and critical technology of physical layer for next generation wireless communications networks.

This thesis investigates the application of MIMO techniques to HAP-based communications systems. It is well known that before the introduction of a new technology into a communications system, a large number of theoretical and experimental investigations have to be made. In particular, the successful design and deployment of HAP-MIMO communications systems requires a detailed knowledge of the wireless radio propagation channel involved in communicating between two ends of the link. Channel knowledge is required to understand various impairments, such as the attenuation, the multipath fading [70], and the space-time variations of the channel [68]. Using this knowledge, communications systems can be designed to obtain optimal or near optimal performance. This philosophy has been the driving force behind the research activity on all types of wireless communications systems. Traditional research topics include the following steps:

- Developing reference (theoretical) non-realizable channel models.
- Conducting real-world channel measurements and deriving empirical channel models from these measurements.
- Developing accurate, efficient and flexible simulation models for computer/software simulation of communications systems.
- Developing hardware-based channel emulators for real-time system analysis and performance testing.

This piece of research was driven to understand, characterize and model the HAP-MIMO channel, verify the applicability of MIMO techniques to HAP-based systems, and quantify the available MIMO gain. The approach used in this research followed a serial path of objectives. To enable successful design of HAP-MIMO

systems, this research initially focuses on the study and characterization of HAP-MIMO multipath fading channels at L and S bands. The first and second objectives of this thesis are to develop three-dimensional (3-D) theoretical models for HAP-MIMO narrowband and wideband mobile fading channels, respectively. Moreover, the third objective of this thesis is to develop 3-D simulation models for HAP-MIMO narrowband and wideband mobile fading channels. Except for delivering future mobile services, HAPs can also provide broadband fixed and mobile services at Ka- and V- bands, where the rain has a significant effect on the quality of the link. Hence, the fourth objective of this thesis is to design HAP-MIMO channel models for BFWA services, under clear sky and rain conditions.

1.4 Research Contributions and Author's Publications

The major achievements and novelty in this thesis are:

1. Design and development of a novel 3-D parametric reference model for narrowband HAP-MIMO channels and analysis of space-time correlation and channel capacity.
2. Design and development of a novel 3-D parametric reference model for wideband HAP-MIMO channels and analysis of statistical properties.
3. Design and development of novel 3-D deterministic simulation models for narrowband and wideband HAP-MIMO mobile fading channels.
4. Design and development of novel 3-D statistical simulation models for narrowband and wideband HAP-MIMO mobile fading channels.
5. Design and development of a novel 3-D channel model for fixed HAP-MIMO communications in mm-wave frequencies.

Part of this thesis resulted in publications in several international journals and conference proceedings (including a Best Paper Award), and in contribution to the European COoperation in Science and Technology (COST) Action IC0802 entitled

“Propagation Tools and Data for Integrated Telecommunication, Navigation, and Earth Observation Systems”.

• Journal Publications

- [1] **E. T. Michailidis** and A. G. Kanatas, “Three-Dimensional HAP-MIMO Channels: Modeling and Analysis of Space-Time Correlation,” *IEEE Transactions on Vehicular Technology*, vol. 59, no. 5, pp. 2232-2242, Jun. 2010.
- [2] P.-D. Arapoglou, **E. T. Michailidis**, A. D. Panagopoulos, A. G. Kanatas, and R. Prieto-Cerdeira, “The Land Mobile Earth-Space Channel: SISO to MIMO Modeling from L- to Ka-Bands,” *IEEE Vehicular Technology Magazine, Special Issue on Trends in Mobile Radio Channels: Modeling, Analysis, and Simulation*, vol. 6, no. 2, pp. 44-53, Jun. 2011.
- [3] **E. T. Michailidis** and A. G. Kanatas, “Statistical Simulation Modeling of 3-D HAP-MIMO Channels,” accepted for publication in *Wireless Personal Communications*.
- [4] **E. T. Michailidis** and A. G. Kanatas, “Capacity Analysis and Simulation of 3-D Space-Time Correlated HAP-MIMO Channels,” accepted for publication in *International Journal on Advances in Telecommunications*. **Invited paper**
- [5] **E. T. Michailidis** and A. G. Kanatas, “Wideband HAP-MIMO Channels: A 3-D Modeling Approach,” submitted to *IEEE Transactions on Wireless Communications*.

• Conference Publications

- [1] **E. T. Michailidis** and A. G. Kanatas, “A Three Dimensional Model for Land Mobile-HAP-MIMO Fading Channels,” in *Proc. 10th International Workshop on Signal Processing for Space Communications (SPSC) 2008*, pp. 1-6, Rhodes, Greece, 6-8 Oct. 2008.
- [2] **E. T. Michailidis**, G. Efthymoglou, and A. G. Kanatas, “Spatially Correlated 3-D HAP-MIMO Fading Channels,” in *Proc. International Workshop on Aerial & Space Platforms: Research, Applications, Vision of IEEE Global Communications Conference (Globecom) 2008*, pp. 1-7, New Orleans, LA, USA, 4 Dec. 2008.
- [3] **E. T. Michailidis** and A. G. Kanatas, “Capacity Optimized Line-of-Sight HAP-MIMO Channels for Fixed Wireless Access,” in *Proc. International Workshop on Satellite and Space Communications (IWSSC) 2009*, pp. 73-77, Siena-Tuscany, Italy, 10-11 Sep. 2009.
- [4] **E. T. Michailidis** and A. G. Kanatas, “On the Capacity of 3-D Space-Time Correlated HAP-MIMO Channels,” in *Proc. 2nd International Conference on Advances in Satellite and Space Communications (SPACOMM) 2010*, Athens-Glyfada, Greece, 13-19 Jun. 2010. **Best Paper Award**
- [5] **E. T. Michailidis** and A. G. Kanatas, “Modeling and Simulation of 3-D Wideband HAP-MIMO Channels,” accepted for publication in *IEEE 74th Vehicular Technology Conference (VTC Fall) 2011*, San Francisco, USA, 5-8 Sep. 2011.

- **Contribution to COST Action IC0802**

- [1] **E. T. Michailidis** and A. G. Kanatas, "Three-dimensional HAP MIMO Channels: Modeling and Analysis of Spatial Correlation," *COST Action IC0802, 1st MCM*, ESA/ESTEC, Noordwijk, Netherlands, 9-11 Mar. 2009.
- [2] **E. T. Michailidis** and A. G. Kanatas, "Effect of 3-D Spatial Correlation on the Capacity of HAP-MIMO Channels," *COST Action IC0802, 3rd MCM*, NTUA, Athens, Greece, 26-28 Apr. 2010.
- [3] **E. T. Michailidis** and A. G. Kanatas, "A Three-Dimensional Statistical Simulation Model for HAP-MIMO Channels," *COST Action IC0802, 3rd MCM*, NTUA, Athens, Greece, 26-28 Apr. 2010.

1.5 Thesis Outline

The remainder of this thesis is organized as follows. Chapter 2 thoroughly presents the basic concepts of radio propagation, describes the characteristics of MIMO technology, and surveys existing models for earth-space radio channels.

Chapter 3 proposes a 3-D reference model for narrowband HAP-MIMO channels, studies the channel statistics, defines and investigates the HAP-MIMO channel capacity, and provides numerical results.

Chapter 4 proposes 3-D deterministic and statistical simulation models for HAP-MIMO mobile fading channels and provides simulation results to validate the theoretical results of the reference model.

Chapter 5 proposes a 3-D reference model for wideband HAP-MIMO channels, studies its statistical properties, and provides numerical results. This chapter also proposes simulation models for wideband HAP-MIMO channels and provides simulation results to validate the reference model.

Chapter 6 proposes a HAP-MIMO channel model for BFWA services at mm-wave frequencies, suggests capacity optimization techniques, and provides numerical results to demonstrate the theoretical derivations.

Finally, Chapter 7 concludes this thesis and addresses open research areas in MIMO channel modeling for wireless communications systems based on HAPs.

Chapter 2

Overview on Propagation Mechanisms, MIMO Principle, and Channel Modeling

2.1 Introduction

The analysis, the design, the operation, and the performance of a wireless communications network are heavily dependent on the characteristics of the wireless propagation channel. Indeed, communicating through a wireless channel is a challenging task because the medium may introduce severe impairments [2], [71]-[74]. Hence, an accurate and thorough characterization of the propagation effects influencing radio waves propagating in a wireless channel is essential, in order to design and implement reliable and efficient HAP-MIMO channel models. These propagation effects vary depending on the operating frequency. Thus, it is important to emphasize considerable differences between the communications systems operating at low frequency bands and the ones operating in upper bands. With these in mind, this chapter aims to describe in detail the fundamental propagation mechanisms that influence the links between HAPs and terrestrial fixed/mobile stations at the licensed L-, S-, Ka-, and V- frequency bands. Moreover, this chapter describes the MIMO principle, reviews existing models for earth-space radio channels, and provides an introduction to HAP-MIMO channel modeling.

2.2 The Wireless Propagation Channel

The propagation characteristics crucially determine the performance of any potentially adopted MIMO technique. This section reviews the most important channel impairments. Particular emphasis is given to issues related to the rain effects and the multipath propagation, which dramatically affect MIMO

performance and control MIMO applicability to fixed and mobile HAP-based systems at frequencies well above 10 GHz and well below 10 GHz, respectively.

The architecture of a generic wireless communications system is illustrated in Fig. 7. Based on this architecture, the transmitter sends a signal through a wireless communications channel, the channel itself distorts the signal in such ways that may be unpredictable to the receiver, and the receiver must be designed to overcome these modifications to deliver the signal to its final destination with as few distortions as possible. Specifically, in the wireless channel, there are multiplicative and additive effects [2], [71], [72].

The multiplicative effects arise from the various processes encountered by the transmitted waves on their way from the transmit end to the receive end. It is conventional to further subdivide the multiplicative processes in the channel into two types of fading, the *large-scale fading* and the *small-scale fading*. The large-scale fading is due to the shadowing of the transmitted signal by objects and scatterers in the channel and is referred to as shadow fading, while the small-scale fading is caused by the multipath propagation and is referred to as multipath fading [2], [71], [72]. Shadow fading and multipath fading will be discussed later in this section.

On the contrary, the additive effects arise from the noise generated within the receiver itself (although external noise contributions may also be significant) and their impact on the performance of a communications system is important, since they determine the received signal-to-noise ratio (SNR). The additive white Gaussian noise (AWGN) is a good example of additive impairments and corresponds to a random process with each realization modeled as a random variable following a Gaussian distribution. The average received SNR is expressed as

$$\text{SNR} = P_R(\text{dB}) - P_N(\text{dB}). \quad (1)$$

The received signal power P_R is given by

$$P_R(\text{dBW}) = P_T(\text{dBW}) + G_T(\text{dBi}) + G_R(\text{dBi}) - L(\text{dB}), \quad (2)$$

where P_T is the transmitted power, G_T and G_R are the transmit and receive antenna gains, respectively, and L is the path loss. The noise power P_N is given by

$$P_N \text{ (dBW)} = 10 \log(N_0 B) = 10 \log(k T_e B), \quad (3)$$

where N_0 is the noise power spectral density (PSD), B is the channel bandwidth, k is the Boltzmann's constant ($1.38 \cdot 10^{-23}$ Joules/Kelvin), and T_e is the system noise temperature.

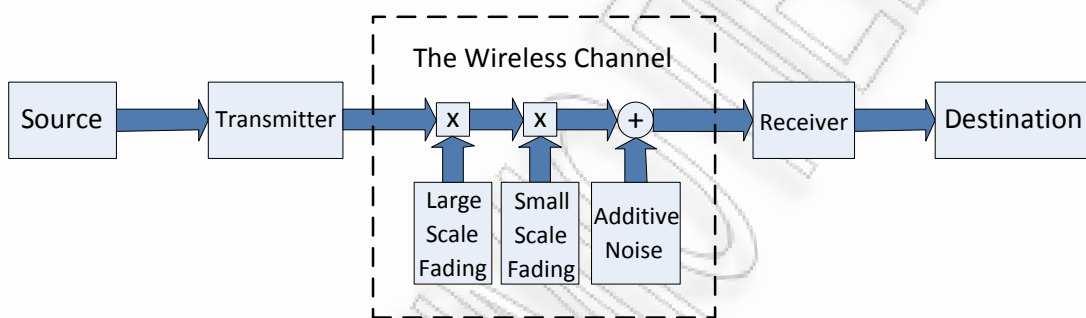


Figure 7: Architecture of a generic wireless communications system.

2.2.1 Path Loss

The path loss (or path attenuation) in any wireless communications radio link is an important effect that contributes to signal degradation by reducing its power. The value of the path loss is usually expressed in decibels (dB) and is highly dependent on many factors, such as the terrain contours, the propagation environment (urban or rural, vegetation and foliage), the propagation medium (dry or moist air), the distance between the transmitter and the receiver, and the height and location of antennas. In the study of wireless communications, path loss is usually represented by the path loss exponent [2]. Path loss models for predicting path loss in urban environments are described in [75], [76].

For a link between HAPs and terrestrial stations, the minimum (reference) path loss is given by the free-space loss (FSL) L_F , which assumes a line-of-sight (LoS) link

between the transmitter and the receiver and propagation in free-space and is given by [11], [37]

$$L_F (\text{dB}) = 32.4 + 20 \log d_{\text{km}} + 20 \log f_{\text{MHz}}, \quad (4)$$

where f_{MHz} is the carrier frequency in MHz, and d_{km} is the distance between the transmitter and the receiver in km. Nevertheless, the signals do not experience free-space propagation due to other sources of loss, such as obstacles in the first Fresnel zone, rain attenuation [11], [37], [77]-[79], gaseous absorption (oxygen absorption and water vapour) [78], cloud attenuation, and attenuation due to vegetation [80], [81]. The summation of any losses caused by the aforementioned propagation effects is considered as the excess loss L_{ex} . Hence, the total loss is given by

$$L(\text{dB}) = L_F (\text{dB}) + L_{ex} (\text{dB}). \quad (5)$$

Note that rain attenuation is the dominant mechanism that significantly affects the quality of the link at frequencies above 10 GHz [11].

2.2.2 Rain Effects

The rain is confined to the first 2.5-5 km of the atmosphere depending on the latitude [11]. Hence, an EM wave propagating in the troposphere is directly affected by rain effects (see Fig. 8). Rain effects primarily refer to the attenuation of a signal. The troposphere consists of a mixture of particles having a wide range of sizes and characteristics. The attenuation is the result of the conversion of EM energy to thermal energy within an attenuating particle. This attenuation increases with the number of raindrops along the path, the size of the drops, the length of the path through the rain, and the carrier frequency. The main particles of interest are hydrometeors, including raindrops, fog and clouds. Note that attenuation is negligible for snow or ice crystals, in which the particles are tightly bound and do not interact with the waves.

The rain attenuation L_r can be empirically obtained using the specific rain attenuation γ_r (dB/km) [82], which is defined as

$$\gamma_r = a_r R_r^{b_r}, \quad (6)$$

where R_r is the rain rate measured on the ground in millimeters per hour (mm/h) and is strongly dependent on the geographical location. Worldwide rain rate contour maps can be found in [83]. Typical rain rate values for Europe are around 30 mm/h, while for some Mediterranean regions the rain rate exceeds 50 mm/h and for equatorial regions the rain rate may reach 150 mm/h. The rain rate corresponds to the measure of the average size of the raindrops. However, the period of time for which the rain rate exceeds a certain value is more important than the total amount of rain falling during a year. The values of the empirical regression coefficients a_r and b_r can be obtained from [82] and depend on the climatic zone, the transmission frequency, and the polarization.

Table 4 shows typical values for a_r and b_r at various frequencies for horizontal and vertical polarization extracted from [82], while Fig. 8 utilizes (6) and demonstrates the specific rain attenuation as a function of the rain rate for different carrier frequency. One observes that the rain attenuation is only significant to communications systems operating above 10 GHz. At these frequencies, the wavelength and raindrop size (about 1.5 millimeters) are comparable and the attenuation is quite large. Thus, HAP-based communications systems operating at Ka- and V- frequency bands are susceptible to rain, while the ones operating at L- and S- frequency bands are not significantly affected by rain.

The total rain attenuation L_r can be obtained as follows

$$L_r = \gamma_r d_r, \quad (7)$$

where d_r is the total rainy path length and can be geometrically obtained as follows (see Fig. 9)

$$d_r = (H_r - H_R) / \sin \beta_T, \quad (8)$$

where H_r is the effective rain height, H_R is the height of the terrestrial station, and β_T is the elevation angle of the platform. Representative values for H_r vary according to the latitude of the terrestrial station [11], [37]. In practice, high rain attenuations are sometimes avoided by using site diversity [84], [85], in which two widely separated terrestrial stations are used. Then, the probability that both terrestrial stations are within the same area of rain concentration is small. Alternatively, a portion of spectrum in a lower frequency band may be used.

TABLE 4
REGRESSION COEFFICIENTS FOR ESTIMATING SPECIFIC RAIN ATTENUATION

FREQUENCY	HORIZONTAL POLARIZATION		VERTICAL POLARIZATION	
	a_r	b_r	a_r	b_r
2 GHz	0.000154	0.963	0.000138	0.923
10 GHz	0.0101	1.276	0.00887	1.264
20 GHz	0.0751	1.099	0.0691	1.065
30 GHz	0.187	1.021	0.167	1.000
40 GHz	0.350	0.939	0.310	0.929
50 GHz	0.536	0.873	0.479	0.868

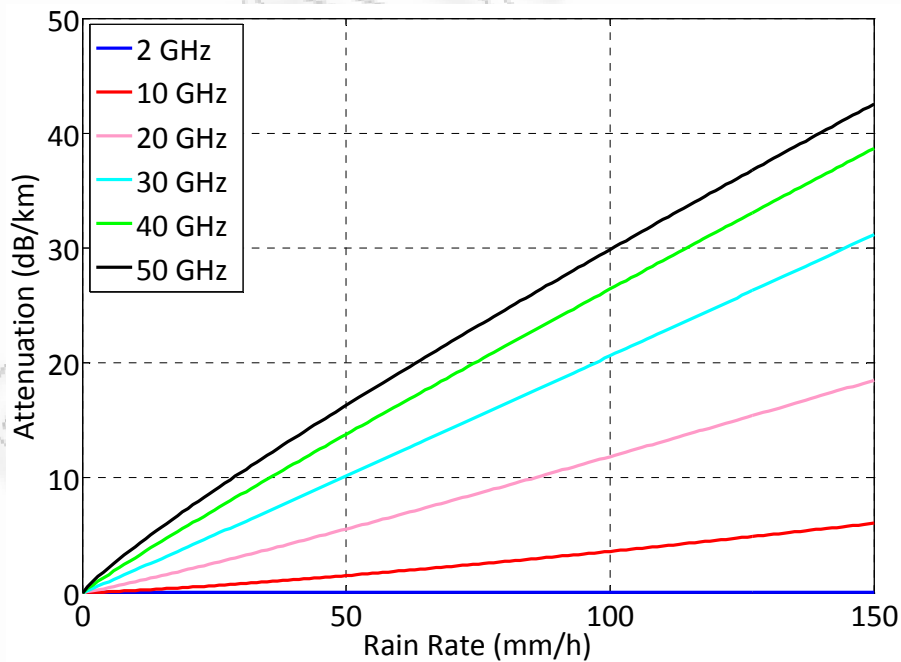


Figure 8: The specific rain attenuation as a function of the rain rate for different carrier frequency.

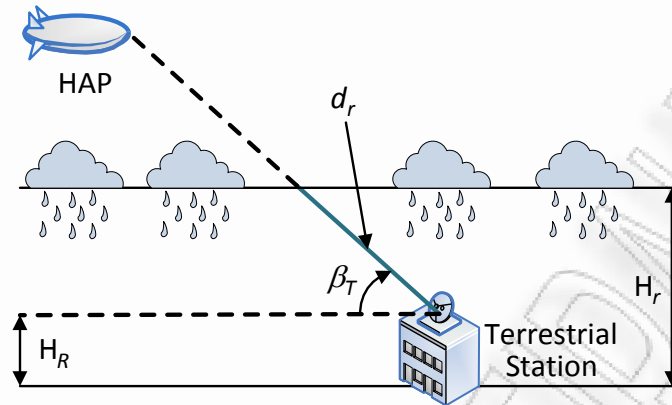


Figure 9: Rain attenuation path geometry.

The aforementioned empirical modeling of the long-term behavior of the rain attenuation effects does not convey any information on the time dynamics of these effects. An alternative and more accurate way of modeling the rain attenuation is through the use of time-series [86]. Since rain is characterized by a significant spatial inhomogeneity within the distances of interest, rain attenuation time-series can be obtained using actual meteorological data accumulated over many years of carefully performed propagation measurements. The possibility of making a computer synthesis of these time-series allows for the implementation of statistical channel models, which are characterized by short-term statistics.

Apart from introducing signal attenuation, rain also introduces scattering processes [87], [88]. This scattering results from redirection of the radio waves in various directions, so that only a fraction of the incident energy is transmitted onwards in the direction of the receiver. The scattering process is strongly frequency-dependent, since wavelengths which are long compared to the particle size will be only weakly scattered.

2.2.3 Shadow Fading

The predicted path loss for a system operated in a particular environment is constant for a given distance. However, the emitted EM waves often do not reach the receive antenna directly due to obstacles that block the LoS link resulting in

random variations of the received power with respect to the nominal value given by the path loss models. This effect is called shadowing or slow (long term) fading and controls the reliability of coverage and the link budget [2], [71]. The density of the obstacles significantly depends on the physical environment. The randomness in this environment is captured by modeling the density of obstacles and their absorption behavior as random numbers. The amplitude variations caused by shadowing is often modeled using a log-normal distribution with a standard deviation according to the log-distance path loss model. The interested reader is referred to [89], [90] for a detailed discussion of the shadow fading characteristics for HAP-based systems. This thesis focuses only on the multipath fading, since this is the dominant fading mechanism that affects the performance of MIMO systems [68], [69].

2.2.4 Multipath Fading

Although LoS conditions are required in the Ka- and V- frequency bands [11], [37] due to the severe attenuation of possible obstructed signal components, non-line-of-sight (NLoS) connections can be used and should also be evaluated for HAP-based communication systems operating in L- and S- frequency bands. Then, it is considered that a signal propagating through a wireless channel usually arrives at its destination along a number of different paths, referred to as multipath components, which arise from single-bounce and/or multiple-bounce scattering, reflection or diffraction of the radiated energy by fixed and/or mobile intervening objects in the environment [2], [71], [91]. These mechanisms affect the amplitude, the direction, and the phase of the propagating radio waves and this effect is known as multipath fading or fast (short term) fading owing to the random rapid fluctuations of the transmitted wave over small areas. Indeed, these fluctuations result in the spreading of the transmitted wave in Doppler and/or time delay and/or angular domain. The received wave is a superposition of the impinging multipath components. Depending on the phase of each partial wave, this superposition can be constructive or destructive. The phase relationships depend

on the speed of motion, frequency of transmission and relative path lengths. Fig. 10 presents a typical scenario affected by multipath fading. One observes that the LoS component reaches the receiver directly. However, single-bounce and double bounce NLoS rays arrive also to the receiver causing multipath.

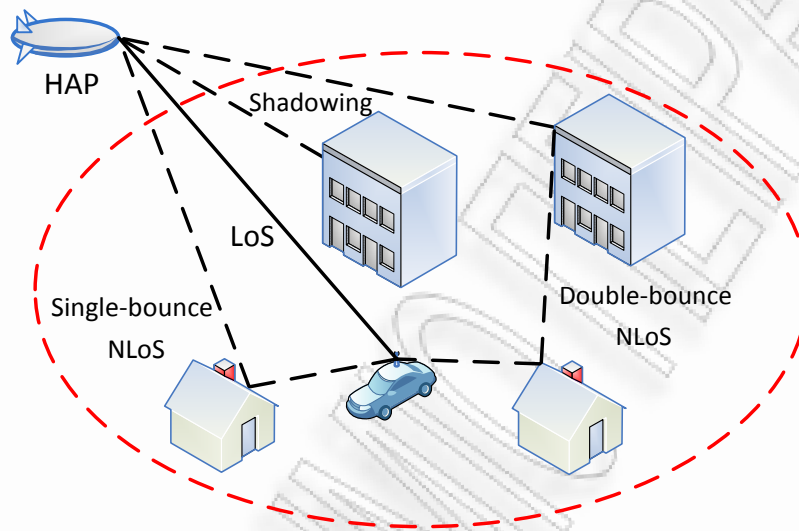


Figure 10: Visualization of a multipath propagation environment.

2.2.5 Time, Frequency, and Space Selectivity

Time selectivity refers to a time-varying multipath channel originated by the motion of the transmitter and/or the receiver and/or the scattering elements [68]-[70]. When viewed in the frequency domain by applying Fourier transform (FT) to the time correlation function, time selectivity appears as different Doppler (frequency) shifts of the individual multipath components over a finite spectral bandwidth and corresponds to a frequency dispersion of the Doppler power spectrum of the transmitted signal. The value of this dispersion and the corresponding maximum Doppler frequency mainly depend on the angle between the direction of motion of the terrestrial mobile station and direction of arrival of the scattered waves, and the amplitudes of the received partial waves. Based on the rate with which the channel impulse response changes relative to the signal transmission rate, channels may be classified as fast fading, i.e., the channel

changes within the transmitted symbol duration, or slow fading, i.e., the channel is approximately constant within symbol duration. A good measure of channel time selectivity is given by the channel coherence time (in the time domain), i.e., the time duration for which the channel can be considered as approximately time-invariant. The larger the coherence time, the slower the channel fluctuation, or equivalently the Doppler spread (in the frequency domain).

Frequency selectivity refers to a frequency-varying multipath channel. When viewed in the time domain by applying inverse Fourier transform (IFT) to the frequency correlation function, frequency selectivity appears as different time delays of the individual multipath components over a finite spectral bandwidth, which corresponds to a time dispersion of the power delay spectrum of the transmitted signal. The span of the delays is called the delay spread. Delay spread causes frequency selective fading as the channel acts like a tapped delay line filter. Based on their degree of frequency selectivity, channels may be classified as frequency-flat or frequency-selective channels. In particular, if all the transmitted frequencies undergo approximately identical amplitude and phase changes, the channel is called frequency-flat. Otherwise, the channel is called frequency-selective and the transmission is wideband. Frequency selectivity is measured in terms of the coherence bandwidth, i.e., the bandwidth over which the channel's frequency response remains constant. The channel can be considered frequency-flat only if the transmission is narrowband compared to the channel's coherence bandwidth. Otherwise, the channel is frequency-selective.

Finally, space selectivity refers to a space-varying multipath channel. When viewed in the angle domain by applying FT to the spatial correlation function, spatial selectivity appears as different azimuth and/or elevation angles of arrival (or departure) of the multipath components at the receive (or transmit) antenna array over a finite spectral bandwidth, which corresponds to an angular dispersion of the power azimuth spectrum and/or the power elevation spectrum of the transmitted signal. Hence, the signal amplitude depends on the spatial location of the antennas. Space selectivity is measured in terms of the coherence distance, i.e., the spatial

separation for which the channel's spatial response remains constant, which is inversely proportional to the angle spread.

Fig. 11 illustrates the relationship through FT between the variances of time Δt , frequency Δf , and space (represented by the receive $\Delta \mathbf{x}_R$ and transmit $\Delta \mathbf{x}_T$ antenna position vectors) and the spreads of Doppler frequency shift ν , propagation delay τ , and direction of arrival or departure (represented by the receive Ω_R and transmit Ω_T direction vectors, respectively).

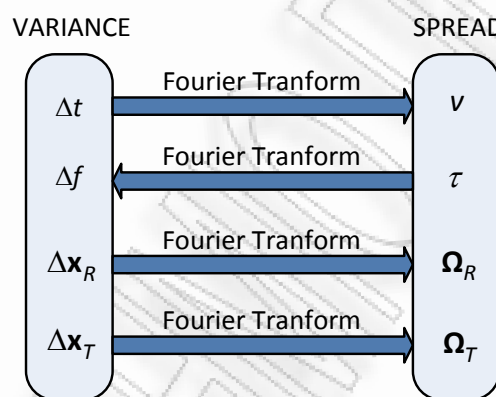


Figure 11: The relationships of the time, frequency, and space domains.

2.2.6 The Diversity Concept

The randomness of the communications channel can be exploited to enhance the performance of a communications system through diversity [2], [68]-[70]. Diversity refers to a method that improves the reliability of the transmission of a signal by using two or more individual communication channels with different characteristics, i.e., different level of fading and interference. In particular, the probability that all channels are simultaneously in a fade condition reduces dramatically. Hence, diversity helps stabilizing the link through channel hardening, which leads to improved performance in terms of the BER. Diversity techniques exploit the multipath fading, resulting in diversity gain. Since multipath fading may take place in time, frequency, and space, diversity techniques may similarly be exploited in each of these domains.

Time diversity can be obtained if multiple versions of the same signal are transmitted at different time instants. Adding a redundant forward error correction code, the message is spread in time by means of bit-interleaving before it is transmitted. Thus, error bursts are avoided, which simplifies the error correction procedure.

Frequency diversity exploits the temporal spreading of the channel through equalization techniques or multi-carrier modulations. Thus, the signal is transmitted using several frequency channels or spread over a wide spectrum that is affected by frequency-selective fading. Naturally, both time and frequency diversity techniques incur a loss in time or bandwidth to allow for the introduction of redundancy.

Although conventional single-input single-output (SISO) systems, i.e., systems utilizing one antenna only at both the transmitter and the receiver, can exploit time and frequency diversity, spatial diversity can be obtained using multiple transmit antennas (transmit diversity) and/or multiple receive antennas (receive diversity). Indeed, single-input multiple-output (SIMO) systems, i.e., systems utilizing one antenna at the transmitter and multiple antennas at the receiver, multiple-input single-output (MISO) systems, i.e., systems utilizing multiple antennas at the transmitter and one antenna at the receiver, and MIMO systems, i.e., systems utilizing multiple antennas at both the transmitter and the receiver, are the potential candidates for providing spatial diversity schemes.

The multi-user MIMO (MU-MIMO) systems also intend to provide diversity by exploiting the availability of multiple independent terminals [92]. Hence, enhancement of the communications capabilities of each individual terminal can be obtained. Although single-user MIMO (SU-MIMO) techniques only consider access to multiple antennas that are physically connected to each individual terminal, MU-MIMO can be seen as the extended concept of space-division multiple access (SDMA) that allows a terminal to transmit (or receive) signal to (or from) multiple users in the same band simultaneously. Fig. 12 demonstrates the aforementioned architectures.

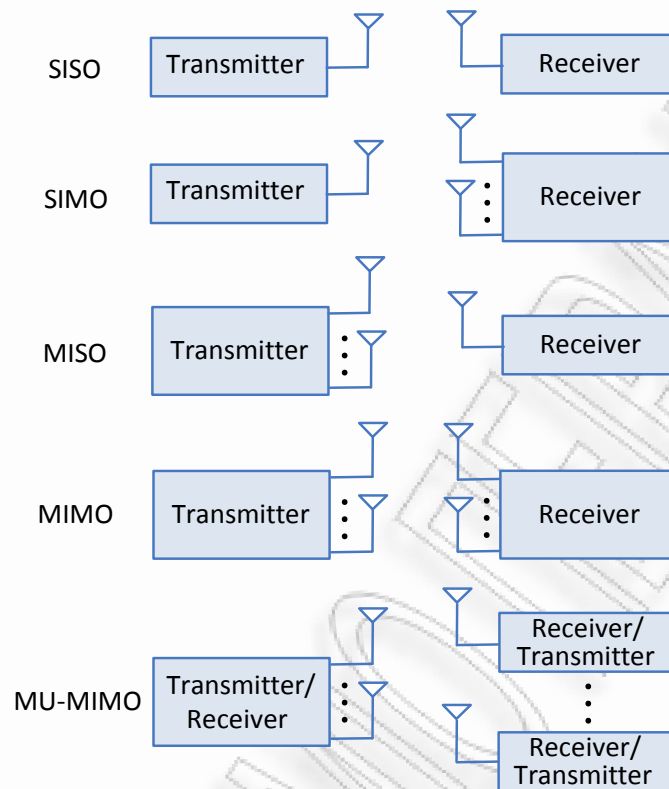


Figure 12: Basic representation of SISO, SIMO, MISO, MIMO, and MU-MIMO systems.

Finally, diversity techniques may also exploit the polarization of antennas. Specifically, multiple versions of a signal are transmitted and received via antennas with different polarization [93], [94]. Polarization diversity can overcome possible space limitation and still achieve the advantages predicted by MIMO theory.

2.3 The MIMO Technology

As modern communications services demand increased channel capacity and the radio spectrum is a limited resource, the research efforts have been focused on the design and development of highly reliable and high-speed wireless communication systems. It is well known that multipath propagation severely affects the quality, the reliability, and the performance of SISO communications systems. Although diversity through SIMO and MISO systems was the first step to mitigate multipath propagation, the emergence of MIMO systems has effectively

converted the multipath effect into a benefit for the communications systems [95], [96]. In a very general way, MIMO technology improves the quality of the received signal and increases the data rate by using digital signal processing techniques to shape and combine the transmitted signals from multiple wireless paths created by the use of multiple receive and transmit antennas. The advent of MIMO technology represents one of the most important advancements in wireless communications and has attracted attention worldwide, since it offers a number of benefits that help achieve significant performance gains and meet the challenges posed by the impairments in the wireless channel as well as resource constraints.

2.3.1 Benefits

The major benefits of MIMO techniques are *array gain*, *spatial diversity gain*, and *spatial multiplexing gain*. Although SIMO and MISO systems offer array gain and spatial diversity gain, only MIMO systems can exploit environments with rich scattering and take advantage of spatial multiplexing gain, which offers a potential increase in channel capacity beyond the Shannon capacity for SISO systems at no cost of extra radio spectrum and/or transmitted power [68]-[70].

Array gain refers to a coherent combining of the transmitted signals at the receiver. In particular, the same signal is emitted from each of the transmit antennas with appropriate phase and amplitude weightings such that the signal power is maximized at the receiver input. This coherent combining realized through spatial processing at the receive antenna array and/or spatial pre-processing at the transmit antenna array improves the resistance to noise and increases the signal gain from constructive interference. Hence, array gain increases the average receive SNR and improves the coverage and range of a wireless communications network. However, this coherent combining requires knowledge of the channel state information (CSI).

Spatial diversity is realized by providing the receiver with multiple (ideally independent) copies of the transmitted signal separated in space. Then, as the

number of these copies increases, the probability that at least one of these copies do not experience deep fading also increases. A MIMO channel with n_T transmit antennas and n_R receive antennas potentially offers $n_T \times n_R$ independently fading links, and hence a spatial diversity order of $n_T \times n_R$. Spatial diversity techniques can be applied using space-time coding, when there is no CSI knowledge. Then, the array gain cannot be exploited.

Spatial multiplexing requires MIMO antenna configuration and takes full advantage of the spatial dimension of the propagation radio channel offering a linear increase in data rate by transmitting multiple, independent data streams within the bandwidth of operation [95]. In particular, a high rate signal is divided into multiple lower rate streams and each stream is transmitted from a different transmit antenna in the same frequency channel. Under suitable channel conditions, such as rich scattering in the propagation environment, these data streams arrive at the receiver antenna array with sufficiently different spatial signatures and can be separated at the receiver end. Each data stream experiences at least the same channel quality that would be experienced by a SISO scenario. Thus, the capacity is effectively enhanced by a multiplicative factor equal to the number of streams. In general, the number of data streams that can be reliably supported by a MIMO channel equals the minimum of the number of transmit and receive antennas, i.e., $\min\{n_T, n_R\}$. Spatial multiplexing can be used with or without transmit channel knowledge, but the practical gain is limited by correlation, which means that some of the parallel streams may have very weak channel gains [97]-[99].

2.3.2 Channel Statistics

Considering a MIMO communications system with n_T transmit antennas and n_R receive antennas and assuming frequency non-selective (flat fading) over the bandwidth of interest, the MIMO radio channel at a given time instant may be represented as a $n_R \times n_T$ matrix \mathbf{H} as follows [68], [69]

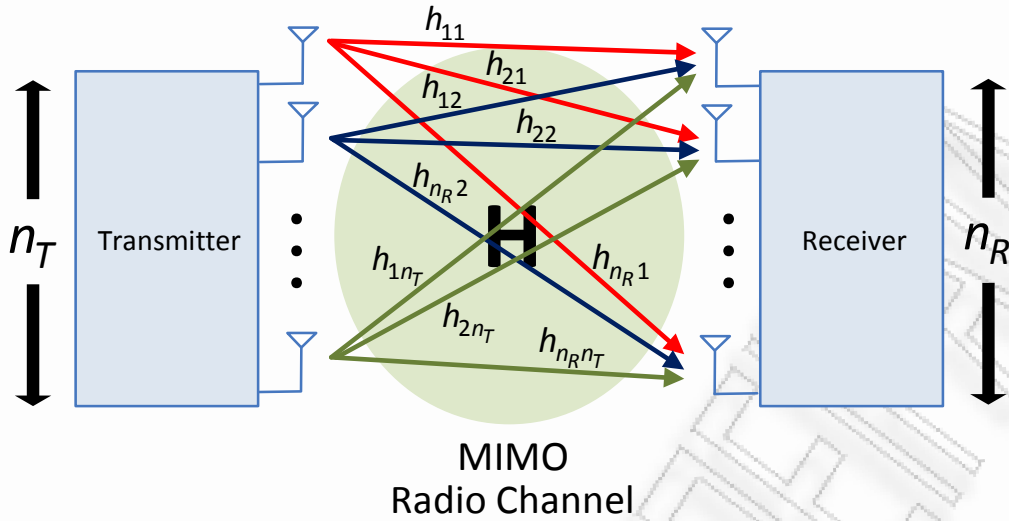


Figure 13: Visualization of the MIMO radio channel.

$$\mathbf{H} = \begin{bmatrix} h_{11} & h_{12} & \cdots & h_{1n_T} \\ h_{21} & h_{22} & \cdots & h_{2n_T} \\ \vdots & \vdots & \ddots & \vdots \\ h_{n_R 1} & h_{n_R 2} & \cdots & h_{n_R n_T} \end{bmatrix}, \quad (9)$$

where h_{ij} is the (SISO) channel gain between the i^{th} receive and j^{th} transmit antenna pair. Note that channel capacity linearly increases according to rank^1 of the channel matrix \mathbf{H} . Fig. 13 visualized the MIMO radio channel.

In the presence of a sufficiently large (theoretically infinite) number of non-coherent diffuse components in dense scattering propagation environment, the fading is described by a Rayleigh distribution [70], [100], the channel matrix is full-rank, and the elements of this matrix are uncorrelated, i.e., independent and identically distributed (i.i.d.). However, when a strong LoS signal also arrives at the receiver, the fading is described by a Rician distribution. Considering coherent diffuse components or sparse scattering and increased correlation in space and/or time and/or frequency, the rank of the channel matrix is deficient and the spectral efficiency is low. Indeed, the degree of correlation is a complicated function of the

¹The rank of a matrix is equal to the number of linearly independent rows (or columns) of the matrix or equivalently the number of non-zero eigenvalues.

degree of scattering in a specific propagation environment and the antenna inter-element spacing at both the transmitter and the receiver. Hence, an increase in this spacing is not sufficient to ensure decorrelation between the responses in the MIMO channel matrix. On the other hand, dense scattering in the propagation environment in combination with adequate² antenna spacing ensures decorrelation. These two factors control the performance measures, i.e., the diversity gain and the spatial multiplexing gain, and therefore the applicability of MIMO techniques to any communications system.

A HAP-based communications channel is expected to be Ricean in its general form, i.e., Rice distribution can be employed to describe the statistics of the channel [11]. Considering this general case of Ricean fading, the HAP-MIMO channel matrix can be modeled as [68]

$$\mathbf{H} = \sqrt{\frac{K}{K+1}} \mathbf{H}_{LoS} + \sqrt{\frac{1}{K+1}} \mathbf{H}_{NLoS}, \quad (10)$$

where \mathbf{H}_{LoS} is the $n_R \times n_T$ matrix containing the free-space LoS responses among the n_T and n_R antenna elements, \mathbf{H}_{NLoS} is the $n_R \times n_T$ matrix containing the responses due to the scattered waves (NLoS), and K is the Ricean factor, which expresses the relative power of the direct and scattered components of the received signal and provides an indication of the link quality. When $K=0$ the channel is described by a Rayleigh distribution, whereas a very large value of K , i.e., $K \rightarrow \infty$, implies the presence of a Gaussian channel. Recent studies have shown that the performance of MIMO systems depends on K [101]. In particular, as K increases, the correlation between MIMO subchannels increases [102]. Hence, efficient and accurate methods for estimating K are of considerable interest [103]. Several values of K have been reported in the literature from measurement campaigns and studies performed in the L and S frequency bands, for satellite [104] and HAP-based [105] communications systems. According to these measurements, the value of K depends on the elevation angle of the

²Antenna spacing equal to half wavelength is usually required for terrestrial mobile terminals [96].

satellite/platform and the operating frequency. In particular, the results of propagation measurements conducted in a semi-urban area [105] showed that K varies between 0.9 and 18.6 dB at frequency 1.2 GHz, and between 1.4 and 16.8 dB at frequency 2.4 GHz, for the elevation angle ranging from 10° to 90° . Nevertheless, the value of K also depends on the propagation area, and the degree of urbanization. Thus, K is expected to be lower in highly urbanized areas, where the scatterers are usually dense and tall. Note that HAP and/or user movement and HAP displacement cause a continuous change in the sub-platform point and in the elevation angle of platform. Thus, the Ricean factor K also varies with the elevation angle variation.

2.4 The Earth-Stratosphere Channel: From SISO to MIMO Modeling

Since many factors influence the channel propagation characteristics, it is of great interest to properly characterize and model the HAP-MIMO channel for different conditions. Then, efficient and reliable HAP-MIMO systems can be designed and accurately evaluated, before their implementation. This section provides an overview of the available HAP-SISO models and discusses some open issues related to channel features not sufficiently reproduced by these models in order to support MIMO extension. In addition, this section outlines the various MIMO channel modeling approaches and categorizes them into main groups. This section also carries out a review of MIMO techniques that have been recently proposed for satellite/HAP communications [106]. Finally, special attention is given to the particular characteristics of the stratospheric channel, which ultimately determine the viability of MIMO over HAP.

2.4.1 Survey of HAP-SISO Channel Models

The propagation effects suffered by a signal transmitted over a HAP-based system are similar to those present over a terrestrial or a satellite system, in terms

mainly of shadowing and multipath, while tropospheric effects substantially control the quality of the link of both satellite and HAP-based systems. Therefore, channel models for HAPs could be based on models applied to terrestrial and satellite systems [11]. However, classical terrestrial modeling artificially separates slow and fast variations due to shadowing and multipath, respectively, and models them independently. Conversely, in satellite systems, these two processes are usually treated statistically in a combined manner. The reason is that terrestrial propagation rarely exhibits LoS conditions and the propagation environment contributes to both slow and fast variations. Nevertheless, direct signal is usually present, when the transmitter is located above the earth due to the higher elevations and impairments of the signal are mainly caused only by the local environment. Indeed, although terrestrial, satellite and stratospheric channels exhibit similar multipath fading, the intensity of this small-scale effect is not the same, since the effective scatterers are present only at specific positions of the link. Nevertheless, HAP-based systems exhibit distinct characteristics compared to satellite and terrestrial systems, with regard to the size of the coverage area, the length of the radio path between transmitter and receiver, the link geometry, and the propagation time delay. Several models for HAP-SISO channels are reported in the literature, and can be categorized as switched-channel models, empirical channel models, and geometry-based channel models [91], [105]-[112].

2.4.1.1 Switched-Channel Models

The changes in shadowing and multipath are typically modeled by different propagation states, e.g., “good” and “bad” states corresponding to LoS/open/light shadowing areas and NLoS/blocked/heavy shadowing areas, respectively [111]-[116]. Then, the goal of a switched channel model is to properly characterize a time-variant channel, which switches from one state to another at any time. These propagation states can be described by a first-order Markov chain with specific state and transition probabilities. The differences between the states are related to the type of fading that is affecting the channel. The classic narrowband model of

switched-channel is the one presented in [113] for the L- band. This model characterizes the process of fading through a switch between two states, one defined as good (Rice distribution) and the other defined as bad (Rayleigh-lognormal distribution). There are also three-state channel models proposed in [114], [115]. The characteristics that define the channel, such as the finite number of states present in a discrete time, make the use of Markov chains possible.

A possible weakness of the Markov model is that utilizes the same distributions for all the channel states. Alternatively, a semi-Markov model for HAP-SISO broadband channels is proposed in [112], which considers that the time duration between states transition is random and can be characterized by some type of probability distribution. One of the greatest advantages of the semi-Markovian process is the possibility to make a clear distinction between the probability distribution of the duration of the fading present in a state and the type of fading present in that state, which helps to get a better approximation of the link channel conditions [116]. A general feature of the Markov and semi-Markov approaches is the memoryless property of the channel, where one state is uncorrelated to other instances of the same state at different times.

2.4.1.2 Empirical Channel Models

Empirical channel models can be obtained based on experimental measurements. In [105], an empirical model for the link between HAPs and terrestrial users was defined and analyzed, based on experiments carried out in a “semi-urban” environment. From this model, narrowband channel characteristics were presented in terms of the Ricean factor and the local mean received power over a wide range of elevation angles. However, this model treated only the total received power, without differentiating the LoS power and the multipath scattered power during measurements. In [117], [118], empirical models to predict penetration loss into buildings in an urban area as a function of the elevation angle were developed, while results from a measurement campaign emulating the HAP-to-indoor channel at S-band were presented in [119]. These empirical models were

established based on experiments performed in a specific area. Hence, it is questionable whether they can be applied to other propagation environments.

2.4.1.3 Geometry-based Channel Models

The channel characterization strongly depends on the location of the transmitter and the receiver. As shown in Fig. 14, the fundamental parameters, which describe the geometry of a basic HAP-based system, are the elevation angle of the platform β_T , the height of the platform H_T , and the distance D between the mobile station and the sub-platform point.

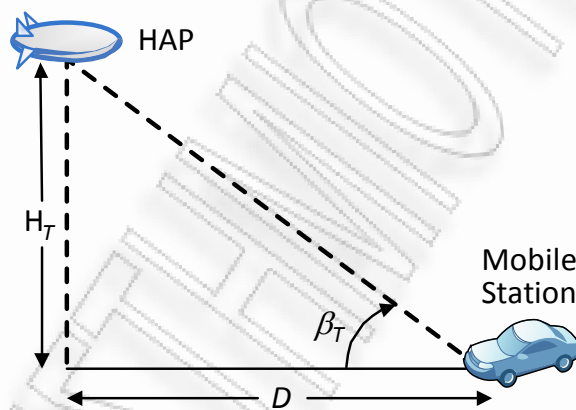


Figure 14: The typical geometry of a HAP-based system.

To the author's best knowledge, two different geometries for HAP-SISO channels were previously proposed. In [91] an ellipsoid was considered as the volume containing all the scatterers in the terrain with transmitter and receiver as foci (see Fig. 15). This model is based on the theoretical model proposed in [120] for a terrestrial station and is extended to the case of a stratospheric station. In this extension, the receiver and the transmitter are no longer on the horizontal plane and the height of the transmitter must be taken into account. This model provides a really convenient method for estimating the small-scale fading of the communication links between HAPs and terrestrial stations and characterizes the mobile channel through the power delay profile and the Doppler spectrum.

However, this model overestimates the effects of large delay components. This deficiency is due to the assumption of uniformly distributed single bounce echoes. Therefore, a blockage-based channel model for HAP-SISO channels was proposed in [109], quantified the existing probability of the single bounce echoes from different scatterers, and obtained an improved distribution function of the excess delay through numerical integration. Although the blockage-based model seems more realistic than the ellipsoid model, it greatly complicates the derived process.

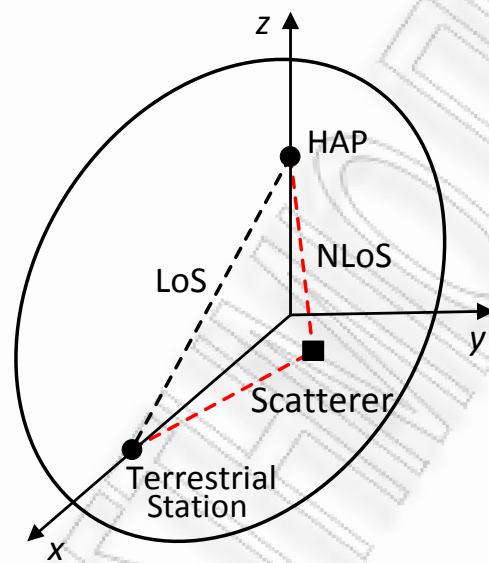


Figure 15: The ellipsoid geometrical model for HAP-SISO channels.

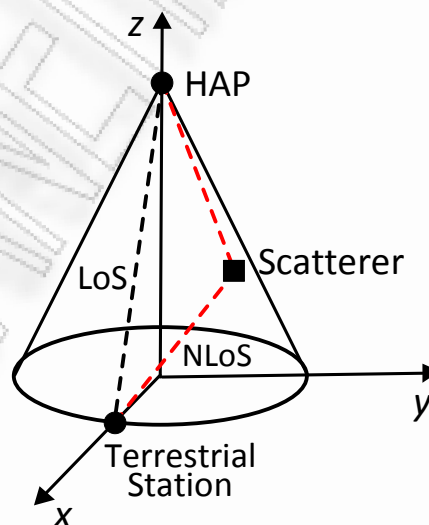


Figure 16: The circular cone geometrical model for HAP-SISO channels.

A multipath model based on circular straight cone geometry (see Fig. 16) was also proposed in [110]. This geometry could be a better approximation to simulate the multipath propagation, since it represents the coverage area of a HAP-based system more accurately. The energy from the scatterers is not considered significant close to the platform, as [91] suggests, but more concentrated close to the base of the cone. This new geometric definition can resemble more accurately the scenario of a directive antenna onboard the HAP illuminating a specific coverage area on the ground.

2.4.2 Classification of MIMO Channel Models

The MIMO models can be classified into categories depending on specific criteria. A potential way of distinguishing the individual models is with regard to the bandwidth. In particular, the MIMO models can be divided into narrowband models, i.e., the multipath fading is frequency flat, and wideband models, i.e., the multipath fading is frequency selective. MIMO models can also be separated into outdoor, indoor, urban, suburban or rural depending on the propagation environment, as well as they can be characterized as mobile or fixed depending on the existence or absence of mobility, respectively. Nevertheless, MIMO models can be generally classified into physical or non-physical (analytical) based on the modeling philosophy [121], [122].

Physical channel models use important physical parameters to provide reasonable description of the MIMO channel characteristics and the surrounding scattering environment. Depending on the chosen complexity, these models allow for an accurate reproduction of the real channel. Indeed, choosing a small number of physical parameters makes it difficult, if not impossible, to identify and validate the models. Physical models can further be classified into deterministic models, geometry-based stochastic models, and non-geometric stochastic models. Deterministic models characterize the physical propagation parameters in a completely deterministic manner, i.e., using ray tracing techniques [123]. With geometry-based stochastic models, the impulse response is characterized by the

entire system and the geometry of the scattering environment. Moreover, non-geometric stochastic models describe physical parameters in a mathematical (analytical) way without assuming an underlying geometry.

On the contrary, non-physical models synthesize the MIMO channel matrices in the context of system and algorithm development and verification. Although the non-physical models are easy to simulate and provide accurate channel characterization for the situations under which they are identified, they give limited insight to the propagation characteristics of the MIMO channels and depend on the measurement equipment, e.g., the bandwidth, the configuration and aperture of the arrays, the heights and response of transmit and receive antennas in the measurements. Non-physical models can be further subdivided into propagation-motivated models and correlation-based models. The interested reader is referred to [121], [122] for a detailed comparison between physical and non-physical models.

Finally, another way to model the MIMO channel is through field measurements of the MIMO channel responses. Empirical models based on MIMO channel measurement campaigns are reported in [124] for terrestrial systems and in [125] for satellite systems. However, the parameters used to generate these models are based on specific measurement campaigns for particular environments. Thus, these models can be used to generate fading effects for similar types of environments, which limit their merit.

2.4.3 Recent Advances in Satellite/HAP MIMO Channel Modeling

The wireless world has seen substantial increase in the demand of high quality broadband wireless services during recent years, which has resulted in the evolution of MIMO communications systems. In an effort to remain competitive with terrestrial systems, satellite and HAP-based systems are trying to follow the progress in MIMO technology and profit from the significant enhancements [106], [126]. In this section some of the recently developed models for satellite/HAP MIMO channels are presented.

2.4.3.1 Physical-Statistical Modeling

As mentioned before, different approaches can be used to build models for MIMO channels. For instance, physical or deterministic channel models based on ray-tracing algorithms can provide accurate results for a particular scenario. However, this approach is not often used due to increased computational complexity. On the other hand, statistical models are built around measurement data and provide reasonable reproduction of the real channel. However, they provide little insight into the propagation mechanisms and depend on the accuracy of the measurements. An intermediate approach between these models is the physical-statistical model. This type of modeling is the most appropriate in predicting the 'ON/OFF' nature and investigating the small-scale fading effects over large coverage areas applicable to satellite/HAP-based communications systems [127].

In [128], a physical-statistical model for land mobile satellite (LMS) and HAP MIMO channels was proposed. This model generates high-resolution time-series data and power delay profile for communication links between satellite (or HAP) and terrestrial terminal antennas and also predicts the correlation between these links. In this model, the obstacles (e.g., buildings, trees) are grouped into clusters of spherical shapes and the clusters centers are randomly positioned. Multiple scatterers are placed randomly around the cluster center and their position follows the Laplacian distribution, while the building heights follow the lognormal distribution. Three paths between a satellite and a mobile terminal are considered: a LoS path, a blocked LoS path, and an attenuated path by trees. To validate this model, the parameters obtained from experimental data collected in Munich, Germany at L-band (1.54 GHz) for urban and high-way environments. The small-scale fading and the wideband parameters can be approximated using the output time-series and spatial power delay profile data of the model.

As the maximum MIMO gain can be achieved with low correlation between antenna elements at both ends of a MIMO communications system, a fundamental

way of achieving low antenna correlation is to use antenna elements with adequate separation. However, owing to size restriction, the physical-statistical model suggests that multiple antennas with large separation cannot be deployed at a single satellite. Hence, two satellites are required to achieve diversity. Nevertheless, employing two satellites gives rise to new challenges, such as waste of the limited satellite bandwidth for the transmission of the same signal, lack of synchronization in reception, and high implementation cost. The synchronization issues can be dealt with by employing cooperative satellite diversity concept [129], [130] or by using compact antennas [94], [131], in which the problem of synchronization does not exist. From this physical-statistical model, one also obtains that the application of multiple antennas at a single HAP may be viable. However, further and extensive research is required to verify the results.

2.4.3.2 Analytical Modeling

The physical-statistical channel model described above is designed for the L- and S- frequency bands. The application of MIMO technology to satellite systems operating at the Ku- frequency band and above was discussed in [132]. In this model, two features of MIMO technology are presented: (i) a 2×2 MIMO spatial multiplexing system is used to achieve capacity improvements and a closed form expression for the outage capacity is derived (ii) a MIMO spatial diversity scheme with receive antenna selection is applied in order to reduce interference in LMS communication links. In addition, an analytical closed form expression for interference mitigation on forward link of a satellite 2×2 MIMO diversity system with antenna selection is also obtained. In order to discuss the features of MIMO techniques, the model assumes high antenna directivity and propagation phenomena, such as clear LoS, rain fading, and rainfall spatial homogeneity. The propagation delay offset (synchronization problem) in LMS communications is also considered and a practical solution to this problem is suggested by applying matched filters, first to the received signals for the detection of propagation delay offset and then the resulting signals are fed to the timing aligner.

2.4.3.3 Polarized Satellite/HAP MIMO Channels

The overwhelming majority of analytical and experimental work carried out on LMS and HAP MIMO channels at L- and S- frequency bands focuses on exploiting polarization diversity at both the transmitter and receiver to form a MIMO channel matrix [93], [94], [131], [133]-[135]. This approach seems beneficial, since a single satellite cannot provide the necessary antenna spacings required by MIMO theory to provide a high degree of channel decorrelation. Spatial, temporal and polarization SIMO and MISO measurements in S- and C- bands for mobile satellite systems have been recently carried out by ESA employing existing satellites [136] and by Centre National d'Etudes Spatiales (CNES) employing a helicopter [137]. A relevant SIMO channel modeling approach is presented in [138]. With regard to MIMO measurement campaigns, the relevant attempts are extremely scarce and have been conducted mainly in the frame of [125] in Guildford, UK, at 2.45 GHz. In order to get benefit from polarization dimension, the cross-polar transmissions (e.g., transmission from vertically polarized antenna to horizontally polarized antenna) should be zero. However, in real scenarios there is always some polarization mismatch since linearly polarized antenna arrays have non-zero patterns for cross-polar fields. In addition, multipath effects (e.g., diffraction, scattering, reflection, etc.) may change the plane of polarization of incident electromagnetic waves at the receiver. A physical-statistical model for dual-polarized satellite links is presented in [134], while the capacity enhancement resulting from the use of a multiple HAP system employing compact MIMO antenna arrays and multiple spatial-polarization states was investigated in [93]-[94].

2.4.4 Potential Application of MIMO Technology over Single HAPs

The prerequisite so that single HAP configurations fully exploit the spatial diversity and spatial multiplexing advantages predicted by information theory is the existence of sufficient antenna spacing at the transmitter and receiver, as well as a rich scattering environment, which renders the fading paths between the antenna

elements of the transmitter and the receiver independent. Insufficient spacing between antenna elements and limited scattering correspond to lower MIMO channel capacity compared to the ideal i.i.d. case. Therefore, future HAP-MIMO channel models should take the distribution of the scatterers and the correlations among signal carriers into account. The application of multiple antennas to single HAPs may be plausible to be pursued in the frame of HAP-MIMO systems, since spatial limitations on board are not as stringent as in satellites. Moreover, the length of the radio path between HAPs and terrestrial stations is significantly smaller than the corresponding one associated with satellites.

Although several MIMO models have been proposed for terrestrial and satellite communications channels, newer models are required to accurately characterize specific issues concerned with HAP-MIMO channels. For these channels, the physical-geometrical characteristics, which define the HAP-MIMO system itself, are highly critical. Most of the physical models of terrestrial channels postulate a scattering environment and attempt to capture the channel characteristics by involving scattering parameters. Such models can often illustrate the essential characteristics of the MIMO channel, as long as the constructed scattering environment is reasonable. The conventional geometry-based models for HAP-SISO channels provide a convenient framework for characterizing the time and frequency domain of the fading channels. Notwithstanding, extending these models to the MIMO case is not straightforward or even not applicable mainly due to the need of utilization of the space domain, which is the essence of MIMO technology. Specifically, it is necessary to incorporate new parameters, such as the angles of arrival and departure, the angle spread, and the utilization of multiple antennas at both the ends of the link. Consequently, the establishment of a particular geometry allows for an accurate characterization of the multipath effects and supports the investigation of MIMO applicability.

Chapter 3 introduces and justifies a novel cylindrical geometry. Based on this geometry, a 3-D reference model for narrowband HAP-MIMO channels is proposed.

Chapter 3

Three-Dimensional Modeling of Space-Time Correlated HAP-MIMO Channels

3.1 Introduction

Chapter 2 reviewed the MIMO principle and underlined its potential advantages. However, the invariable non-zero correlation of MIMO subchannels in space and/or time can significantly degrade and limit the prospective MIMO gain [97], [98]. Spatial correlation is measured among the elements of the channel matrix for each realization, while temporal correlation is measured between channel matrix realizations at different time instants. In practice, due to the length of the radio path between HAPs and terrestrial stations, the transmit and/or receive antennas should be placed at significant distances from each other to ensure that the paths are really diverse. In [93], [94] virtual MIMO (V-MIMO) techniques were used exploiting the diversity provided by multiple HAPs, while in [128] a general estimation of the required antenna element separation at a HAP to achieve uncorrelated responses in the MIMO channel matrix was provided. Nevertheless, whether the size of a single HAP can support spatial diversity is still questionable. Hence, further and extensive research is necessary.

Analysis and design of HAP-MIMO communications systems require the development of space-time models, which enable us to properly characterize the stochastic fading channel and thoroughly study the channel statistics. Since impairments of the signal are mainly caused by the environment near to the user, a realistic positioning of the scatterers is essential for an accurate channel model. Thus, when terrain and scattering distributions are available, physical-geometrical models are preferred. In [91], a geometrical model applied to HAP-SISO channels

was proposed. According to this model, the scatterers are uniformly distributed in space, i.e., the user receives signals from all directions with equal probabilities (see Fig. 17). However, this assumption deviates from practical situations. In addition, the influence of the HAP elevation angle was not considered for the performance evaluation. In [128], a physical-statistical MIMO model applied to satellites/HAPs was presented. According to this model, the scatterers are non-uniformly distributed, i.e., the user receives the signal only from particular directions (see Fig. 18). Nevertheless, analytical expressions for the space-time correlation function (STCF) were not derived and the effect of the array configuration was not studied. Thus, newer models are essential on mathematically analyzing the impact of any system parameter on the performance and providing in-depth understanding and description of the statistical properties of HAP-MIMO channels.

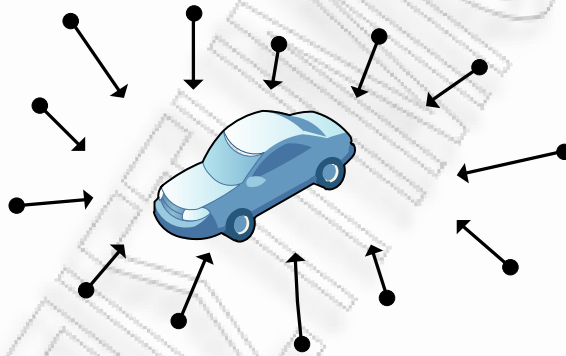


Figure 17: Visualization of isotropic scattering conditions in an open area.

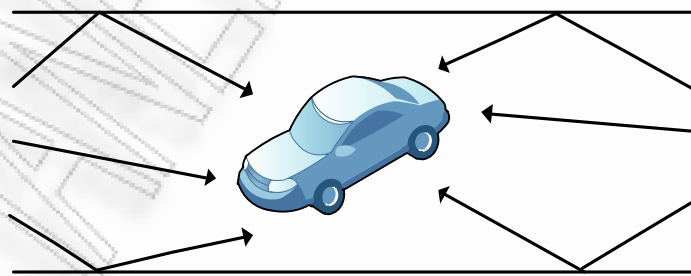


Figure 18: Visualization of non-isotropic scattering conditions in a narrow street.

This chapter proposes a novel 3-D geometry-based single-bounce (GBSB) reference model [139] for HAP-MIMO channels and constructs the received

complex faded envelope as a superposition of the LoS and the NLoS rays. This model utilizes L- (1/2 GHz) and S- (2/4 GHz) frequency bands and assumes that the local scatterers in the vicinity of the mobile user are non-uniformly distributed within a cylinder. An alternative version of the proposed model was presented in [140] and [141], but only the first tier of scatterers lying on the surface of a cylinder was taken into account. These studies were based on existing terrestrial 3-D MIMO channel models that deal with fixed-to-mobile [142] or mobile-to-mobile [143] cases. The proposed model derives the STCF considering several parameters, such as the elevation angle of the platform, the array configuration, the Doppler spread, and the distribution of the scatterers. The numerical results demonstrate the impact of these parameters on the space-time correlation and the channel capacity. These results also estimate the required HAP antenna spacing to achieve uncorrelated HAP-MIMO channels and show that if HAP length is adequate, MIMO techniques are applicable on a single HAP.

The remainder of this chapter is organized as follows. In Section 3.2 the HAP-MIMO communication system is described. Section 3.3 introduces a 3-D geometrical model for HAP-MIMO channels, proposes a reference model, and derives its channel impulse response. Section 3.4 derives the STCF, investigates the influence of model parameters on the STCF, and studies the effect of the stratospheric winds on the correlation. Section 3.5 defines and investigates the HAP-MIMO channel capacity for different values of the model parameters. Finally, Section 3.6 summarizes this chapter.

3.2 The HAP-MIMO System Model

The system model employed throughout this chapter considers a downlink narrowband MIMO Stratospheric-Terrestrial communication channel with n_T transmit and n_R receive antenna elements. All antennas are fixed, omnidirectional, and are numbered as $1 \leq p \leq q \leq n_T$ and $1 \leq l \leq m \leq n_R$, respectively. The

n_T antenna elements of the stratospheric base station (SBS) are situated approximately 20 km above the ground and it is assumed that the n_R antenna elements of the terrestrial mobile station (TMS) are in motion. Considering slowly varying and frequency-flat-fading channels, the link between the SBS and TMS antenna arrays is represented using the following complex baseband vector equation

$$\mathbf{r}(t) = \mathbf{H}(t)\mathbf{s}(t) + \mathbf{n}(t), \quad (11)$$

where $\mathbf{s}(t) \in \mathbb{C}^{n_T \times 1}$ is the transmitted signal vector, $\mathbf{r}(t) \in \mathbb{C}^{n_R \times 1}$ is the received signal vector, and $\mathbf{n}(t) \in \mathbb{C}^{n_R \times 1}$ is the noise vector, which denotes the AWGN at the receiver branches. The entries of the noise vector are i.i.d. complex Gaussian random variables with zero-mean and variance N_0 , where N_0 is the noise PSD. Finally, $\mathbf{H}(t) = [h_{ij}(t)]_{n_R \times n_T} \in \mathbb{C}^{n_R \times n_T}$ is the matrix of complex faded channel gains.

3.3 A Reference Model for HAP-MIMO Channels

In this section, a 3-D GBSB reference model for HAP-MIMO channels is introduced and its geometrical characteristics are described. Based on this model, the channel impulse response is derived.

Let us initially consider a stratospheric platform free of local scattering, and a terrestrial single user, which is located in the center of a disc-shaped region of scattering elements. As shown in Fig. 19, the distance between the user and the scatterers is not constant in reality. Moreover, the radius of the disc corresponds to the maximum distance between the user and an effective scatterer. This approach is realistic for HAP-based scenarios, due to the high elevation angles and the use of omni-directional antennas at the user terminals. In addition, the platform is placed in the stratosphere and the user is often located lower than the surrounding scatterers. Therefore, the waves may travel in both horizontal and vertical planes,

and the propagation environment has to be characterized by 3-D scattering conditions, i.e., the heights of the scatterers need to be taken into account. Since the scattered waves are mostly owing to buildings, poles, trees, and hills that can be found only up to a predefined maximum height, a cylinder is finally considered as the volume containing all the scatterers, and the maximum scatterer height corresponds to the height of the cylinder.

The geometrical characteristics of the proposed model and the definition of the Cartesian coordinate system are discussed in Figs. 20-23. Fig. 20 shows the LoS paths of the 3-D geometrical model for a 2×2 HAP-MIMO channel, while Fig. 21 presents the projection of this model to the x - y plane. Figs. 22 and 23 show the NLoS paths for the same channel. Based on this simple configuration, uniform linear arrays (ULAs) with arbitrary number of antennas can be constructed. Note that shadowing within the cylinder is neglected in this model. In addition, attenuation due to rain, oxygen absorption, water vapor, clouds, precipitation, and vegetation is bypassed, since these atmospheric-environmental phenomena do not significantly affect communication links at L- and S- frequency bands [11]. For ease of reference, the parameters of the proposed model are summarized in Table 5.

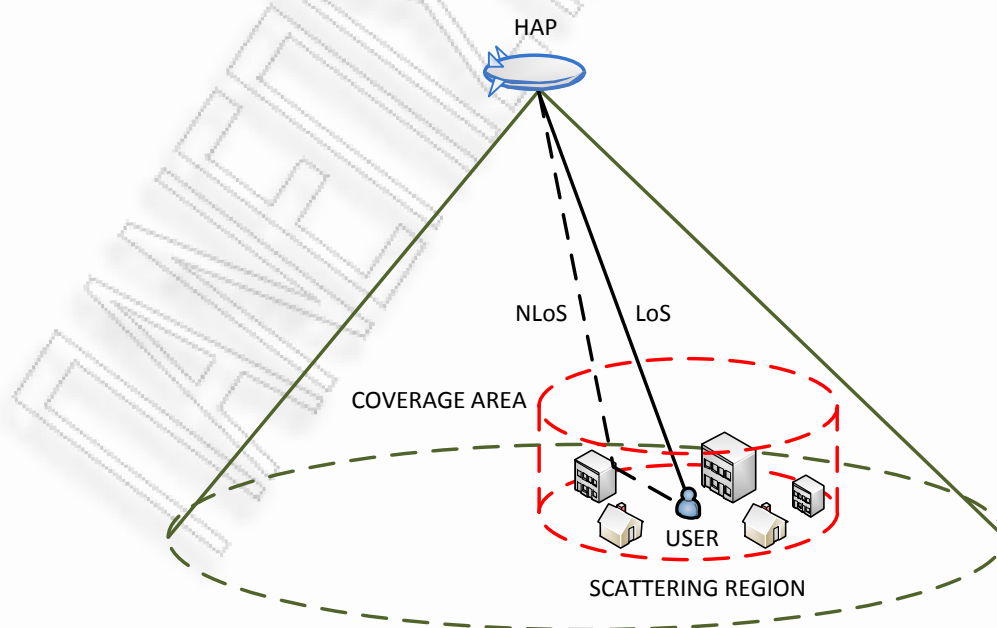


Figure 19: Basic concept of a HAP-based communication system and a cylindrical scattering region inside the coverage area.

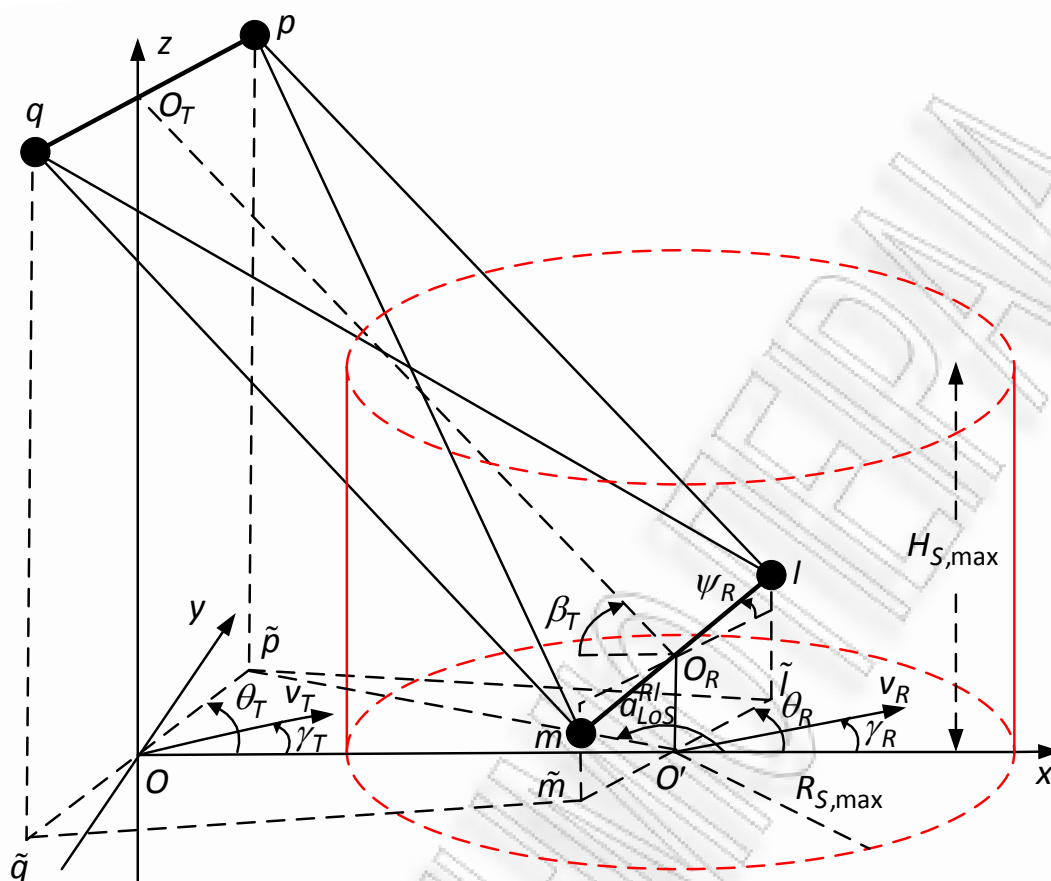


Figure 20: The LoS paths of the 3-D geometrical model for a 2×2 HAP-MIMO channel.

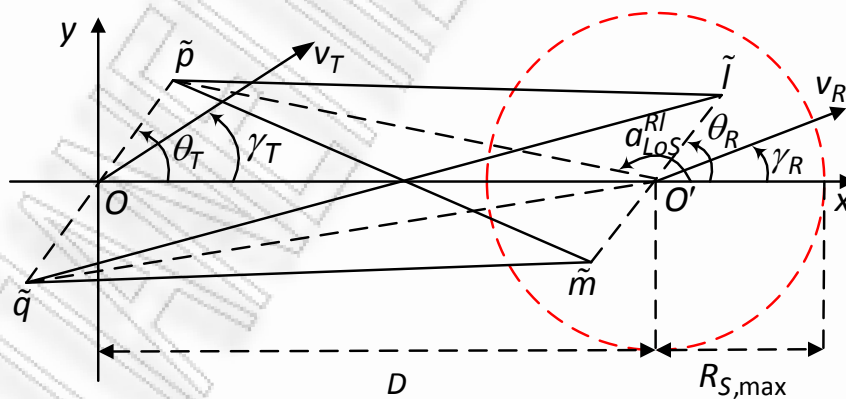


Figure 21: The LoS paths of the projection of the 3-D geometrical model for a 2×2 HAP-MIMO channel.

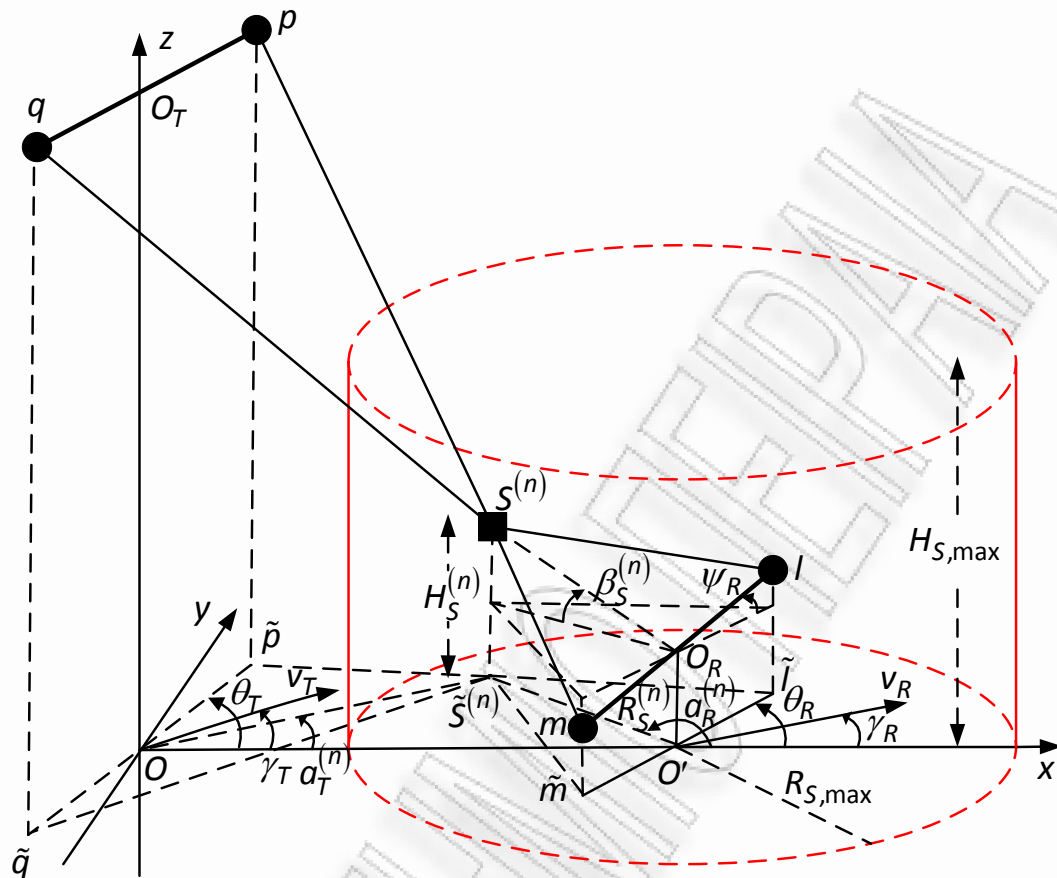


Figure 22: The NLoS paths of the 3-D geometrical model for a 2×2 HAP-MIMO channel.

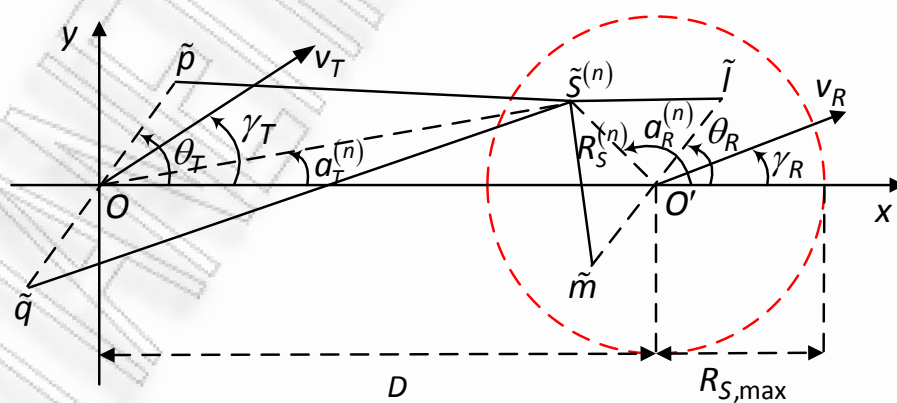


Figure 23: The NLoS paths of the projection of the 3-D geometrical model for a 2×2 HAP-MIMO channel.

TABLE 5
DEFINITION OF THE PARAMETERS USED IN THE REFERENCE MODEL

D	The distance between the centre O of the projections of the SBS antenna elements to the x - y plane and the lower centre O' of the cylinder.
$R_{S,\max}, H_{S,\max}$	The radius and the height of the cylinder with the scatterers, respectively.
δ_T, δ_R	The spacing between two adjacent antenna elements at the SBS and TMS, respectively.
θ_T, θ_R	The orientation of the SBS and TMS antenna array in the x - y plane (relative to the x -axis), respectively.
ψ_T, ψ_R	The elevation angle of the p^{th} SBS and l^{th} TMS antenna element, relative to the x - y plane, respectively.
v_T, v_R	The velocities of the SBS and TMS, respectively.
γ_T, γ_R	The moving directions of the SBS and TMS, respectively.
$f_{T,\max}, f_{R,\max}$	The maximum Doppler frequency shift of the SBS and TMS, respectively.
β_T	The elevation angle of the SBS relative to O_R .
$H_T, H_R, H_S^{(n)}$	The height of the SBS, the TMS, and the n^{th} scatterer, respectively.
$a_{\text{LOS}}^{\text{RI}}$	The azimuth angle of arrival of the LoS paths.
$a_T^{(n)}, a_R^{(n)}$	The azimuth angle of arrival and the azimuth angle of departure at/from the n^{th} scatterer, respectively
$R_S^{(n)}$	The distance between O' and the projection of the n^{th} scatterer to the x - y plane.
$\beta_S^{(n)}$	The elevation angle of the n^{th} scatterer relative to O_R .
$\varphi^{(n)}, g^{(n)}$	The random phase and the amplitude introduced by the n^{th} scatterer, respectively.
μ	The mean azimuth angle at which the scatterers are distributed in the x - y plane (von Mises pdf).
k	The spread of the scatterers around the mean azimuth angle (von Mises pdf).
a	The spread of the scatterers around the TMS (hyperbolic pdf).
$H_{S,\text{mean}}$	The mean of scatterer's height (log-normal pdf).
σ	The standard deviation of scatterer's height (log-normal pdf).

According to Figs. 20-23, the x -axis is the line that connects coordinate origin O (the centre of the projections \tilde{p} and \tilde{q} of the SBS antenna elements p and q to the x - y plane), and O' (the lower center of the cylinder). In addition, O_T and O_R are the array centers at the SBS and TMS, respectively. To aid the analysis, the distance between two points a and b is denoted as $d(a,b)$. Then, the distance between O and O' is $d(O,O')=D$, and the heights of the SBS and TMS antennas arrays are $d(O,O_T)=H_T$ and $d(O',O_R)=H_R$, respectively. Note that $H_T \gg H_R$ and that the elevation angle of SBS relative to O_R is given by

$$\beta_T \approx \arctan(H_T / D). \quad (12)$$

The spacing between two adjacent antenna elements at the SBS and TMS is denoted by δ_T and δ_R , respectively. Angles θ_T and θ_R represent the orientation of the SBS and TMS antenna arrays respectively, relative to the x -axis. In addition, the angle ψ_R describes the elevation angle of the l^{th} TMS antenna element, relative to the x - y plane, and the angle a_{LOS}^{Rl} denotes the azimuth angle of arrival (AoA) of the LoS paths. Finally, it is considered that SBS (aircraft case) and TMS are moving with speeds v_T and v_R in the directions determined by the angles γ_T and γ_R , respectively. Since aircrafts fly on a circle, v_T is related to the angular velocity of SBS. Then, $v_T = \omega R_T = 2\pi R_T / T$, where ω is the angular frequency, T is the period, and R_T is the radius of the rotation. Therefore, γ_T is always perpendicular to R_T .

The proposed model assumes $N \rightarrow \infty$ fixed, omni-directional scatterers and single scattering conditions. Then, the n^{th} scatterer is denoted by $S^{(n)}$, the distance between its projection to the x - y plane and O' is denoted by $d(\tilde{S}^{(n)}, O') = R_S^{(n)} \in (0, R_{S,\max}]$, and its height is designated by $d(\tilde{S}^{(n)}, S^{(n)}) = H_S^{(n)} \in (0, H_{S,\max}]$, where $R_{S,\max}$ and $H_{S,\max}$ represent the radius and the height of

the cylinder, respectively. Note that $H_{S,\max} \ll H_T$ and that the elevation angle of the n^{th} scatterer relative to O_R is given by

$$\beta_S^{(n)} \approx \arctan\left(H_S^{(n)} / R_S^{(n)}\right). \quad (13)$$

The angles $a_T^{(n)}$ and $a_R^{(n)}$ denote the azimuth angle of departure (AoD) of the waves that impinge on the scatterer $S^{(n)}$ and the azimuth AoA of the waves scattered from $S^{(n)}$, respectively. It is assumed that $a_T^{(n)}$, $a_R^{(n)}$, $R_S^{(n)}$, $H_S^{(n)}$, and $\beta_S^{(n)}$ are random variables. According to Fig. 22, $a_T^{(n)}$ is dependent on $a_R^{(n)}$ and $R_S^{(n)}$, while $\beta_S^{(n)}$ is dependent on $R_S^{(n)}$ and $H_S^{(n)}$. However, $a_R^{(n)}$, $R_S^{(n)}$, and $H_S^{(n)}$ are independent.

It is assumed that $R_{S,\max}$ is much smaller than D , i.e., $R_{S,\max} \ll D$.³ Then, one concludes that $a_T^{(n)} = \arcsin\left(R_S^{(n)} / D\right) \leq \arcsin\left(R_{S,\max} / D\right)$ is a small angle for every $R_S^{(n)} \in (0, R_{S,\max}]$. Furthermore, it is assumed that δ_R is much smaller than $R_S^{(n)}$, i.e., $\delta_R \ll \min\{R_S^{(n)}\}$. Finally, it is assumed that δ_T is much smaller than D , i.e., $\delta_T \ll D$.³ Then, $a_{LoS}^{RI} \approx \pi$.

3.3.1 Channel Impulse Response

Based on the 3-D reference model, the impulse response $h_{pl}(t)$ of the subchannel p - l is a superposition of the LoS and NLoS rays and can be written as

$$h_{pl}(t) = h_{pl,LoS}(t) + h_{pl,NLoS}(t). \quad (14)$$

³Note that as the SBS elevation angle β_T increases, the distance D decreases. Without loss of generality, it is assumed that $\beta_T \leq 85^\circ$. From (12), for $\beta_T = 85^\circ$ (maximum value of the aforementioned inequality) and $H_T = 20$ km, one can obtain that $D \approx 1750$ m. As long as $R_{S,\max}$ and δ_T are equal to a few hundreds of wavelengths, the assumptions $R_{S,\max} \ll D$ and $\delta_T \ll D$ are valid.

Since the number of local scatterers is infinite, central limit theorem [144] implies that $h_{pl}(t)$ is a low-pass nonzero-mean complex Gaussian process. Hence, the envelope $|h_{pl}(t)|$ is a Rice process. In addition, $h_{pl,NLoS}(t)$ is a low-pass zero-mean complex Gaussian process, and the envelope $|h_{pl,NLoS}(t)|$ is Rayleigh distributed, while $h_{pl,LoS}(t)$ is a deterministic process.

The LoS and NLoS components of the impulse response can be written as

$$h_{pl,LoS}(t) = \sqrt{\frac{K_{pl}\Omega_{pl}}{K_{pl}+1}} e^{-j\frac{2\pi}{\lambda}d(p,l)} e^{j2\pi t[f_{T,\max}\cos(\pi-\alpha_{LoS}^R-\gamma_T)+f_{R,\max}\cos(\alpha_{LoS}^R-\gamma_R)]}, \quad (15)$$

$$h_{pl,NLoS}(t) = \sqrt{\frac{\Omega_{pl}}{K_{pl}+1}} \lim_{N \rightarrow \infty} \frac{1}{\sqrt{N}} \sum_{n=1}^N g^{(n)} e^{-j\frac{2\pi}{\lambda}[d(p,s^{(n)})+d(s^{(n)},l)]} \times e^{j\varphi^{(n)}} e^{j2\pi t[f_{T,\max}\cos(\alpha_T^{(n)}-\gamma_T)+f_{R,\max}\cos(\alpha_R^{(n)}-\gamma_R)\cos\beta_S^{(n)}]}, \quad (16)$$

where $j^2 = -1$, $f_{T,\max} = v_T / \lambda$ and $f_{R,\max} = v_R / \lambda$ are the maximum Doppler shifts associated with SBS and TMS, respectively, and λ is the carrier wavelength. It is assumed that the phase $\varphi^{(n)}$ introduced by the n^{th} scatterer is an i.i.d. random variable uniformly distributed in the interval $[-\pi, \pi)$ and independent from $\alpha_T^{(n)}$, $\alpha_R^{(n)}$, $R_S^{(n)}$, $H_S^{(n)}$, and $\beta_S^{(n)}$. Considering a unit transmit power, $\Omega_{pl} = E[|h_{pl}(t)|^2] \leq 1$ denotes the transmitted power of the subchannel $p-l$, where $E[\cdot]$ is the statistical expectation operator. In addition, $K_{pl} = |h_{pl,LoS}(t)|^2 / E[|h_{pl,NLoS}(t)|^2]$ denotes the Ricean factor of the subchannel $p-l$ and $g^{(n)}$ represents the amplitude of the n^{th} scattered wave such that $N^{-1} \sum_{n=1}^N E[|g^{(n)}|^2] = 1$ as $N \rightarrow \infty$. The set $\{g^{(n)}\}_{n=1}^{\infty}$ consists of independent positive random variables with finite variances, independent of $\{\varphi^{(n)}\}_{n=1}^{\infty}$.

As shown in the Appendix A, the distances $d(p,l)$, $d(p,S^{(n)})$, and $d(S^{(n)},l)$ are approximated as

$$d(p,l) \approx (D - D_{T_1} + D_{R_1}) / \cos \beta_T, \quad (17)$$

$$d(p,S^{(n)}) \approx (D - D_{T_1} - D_{T_2} R_S^{(n)} \sin a_R^{(n)}) / \cos \beta_T, \quad (18)$$

$$d(S^{(n)},l) \approx R_S^{(n)} / \cos \beta_S^{(n)} - D_{R_1} \cos a_R^{(n)} \cos \beta_S^{(n)} - D_{R_2} \sin \beta_S^{(n)} - D_{R_3} \sin a_R^{(n)} \cos \beta_S^{(n)}, \quad (19)$$

where

$$D_{T_1} = 0.5(n_T + 1 - 2p) \delta_T \cos \theta_T, \quad (20)$$

$$D_{T_2} = 0.5(n_T + 1 - 2p) \delta_T \sin \theta_T / D, \quad (21)$$

$$D_{R_1} = 0.5(n_R + 1 - 2l) \delta_R \cos \theta_R \cos \psi_R, \quad (22)$$

$$D_{R_2} = 0.5(n_R + 1 - 2l) \delta_R \sin \psi_R, \quad (23)$$

$$D_{R_3} = 0.5(n_R + 1 - 2l) \delta_R \sin \theta_R \cos \psi_R. \quad (24)$$

Finally, using (13) and (17)-(24), and the approximation $a_T^{(n)} \approx \sin a_R^{(n)} R_S^{(n)} / D$ (see Appendix A), the LoS and NLoS components of the impulse response become, respectively

$$h_{pl,LoS}(t) = \sqrt{\frac{K_{pl} \Omega_{pl}}{K_{pl} + 1}} e^{-j \frac{2\pi(D - D_{T_1} + D_{R_1})}{\lambda \cos \beta_T}} e^{j2\pi t(F_{T,LoS} + F_{R,LoS})}, \quad (25)$$

$$h_{pl,NLoS}(t) = \sqrt{\frac{\Omega_{pl}}{K_{pl} + 1}} \lim_{N \rightarrow \infty} \frac{1}{\sqrt{N}} \sum_{n=1}^N g^{(n)} A_{p,S^{(n)}} A_{S^{(n)},l} e^{j\varphi^{(n)}} e^{j2\pi t(F_{T,NLoS} + F_{R,NLoS})}, \quad (26)$$

where

$$F_{T,LoS} = f_{T,max} \cos(\pi - a_{LoS}^{Rl} - \gamma_T), \quad (27)$$

$$F_{R,LoS} = f_{R,max} \cos(a_{LoS}^{Rl} - \gamma_R), \quad (28)$$

$$A_{p,S^{(n)}} = e^{-j \frac{2\pi}{\lambda \cos \beta_T} (D - D_{T_1} - D_{T_2} R_S^{(n)} \sin \alpha_R^{(n)})}, \quad (29)$$

$$A_{S^{(n)},I} = e^{-j \frac{2\pi R_S^{(n)}}{\lambda \cos \left[\arctan \left(H_S^{(n)} / R_S^{(n)} \right) \right]}} e^{j \frac{2\pi D_{R_1} \cos \alpha_R^{(n)} \cos \left[\arctan \left(H_S^{(n)} / R_S^{(n)} \right) \right]}{\lambda}} \\ \times e^{j \frac{2\pi D_{R_2} \sin \left[\arctan \left(H_S^{(n)} / R_S^{(n)} \right) \right]}{\lambda}} e^{j \frac{2\pi D_{R_3} \sin \alpha_R^{(n)} \cos \left[\arctan \left(H_S^{(n)} / R_S^{(n)} \right) \right]}{\lambda}}, \quad (30)$$

$$F_{T,NLoS} = f_{T,\max} \left(R_S^{(n)} \sin \gamma_T \sin \alpha_R^{(n)} / D + \cos \gamma_T \right), \quad (31)$$

$$F_{R,NLoS} = f_{R,\max} \cos \left(\alpha_R^{(n)} - \gamma_R \right) \cos \left[\arctan \left(H_S^{(n)} / R_S^{(n)} \right) \right]. \quad (32)$$

3.4 Space-Time Correlation Function

Considering a 3-D non-isotropic scattering environment, the STCF between two arbitrary subchannels $h_{pl}(t)$ and $h_{qm}(t)$ is defined as

$$R_{pl,qm}(\delta_T, \delta_R, \tau, t) = E \left[h_{pl}(t) h_{qm}^*(t + \tau) \right] / \sqrt{\Omega_{pl} \Omega_{qm}}, \quad (33)$$

where $(\cdot)^*$ denotes complex conjugate operation and $E[\cdot]$ is the statistical expectation operator. Since both $h_{pl,NLoS}(t)$ and $h_{qm,NLoS}(t)$ are zero-mean processes, i.e., $E[h_{pl,NLoS}(t)] = E[h_{qm,NLoS}(t)] = 0$, (33) can be written as

$$R_{pl,qm}(\delta_T, \delta_R, \tau, t) \\ = E \left[\left(h_{pl,LoS}(t) + h_{pl,NLoS}(t) \right) \left(h_{qm,LoS}^*(t + \tau) + h_{qm,NLoS}^*(t + \tau) \right) \right] / \sqrt{\Omega_{pl} \Omega_{qm}} \\ = h_{pl,LoS}(t) h_{qm,LoS}^*(t + \tau) / \sqrt{\Omega_{pl} \Omega_{qm}} \\ + h_{pl,LoS}(t) E \left[h_{qm,NLoS}^*(t + \tau) \right] / \sqrt{\Omega_{pl} \Omega_{qm}} \\ + h_{qm,LoS}^*(t + \tau) E \left[h_{pl,NLoS}(t) \right] / \sqrt{\Omega_{pl} \Omega_{qm}} \\ + E \left[h_{pl,NLoS}(t) h_{qm,NLoS}^*(t + \tau) \right] / \sqrt{\Omega_{pl} \Omega_{qm}} \\ = R_{pl,qm}^{LoS}(\delta_T, \delta_R, \tau, t) + R_{pl,qm}^{NLoS}(\delta_T, \delta_R, \tau, t), \quad (34)$$

where $R_{pl,qm}^{LoS}(\delta_T, \delta_R, \tau, t)$ and $R_{pl,qm}^{NLoS}(\delta_T, \delta_R, \tau, t)$ denote the STCFs of the LoS and the NLoS component, respectively. Using (15), (27), (28), and (33), the STCF of the LoS component can be written as

$$\begin{aligned}
R_{pl,qm}^{LoS}(\delta_T, \delta_R, \tau, t) &= \sqrt{\frac{K_{pl}K_{qm}}{(K_{pl}+1)(K_{qm}+1)}} e^{-j\frac{2\pi}{\lambda}[d(p,l)-d(q,m)]} e^{-j2\pi\tau[f_{T,\max}\cos(\pi-a_{LoS}^{Rm}-\gamma_T)+f_{R,\max}\cos(a_{LoS}^{Rm}-\gamma_R)]} \\
&\quad \times e^{j2\pi\tau f_{T,\max}[\cos(\pi-a_{LoS}^{Rl}-\gamma_T)-\cos(\pi-a_{LoS}^{Rm}-\gamma_T)]} e^{j2\pi\tau f_{R,\max}[\cos(a_{LoS}^{Rl}-\gamma_R)-\cos(a_{LoS}^{Rm}-\gamma_R)]}. \quad (35)
\end{aligned}$$

Using (17), (20), (22), and the approximation $a_{LoS}^{Rl} = a_{LoS}^{Rm} \approx \pi$, (35) becomes

$$\begin{aligned}
R_{pl,qm}^{LoS}(\delta_T, \delta_R, \tau, t) &\approx R_{pl,qm}^{LoS}(\delta_T, \delta_R, \tau) \\
&= \sqrt{\frac{K_{pl}K_{qm}}{(K_{pl}+1)(K_{qm}+1)}} e^{j\frac{2\pi[(q-p)\delta_T\cos\theta_T-(m-l)\delta_R\cos\theta_R\cos\psi_R]}{\lambda\cos\beta_T}} \\
&\quad \times e^{-j2\pi\tau(f_{T,\max}\cos\gamma_T-f_{R,\max}\cos\gamma_R)}. \quad (36)
\end{aligned}$$

Moreover, using (26) and (33), the STCF of the NLoS component can be written as

$$\begin{aligned}
R_{pl,qm}^{NLoS}(\delta_T, \delta_R, \tau, t) &= R_{pl,qm}^{NLoS}(\delta_T, \delta_R, \tau) \\
&= \frac{1}{\sqrt{(K_{pl}+1)(K_{qm}+1)}} \\
&\quad \times \lim_{N \rightarrow \infty} \frac{1}{N} \sum_{n=1}^N \mathbb{E} \left[\left| g^{(n)} \right|^2 \mathbf{A}_{p,S^{(n)}} \mathbf{A}_{S^{(n)},l} \mathbf{A}_{q,S^{(n)}}^* \mathbf{A}_{S^{(n)},m}^* e^{-j2\pi\tau(F_{T,NLoS}+F_{R,NLoS})} \right]. \quad (37)
\end{aligned}$$

The number of scatterers in the reference model is infinite. Thus, the discrete variables $a_R^{(n)}$, $R_S^{(n)}$, and $H_S^{(n)}$ can be replaced with continuous random variables a_R , R_S , and H_S with joint probability density function (pdf) $f(a_R, R_S, H_S)$. Since $a_R^{(n)}$, $R_S^{(n)}$, and $H_S^{(n)}$ are independent, the joint pdf $f(a_R, R_S, H_S)$ can be

decomposed to $f(a_R)f(R_S)f(H_S)$. Hence, using (29)-(32), the STCF of the NLoS component becomes [145, p.23]

$$\begin{aligned}
& R_{pl,qm}^{NLoS}(\delta_T, \delta_R, \tau) \\
&= \frac{1}{\sqrt{(K_{pl}+1)(K_{qm}+1)}} \int_0^{H_{S,\max}} \int_0^{R_{S,\max}} \int_{-\pi}^{\pi} e^{j\frac{2\pi(q-p)\delta_T \cos\theta_T}{\lambda \cos\beta_T}} e^{j\frac{2\pi(q-p)\delta_T \sin\theta_T R_S \sin a_R}{\lambda D \cos\beta_T}} \\
&\quad \times e^{j\frac{2\pi(m-l)\delta_R \sin\psi_R \sin[\arctan(H_S/R_S)]}{\lambda}} e^{j\frac{2\pi(m-l)\delta_R \sin\theta_R \cos\psi_R \sin a_R \cos[\arctan(H_S/R_S)]}{\lambda}} \\
&\quad \times e^{j\frac{2\pi(m-l)\delta_R \cos\theta_R \cos\psi_R \cos a_R \cos[\arctan(H_S/R_S)]}{\lambda}} e^{-j2\pi\tau f_{T,\max} \left(\frac{R_S \sin\gamma_T \sin a_R}{D} + \cos\gamma_T \right)} \\
&\quad \times e^{-j2\pi\tau f_{R,\max} \cos(a_R - \gamma_R) \cos[\arctan(H_S/R_S)]} f(a_R) f(R_S) f(H_S) da_R dR_S dH_S. \quad (38)
\end{aligned}$$

Several different distributions, such as uniform [97], von Mises [102] and Laplacian [128], [146], were used in prior work to characterize the azimuth angle a_R . In this work, the von Mises pdf (also known as the circular normal distribution) is used, because it approximates many of the aforementioned distributions, and is empirically justified in urban and suburban areas in [147]. The von Mises pdf is defined as

$$f(a_R) = \frac{e^{k \cos(a_R - \mu)}}{2\pi I_0(k)}, \quad -\pi \leq a_R \leq \pi, \quad (39)$$

where $I_0(\cdot)$ is the zeroth-order modified Bessel function of the first kind, $\mu \in [-\pi, \pi]$ is the mean angle at which the scatterers are distributed in the x - y plane, and $k \geq 0$ controls the spread around the mean. This pdf was initially introduced by R. von Mises in 1918 to study the deviations of measured atomic weights from integral values [149] and has played a prominent role in statistical modeling and analysis of angular variables [150, pp. 57-68]. It is interesting to note that the von Mises pdf has appeared in a number of other communication contexts. For example, this pdf is referred to as the Tikhonov pdf in partially coherent communication [151, p. 406], has been used in phase-locked loop related

problems [152], and has been shown to represent the pdf of the phase of a sine wave in Gaussian noise for large signal to noise ratios [153].

Fig. 24 demonstrates the von Mises pdf for different values of the parameter k and $\mu=0$. One observes that setting $k=0$, i.e., $f(a_R)=1/2\pi$, incurs isotropic scattering. As k increases, the scattering becomes increasingly non-isotropic. For small k , the von Mises pdf approximates the cardioid pdf [149, p.60], which is rather similar to the cosine pdf [153], while for large k it resembles a Gaussian pdf [149, p.60] with mean μ and standard deviation $1/\sqrt{k}$. For $k=\infty$ (extremely non-isotropic scattering), the von Mises pdf becomes a Dirac delta function concentrated at $a_R=\mu$, i.e., $f(a_R)=\delta(a_R-\mu)$, where $\delta(\cdot)$ denotes the Dirac delta function.

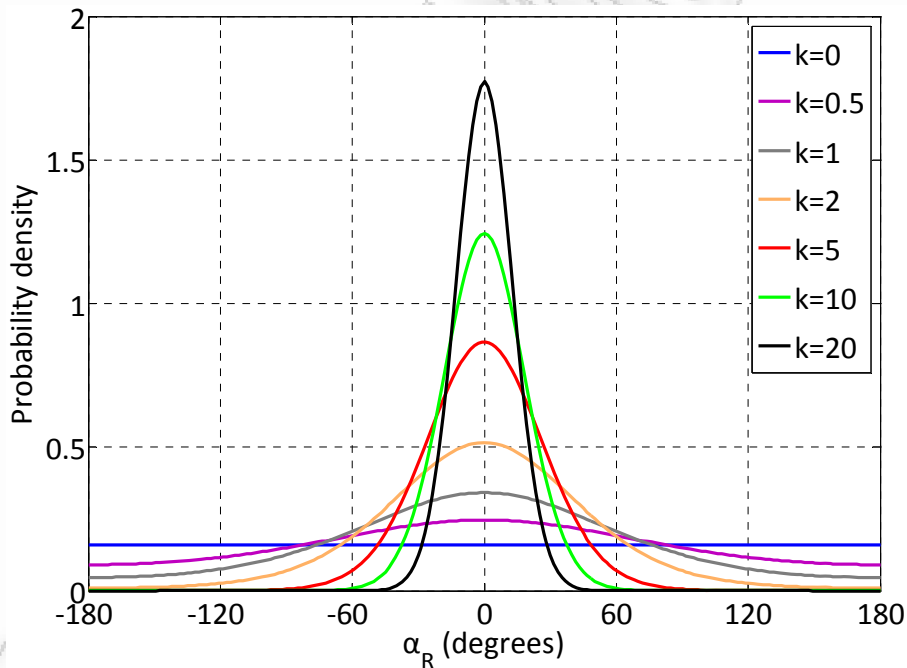


Figure 24: The probability density for the distribution of the angle of arrival of the scattered waves for different degree of scattering.

In order to characterize the distance R_S , the hyperbolic pdf [154] is used, which is empirically justified in [155], [156]. This distribution is more realistic and flexible than other commonly used distributions, such as the uniform distribution [91],

[120], because it allows scatterers to assume higher concentration in a flexible area in the vicinity of the TMS. The hyperbolic pdf is defined as follows [154]-[156]

$$f(R_S) = \frac{a}{\tanh(aR_{S,\max}) \cosh^2(aR_S)}, \quad 0 < R_S \leq R_{S,\max}. \quad (40)$$

The parameter a controls the spread (standard deviation) of the scatterers around the TMS and its applicable value is in the interval $(0,1)$.

Figs. 25 and 26 show the hyperbolic pdf and the mean distance between TMS and the scatterers, respectively, for several values of the parameter a and $R_{S,\max} = 200$ m. One observes that decreasing a increases the spread of the pdf of R_S and increases the mean distance between the scatterers and the terrestrial user. Considering a HAP-based communications system, as the elevation angle of the platform decreases, the scatterers are expected to be more widely distributed, which corresponds to a possible decrease of a . Nevertheless, a can be accurately obtained through measurements in different propagation environments, i.e., urban, suburban or rural environments.

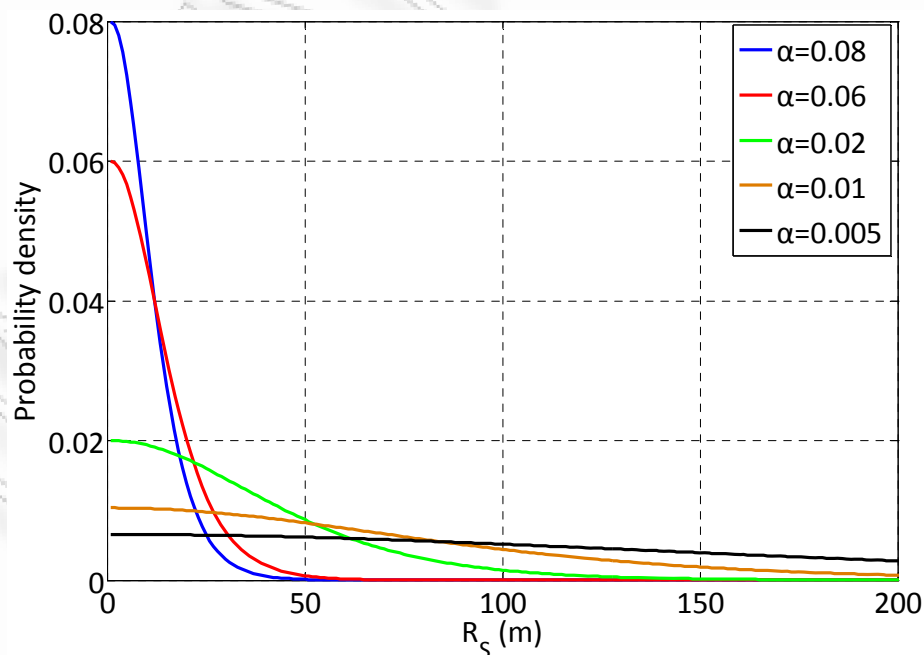


Figure 25: The probability density for the distribution of the distance between TMS and the scatterers for different values of the parameter a .

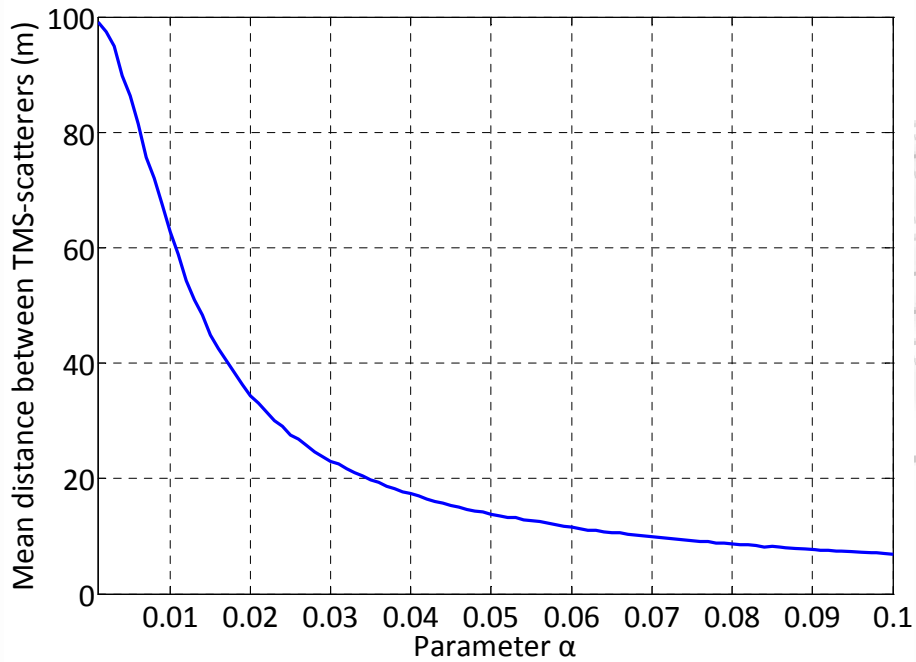


Figure 26: The mean distance between the TMS and the scatterers for different values of the parameter α .

The building height was found to follow normal [157], log-normal [157]-[159] or Rayleigh distribution [160], depending on the selected urban or suburban environment. Specifically, the corresponding distributions matched geographical data values obtained from measurements of building heights conducted in high and medium built-up density areas in different European countries. In order to characterize the height H_S , the log-normal pdf is adopted, which is defined as

$$f(H_S) = \frac{e^{-\frac{[\ln(H_S) - \ln(H_{S,\text{mean}})]^2}{2\sigma^2}}}{H_S \sigma \sqrt{2\pi}}, \quad 0 < H_S \leq H_{S,\text{max}}, \quad (41)$$

where the parameters $H_{S,\text{mean}}$ and σ are the mean and standard deviation of H_S , respectively. Fig. 27 demonstrates the experimentally verified log-normal distribution of building heights in London, U.K. (densely built-up district) and Guildford, U.K. (medium-size town) with parameters $H_{S,\text{mean}} = 17.6$ m and $\sigma = 0.31$, and $H_{S,\text{mean}} = 7.2$ m and $\sigma = 0.26$, respectively [157].

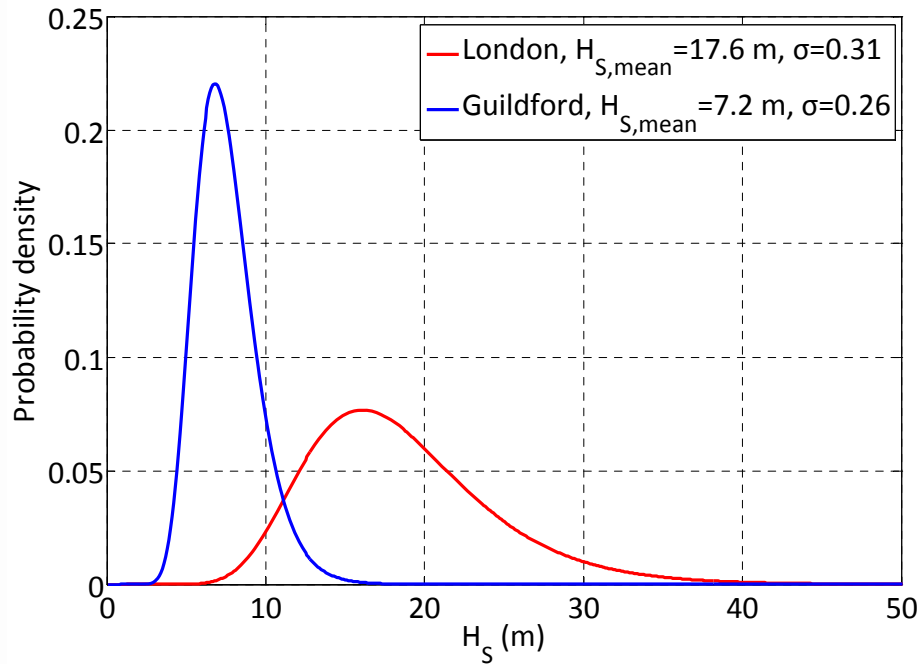


Figure 27: The probability density for the distribution of the building heights in London (U.K.) and Guildford (U.K.).

Finally, using (39)-(41), and the equality $\int_{-\pi}^{\pi} e^{a\sin(c)+b\cos(c)} dc = 2\pi I_0(\sqrt{a^2+b^2})$ [161, eq.3.338-4], (38) becomes

$$R_{pl,qm}^{NLoS}(\delta_T, \delta_R, \tau) = r_1 \int_0^{H_{S,max}} \int_0^{R_{S,max}} r_2 I_0(\sqrt{r_3^2 + r_4^2}) dR_S dH_S, \quad (42)$$

where

$$r_1 = \frac{j2\pi \left[\frac{(q-p)\delta_T \cos\theta_T}{\lambda \cos\beta_T} - \tau f_{T,max} \cos\gamma_T \right]}{\sigma \sqrt{2\pi} \tanh(aR_{S,max}) I_0(k) \sqrt{(K_{pl}+1)(K_{qm}+1)}}, \quad (43)$$

$$r_2 = \frac{e^{-\frac{[\ln(H_S) - \ln(H_{S,mean})]^2}{2\sigma^2}} e^{j \frac{2\pi(m-l)\delta_R \sin\psi_R \sin[\arctan(H_S/R_S)]}{\lambda}}}{H_S \cosh^2(aR_S)}, \quad (44)$$

$$\begin{aligned} r_3 = & j \frac{2\pi(q-p)\delta_T \sin\theta_T R_S}{\lambda D \cos\beta_T} - j2\pi\tau f_{T,max} \sin\gamma_T R_S / D \\ & + j2\pi(m-l)\delta_R \sin\theta_R \cos\psi_R \cos[\arctan(H_S/R_S)] / \lambda \\ & - j2\pi\tau f_{R,max} \sin\gamma_R \cos[\arctan(H_S/R_S)] + k \sin\mu, \end{aligned} \quad (45)$$

$$r_4 = j2\pi(m-l)\delta_R \cos\theta_R \cos\psi_R \cos[\arctan(H_S/R_S)] / \lambda - j2\pi\tau f_{R,\max} \cos\gamma_R \cos[\arctan(H_S/R_S)] + k \cos\mu. \quad (46)$$

To obtain the STCF of the NLoS component, the integral in (42) has to be numerically evaluated, since there is no closed-form solution.

Finally, the STCF between two arbitrary subchannels $h_{pl}(t)$ and $h_{qm}(t)$ becomes a summation of the STCFs of the LoS and NLoS components defined in (36) and (42)-(46), respectively.

3.4.1 Investigation of Space-Time Correlation of HAP-MIMO Channels

This subsection investigates the absolute spatial and temporal correlation, and demonstrates the impact of the antenna elements spacing and arrangement. Unless indicated otherwise, the values of the model parameters used to obtain the curves are $n_T = n_R = 2$, $\beta_T = 60^\circ$, $\theta_T = \theta_R = 90^\circ$, $\psi_R = 0^\circ$, $H_T = 20$ km, $k = 3$, $\mu = 0^\circ$ and $R_{S,\max} = 200$ m. Moreover, a typical densely built-up district (London, U.K. [157]) is considered to be the scattering region, i.e., the surrounding buildings act as scatterers, and the values of the corresponding model parameters used are $H_{S,\max} = 100$ m, $H_{S,\text{mean}} = 17.6$ m, and $\sigma = 0.31$. In addition, it is assumed that $\alpha = 0.01$, which corresponds to a reasonable average distance between the TMS and an effective scatterer of approximately 60 m (see Fig. 26). This value was observed by applying ray-tracing techniques to 3-D digital maps of European typical urban environments (Fig. 28). Specifically, the AWE Communications Winprop software package was used, which is designed to accurately predict the propagation characteristics between the link of a transmitter and a receiver including all important parameters of the mobile radio channel. To properly simulate the desired HAP-based scenario, single bounce scattering conditions, i.e., either reflection or diffraction, were considered for an elevated transmitter at 20 km and an elevation angle of 60° . Finally, in order to clearly present the influence

of each model parameter on the correlation, and indicate the minimum achieved correlation, it is considered that $K_{pl} = K_{qm} = K = 0$ (Rayleigh channel). However, in many cases a LoS component exists, i.e., $K > 0$. Fig. 29 demonstrates the correlation as a function of the Ricean factor, in the general case. One observes that the absolute correlation easily exceeds 0.15, 0.5 and 0.7, as soon as the Ricean factor exceeds -7 dB, 0 dB and 3 dB, respectively.

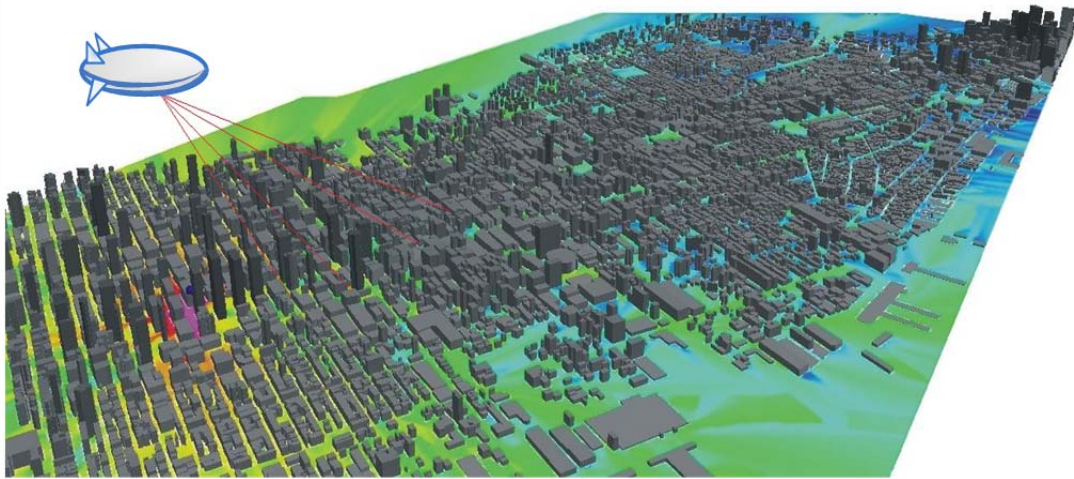


Figure 28: 3-D building distribution in a typical urban propagation environment.

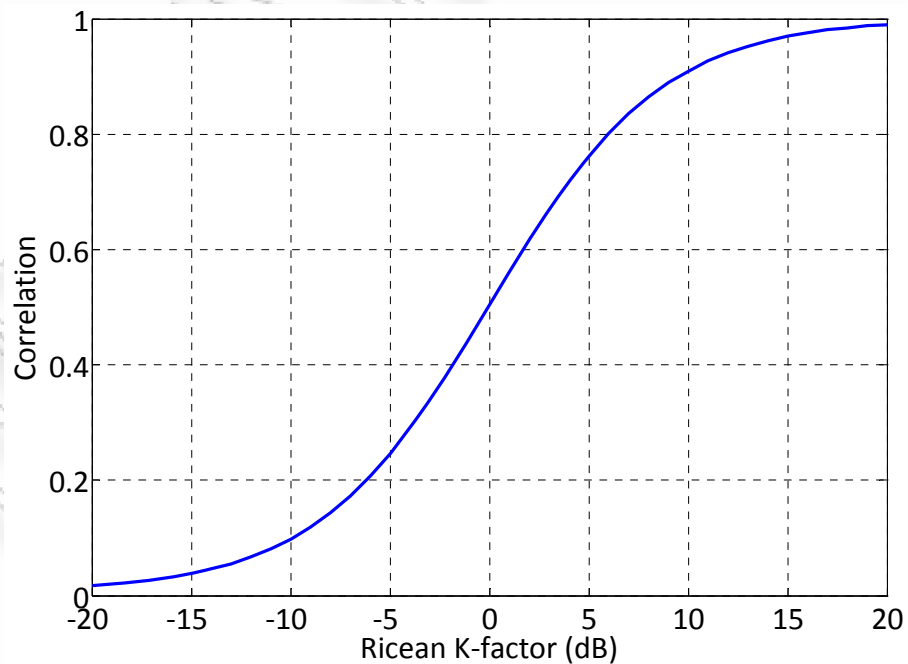


Figure 29: The absolute correlation of HAP-MIMO channels for various values of the Ricean factor.

Fig. 30 depicts the transmit spatial correlation function (SCF) $R_{pl,ql}^{NLoS}(\delta_T)$ as a function of the antenna separation at the SBS for different elevation angle β_T . Observe that as the elevation angle β_T increases, the SCF drastically decreases, under both isotropic and non-isotropic scattering environments. From Fig. 30 the proper HAP antenna separation to achieve an uncorrelated MIMO channel matrix can be also indicated. For instance, assuming that an absolute correlation of 0.15 or less amounts to nearly uncorrelated links, and considering 2.1 GHz carrier frequency [35], i.e., the wavelength is equal to approximately 0.14 m, and $\beta_T = 60^\circ$, HAP antennas require a separation of around 10 and 18 m in isotropic and non-isotropic scattering environments, respectively. This suggests that utilizing MIMO techniques on a single aircraft or airship is a viable solution, as long as the Ricean factor is small. Moreover, if HAP length is adequate, more than two antennas may be used to further increase the prospective MIMO multiplexing/capacity gain.⁴

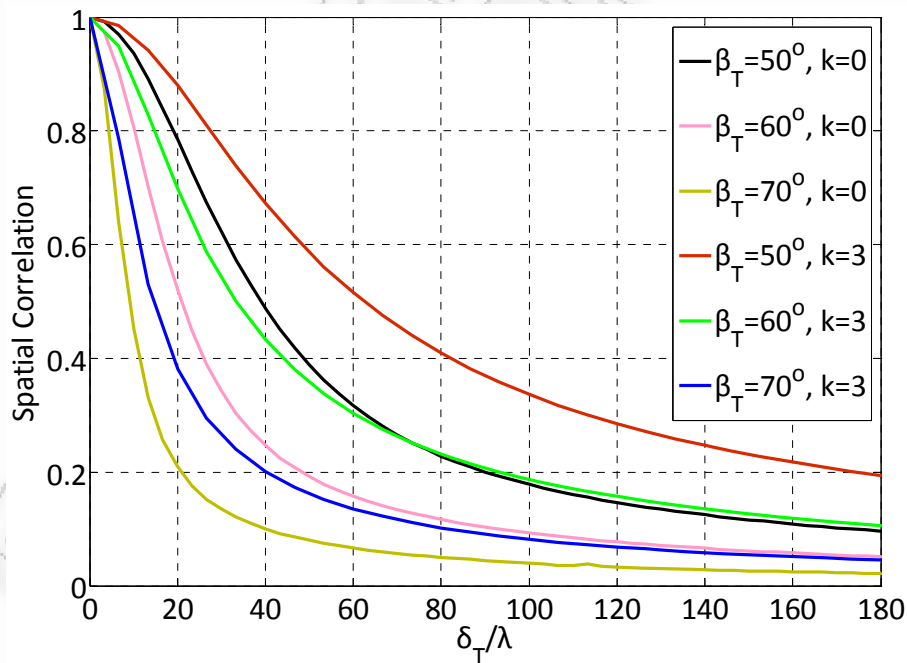


Figure 30: The transmit SCF of a 2×2 HAP-MIMO Rayleigh channel for various elevation angles of the SBS, in isotropic ($k=0$) and non-isotropic ($k=3$) scattering environments.

⁴The capacity of MIMO channels linearly increases with the number of antenna elements [95].

Fig. 31 shows the transmit $R_{pl,ql}^{NLoS}(\delta_T)$ and receive $R_{pl,pm}^{NLoS}(\delta_R)$ SCF as a function of the antenna separation at the SBS/TMS for different orientation of the SBS/TMS antenna array. Note that SBS broadside antenna arrays, i.e., $\theta_T = 90^\circ$, provide minimum spatial correlation, while SBS inline antennas, i.e., $\theta_T = 0^\circ$, are fully correlated. In addition, the receive correlation depends on the relative angle between the TMS antenna array, and the local scatterers around TMS, i.e., $\theta_R - \mu$, and is minimized, when the difference between θ_R and μ is 90° .

Fig. 32 depicts the transmit $R_{pl,ql}^{NLoS}(\delta_T)$ and receive $R_{pl,pm}^{NLoS}(\delta_R)$ SCF as a function of the antenna separation at the SBS/TMS, for different degrees of local scattering (in the azimuth domain) at the TMS. Note that as k increases, the scattering becomes increasingly non-isotropic and the correlation significantly increases. For highly concentrated scatterers around the mean angle, i.e., for $k = 10$, the required separation at the SBS for uncorrelated subchannels is $\delta_T > 200\lambda$, while the required separation at the TMS is $\delta_R > 1.5\lambda$.

Fig. 33 shows the transmit $R_{pl,ql}^{NLoS}(\delta_T)$ and receive $R_{pl,pm}^{NLoS}(\delta_R)$ SCF as a function of the antenna separation at the SBS/TMS for different spread of the scatterers around the TMS, which is controlled by the parameter a of the hyperbolic distribution. In particular, a values of 0.1, 0.05, and 0.005 are used, which correspond to an average distance between the TMS and an effective scatterer of approximately 7 m, 13.5 m, and 88 m, respectively (see Fig. 26). Observe that as a increases, the spread of scatterers decreases and the correlation drastically increases.

Fig. 34 shows the transmit $R_{pl,ql}^{NLoS}(\delta_T)$ and receive $R_{pl,pm}^{NLoS}(\delta_R)$ SCF as a function of the antenna separation at the SBS/TMS for different distance $R_{S,max}$ between the projections to the x - y plane of TMS and an effective scatterer, when $a = 0.01$. One observes that increasing $R_{S,max}$ beyond 150 m has a negligible effect on the correlation.

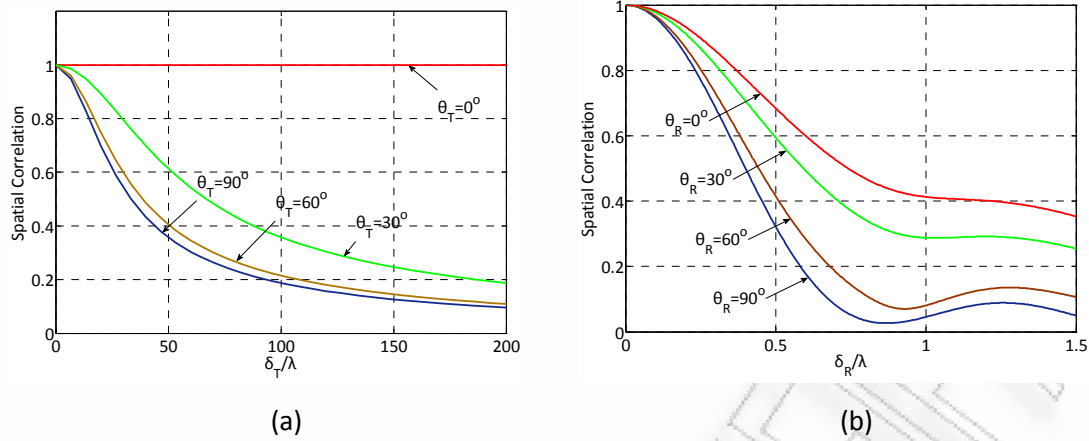


Figure 31: The transmit (a) and receive (b) SCF of a 2×2 HAP-MIMO Rayleigh channel for different orientation of the SBS and TMS antenna array, respectively.

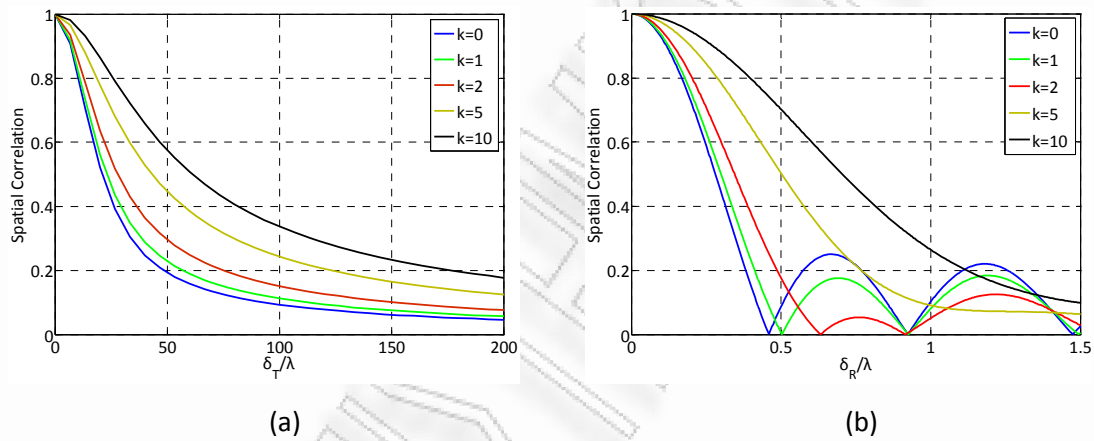


Figure 32: The transmit (a) and receive (b) SCF of a 2×2 HAP-MIMO Rayleigh channel for different degree of local scattering at the TMS.

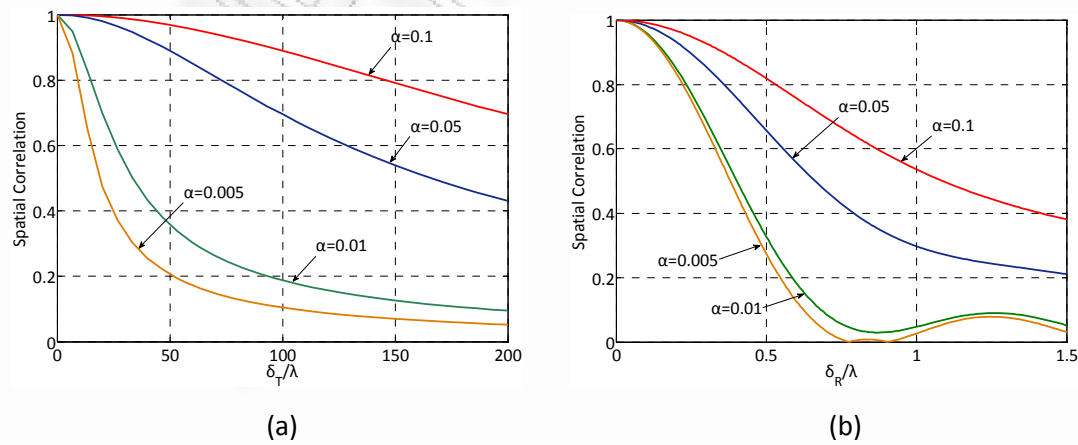


Figure 33: The transmit (a) and receive (b) SCF of a 2×2 HAP-MIMO Rayleigh channel for different spread of the scatterers around the TMS.

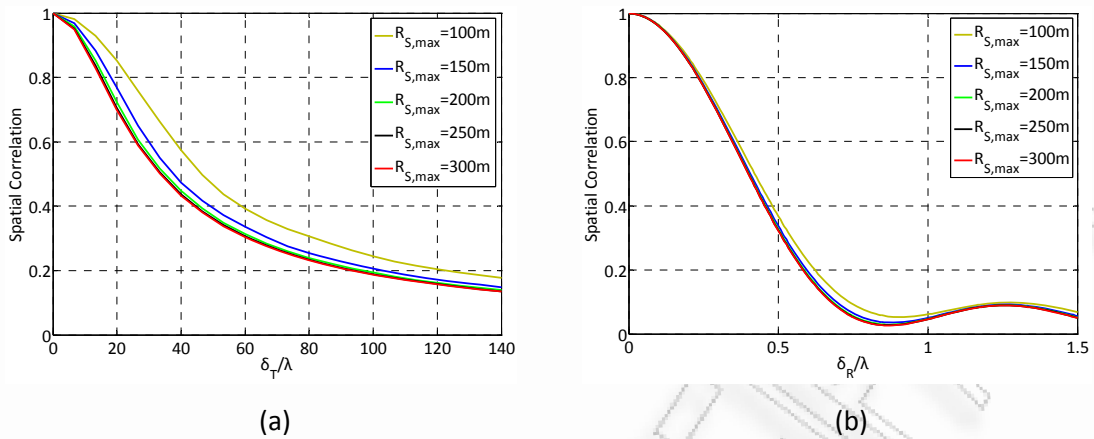


Figure 34: The transmit (a) and receive (b) SCF of a 2×2 HAP-MIMO Rayleigh channel for different maximum distance between the projections to the x - y plane of the TMS and an effective scatterer.

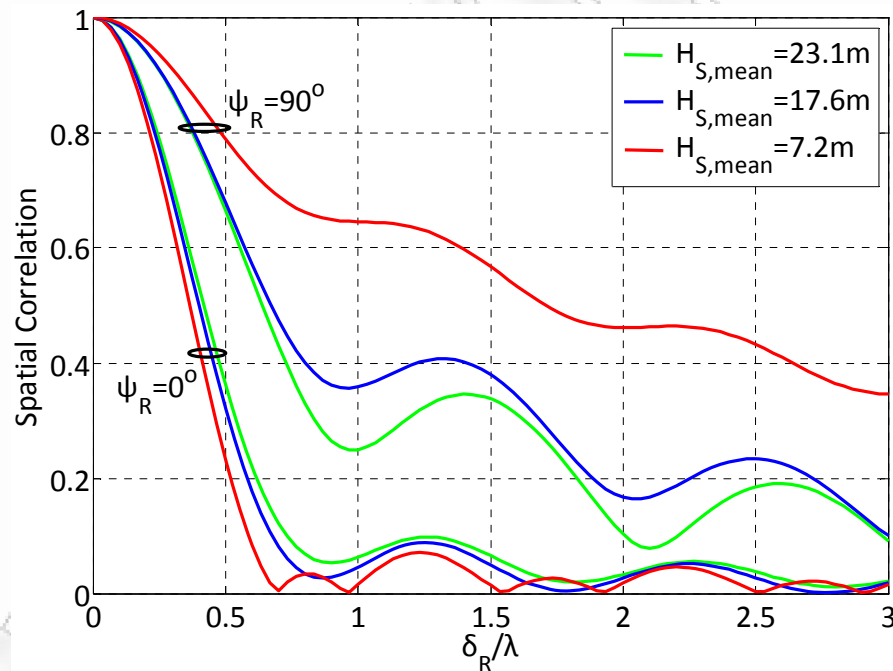


Figure 35: The receive SCF of a 2×2 HAP-MIMO Rayleigh channel with horizontally ($\psi_R = 0^\circ$) or vertically ($\psi_R = 90^\circ$) placed TMS antennas, for various mean values of the scatterer height.

Fig. 35 shows the receive SCF $R_{pl,pm}^{NLoS}(\delta_R)$ of horizontally, i.e., $\psi_R = 0^\circ$, and vertically, i.e., $\psi_R = 90^\circ$, placed TMS antenna arrays as a function of the antenna separation at the TMS for different mean of the scatterer height $H_{S,mean}$. Note that

for horizontally placed arrays, changing $H_{S,\text{mean}}$ has an insignificant influence on the spatial correlation, whereas for vertically placed arrays the spatial correlation drastically decreases, as $H_{S,\text{mean}}$ increases. Fig. 35 suggests that two vertically placed antennas can have small correlations and provide considerable diversity gain in highly urbanized areas. It also justifies the inclusion of the third dimension of the model.

The shape of the SCF $R_{pl,qm}^{NLoS}(\delta_T, \delta_R)$ is illustrated in Fig. 36. Both Rayleigh and Ricean fading conditions are considered, and the Ricean factor is set to 0 and 3 dB, respectively. It is clear that the SCF is significantly affected not only by the spacing but also by the arrangement of the antenna elements. Providing that the Ricean factor is small, and the SBS and TMS antenna elements are carefully arranged, low spatial correlation can be obtained.

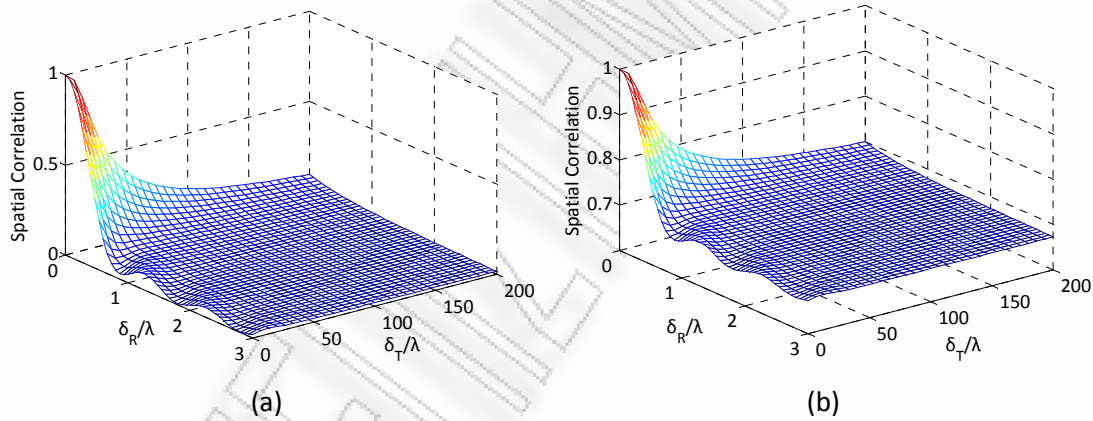


Figure 36: The SCF of a 2×2 HAP-MIMO (a) Rayleigh and (b) Ricean channel.

Figs. 37-40 investigate the effect of model parameters on the temporal correlation function (TCF), i.e., $\delta_T = \delta_R = 0$, $R_{pl}^{NLoS}(\tau)$ of a Rayleigh HAP-SISO channel. The quasi-stationary airship is considered and the corresponding maximum Doppler frequency shift used is $f_{T,\text{max}}^{\text{Airship}} \approx 0$ Hz. In addition, the maximum Doppler frequency shift and the moving direction of TMS are $f_{R,\text{max}} = 100$ Hz and $\gamma_R = 60^\circ$, respectively.

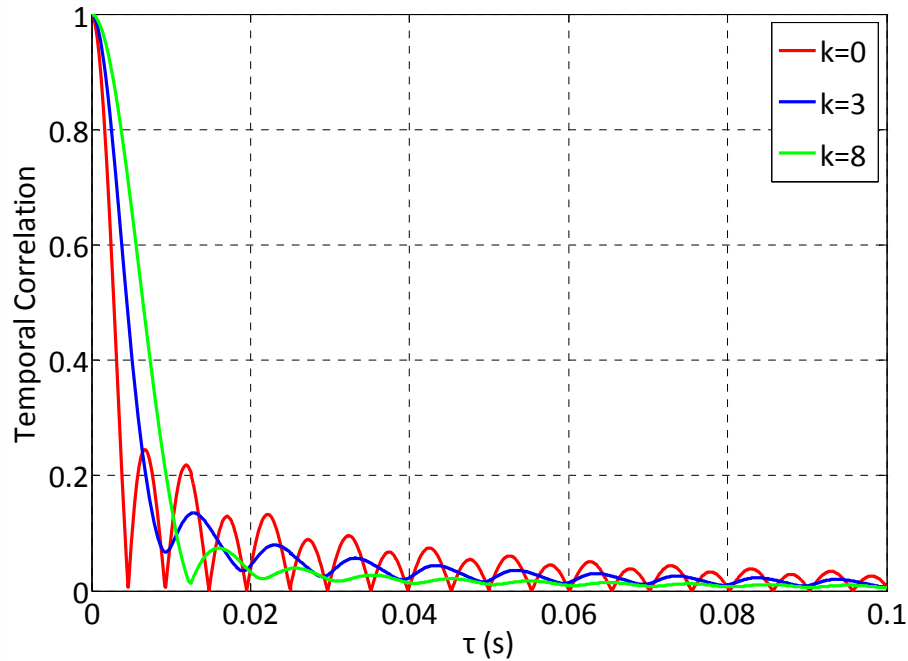


Figure 37: The TCF of a HAP-SISO Rayleigh channel for different degree of local scattering at the TMS.

Fig. 37 depicts the TCF $R_{pl}^{NLoS}(\tau)$ for different degrees of local scattering (in the azimuth domain) at the TMS. Note that as k increases, the temporal correlation increases.

Fig. 38 shows the TCF $R_{pl}^{NLoS}(\tau)$ for different spread of the scatterers around the TMS, i.e., different α , and different distances $R_{S,max}$ between the projections to the x - y plane of TMS and an effective scatterer. Observe that as α increases, the temporal correlation drastically increases. However, changing $R_{S,max}$ has a negligible effect on the temporal correlation.

Fig. 39 depicts the TCF $R_{pl}^{NLoS}(\tau)$ for different mean of the scatterer height. Note that as $H_{S,mean}$ increases, the temporal correlation fairly decreases.

Fig. 40 demonstrates the TCF $R_{pl}^{NLoS}(\tau)$ for different maximum Doppler frequency $f_{R,max}$ and moving direction γ_R at the TMS. One observes that an increase in $f_{R,max}$ results in a decrease in temporal correlation. Furthermore, as γ_R

increases, the TMS moves toward the SBS and the temporal correlation drastically decreases.

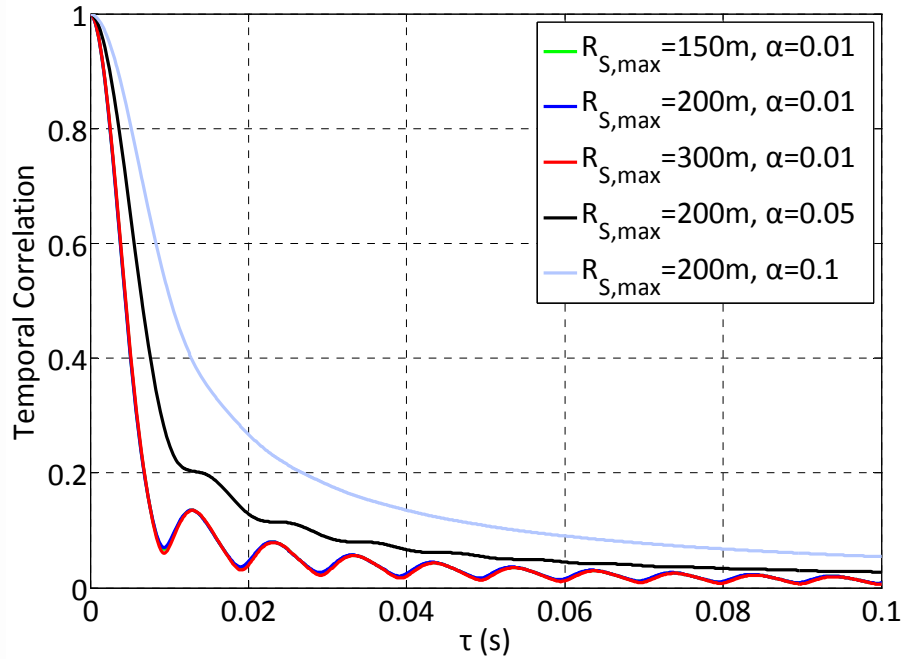


Figure 38: The TCF of a HAP-SISO Rayleigh channel for different spread of the scatterers around the TMS and different maximum distance between the projections to the x - y plane of TMS and an effective scatterer.

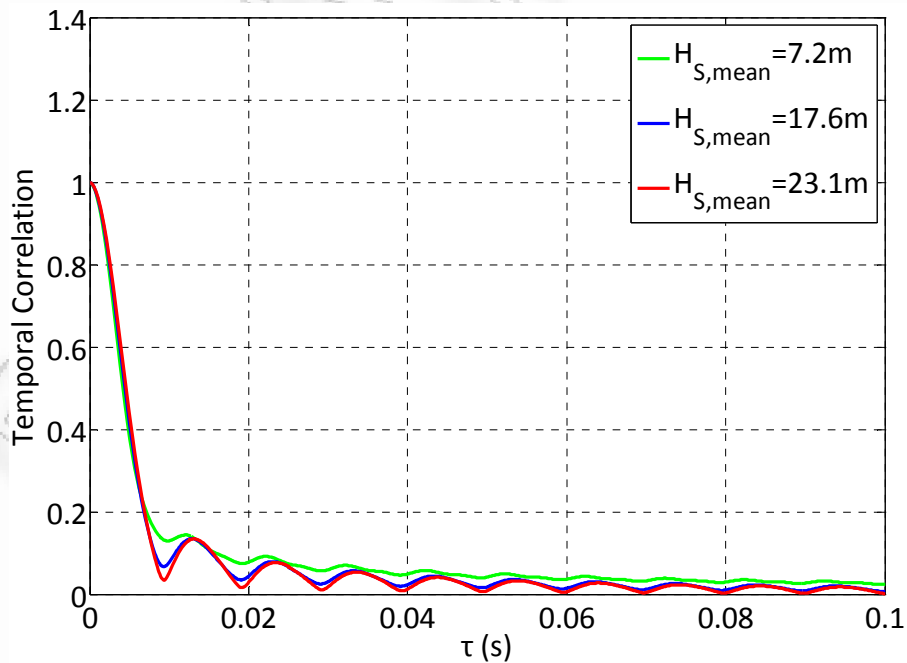


Figure 39: The TCF of a HAP-SISO Rayleigh channel for various mean values of the scatterer height.

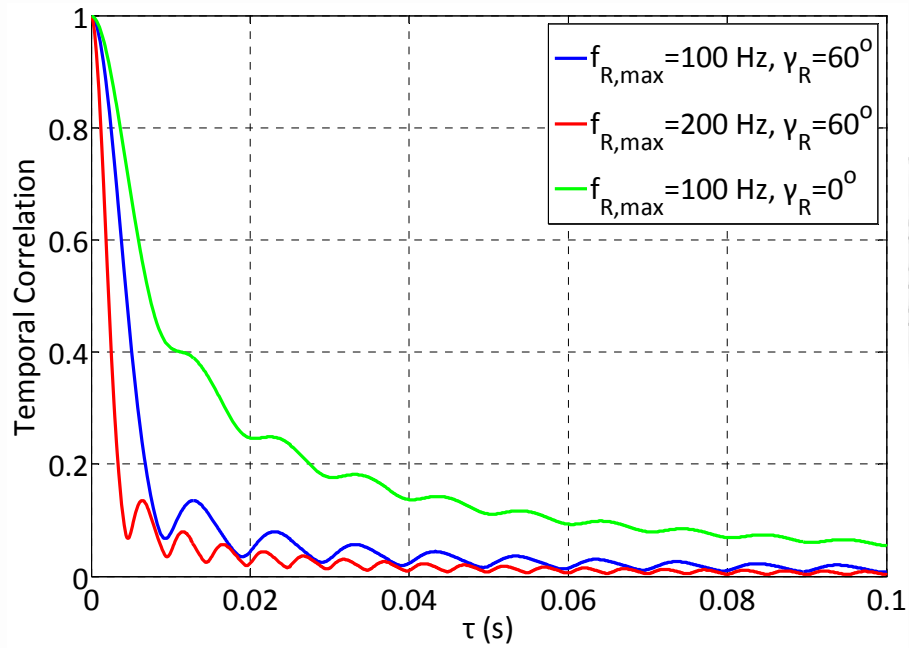


Figure 40: The TCF of a HAP-SISO Rayleigh channel for different maximum Doppler frequency and different moving direction at the TMS.

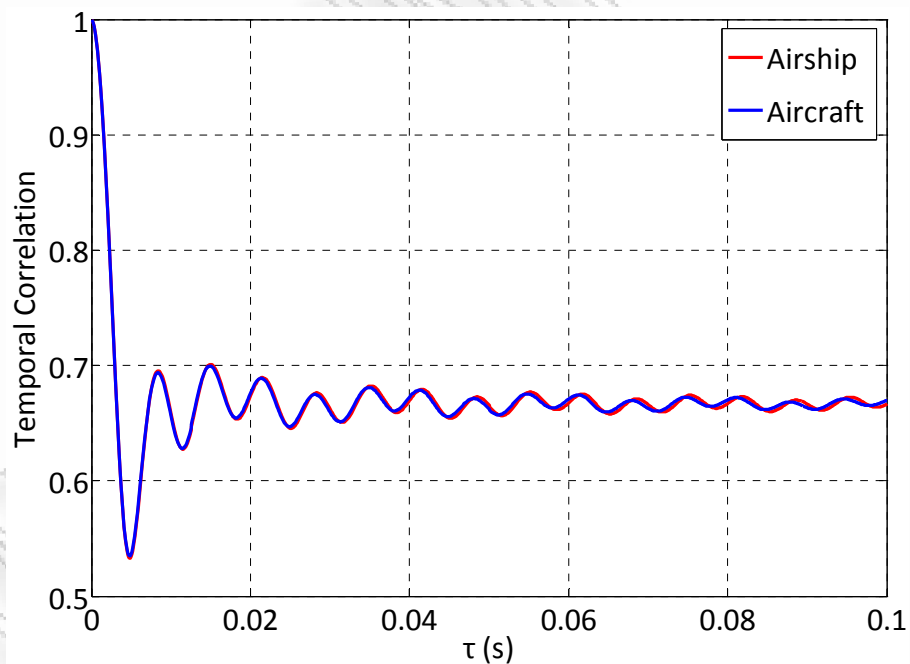


Figure 41: The TCF of a HAP-SISO Ricean channel for different HAP structures.

Fig. 41 depicts the TCF of a Ricean HAP-SISO channel, when $K_{pl} = K = 3$ dB. Both the quasi-stationary airship and the moving aircraft structures are considered, and the corresponding maximum Doppler frequency shifts used are $f_{T,max}^{Airship} \approx 0$ Hz and

$f_{T,\max}^{Aircraft} = 300$ Hz, respectively, while the moving direction of SBS (aircraft case) is set to $\gamma_T = 30^\circ$. One observes that the two structures have almost identical temporal correlation properties. Fig. 41 also implies that velocity variations at the SBS due to the stratospheric winds do not significantly affect the temporal correlation.

Finally, the shape of the transmit $R_{pl,ql}^{NLoS}(\delta_T, \tau)$ and the receive $R_{pl,pm}^{NLoS}(\delta_R, \tau)$ STCF of HAP-MIMO Rayleigh ($K=0$) and Ricean ($K=3$ dB) channels is illustrated in Figs. 42 and 43, respectively.

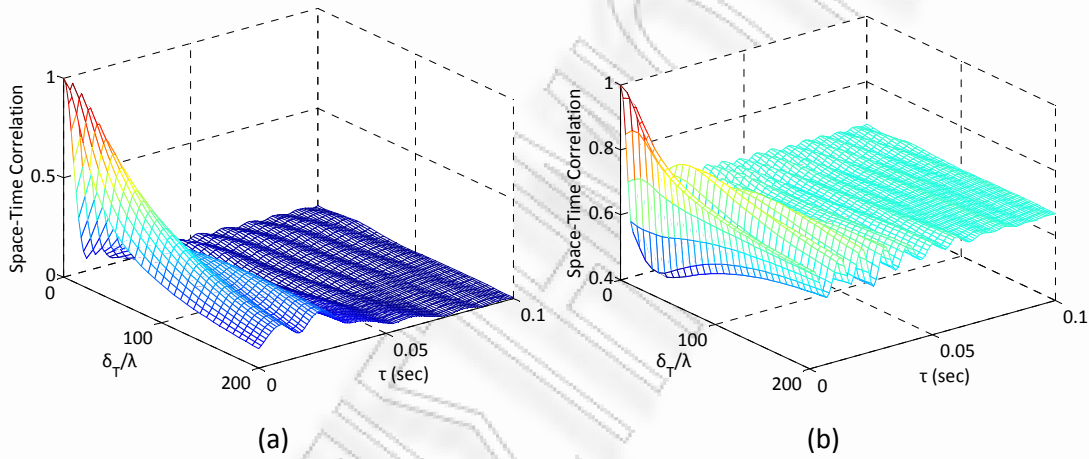


Figure 42: The transmit STCF of a 2×2 HAP-MIMO (a) Rayleigh and (b) Ricean channel.

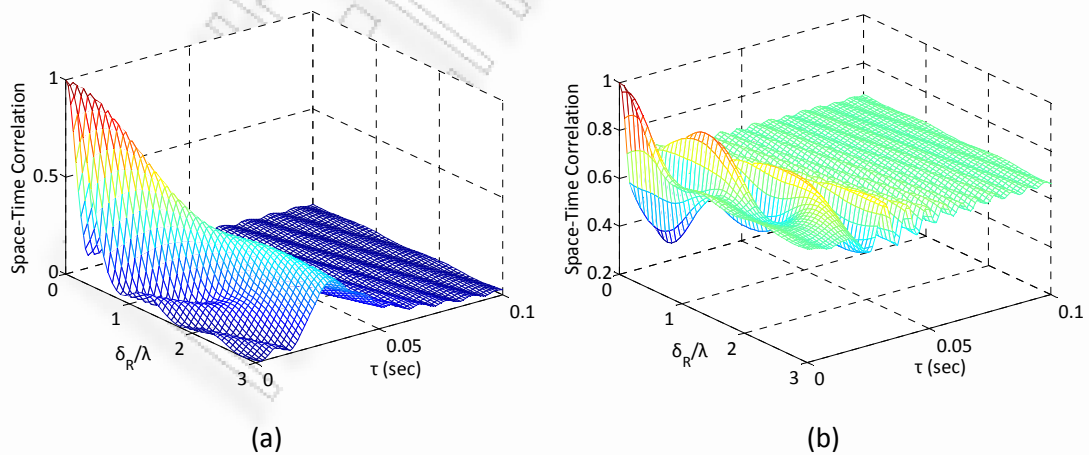


Figure 43: The receive STCF of a 2×2 HAP-MIMO (a) Rayleigh and (b) Ricean channel.

3.4.1.1 Effect of HAP Antenna Displacement

This subsection investigates the effect of HAP antenna displacement due to the stratospheric winds on the transmit spatial correlation of HAP-MIMO channels. In practice, there are six degrees of freedom (DoF) to which HAPs are subjected. Specifically, HAPs may be displaced in any direction at a varying speed, and the displacements can be shifting along the x -, y -, and z -axes, as well as roll, pitch, and yaw [24]-[26]. According to the geometry of the reference model and considering that SBS antenna elements are installed along the SBS, rotation with respect to the x -axis corresponds to pitch, rotation on the y -axis corresponds to roll and rotation along z -axis corresponds to yaw (see Fig. 44). Roll and pitch can be considered identical to each other, since both are based on similar principles. Thus, the effect of only pitch and yaw on the correlation is studied. As shown in Fig. 44, pitch corresponds to an elevation of the p^{th} SBS antenna element, which is described by the angle ψ_T .

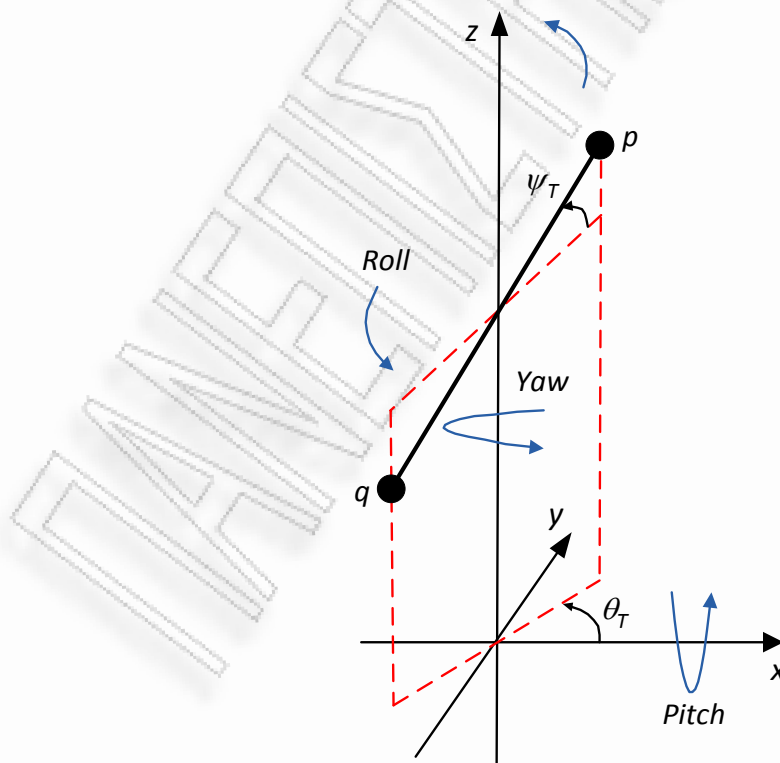


Figure 44: Geometrical representation of roll, pitch, and yaw effects.

The influence of each DoF is examined independently (keeping all other parameters fixed) in the following figures. The values of the parameters used to obtain the curves are the same as in the previous subsection. Fig. 45 demonstrates the influence of 5 km shifting along either x -, y - or z -axis on the transmit SCF. One observes that the correlation is relatively insensitive to displacements along y -axis, while fairly increases when the displacements take place along z -axis. However, shifting along x -axis significantly increases correlation.

Fig. 46 studies the pitch effect and shows the transmit SCF $R_{pl,q}^{NLoS}(\delta_T)$ as a function of the angle ψ_T . One observes that increasing angle ψ_T from 0° to 30° has a negligible effect on the transmit spatial correlation. However, further increase in ψ_T drastically increases the correlation, and when $\psi_T = 90^\circ$, the antennas are fully correlated.

Finally, yaw corresponds to a change in the orientation of the SBS antenna array, which is described by the angle θ_T . Therefore, Fig. 31(a) represents also the yaw effect.

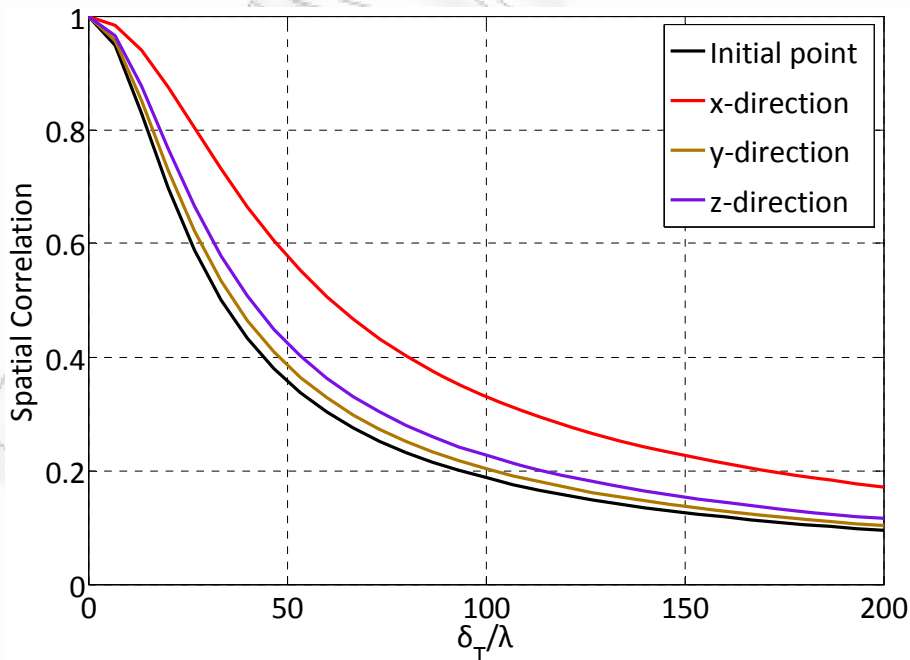


Figure 45: The transmit SCF of a 2×2 HAP-MIMO Rayleigh channel for different directions of HAP displacement due to stratospheric winds.

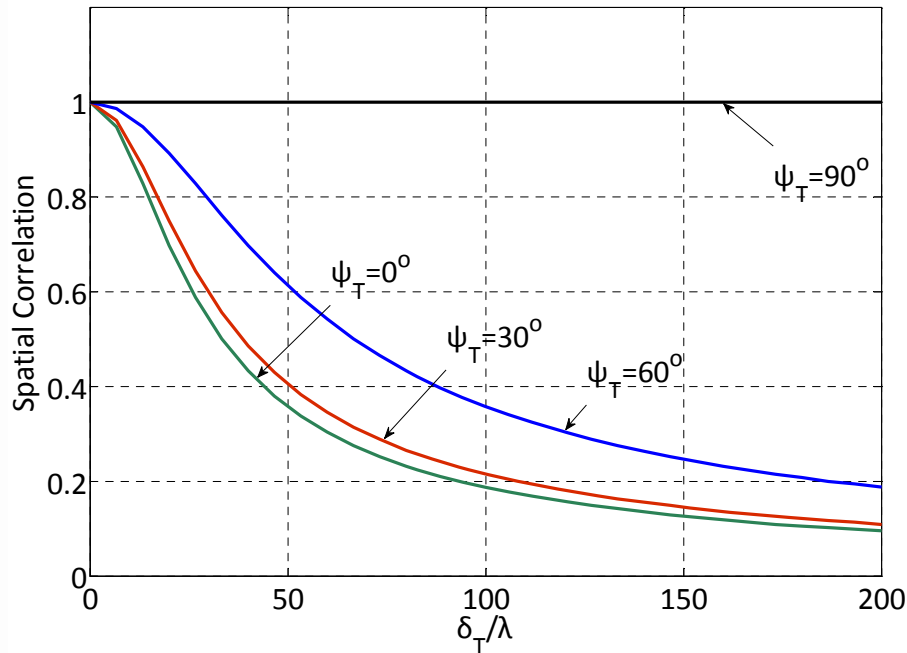


Figure 46: The transmit SCF of a 2×2 HAP-MIMO Rayleigh channel for different elevation angle of the p^{th} SBS antenna element (pitch effect).

3.5 Analysis of HAP-MIMO Channel Capacity

This section utilizes the reference model described above and defines the HAP-SISO and HAP-MIMO channel capacity.⁵ It also compares the capacity of a 2×2 HAP-MIMO channel with that of a HAP-SISO channel and investigates the impact of model parameters on the capacity of HAP-MIMO channels [162], [163].

3.5.1 Definition of HAP-MIMO Channel Capacity

For a HAP-SISO channel, the Shannon upper bound limit on capacity is given by

$$C_{SISO} = \log_2 \left(1 + \text{SNR} |h_{11}|^2 \right) \text{ bps/Hz}, \quad (47)$$

where h_{11} is a normalized complex faded channel gain and SNR corresponds to the average signal-to-noise ratio at the input of the receiver. Assuming that the channel is known to the TMS and unknown to the SBS, the available capacity of a HAP-MIMO channel can be obtained as follows [95]

⁵Channel capacity is defined as the maximum rate at which data can be transmitted at an arbitrarily small error probability.

$$C_{MIMO} = \log_2 \det \left(\mathbf{I}_{n_R} + \left(\frac{\text{SNR}}{n_T} \right) \mathbf{H}\mathbf{H}^H \right) \text{ bps/Hz}, \quad (48)$$

where \mathbf{H} is the $n_R \times n_T$ matrix of complex faded channel gains, \mathbf{I}_{n_R} is an identity matrix of size n_R , n_T and n_R are the number of SBS and TMS antennas respectively, $(\cdot)^H$ denotes the complex conjugate (Hermitian) transpose operator, and $\det(\cdot)$ denotes the matrix determinant. Throughout this section, the notion of ergodic capacity [95] is also employed, which corresponds to the expectation of the capacity

$$C_{erg,MIMO} = \mathbb{E} \left[\log_2 \det \left(\mathbf{I}_{n_R} + \left(\frac{\text{SNR}}{n_T} \right) \mathbf{H}\mathbf{H}^H \right) \right] \text{ bps/Hz}. \quad (49)$$

Note that when the channel is known to the TMS, the temporal correlations do not directly affect the ergodic capacity. However, the performance of practical coding schemes is affected by the temporal correlation. In particular, strong temporal correlations signify a slowly varying channel that would require longer codewords to realize the ergodic capacity. On the contrary, many low complexity coding schemes rely on the channel remaining constant over several symbols, and therefore may perform better for slowly varying channels.

Since the HAP-MIMO channel is Ricean in general, the matrix \mathbf{H} can be obtained using (10). For a unit transmit power and assuming that the value of the Ricean factor of each subchannel is approximately equal to K , the normalized matrix \mathbf{H}_{LoS} can be generated using (25), (27) and (28) as follows

$$\mathbf{H}_{LoS} = \sqrt{\frac{K+1}{K}} \begin{bmatrix} h_{11,LoS} & \cdots & h_{1n_T,LoS} \\ \vdots & \ddots & \vdots \\ h_{n_R1,LoS} & \cdots & h_{n_Rn_T,LoS} \end{bmatrix}. \quad (50)$$

Considering a 2×2 HAP-MIMO channel, \mathbf{H}_{LoS} is simplified as follows

$$\mathbf{H}_{LoS} = \sqrt{\frac{K+1}{K}} \begin{bmatrix} h_{11,LoS} & h_{12,LoS} \\ h_{21,LoS} & h_{22,LoS} \end{bmatrix}. \quad (51)$$

The matrix \mathbf{H}_{NLoS} can be evaluated from a large number of channel realizations using the following equation [98]

$$\text{vec}(\mathbf{H}_{NLoS}) = \mathbf{R}_{NLoS}^{1/2} \text{vec}(\mathbf{H}_{iid}), \quad (52)$$

where $\text{vec}(\cdot)$ denotes matrix vectorization⁶, \mathbf{R}_{NLoS} is the $n_R n_T \times n_R n_T$ correlation matrix associated with the NLoS component, $\mathbf{R}_{NLoS}^{1/2}$ is the square root of \mathbf{R}_{NLoS} that satisfies $\mathbf{R}_{NLoS}^{1/2} \mathbf{R}_{NLoS}^{H/2} = \mathbf{R}_{NLoS}$, and \mathbf{H}_{iid} is a $n_R \times n_T$ stochastic matrix with i.i.d. zero-mean complex Gaussian entries and unit variance. The $(n_R n_T)^2$ elements of \mathbf{R}_{NLoS} can be obtained using (42)-(46). In particular, \mathbf{R}_{NLoS} can be generated as

$$\mathbf{R}_{NLoS} = \sqrt{(K+1)(K+1)} \begin{bmatrix} R_{11,11}^{NLoS} & R_{11,21}^{NLoS} & \dots & R_{11,n_R n_T}^{NLoS} \\ R_{21,11}^{NLoS} & \ddots & & R_{21,n_R n_T}^{NLoS} \\ \vdots & & \ddots & \vdots \\ R_{n_R n_T,11}^{NLoS} & \dots & & R_{n_R n_T, n_R n_T}^{NLoS} \end{bmatrix}. \quad (53)$$

Considering a 2×2 HAP-MIMO channel, \mathbf{R}_{NLoS} is simplified as follows

$$\mathbf{R}_{NLoS} = \sqrt{(K+1)(K+1)} \begin{bmatrix} R_{11,11}^{NLoS} & R_{11,21}^{NLoS} & R_{11,12}^{NLoS} & R_{11,22}^{NLoS} \\ R_{21,11}^{NLoS} & R_{21,21}^{NLoS} & R_{21,12}^{NLoS} & R_{21,22}^{NLoS} \\ R_{12,11}^{NLoS} & R_{12,21}^{NLoS} & R_{12,12}^{NLoS} & R_{12,22}^{NLoS} \\ R_{22,11}^{NLoS} & R_{22,21}^{NLoS} & R_{22,12}^{NLoS} & R_{22,22}^{NLoS} \end{bmatrix}. \quad (54)$$

Finally, in order to remove the effects of the average SNR on the channel capacity, the channel response is normalized so that the constraint

$$\mathbb{E} \left[\|\mathbf{H}\|_F^2 \right] = n_T n_R \quad (55)$$

is fulfilled. The term $\|\cdot\|_F$ corresponds to the Frobenius norm of a matrix.

⁶The vectorization of a matrix is a linear transformation which converts the matrix into a column vector. Specifically, the vectorization of a $m \times n$ matrix A denoted by $\text{vec}(A)$, is the $mn \times 1$ column vector obtained by stacking the columns of the matrix A on top of one another.

3.5.2 Numerical Results

In this subsection, the effect of the model parameters on the capacity of a 2×2 HAP-MIMO channel is investigated. Unless indicated otherwise, the values of the parameters used to obtain the following curves are $n_T = n_R = 2$, $\text{SNR} = 18$ dB, $K = 3$ dB, $H_T = 20$ km, $\beta_T = 60^\circ$, $\delta_T = 50\lambda$, $\delta_R = 0.5\lambda$, $\theta_T = \theta_R = 90^\circ$, $\psi_R = 0^\circ$, $k = 3$, $\mu = 0^\circ$, $R_{S,\max} = 200$ m, $a = 0.01$, $H_{S,\max} = 70$ m, $H_{S,\text{mean}} = 17.6$ m, $\sigma = 0.31$, $f_{T,\max} = 0$ Hz, $f_{R,\max} = 100$ Hz, $\gamma_R = 60^\circ$. Finally, a normalized Doppler frequency $f_n = f_{R,\max} T_s = 0.01$ is used, where T_s is the sampling period.

Figs. 47 and 48 compare the ergodic capacity obtained using a 2×2 HAP-MIMO architecture, i.e., $n_T = n_R = 2$, and a HAP-SISO architecture, i.e., $n_T = n_R = 1$, by varying the Ricean factor and the received SNR. One observes that maximum capacity is obtained in an ideal HAP-MIMO Rayleigh channel scenario. Then, the capacity increases up to 10.6 bps/Hz compared to the capacity of a HAP-SISO channel. However, the potential MIMO gain drastically degrades with the strength of the LoS component, i.e., increasing the Ricean factor increases the correlation and decreases the multiplexing/capacity gain. On the contrary, HAP-SISO channels take advantage of the existence of a strong LoS signal, i.e., increasing the Ricean factor drastically increases the capacity. Note that the differences between HAP-MIMO and HAP-SISO architectures become more obvious as the SNR increases. Then, the rank of the channel matrix plays an important role. In addition, the channel capacity achieved using both architectures is invariable for $K > 10$ dB.

Figs. 49-53 investigate the effect of spatial and temporal correlation on the capacity. Fig. 49 shows the ergodic capacity as a function of the spacing δ_T between SBS antenna elements for different SBS elevation angle β_T and $K_{pl} = K_{qm} = K = 0$. One observes that increasing δ_T beyond approximately 70λ , 50λ and 30λ , when $\beta_T = 50^\circ$, $\beta_T = 60^\circ$ and $\beta_T = 70^\circ$, respectively, has a negligible effect on the capacity.

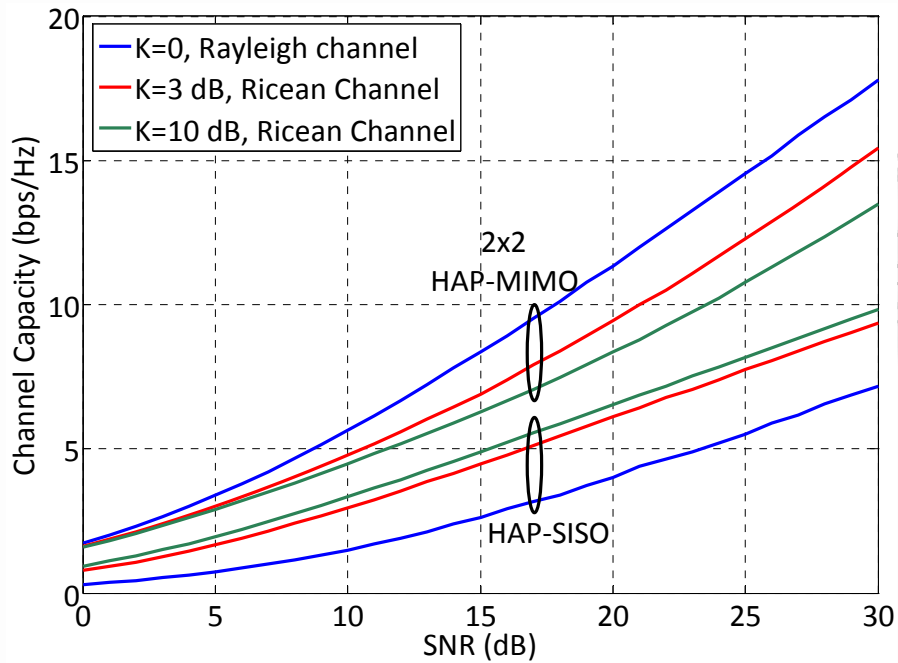


Figure 47: Comparison of the ergodic channel capacities obtained using a 2×2 HAP-MIMO architecture and a HAP-SISO architecture as a function of the received SNR for different Ricean factor.

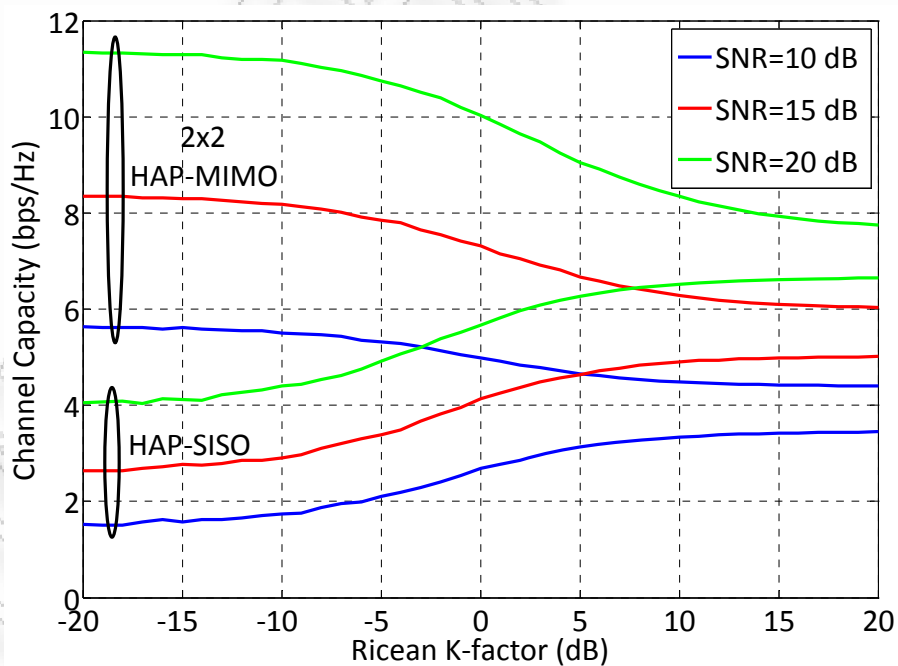


Figure 48: Comparison of the ergodic channel capacities obtained using a 2×2 HAP-MIMO architecture and a HAP-SISO architecture as a function of the Ricean factor for different received SNR.

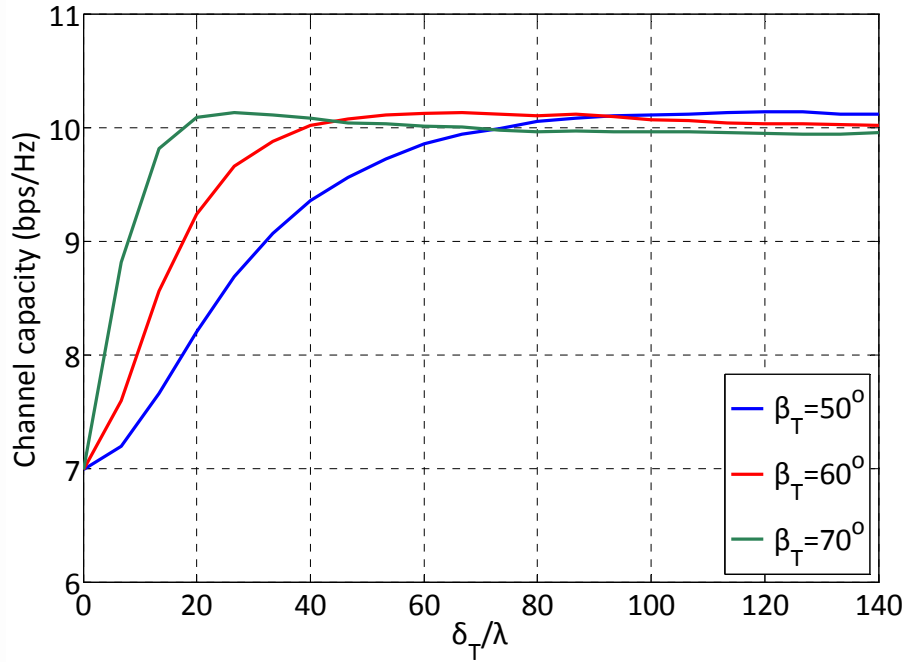


Figure 49: The ergodic capacity of a 2×2 HAP-MIMO channel as a function of the spacing between the SBS antenna elements for different SBS elevation angle.

Fig. 50 depicts the complementary cumulative distribution function (CCDF) of the capacity and examines the effect of SBS antenna array orientation on the capacity. One observes that SBS broadside antenna arrays, i.e., $\theta_T = 90^\circ$, provide maximum capacity. Decreasing θ_T from 90° to 60° has a negligible effect on the capacity. However, further decrease in θ_T significantly decreases the capacity. Note that according to [143], capacity also depends on the relative angle between the TMS antenna array and the local scatterers around the TMS, i.e., $\theta_R - \mu$. In particular, the capacity is maximized, when the difference between θ_R and μ is equal to 90° .

Fig. 51 depicts the influence of the parameters k , $R_{S,\max}$, and α on the capacity, i.e., the influence of 2-D scattering. Considering that the influence of each parameter is examined independently (keeping all other parameters fixed), one observes that increasing k decreases the capacity. Moreover, increasing α decreases the spread of scatterers and decreases the capacity. However, changing $R_{S,\max}$ has a negligible effect on the capacity.

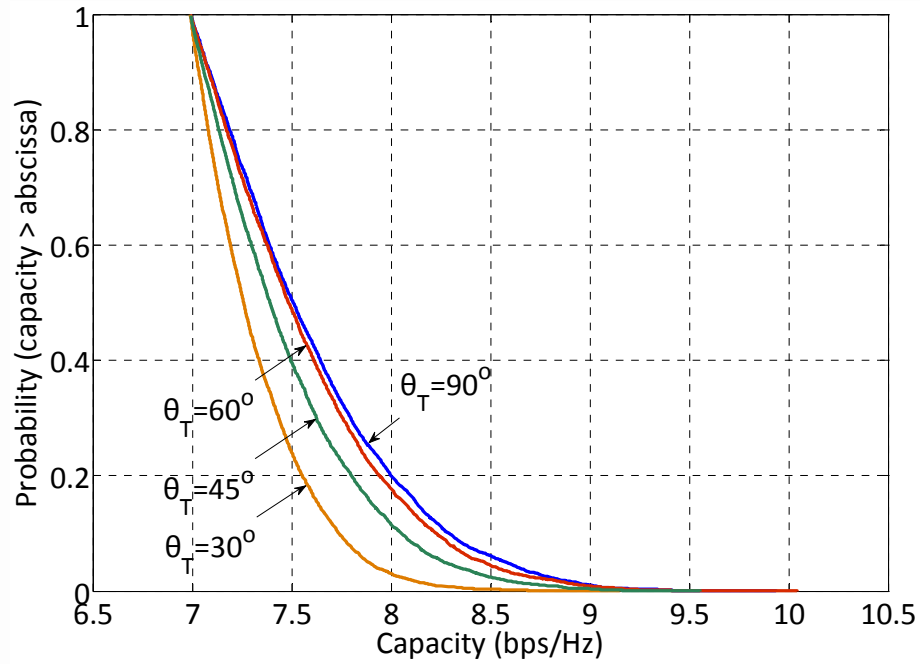


Figure 50: The complementary cumulative distribution function of the capacity of a 2×2 HAP-MIMO channel for different antenna array orientation at the SBS.

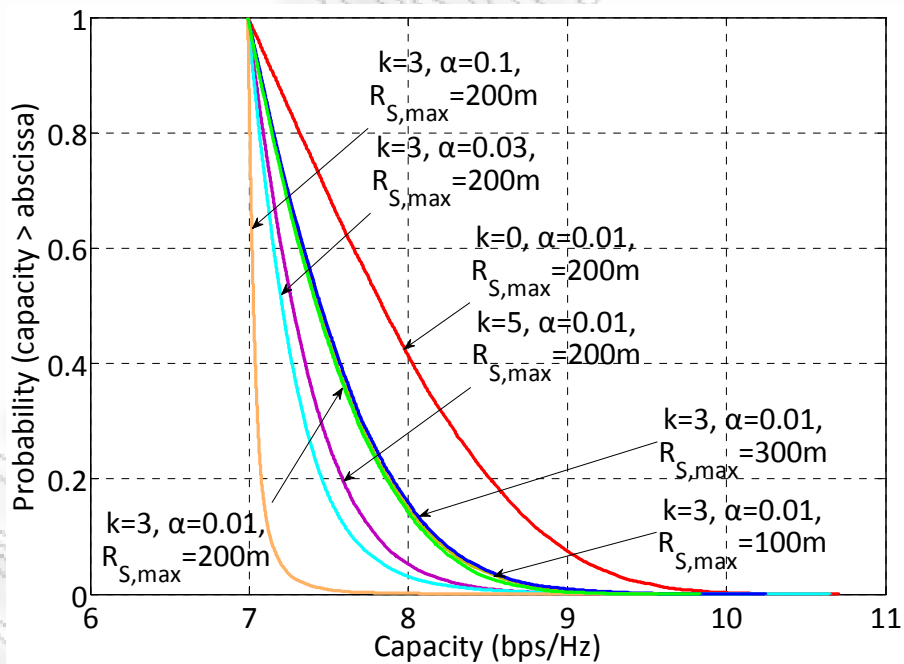


Figure 51: The complementary cumulative distribution function of the capacity of a 2×2 HAP-MIMO channel for different degree of scattering, spread of the scatterers around TMS, and maximum distance between the TMS and the scatterers.

Fig. 52 shows the CCDF of the capacity, when the TMS antenna array is horizontally, i.e., $\psi_R = 0^\circ$, or vertically placed, i.e., $\psi_R = 90^\circ$, for different $H_{S,\text{mean}}$.

Note that changing $H_{S,\text{mean}}$ has an insignificant influence on the channel capacity, when the TMS antenna array is horizontally placed. However, the capacity depends on the degree of urbanization, i.e., the heights of the scatterers, when the TMS antenna array is vertically placed. Then, increasing $H_{S,\text{mean}}$ increases the capacity. In addition, the difference between capacities of systems with horizontally and vertically placed TMS antenna array is nullified in highly urbanized areas. Fig. 52 suggests that if the available area in the x - y plane is limited for antenna array realization, the TMS antenna array can be tilted without significant loss of channel capacity.

Finally, the effect of the temporal correlation on the capacity is investigated in Fig. 53 by separately varying the normalized Doppler frequency f_n and the moving direction γ_R of the TMS. Observe that an increase in f_n results in an increase in channel capacity due to the decrease in temporal correlation. Furthermore, as γ_R increases (up to 180°), the TMS moves toward the SBS, the temporal correlation decreases, and the channel capacity increases.

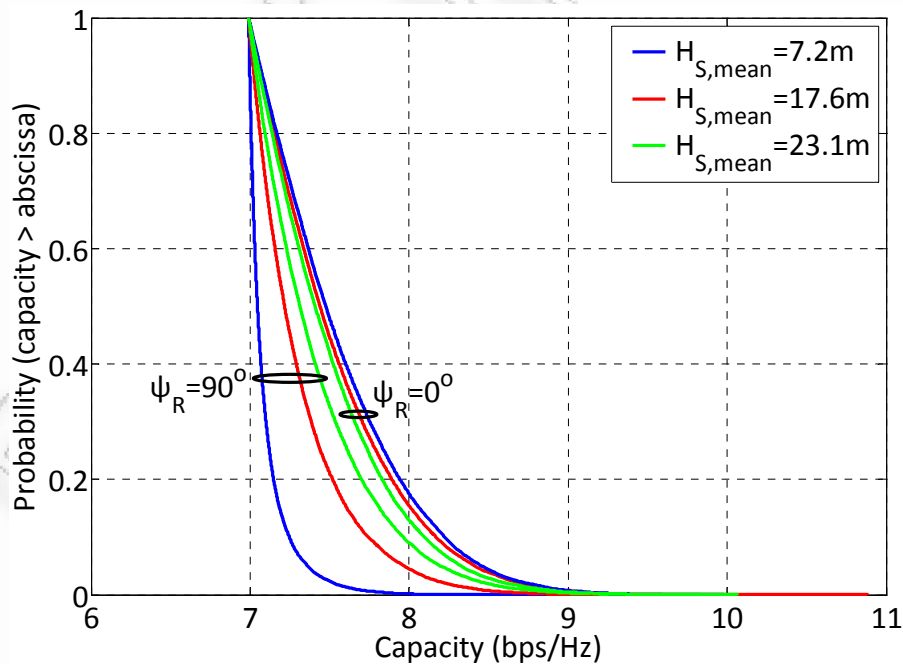


Figure 52: The complementary cumulative distribution function of the capacity of a 2×2 HAP-MIMO channel for horizontally or vertically placed TMS antennas and different mean of the scatterer height.

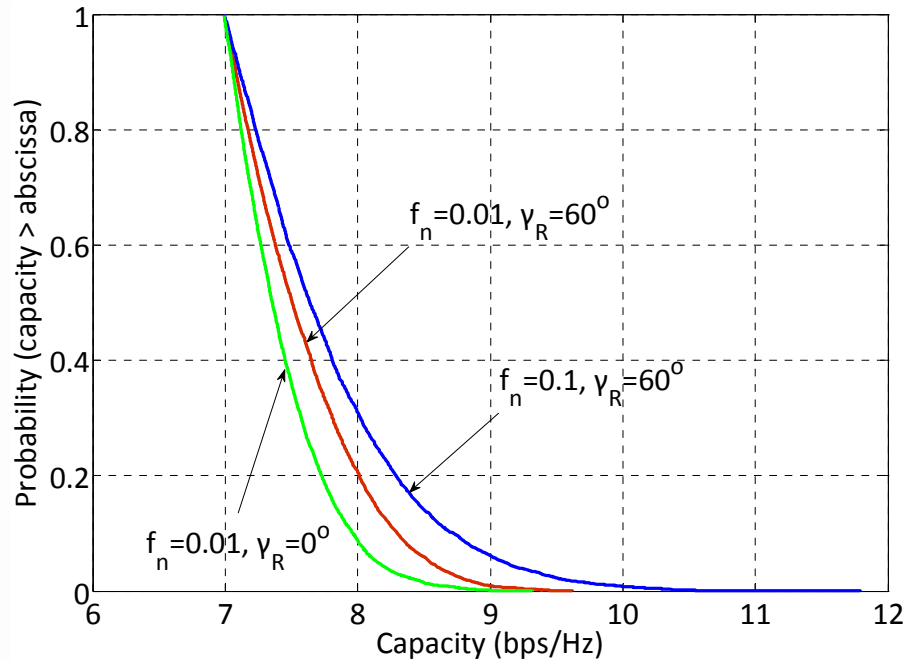


Figure 53: The complementary cumulative distribution function of the capacity of a 2×2 HAP-MIMO channel for different normalized Doppler frequency and different moving direction at the TMS.

3.6 Summary

In this chapter, a reference model for HAP-MIMO Ricean channels has been proposed, where both the HAP and the terrestrial mobile user are equipped with uniform linear multi-element antenna arrays. In particular, a 3-D cylinder model has been designed to characterize the scattering environment that encloses the user. Several parameters related to the physical properties of the stratospheric communication system have been considered, e.g., the elevation angle of the platform, the array orientation and elevation, the degree and spread of scattering for the terrestrial user, the height of the scatterers, and the HAP displacement due to the stratospheric winds. In this model, the effects of time and space selectivity have been taken into account, as a result of the user/HAP mobility, and the 3-D non-isotropic scattering conditions, respectively.

Based on this model the STCF has been derived, under a 3-D non-isotropic fading environment. The distributions for the azimuth AoA of the scattered waves, the distance between the effective scatterers and the user, and the height of the

effective scatterers have been modeled by the von Mises, the hyperbolic and the log-normal distributions, respectively, which all have previously shown to be successful in describing measured data. Extensive numerical calculations have been carried out to demonstrate theoretical derivations. The results have pointed out the effect of the model parameters on the correlation. The results have also indicated the required HAP antenna separation to attain uncorrelated HAP-MIMO channels in different propagation environments. In particular, as long as the HAP length is adequate and the Ricean factor is small, i.e., the propagation conditions are characterized by rich multipath and weak LoS component (considering dense urban areas, where the scatterers are usually dense and tall), a single airship or aircraft can be employed to successfully exploit MIMO benefits.

This chapter has also utilized the proposed model to study the HAP-MIMO channel capacity. The results have revealed that the capacity depends on the strength of the LoS signal, and the received SNR. In particular, increasing the Ricean factor decreases the capacity, while increasing the SNR increases the capacity. These results have also demonstrated the influence of the spatial and temporal correlation on the capacity. Specifically, it has been shown that increasing the elevation angle of the platform increases the capacity, while increasing the density of the scatterers in the vicinity of the user and the spacing between the antennas increases the capacity. Moreover, broadside HAP antennas maximize the capacity, while vertically placed antennas at the mobile terminal provide considerable capacity gain in highly urbanized areas. Finally, the results have underlined that changing the velocity and the moving direction of the user significantly affects the capacity.

The proposed model provides theoretical guidelines and a useful framework for designing and testing future HAP-MIMO communication systems at L- and S-frequency bands, under LoS and NLoS conditions. Notwithstanding, future real-time field measurements or at least simulation trials are needed to verify the theoretical results. Hence, next chapter proposes deterministic and statistical simulation models for HAP-MIMO channels and examines their performance.

Chapter 4

Three-Dimensional Simulation of HAP-MIMO Channels

4.1 Introduction

Although theoretical channel models can be ideally verified through experimental real-time field trials, simulation of the radio propagation environment is commonly used as an alternative, cost-effective, and time-saving approach to the test, optimization, and performance evaluation of wireless communications systems. Hence, the development and design of accurate and efficient simulation models for HAP-MIMO channels is a major research issue. The prime requirement of a simulation set-up is to capture the fading effects created by the radio channel and the goal of any simulation model is to properly reproduce the channel properties. Indeed, many different methods have been adopted for the simulation of fading channels. The most widely accepted methods are the filtered noise models [164]-[166] and the sum-of-sinusoids (SoS) models [143], [167]-[177]. Before the contributions of this chapter are discussed, it is necessary to understand the major characteristics of these two different simulation philosophies commonly employed to simulate fading channels.

The filtered noise models intend to simulate the channel properties by means of signal processing techniques, without considering the underlying propagation mechanisms. These models filter Gaussian noise through appropriately designed linear time-invariant filters to generate the channel waveform with the desired channel PSD and capture the important first- and second-order channel statistics. However, the efficiency of this approach is limited by the utilized filter. In particular, a high-order filter is usually required to accurately approximate the

desired statistical properties. Nevertheless, high-order filters have a long impulse response, which significantly increases the simulation time. Furthermore, since filters with sharp stop-bands are difficult to implement in practice, the power spectrum obtained using this method is not band-limited.

The SoS principle introduced by Rice [168] has been widely accepted by academia and industry as an adequate basis for the design of simulation models due to its reasonably low computational costs. According to this principle, the overall channel waveform is the sum of several complex sinusoids having frequencies, amplitudes and phases that are appropriately selected to accurately approximate the desired statistical properties. Two main categories of SoS-based simulation models are reported in the literature, the *deterministic* simulation models [170] and the *statistical* simulation models [172]. The deterministic (ergodic statistical) models are easy to implement and have short simulation times. Specifically, they have fixed parameters for all simulation trials and converge to the desired properties in a single simulation trial leading to deterministic statistical properties. On the contrary, the statistical (Monte Carlo) models have at least one of the parameters as random variables that vary with each simulation trial. Hence, their statistical properties also vary for each simulation trial and converge to the desired ones in the statistical sense, i.e., when averaged over a sufficiently large number of simulation trials. In contrast to filtered noise models, SoS-based models produce channel waveforms that have high accuracy and a perfectly band-limited spectrum. In addition, their complexity is typically reduced by cleverly choosing the model parameters to reduce the computation load. Furthermore, SoS-based models can be easily extended to develop simulation channel models for MIMO communications systems due to the explicit inclusion of spatial information, such as the multipath angles of arrival and departure. Owing to these advantages, our research focuses on SoS-based models and proposes deterministic and statistical simulation models for HAP-MIMO channels, under the framework of the reference model described in Chapter 3. Theoretical and simulation results are employed to verify the reliability and the usefulness of the proposed models.

The remainder of this chapter is organized as follows. Section 4.2 derives a 3-D generic non-efficient stochastic simulation model, while Sections 4.3 and 4.4 derive 3-D efficient deterministic and statistical simulation models, respectively. Section 4.5 present simulations results and examines the performance and the complexity of the proposed simulation models. Finally, Section 4.6 summarizes this chapter.

4.2 The Stochastic Simulation Model

The reference model for HAP-MIMO channels proposed in Chapter 3 assumes an infinite number of scatterers, which prevents practical realization, i.e., software/hardware implementation. However, this model can be used as the starting point for the design of simulation models with a finite number of scatterers, which have similar statistical properties. Indeed, a stochastic simulation model can be directly obtained by using a finite number N of scatterers. Then, the impulse response of the sub-channel p - l is given by

$$\hat{h}_{pl}(t) = h_{pl,LoS}(t) + \hat{h}_{pl,NLoS}(t), \quad (56)$$

where

$$\hat{h}_{pl,NLoS}(t) = \sqrt{\frac{\Omega_{pl}}{K_{pl} + 1}} \frac{1}{\sqrt{N}} \sum_{n=1}^N e^{-j\frac{2\pi}{\lambda} [d(p, S^{(n)}) + d(S^{(n)}, l)]} e^{j\varphi^{(n)}} e^{j2\pi t(F_{T,NLoS} + F_{R,NLoS})} \quad (57)$$

is the NLoS component of the impulse response, $h_{pl,LoS}(t)$ is defined in (25), (27), (28), $d(p, S^{(n)})$, $d(S^{(n)}, l)$, $F_{T,NLoS}$, and $F_{R,NLoS}$ are defined in (18)-(24), (31), (32), and “ \cdot ” describes a stochastic process. The random variables $a_R^{(n)}$, $R_S^{(n)}$, and $H_S^{(n)}$ can be generated utilizing the distributions defined in the previous chapter, while $\varphi^{(n)}$ is generated as a random variable uniformly distributed in the interval $[-\pi, \pi)$. All other parameters of the simulation model are identical with those of the reference model. Specifically, $a_R^{(n)}$ is modeled using the von Mises pdf and can be generated as

$$a_R^{(n)} = F_{a_R}^{-1}(\delta), \quad (58)$$

where δ is a random variable uniformly distributed in the interval $(0,1)$. The function $F_{a_R}^{-1}(\cdot)$ denotes the inverse function of the von Mises cumulative distribution function (cdf) and can be evaluated using the numerical method presented in [149] (no analytical method is available). Fig. 54 depicts the von Mises cdf for different values of k and $\mu=0$.

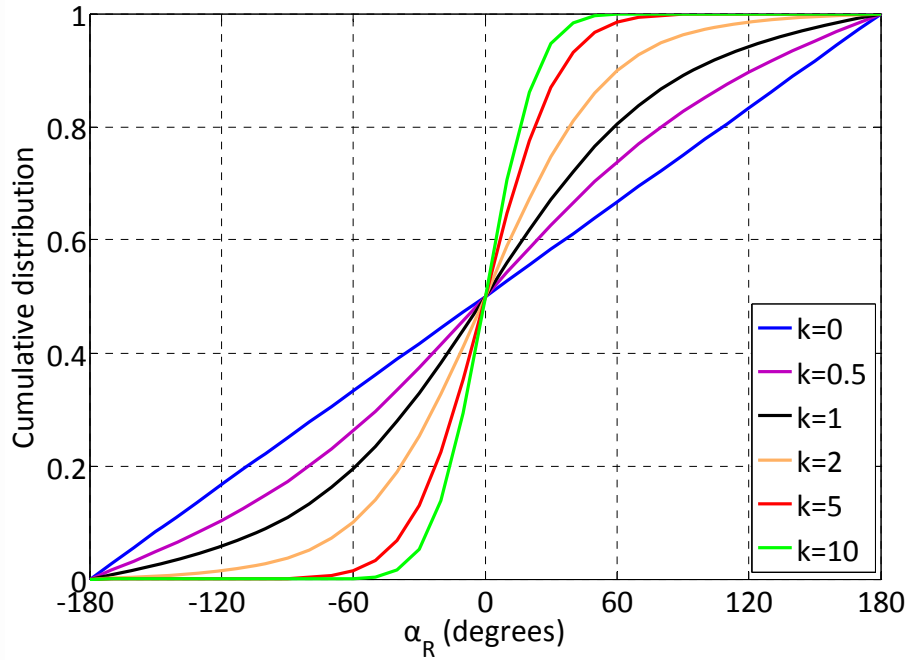


Figure 54: The cumulative distribution of the angle of arrival of the scattered waves for different degree of scattering.

In addition, $R_S^{(n)}$ is modeled using the hyperbolic pdf and can be generated as

$$R_S^{(n)} = F_{R_S}^{-1}(\zeta), \quad (59)$$

where ζ is a random variable uniformly distributed in the interval $(0,1)$. The function $F_{R_S}(\cdot)$ denotes the hyperbolic cdf, which is given by

$$F_{R_S}(R_S) = \tanh(aR_S) / \tanh(aR_{S,\max}). \quad (60)$$

Specifically, using (59), (60), $R_S^{(n)}$ is generated as follows

$$R_S^{(n)} = \frac{1}{\alpha} \tanh^{-1} \left(\zeta \tanh(\alpha R_{S,\max}) \right). \quad (61)$$

Fig. 55 demonstrates the hyperbolic cdf for several values of the parameter α and $R_{S,\max} = 200$ m.

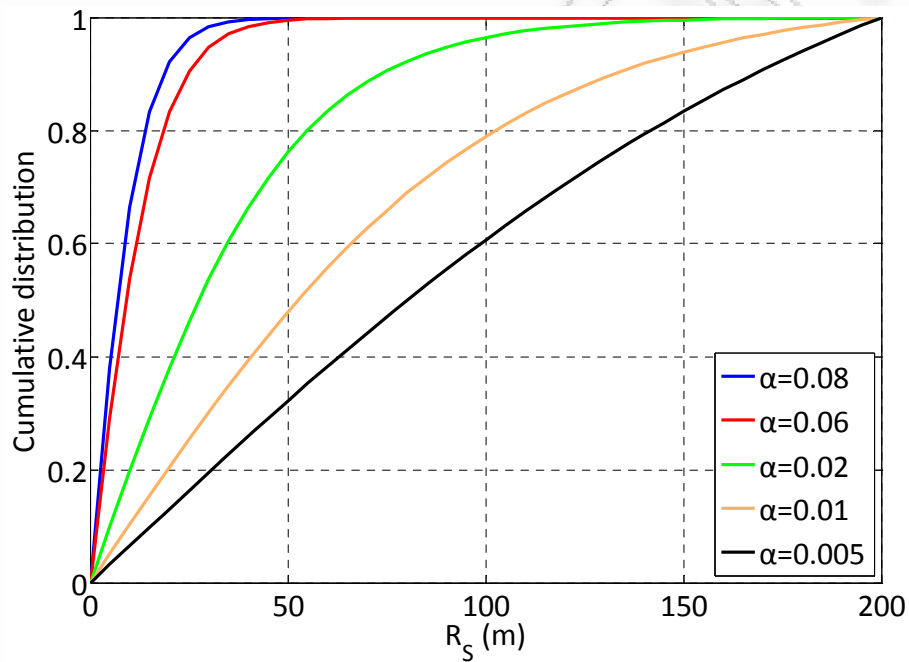


Figure 55: The cumulative distribution of the distance between TMS and the scatterers for different values of the parameter α .

Finally, $H_S^{(n)}$ is modeled using the log-normal pdf and can be generated as

$$H_S^{(n)} = F_{H_S}^{-1}(\xi), \quad (62)$$

where ξ is a random variable uniformly distributed in the interval (0,1). The function $F_{H_S}(\cdot)$ denotes the log-normal cdf, which is given by

$$F_{H_S}(H_S) = \frac{1}{2} \operatorname{erfc} \left[-\frac{\ln(H_S) - \ln(H_{S,\text{mean}})}{\sigma\sqrt{2}} \right], \quad (63)$$

where $\text{erfc}(x) = \left(2/\sqrt{\pi}\right) \int_x^\infty e^{-u^2} du$ is the complementary error function. Fig. 56 shows the log-normal cdf for the corresponding values of $H_{S,\text{mean}}$ and σ associated with London (U.K.) and Guildford (U.K.) [157].

To simulate a HAP-MIMO channel, this generic stochastic simulation model can be directly applied by generating the variables $a_R^{(n)}$, $R_S^{(n)}$, $H_S^{(n)}$, and $\varphi^{(n)}$. However, due to the high degree of randomness during the computation of these variables, an infinite number of simulation trials is required and the stochastic model is non-realizable and inefficient. Hence, one must otherwise determine the model parameters, in order to fully exploit the inherent advantages of the SoS principle. This procedure is called the parameter computation method and the type of a simulation model is directly related to this method.

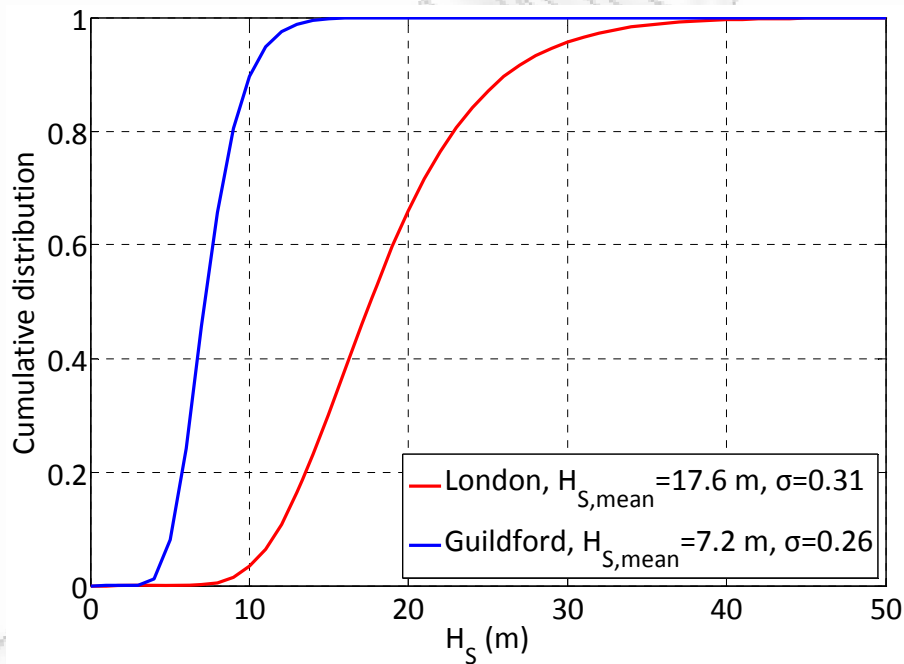


Figure 56: The cumulative distribution of the building heights in London (U.K.) and Guildford (U.K.).

4.3 The Deterministic Simulation Model

This section proposes a SoS-based deterministic simulation model for HAP-MIMO channels. As mentioned in Section 4.1, the deterministic models have all

parameters fixed for all simulation trials, thereby, leading to deterministic properties, i.e., only one simulation trial is needed to obtain the desired properties and the statistical behavior does not vary from one simulation trial to another.

Since the location of each scatterer inside the cylinder can be fully described by $a_R^{(n)}$, $R_S^{(n)}$, and $H_S^{(n)}$, the entire scattering region is considered as a 3D-point lattice partitioned into three scattering sub-regions, which are individually associated with one of these variables [179]. In particular, it is considered that N_1 coordinates of scattering points are non-uniformly distributed around a ring, N_2 coordinates of scattering points are non-uniformly distributed along a radial line, and N_3 coordinates of scattering points are non-uniformly distributed along a vertical line. Then, the product $N = N_1 N_2 N_3$ is the total finite number of discrete scatterers. This design method is visualized in Fig. 57, for ease of comprehension. Note that a random scatterer is now designated by $S^{(n_1, n_2, n_3)}$ and its location is controlled by $a_R^{(n_1)}$, $R_S^{(n_2)}$, and $H_S^{(n_3)}$, where $n_1 \in \{1, \dots, N_1\}$, $n_2 \in \{1, \dots, N_2\}$, and $n_3 \in \{1, \dots, N_3\}$.

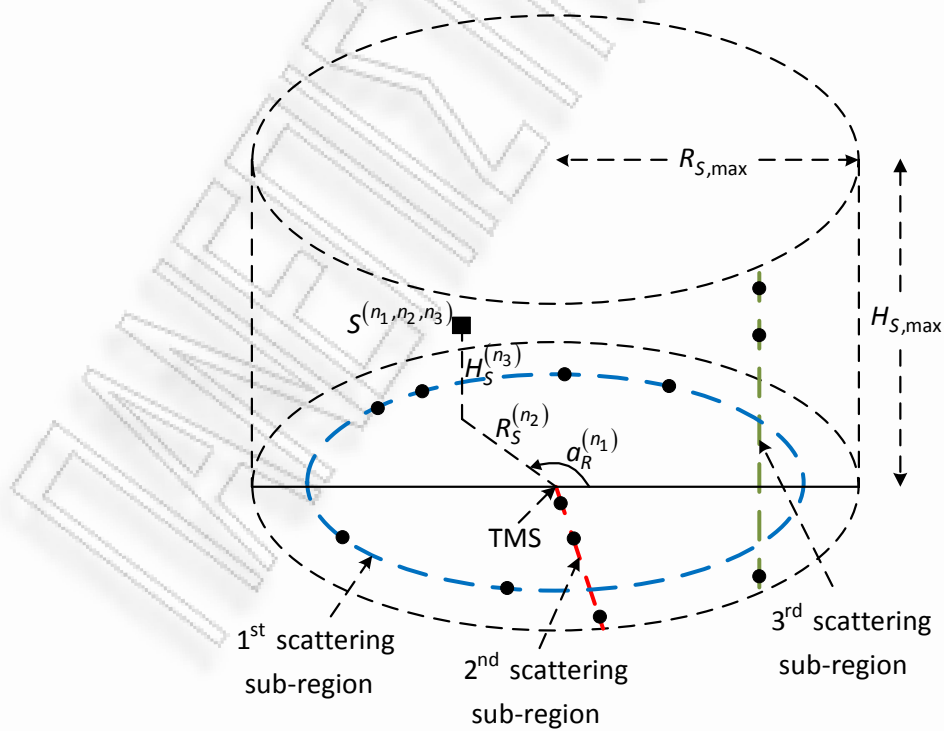


Figure 57: Visualization of the three scatterer sub-regions, each consisting of N_1 , N_2 , and N_3 coordinates (“•”) of scattering points, respectively.

The impulse response of the sub-channel p - l can be written as

$$\tilde{h}_{pl}(t) = h_{pl,LoS}(t) + \tilde{h}_{pl,NLoS}(t), \quad (64)$$

where

$$\tilde{h}_{pl,NLoS}(t) = \sqrt{\frac{\Omega_{pl}}{K_{pl} + 1}} \frac{1}{\sqrt{N_1 N_2 N_3}} \sum_{n_1=1}^{N_1} \sum_{n_2=1}^{N_2} \sum_{n_3=1}^{N_3} e^{j\phi^{(n_1, n_2, n_3)}} \times e^{-j\frac{2\pi}{\lambda} [d(p, S^{(n_1, n_2, n_3)}) + d(S^{(n_1, n_2, n_3)}, l)]} e^{j2\pi t (F'_{T, NLoS} + F'_{R, NLoS})} \quad (65)$$

is the NLoS component of the impulse response, $h_{pl,LoS}(t)$ is defined in (25), (27), (28), “ \approx ” describes a deterministic time averaged quantity, $n_1 \in \{1, \dots, N_1\}$, $n_2 \in \{1, \dots, N_2\}$, $n_3 \in \{1, \dots, N_3\}$, and $d(p, S^{(n_1, n_2, n_3)})$, $d(S^{(n_1, n_2, n_3)}, l)$, $F'_{T, NLoS}$, and $F'_{R, NLoS}$ are defined, respectively, as follows

$$d(p, S^{(n_1, n_2, n_3)}) \approx (D - D_{T_1} - D_{T_2} R_S^{(n_2)} \sin \alpha_R^{(n_1)}) / \cos \beta_T, \quad (66)$$

$$\begin{aligned} d(S^{(n_1, n_2, n_3)}, l) \approx & R_S^{(n_2)} / \cos \left[\arctan(H_S^{(n_3)} / R_S^{(n_2)}) \right] \\ & - D_{R_1} \cos \alpha_R^{(n_1)} \cos \left[\arctan(H_S^{(n_3)} / R_S^{(n_2)}) \right] \\ & - D_{R_2} \sin \left[\arctan(H_S^{(n_3)} / R_S^{(n_2)}) \right] \\ & - D_{R_3} \sin \alpha_R^{(n_1)} \cos \left[\arctan(H_S^{(n_3)} / R_S^{(n_2)}) \right], \end{aligned} \quad (67)$$

$$F'_{T, NLoS} = f_{T, \max} \left(R_S^{(n_2)} \sin \gamma_T \sin \alpha_R^{(n_1)} / D + \cos \gamma_T \right), \quad (68)$$

$$F'_{R, NLoS} = f_{R, \max} \cos \left(\alpha_R^{(n_1)} - \gamma_R \right) \cos \left[\arctan(H_S^{(n_3)} / R_S^{(n_2)}) \right]. \quad (69)$$

Providing that a sufficient large number of scatterers is used, i.e., $N = N_1 N_2 N_3 \geq 20$, central limit theorem implies that $\tilde{h}_{pl, NLoS}(t)$ is close to a low-pass zero-mean complex Gaussian process. Then, using a similar derivation to that described in Chapter 3, the STCF between $\tilde{h}_{pl}(t)$ and $\tilde{h}_{qm}(t)$ can be simplified as

$$\tilde{R}_{pl, qm}(\delta_T, \delta_R, \tau) = R_{pl, qm}^{LoS}(\delta_T, \delta_R, \tau) + \tilde{R}_{pl, qm}^{NLoS}(\delta_T, \delta_R, \tau), \quad (70)$$

where

$$\begin{aligned}
& \tilde{R}_{pl,qm}^{NLoS}(\delta_T, \delta_R, \tau) \\
& := \mathbb{E} \left[\tilde{h}_{pl,NLoS}(t) \tilde{h}_{qm,NLoS}^*(t+\tau) \right] / \sqrt{\Omega_{pl} \Omega_{qm}} \\
& \approx \frac{1}{\sqrt{(K_{pl}+1)(K_{qm}+1)}} \frac{1}{N_1 N_2 N_3} \sum_{n_1=1}^{N_1} \sum_{n_2=1}^{N_2} \sum_{n_3=1}^{N_3} e^{j \frac{2\pi(q-p)\delta_T \cos \theta_T}{\lambda \cos \beta_T}} e^{j \frac{2\pi(q-p)\delta_T \sin \theta_T R_S^{(n_2)} \sin a_R^{(n_1)}}{\lambda D \cos \beta_T}} \\
& \quad \times e^{\frac{j2\pi(m-l)\delta_R \sin \psi_R \sin \left[\arctan \left(H_S^{(n_3)} / R_S^{(n_2)} \right) \right]}{\lambda}} \\
& \quad \times e^{\frac{j2\pi(m-l)\delta_R \cos \theta_R \cos \psi_R \cos a_R^{(n_1)} \cos \left[\arctan \left(H_S^{(n_3)} / R_S^{(n_2)} \right) \right]}{\lambda}} \\
& \quad \times e^{\frac{j2\pi(m-l)\delta_R \sin \theta_R \cos \psi_R \sin a_R^{(n_1)} \cos \left[\arctan \left(H_S^{(n_3)} / R_S^{(n_2)} \right) \right]}{\lambda}} e^{-j2\pi\tau(F_T^{NLoS} + F_R^{NLoS})} \quad (71)
\end{aligned}$$

is the STCF of the NLoS component and $R_{pl,qm}^{LoS}(\delta_T, \delta_R, \tau)$ is defined in (36). From (71), it is obvious that proper finite sets $\left\{ a_R^{(n_1)} \right\}_{n_1=1}^{N_1}$, $\left\{ R_S^{(n_2)} \right\}_{n_2=1}^{N_2}$, and $\left\{ H_S^{(n_3)} \right\}_{n_3=1}^{N_3}$ for the parameters $a_R^{(n_1)}$, $R_S^{(n_2)}$, and $H_S^{(n_3)}$ must be determined, which lead to a good approximation to the statistical properties of the reference model. Note that no parameter computation method will be applied to the phases $\varphi^{(n_1, n_2, n_3)}$, since the STCF does not depend on them. Notwithstanding, the interest reader is referred to [170], where an efficient method to compute the phases is given.

Although the L_p -norm method (LPNM) used in [171], [180] provides maximum accuracy and versatility, it requires the minimization of two error functions in order to obtain proper temporal and spatial correlation properties. Since this minimization must be simultaneously proceeded for $a_R^{(n_1)}$, $R_S^{(n_2)}$, and $H_S^{(n_3)}$, it is obvious that simpler and less complex parameter computation methods are desirable. Hence, following a similar approach to that proposed in [143], the aforementioned parameters are generated as follows [163]

$$a_R^{(n_1)} = F_{a_R}^{-1}(\delta'), \quad (72)$$

$$R_S^{(n_2)} = F_{R_S}^{-1}(\zeta'), \quad (73)$$

$$H_S^{(n_3)} = F_{H_S}^{-1}(\xi'), \quad (74)$$

where

$$\delta' = (n_1 - 0.5) / N_1, \quad (75)$$

$$\zeta' = (n_2 - 0.5) / N_2, \quad (76)$$

$$\xi' = (n_3 - 0.5) / N_3 \quad (77)$$

for $n_1 = 1, \dots, N_1$, $n_2 = 1, \dots, N_2$, and $n_3 = 1, \dots, N_3$, respectively.

4.3.1 The Deterministic Simulation Model Based on Set Partitioning

The performance of the proposed deterministic simulation model can only be improved by increasing the number of the discrete scatterers, i.e., the number of N_1 , N_2 , and N_3 , and thus the complexity, but not by averaging over the simulation results achieved by multiple simulation runs. Moreover, the performance has to be investigated for practical values of these numbers, which may not lead to proper and accurate statistical properties. In [181] and [182] an alternative deterministic parameter computation method was proposed for isotropic and non-isotropic scattering environments, respectively. This method utilizes the principle of set partitioning (SP), which was initially used to design trellis-coded modulation schemes [183]. Based on this principle, it is assumed that a constellation (scatter diagram) with N relevant scatterers is separated into V sub-constellations, each of which consists of N' scatterers, such that $N = V \cdot N'$, where V is an integer number.

This subsection applies the principle of SP to the deterministic simulation model for HAP-MIMO channels described above. Hence, it is similarly assumed that $N_1 = V_1 \cdot N'_1$ coordinates of scattering points are located around a ring constellation. This ring constellation is separated into V_1 sub-constellations (partitions), each of which consists of N'_1 coordinates of relevant scattering points. In addition, it is

assumed that $N_2 = V_2 \cdot N'_2$ coordinates of scattering points are located along a radial line constellation. This radial line constellation is separated into V_2 sub-constellations, each of which consists of N'_2 coordinates of relevant scattering points. Finally, it is assumed that $N_3 = V_3 \cdot N'_3$ coordinates of scattering points are located along a vertical line constellation. This vertical line constellation is separated into V_3 sub-constellations, each of which consists of N'_3 coordinates of relevant scattering points. Fig. 58 explains the proposed SP method and illustrates the v_1^{th} , v_2^{th} , and v_3^{th} sub-constellations of relevant scattering points, when $N'_1 = N'_2 = N'_3 = 3$.

Under these considerations and for $n'_1 = 1, \dots, N'_1$, $n'_2 = 1, \dots, N'_2$, $n'_3 = 1, \dots, N'_3$, $v_1 = 1, \dots, V_1$, $v_2 = 1, \dots, V_2$, and $v_3 = 1, \dots, V_3$ the model parameters are generated using a similar approach to that proposed in [181], [182]

$$a_R^{(n'_1, v_1)} = F_{a_R}^{-1}(\delta^n), \quad (78)$$

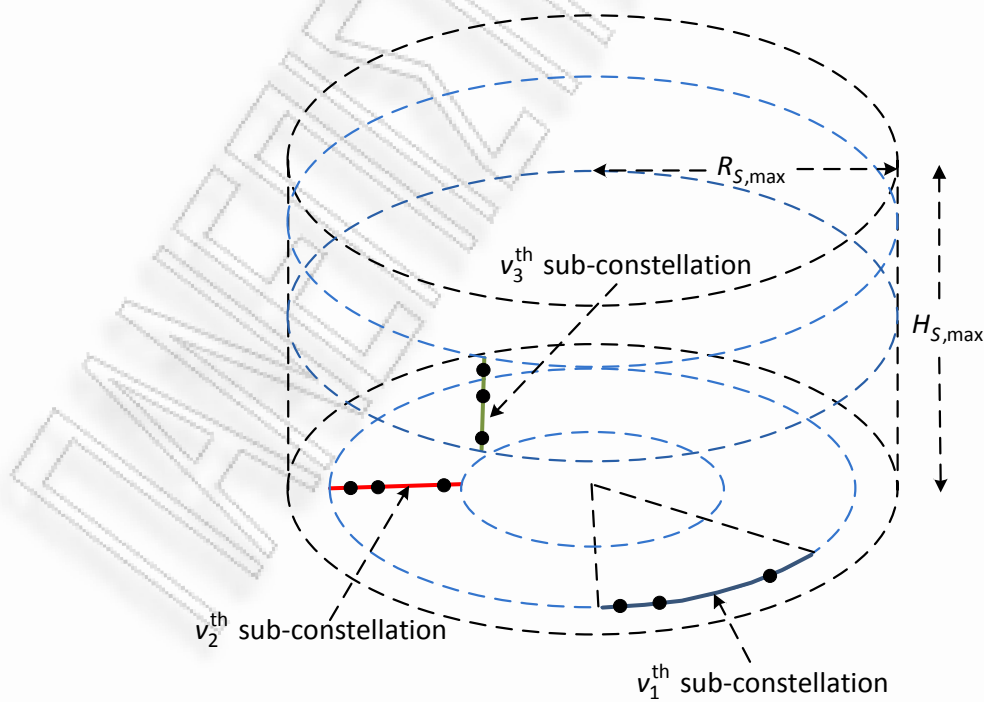


Figure 58: The set partitioning of three scatterer constellations into V_1 , V_2 and V_3 sub-constellations, each consisting of 3 coordinates (“•”) of relevant scattering points.

$$R_S^{(n'_2, v_2)} = F_{R_S}^{-1}(\zeta''), \quad (79)$$

$$H_S^{(n'_3, v_3)} = F_{H_S}^{-1}(\xi''), \quad (80)$$

where

$$\delta'' = \frac{n'_1 - 0.25}{N'_1} + \varepsilon_{v_1}, \quad (81)$$

$$\zeta'' = \frac{n'_2 - 0.25}{N'_2} + \varepsilon_{v_2}, \quad (82)$$

$$\xi'' = \frac{n'_3 - 0.25}{N'_3} + \varepsilon_{v_3}, \quad (83)$$

$$\varepsilon_{v_1} = \frac{2v_1 - V_1 - 1}{2V_1N'_1}, \quad (84)$$

$$\varepsilon_{v_2} = \frac{2v_2 - V_2 - 1}{2V_2N'_2}, \quad (85)$$

$$\varepsilon_{v_3} = \frac{2v_3 - V_3 - 1}{2V_3N'_3}. \quad (86)$$

In practice, it is recommended to simulate the deterministic processes $\tilde{h}_{pl}^{(v_1, v_2, v_3)}(t)$ successively by computing from time to time a new set of parameters

$\left\{ \alpha_R^{(n'_1, v_1)} \right\}_{n'_1=1}^{N'_1}$, $\left\{ R_S^{(n'_2, v_2)} \right\}_{n'_2=1}^{N'_2}$, and $\left\{ H_S^{(n'_3, v_3)} \right\}_{n'_3=1}^{N'_3}$ using (78)-(80).

The STCF associated with the proposed deterministic SP simulation model is given by

$$\bar{R}_{pl, qm}(\delta_T, \delta_R, \tau) := \frac{1}{V_1 V_2 V_3} \sum_{v_1=1}^{V_1} \sum_{v_2=1}^{V_2} \sum_{v_3=1}^{V_3} \tilde{R}_{pl, qm}^{(v_1, v_2, v_3)}(\delta_T, \delta_R, \tau), \quad (87)$$

where “ $\bar{\cdot}$ ” describes an average process and $\tilde{R}_{pl, qm}^{(v_1, v_2, v_3)}(\delta_T, \delta_R, \tau)$ is calculated using (70) and (78)-(86) for $n'_1 = 1, \dots, N'_1$, $n'_2 = 1, \dots, N'_2$, and $n'_3 = 1, \dots, N'_3$.

Note that $\bar{R}_{pl, qm}(\delta_T, \delta_R, \tau)$ is equal to $\tilde{R}_{pl, qm}(\delta_T, \delta_R, \tau)$ defined in (70) for $N = N' \cdot V$ scatterers, where $N' = N'_1 N'_2 N'_3$ and $V = V_1 V_2 V_3$. Thus, instead of simulating a single deterministic process with N scatterers, V mutually uncorrelated

deterministic processes with reduced complexity determined by $N' = N/V$ can be alternatively simulated. Although the statistical properties of this deterministic model vary for each simulation trial, they will converge to the statistical properties of the reference model after a sufficient number of simulation trials controlled by V_1 , V_2 , and V_3 and for an arbitrary number of scatterers, i.e., for any $\{N_1, N_2, N_3\} \geq 1$. They will also converge to the desired statistical properties after an arbitrary number of simulation trials, i.e., for any $\{V_1, V_2, V_3\} \geq 1$, but with a sufficient number of scatterers, i.e., for sufficient N_1 , N_2 , and N_3 .

4.4 The Statistical Simulation Model

This section proposes a SoS-based statistical simulation model for HAP-MIMO channels. As mentioned in Section 4.1, the statistical models are not ergodic and have at least one of the parameters as a random variable for each simulation trial. Thus, their properties have to be analyzed by statistical averages after a number of simulation trials. Based on [143], the parameters $a_R^{(n_1)}$, $R_S^{(n_2)}$, and $H_S^{(n_3)}$ are generated as random variables for each simulation trial as follows [179]

$$a_R^{(n_1)} = F_{a_R}^{-1}(\delta'''), \quad (88)$$

$$R_S^{(n_2)} = F_{R_S}^{-1}(\zeta'''), \quad (89)$$

$$H_S^{(n_3)} = F_{H_S}^{-1}(\xi'''), \quad (90)$$

where

$$\delta''' = (n_1 + \kappa_1 - 1) / N_1, \quad (91)$$

$$\zeta''' = (n_2 + \kappa_2 - 1) / N_2, \quad (92)$$

$$\xi''' = (n_3 + \kappa_3 - 1) / N_3, \quad (93)$$

where κ_1 , κ_2 , and κ_3 are independent random variables uniformly distributed in the interval $[0,1)$. Since the proposed statistical model has three of its parameters

as random variables for each simulation trial, its statistical properties have to be analyzed by statistical averages. Hence, although the statistical properties vary for each simulation trial, they will converge to the statistical properties of the reference model after a sufficient number of simulation trials for an arbitrary number of scatterers, i.e., for any $\{N_1, N_2, N_3\} \geq 1$.

The STCF associated with the statistical model is given by

$$\bar{R}'_{pl,qm}(\delta_T, \delta_R, \tau) = \frac{1}{N_{trials}} \sum_{n_{trials}=1}^{N_{trials}} \hat{R}'_{pl,qm}(\delta_T, \delta_R, \tau) \quad (94)$$

for $n_{trials} = 1, \dots, N_{trials}$, where N_{trials} denotes the number of simulation trials and $\hat{R}'_{pl,qm}(\delta_T, \delta_R, \tau)$ can be obtained using (70) and (88)-(93), providing that a sufficient number of scatterers is used, i.e., $N = N_1 N_2 N_3 \geq 20$. Since the proposed statistical simulation model statistically converges to the desired properties, it is important to determine the number of simulation trials needed to achieve a desired convergence level. Indeed, the complexity of the statistical simulation model is controlled by N_1 , N_2 , N_3 , and N_{trials} . Thus, N_1 , N_2 , and N_3 should be carefully determined to reduce the number of trials required for convergence.

Table 6 reviews and compares the relative complexity of the proposed simulation models, which generally depends on the number of the utilized scatterers, the number of the performed simulation trials, and the number of the required random variables.

TABLE 6
THE COMPLEXITY OF THE SIMULATION MODELS

Simulation Model	Number of scatterers	Number of simulation trials	Relative number of calculations	Number of random variables
Stochastic	N_{Stoc}	∞	∞	3
Deterministic	N_{Det}	1	N_{Det}	0
Deterministic SP	$N_{Det,SP}$	$V = V_1 V_2 V_3$	$N_{Det,SP} V$	0
Statistical	N_{Stat}	N_{trials}	$N_{Stat} N_{trials}$	3

4.5 Simulation Results

In this section, the performance of the proposed simulation models is evaluated for different complexity and a finite number of scatterers. The values of the model parameters used to obtain the following curves are $n_T = n_R = 2$, $K_{pl} = K_{qm} = 3$ dB, $H_T = 20$ km, $\beta_T = 60^\circ$, $D = H / \tan\beta_T \approx 11.5$ km, $\theta_T = \theta_R = 90^\circ$, $\psi_R = 30^\circ$, $k = 3$, $\mu = 30^\circ$, $\alpha = 0.01$, $R_{S,\max} = 200$ m, $H_{S,\max} = 70$ m, $H_{S,\text{mean}} = 17.6$ m, $\sigma = 0.31$, $\gamma_T = 60^\circ$, $\gamma_R = 30^\circ$, $f_{T,\max} = 300$ Hz, and $f_{R,\max} = 100$ Hz.

Tables 7 and 8 investigate the performance of the deterministic model for different complexity, i.e., different N_1 , N_2 , and N_3 , in terms of the TCF for the time delay range $0 \leq \tau \leq 0.1$ s, which is typically of interest for many communications systems, and the SCF for the ranges $0 \leq \delta_T \leq 200\lambda$ and $0 \leq \delta_R \leq 3\lambda$, respectively. As soon as the value of the Ricean factor is sufficiently small, the maximum values of the range of the inter-element distances chosen, i.e., 200λ and 3λ , ensure low spatial correlation in many propagation scenarios, as shown in Chapter 3. The effect of the variation of each number of coordinates of scattering points is examined independently, provided that the other numbers are sufficiently large and do not affect the results. The performance evaluation is realized in terms of the root mean square error (RMSE) between the absolute TCFs and SCFs of the simulation model and the reference model, as well as the maximum deviation (MD) of the absolute TCF and SCF of the simulation model from the corresponding theoretical values. According to Tables 7 and 8, the performance can be improved by increasing the number of the discrete scatterers and thus the complexity. Tables 7 and 8 also suggest that reasonable values for N_1 (associated with α_R), N_2 (associated with R_S), and N_3 (associated with H_S) are in the order of 30, 20, and 5, respectively.

Fig. 59 illustrates the absolute value of the TCFs of the reference and the deterministic simulation model, respectively, for $N_1 = 30$, $N_2 = 20$, $N_3 = 5$ and

$N_1 = 40$, $N_2 = 30$, $N_3 = 8$, respectively. One observes that the TCF of deterministic model approximates the theoretical one for the range $0 \leq \tau(s) \leq 0.1$, as the number of the scatterers increases. From the simulation results, the RMSE is approximately $20.5 \cdot 10^{-3}$ and $19.3 \cdot 10^{-3}$, respectively, while the MD is approximately $33.4 \cdot 10^{-3}$ and $31.9 \cdot 10^{-3}$, respectively.

Fig. 60 depicts the absolute error between the absolute SCFs of the reference model and the simulation model for the ranges $0 \leq \delta_T \leq 200\lambda$ and $0 \leq \delta_R \leq 3\lambda$. From the simulation results obtained for $N_1 = 30$, $N_2 = 20$, and $N_3 = 5$, the RMSE is approximately $2.1 \cdot 10^{-3}$, while the MD is approximately $7.3 \cdot 10^{-3}$. Overall, the deterministic simulation model satisfactorily matches the temporal and spatial correlation properties of the reference model.

TABLE 7
PERFORMANCE EVALUATION OF THE DETERMINISTIC SIMULATION MODEL (A)

TEMPORAL CORRELATION						
Number of scatterers	N_1		N_2		N_3	
	RMSE	MD	RMSE	MD	RMSE	MD
1	$88.7 \cdot 10^{-3}$	$135 \cdot 10^{-3}$	$62.1 \cdot 10^{-3}$	$101 \cdot 10^{-3}$	$24.5 \cdot 10^{-3}$	$48.1 \cdot 10^{-3}$
2	$71.4 \cdot 10^{-3}$	$124 \cdot 10^{-3}$	$34.5 \cdot 10^{-3}$	$62.6 \cdot 10^{-3}$	$19.6 \cdot 10^{-3}$	$38.9 \cdot 10^{-3}$
5	$51.8 \cdot 10^{-3}$	$109 \cdot 10^{-3}$	$24.2 \cdot 10^{-3}$	$36.3 \cdot 10^{-3}$	$15.1 \cdot 10^{-3}$	$32.4 \cdot 10^{-3}$
6	$48.1 \cdot 10^{-3}$	$83.2 \cdot 10^{-3}$	$23.2 \cdot 10^{-3}$	$35.2 \cdot 10^{-3}$	$15.1 \cdot 10^{-3}$	$31.2 \cdot 10^{-3}$
7	$44.9 \cdot 10^{-3}$	$78.3 \cdot 10^{-3}$	$20.5 \cdot 10^{-3}$	$34.5 \cdot 10^{-3}$	$15.1 \cdot 10^{-3}$	$26.7 \cdot 10^{-3}$
8	$41.1 \cdot 10^{-3}$	$71.4 \cdot 10^{-3}$	$19.4 \cdot 10^{-3}$	$29.8 \cdot 10^{-3}$	$14.9 \cdot 10^{-3}$	$28.5 \cdot 10^{-3}$
9	$38.7 \cdot 10^{-3}$	$67.9 \cdot 10^{-3}$	$18.9 \cdot 10^{-3}$	$30.9 \cdot 10^{-3}$	$14.9 \cdot 10^{-3}$	$26.3 \cdot 10^{-3}$
10	$33.3 \cdot 10^{-3}$	$55.8 \cdot 10^{-3}$	$17.7 \cdot 10^{-3}$	$28.9 \cdot 10^{-3}$	$14.8 \cdot 10^{-3}$	$25.2 \cdot 10^{-3}$
15	$29.4 \cdot 10^{-3}$	$45.5 \cdot 10^{-3}$	$17.3 \cdot 10^{-3}$	$28.2 \cdot 10^{-3}$	$14.8 \cdot 10^{-3}$	$28.3 \cdot 10^{-3}$
20	$25.5 \cdot 10^{-3}$	$39.6 \cdot 10^{-3}$	$16.4 \cdot 10^{-3}$	$27.4 \cdot 10^{-3}$	$14.8 \cdot 10^{-3}$	$23.1 \cdot 10^{-3}$
30	$19.5 \cdot 10^{-3}$	$33.1 \cdot 10^{-3}$	$16.1 \cdot 10^{-3}$	$28.1 \cdot 10^{-3}$	$14.8 \cdot 10^{-3}$	$23.6 \cdot 10^{-3}$
40	$18.5 \cdot 10^{-3}$	$31.3 \cdot 10^{-3}$	$15.8 \cdot 10^{-3}$	$27.2 \cdot 10^{-3}$	$14.7 \cdot 10^{-3}$	$22.4 \cdot 10^{-3}$
60	$16.3 \cdot 10^{-3}$	$28.5 \cdot 10^{-3}$	$15.2 \cdot 10^{-3}$	$24.5 \cdot 10^{-3}$	$14.7 \cdot 10^{-3}$	$22.3 \cdot 10^{-3}$

TABLE 8
PERFORMANCE EVALUATION OF THE DETERMINISTIC SIMULATION MODEL (B)

SPATIAL CORRELATION						
Number of scatterers	N_1		N_2		N_3	
	RMSE	MD	RMSE	MD	RMSE	MD
1	$163 \cdot 10^{-3}$	$329 \cdot 10^{-3}$	$49.4 \cdot 10^{-3}$	$141 \cdot 10^{-3}$	$2.4 \cdot 10^{-3}$	$7.3 \cdot 10^{-3}$
2	$117 \cdot 10^{-3}$	$202 \cdot 10^{-3}$	$36.3 \cdot 10^{-3}$	$93.0 \cdot 10^{-3}$	$2.3 \cdot 10^{-3}$	$5.9 \cdot 10^{-3}$
5	$45.2 \cdot 10^{-3}$	$62.2 \cdot 10^{-3}$	$16.7 \cdot 10^{-3}$	$35.2 \cdot 10^{-3}$	$1.5 \cdot 10^{-3}$	$4.2 \cdot 10^{-3}$
6	$31.3 \cdot 10^{-3}$	$57.2 \cdot 10^{-3}$	$14.9 \cdot 10^{-3}$	$31.8 \cdot 10^{-3}$	$1.5 \cdot 10^{-3}$	$4.2 \cdot 10^{-3}$
7	$22.7 \cdot 10^{-3}$	$44.2 \cdot 10^{-3}$	$13.7 \cdot 10^{-3}$	$28.5 \cdot 10^{-3}$	$1.5 \cdot 10^{-3}$	$4.1 \cdot 10^{-3}$
8	$18.1 \cdot 10^{-3}$	$37.3 \cdot 10^{-3}$	$10.2 \cdot 10^{-3}$	$23.7 \cdot 10^{-3}$	$1.4 \cdot 10^{-3}$	$4.0 \cdot 10^{-3}$
9	$13.7 \cdot 10^{-3}$	$33.6 \cdot 10^{-3}$	$8.3 \cdot 10^{-3}$	$20.8 \cdot 10^{-3}$	$1.4 \cdot 10^{-3}$	$4.0 \cdot 10^{-3}$
10	$10.6 \cdot 10^{-3}$	$25.8 \cdot 10^{-3}$	$7.2 \cdot 10^{-3}$	$16.2 \cdot 10^{-3}$	$1.4 \cdot 10^{-3}$	$4.0 \cdot 10^{-3}$
15	$7.4 \cdot 10^{-3}$	$19.5 \cdot 10^{-3}$	$4.9 \cdot 10^{-3}$	$12.2 \cdot 10^{-3}$	$1.4 \cdot 10^{-3}$	$4.0 \cdot 10^{-3}$
20	$4.8 \cdot 10^{-3}$	$13.2 \cdot 10^{-3}$	$2.4 \cdot 10^{-3}$	$9.3 \cdot 10^{-3}$	$1.3 \cdot 10^{-3}$	$3.9 \cdot 10^{-3}$
30	$1.9 \cdot 10^{-3}$	$7.1 \cdot 10^{-3}$	$1.7 \cdot 10^{-3}$	$7.1 \cdot 10^{-3}$	$1.3 \cdot 10^{-3}$	$3.9 \cdot 10^{-3}$
40	$1.7 \cdot 10^{-3}$	$6.9 \cdot 10^{-3}$	$1.6 \cdot 10^{-3}$	$5.9 \cdot 10^{-3}$	$1.3 \cdot 10^{-3}$	$3.9 \cdot 10^{-3}$
60	$1.6 \cdot 10^{-3}$	$5.3 \cdot 10^{-3}$	$1.4 \cdot 10^{-3}$	$4.9 \cdot 10^{-3}$	$1.2 \cdot 10^{-3}$	$3.8 \cdot 10^{-3}$

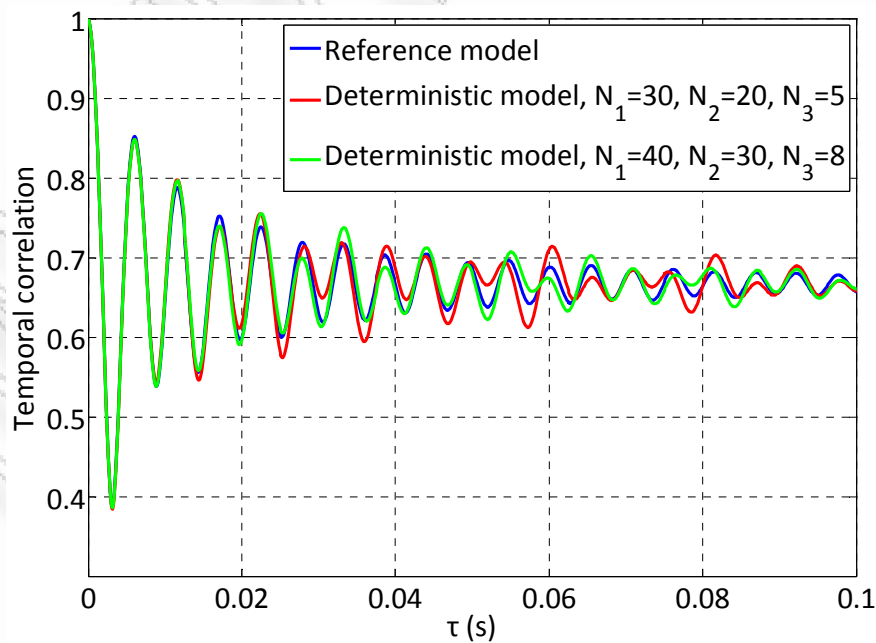


Figure 59: Comparison between the TCFs of the reference model and the deterministic simulation model.

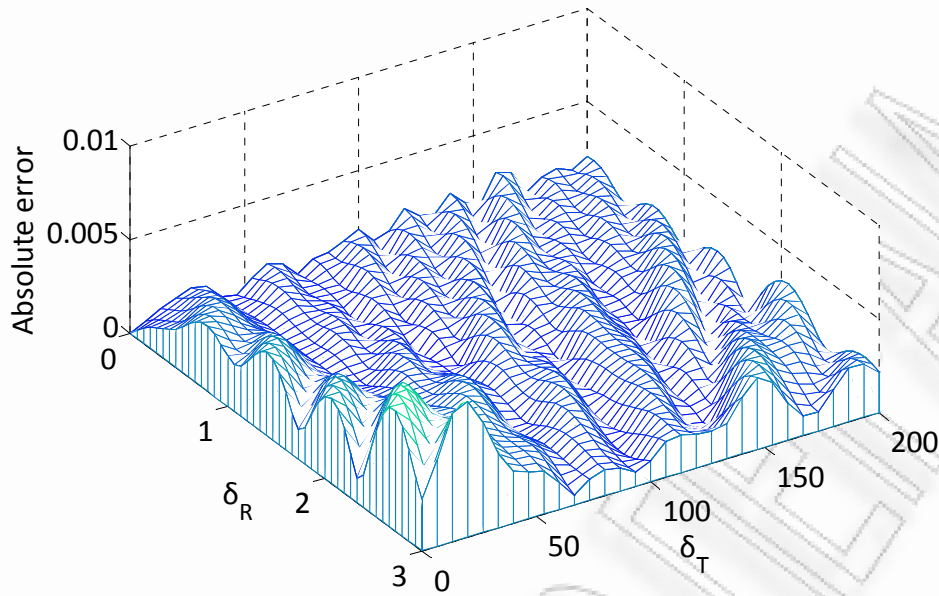


Figure 60: The absolute error between the SCFs of the reference model and the deterministic simulation model.

Fig. 61 depicts the absolute value of the TCF of the reference model and the TCF of the deterministic SP simulation model averaged over $V=1$ simulation trial, when $V_1=1$, $V_2=1$, and $V_3=1$, over $V=10$ simulation trials, when $V_1=5$, $V_2=2$, and $V_3=1$, and over $V=50$ simulation trials, when $V_1=5$, $V_2=5$, and $V_3=2$. Moreover, $N_1=10$, $N_2=8$, and $N_3=3$, i.e., $N=240$. One observes that increasing the number of trials significantly improves the performance of this simulation model for the range $0 \leq \tau \leq 0.1$ s. From the simulation results, the RMSE between the absolute TCFs of the deterministic SP model and the reference model is approximately $35.1 \cdot 10^{-3}$, $18.2 \cdot 10^{-3}$, and $11.2 \cdot 10^{-3}$, respectively, while the MD of the absolute TCFs of the deterministic SP model from the corresponding theoretical values is approximately $59.2 \cdot 10^{-3}$, $34.6 \cdot 10^{-3}$, and $18.9 \cdot 10^{-3}$, respectively.

Fig. 62 depicts the absolute error between the absolute SCFs of the reference model and the deterministic SP model after $V=50$ simulation trials, when $V_1=5$, $V_2=5$, and $V_3=2$ and for $N=240$, when $N_1=10$, $N_2=8$, and $N_3=3$. From the simulation results, the RMSE between the absolute SCFs of the deterministic SP model and the reference model is approximately $1.8 \cdot 10^{-3}$, while the MD of the

absolute SCFs of the deterministic SP model from the corresponding theoretical values is approximately $4.8 \cdot 10^{-3}$. Consequently, the deterministic SP simulation model closely matches the TCF of the reference model, while approximates the SCF of the reference model with high precision.

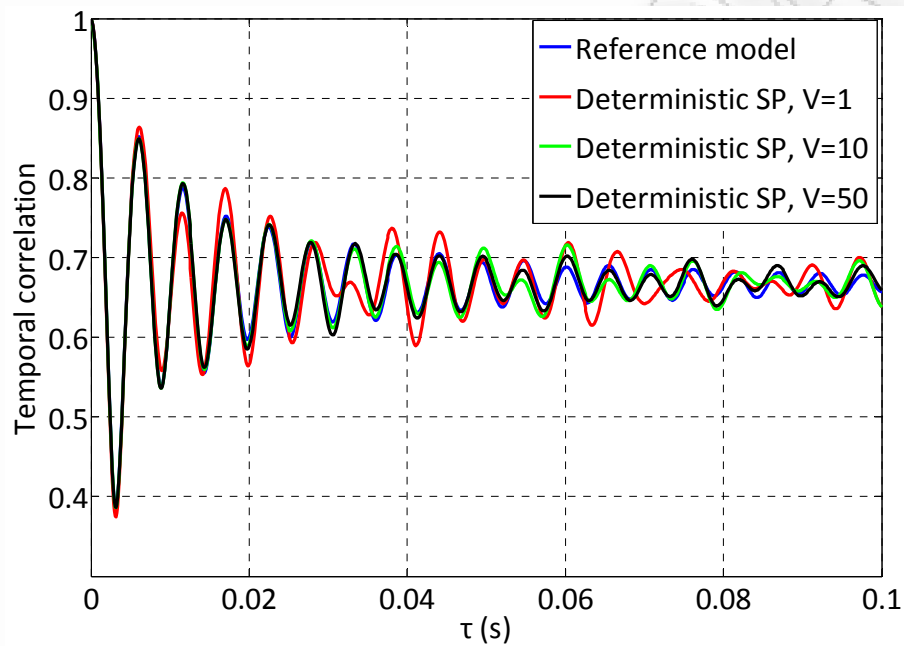


Figure 61: Comparison between the TCFs of the reference model and the deterministic SP simulation model.

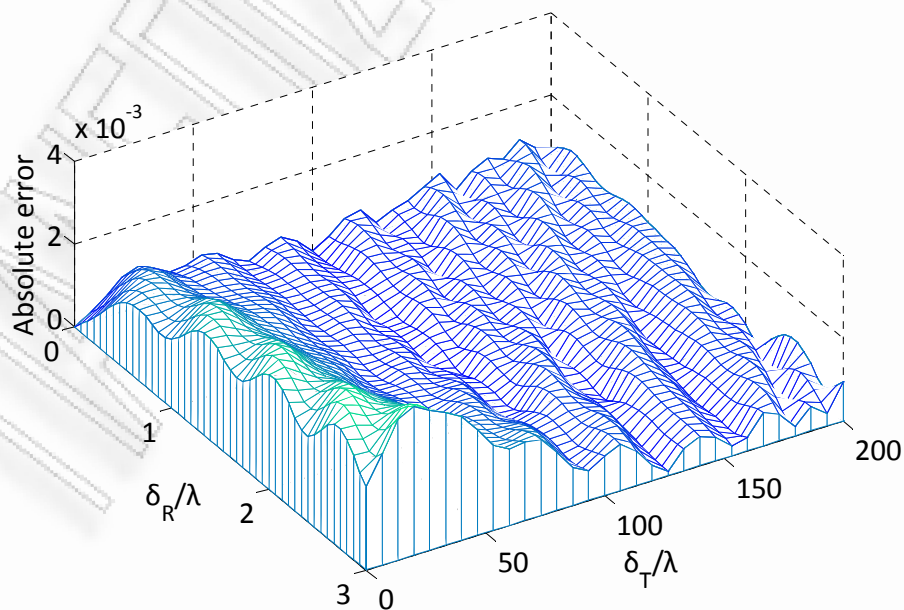


Figure 62: The absolute error between the SCFs of the reference model and the deterministic SP simulation model.

Fig. 63 illustrates the absolute value of the TCFs of the reference and the statistical model averaged over 50 simulation trials for $N=240$, when $N_1=10$, $N_2=8$, and $N_3=3$. One observes that the TCF of the statistical model almost perfectly matches the theoretical one for the range $0 \leq \tau \leq 0.1$ s. From the simulation results, the RMSE between the absolute TCFs of the statistical model and the reference model is approximately $2.4 \cdot 10^{-3}$, while the MD of the absolute TCFs of the statistical model from the corresponding theoretical values is approximately $7.6 \cdot 10^{-3}$.

Fig. 64 demonstrates the absolute error between the absolute SCFs of the reference model and the statistical model after 50 simulation trials. From the simulation results the RMSE between the absolute SCFs of the statistical model and the reference model is approximately $1.6 \cdot 10^{-3}$, while the MD of the absolute SCFs of the statistical model from the corresponding theoretical values is approximately $4.7 \cdot 10^{-3}$. Hence, the statistical simulation model approximates the space-time correlation properties of the reference model in all cases.

Tables 9 and 10 thoroughly investigate the performance of the statistical simulation model for $0 \leq \tau \leq 0.1$ s, $0 \leq \delta_\tau \leq 200\lambda$, and $0 \leq \delta_R \leq 3\lambda$. Table 9 examines the accuracy of the simulation model for different values of the model parameters that control the location of the scatterers inside the cylinder. The performance evaluation is realized in terms of the RMSE between the absolute TCFs and SCFs of the statistical model and the reference model, as well as the MD of the absolute TCF and SCF of the statistical model from the corresponding theoretical values. One observes that all quantities are very small in the scenarios simulated. The close agreement between the channel statistics confirms the utility of the simulation model and the method used to estimate the model parameters. Table 10 studies the efficiency of the simulation model and tests its performance for different complexity, i.e., different number of simulation trials, in terms of the RMSE and the MD. From the results, adequate statistics can be achieved with only 10 simulation trials. It is also evident that by averaging over more simulation trials,

the performance of the simulation model improves. From the entire simulation results, the statistical simulation model outperforms the other simulation models and provides the best solution for the design of simulation models for HAP-MIMO mobile fading channels.

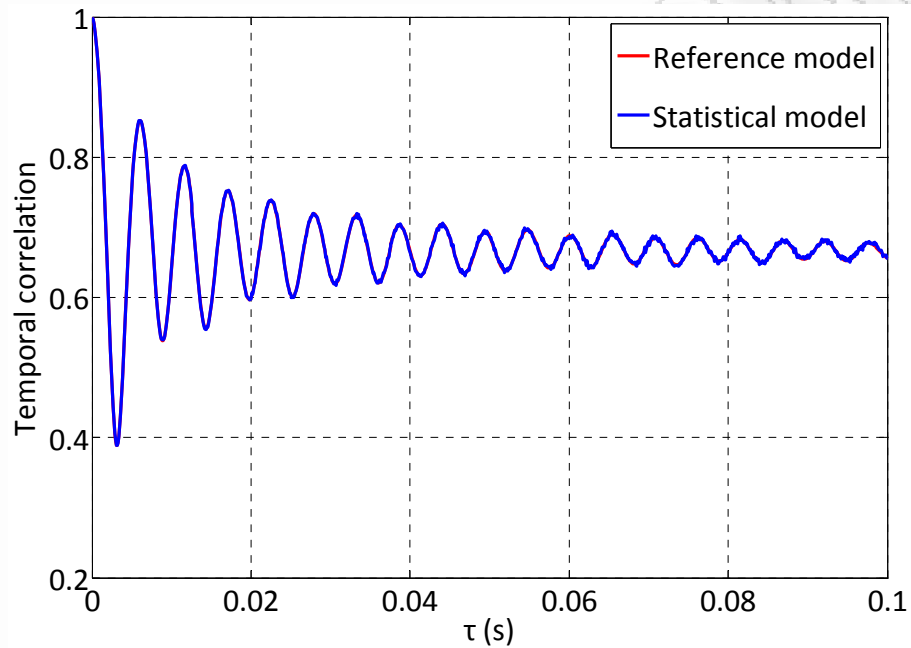


Figure 63: Comparison between the TCFs of the reference model and the statistical simulation model.

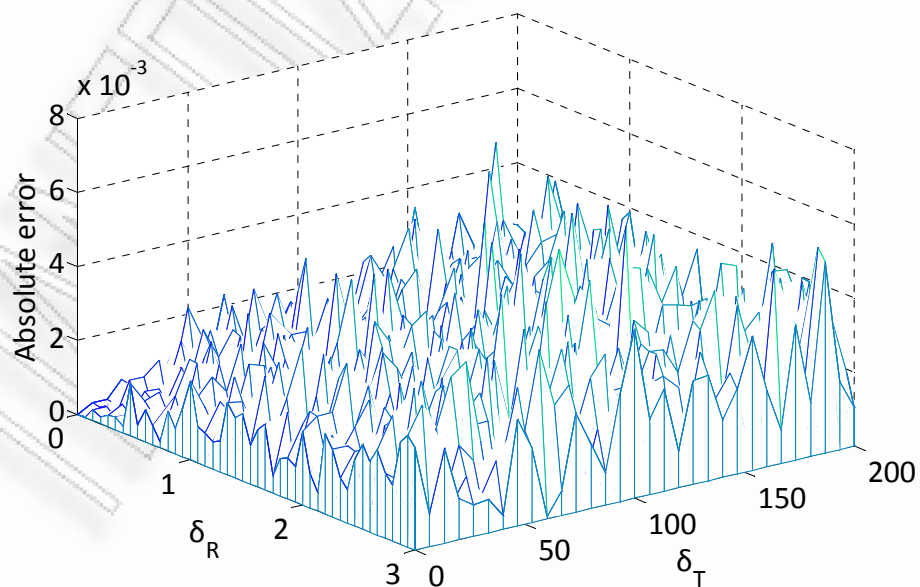


Figure 64: The absolute error between the SCFs of the reference model and the statistical simulation model.

TABLE 9
ACCURACY EVALUATION OF THE STATISTICAL SIMULATION MODEL

Values of the model parameters		TCF		SCF	
		RMSE	MD	RMSE	MD
k	0	$2.5 \cdot 10^{-3}$	$8.2 \cdot 10^{-3}$	$1.8 \cdot 10^{-3}$	$6.2 \cdot 10^{-3}$
	3	$2.3 \cdot 10^{-3}$	$7.4 \cdot 10^{-3}$	$1.5 \cdot 10^{-3}$	$5.1 \cdot 10^{-3}$
	8	$2.1 \cdot 10^{-3}$	$6.8 \cdot 10^{-3}$	$1.3 \cdot 10^{-3}$	$4.9 \cdot 10^{-3}$
μ	30°	$2.3 \cdot 10^{-3}$	$7.4 \cdot 10^{-3}$	$1.5 \cdot 10^{-3}$	$5.1 \cdot 10^{-3}$
	60°	$2.3 \cdot 10^{-3}$	$8.2 \cdot 10^{-3}$	$1.5 \cdot 10^{-3}$	$5.6 \cdot 10^{-3}$
	90°	$2.3 \cdot 10^{-3}$	$7.5 \cdot 10^{-3}$	$1.4 \cdot 10^{-3}$	$4.9 \cdot 10^{-3}$
α	0.01	$2.3 \cdot 10^{-3}$	$7.4 \cdot 10^{-3}$	$1.5 \cdot 10^{-3}$	$5.1 \cdot 10^{-3}$
	0.05	$2.1 \cdot 10^{-3}$	$6.8 \cdot 10^{-3}$	$1.2 \cdot 10^{-3}$	$4.5 \cdot 10^{-3}$
	0.1	$1.8 \cdot 10^{-3}$	$5.4 \cdot 10^{-3}$	$0.8 \cdot 10^{-3}$	$3.7 \cdot 10^{-3}$
$H_{S,mean}$	8 m	$2.2 \cdot 10^{-3}$	$6.9 \cdot 10^{-3}$	$1.4 \cdot 10^{-3}$	$4.8 \cdot 10^{-3}$
	17 m	$2.3 \cdot 10^{-3}$	$7.4 \cdot 10^{-3}$	$1.5 \cdot 10^{-3}$	$5.1 \cdot 10^{-3}$
	23 m	$2.4 \cdot 10^{-3}$	$7.7 \cdot 10^{-3}$	$1.6 \cdot 10^{-3}$	$5.5 \cdot 10^{-3}$

TABLE 10
EFFICIENCY EVALUATION OF THE STATISTICAL SIMULATION MODEL

Simulation trials	TCF		SCF	
	RMSE	MD	RMSE	MD
10	$5.3 \cdot 10^{-3}$	$14.6 \cdot 10^{-3}$	$3.4 \cdot 10^{-3}$	$12.4 \cdot 10^{-3}$
20	$3.8 \cdot 10^{-3}$	$11.3 \cdot 10^{-3}$	$2.5 \cdot 10^{-3}$	$7.2 \cdot 10^{-3}$
30	$3.2 \cdot 10^{-3}$	$9.3 \cdot 10^{-3}$	$2.2 \cdot 10^{-3}$	$6.5 \cdot 10^{-3}$
40	$2.8 \cdot 10^{-3}$	$8.7 \cdot 10^{-3}$	$1.9 \cdot 10^{-3}$	$5.8 \cdot 10^{-3}$
50	$2.3 \cdot 10^{-3}$	$7.4 \cdot 10^{-3}$	$1.5 \cdot 10^{-3}$	$5.1 \cdot 10^{-3}$
100	$1.6 \cdot 10^{-3}$	$5.2 \cdot 10^{-3}$	$1.2 \cdot 10^{-3}$	$3.3 \cdot 10^{-3}$

Finally, Fig. 65 compares the ergodic capacity defined in (48), (49) against SNR obtained using the reference model and the simulation models for $\delta_T = 60\lambda$, $\delta_R = 0.5\lambda$, and a normalized Doppler frequency $f_n = f_{R,\max}T_s = 0.01$. Due to the different way of generation of \mathbf{H}_{NLoS} in (49), the reference model is referred to as the non-physical model (see Chapter 3, Eq. (52)), while the simulation models are referred to as the physical models, since the elements of \mathbf{H} can be directly obtained using the procedures described in this chapter. The results show very good agreement between the non-physical and the physical models [163].

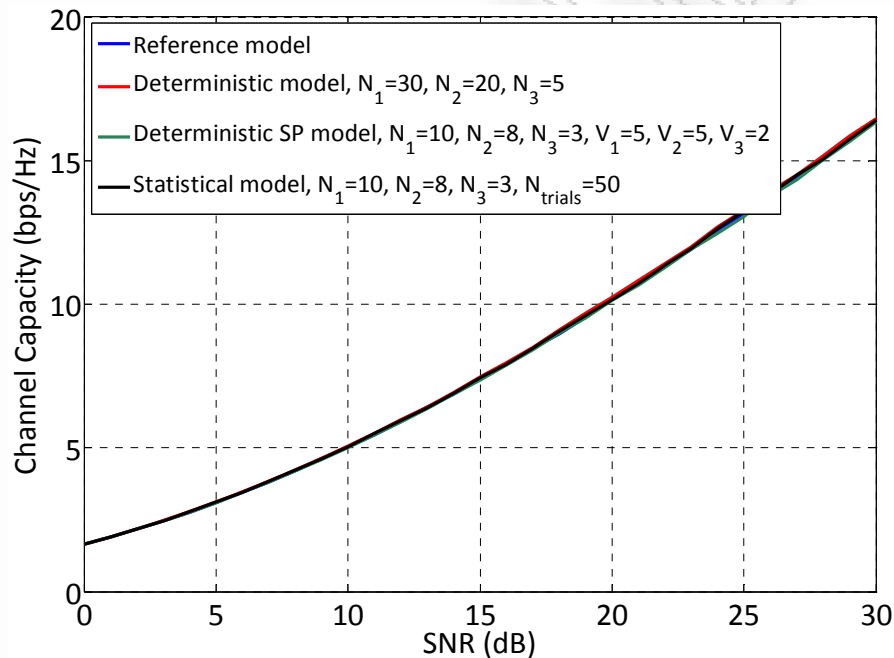


Figure 65: Comparison between the ergodic capacities obtained using the reference model and the simulation models.

4.6 Summary

In this chapter, methodologies for simulating HAP-MIMO Ricean faded channels have been presented, under 3-D non-isotropic scattering conditions. Specifically, parametric deterministic and statistical simulation models based on the SoS principle have been developed and the reference non-realizable HAP-MIMO channel model has served as the initial point. The proposed deterministic simulation model enables the generation of multiple deterministic waveforms and

provides an adequate approach for the simulation of HAP-MIMO channels in a single simulation trial. Nevertheless, its performance can only be improved by increasing the number of sinusoids, i.e., the number of the discrete scatterers. An alternative advantageous deterministic design method using the principle of SP has also been introduced. This method keeps the computational costs low, while significantly improves the performance simply by averaging across several simulation runs. Finally, a method that applies Monte Carlo techniques has been proposed to construct a statistical simulation model with at least one parameter as random variable. Since, this method statistically converges to the desired statistical properties, it is important to determine the number of simulation trials needed to achieve a specific convergence level.

By assuming that the AoA of the scattered waves, the distance between the user and the scatterers in azimuth domain and the height of the scatterers follow the von Mises, the hyperbolic and the log-normal distribution, respectively, the performance and the complexity of the proposed simulation models have been demonstrated by extensive simulation results. Based on these results, one concludes that the simulation models accurately and efficiently reproduce the SCFs and TCFs of the reference model and provide similar channel capacity estimations. Although the proposed deterministic simulation model has the potential of becoming a standard procedure due to its simplicity, efficiency, and reproducibility, the slightly complex statistical simulation model provides the highest performance with a relative small number of simulation trials, while the deterministic SP simulation model provides a good trade-off between complexity and performance.

Heretofore, 3-D narrowband reference and simulation models for HAP-MIMO channels have been developed. Notwithstanding, wideband channel modeling has received significant attention worldwide due to the increasing demand for high-speed broadband communications. To completely characterize HAP-MIMO multipath fading channels, it is necessary to develop realistic wideband HAP-MIMO channel models. Hence, Chapter 5 deals with this objective and proposes 3-D reference and simulation models for wideband HAP-MIMO channels.

Chapter 5

Three-Dimensional Modeling and Simulation of Wideband HAP-MIMO Channels

5.1 Introduction

Prospective 4G advanced multimedia and broadcasting communications services demand increased bandwidth and enhanced data rates. These services are mainly based on wideband transmissions and can be potentially upgraded if MIMO techniques are used. Thus, realistic wideband HAP-MIMO channel models are essential for the design and concise evaluation of future HAP-based systems. Wideband effects usually impose a time-variant impulse response, which can be modeled by a tapped delay line (TDL) with each tap defined using different weights and distributions [184]. In agreement with the TDL concept, a statistical switched (state-oriented) broadband channel model for HAP-based communications systems was presented in [111], while a model based on semi-Markovian processes was presented in [112]. These models allow for convenient and time-efficient system analysis of the links between HAPs and terrestrial stations, when the channel characteristics are dynamic and vary in time. Nevertheless, the propagation environment necessitates fundamental limitations on the performance. Hence, when terrain and scattering distributions are available, physical-geometrical channel modeling is preferred to ensure model accuracy and versatility.

To the author's best knowledge, only terrestrial geometry-based wideband MIMO channel models are available. Two-dimensional (2-D) models for non-isotropic scattering environments were presented in [185]-[187] and assumed that the radio waves travel only horizontally, which is an acceptable approximation for certain scenarios. As described in Chapter 3, HAP-based channel models should

consider 3-D scattering conditions. In [188] and [189], a 3-D wideband channel model was presented and introduced an elevation angle for the incidence of the radio waves in addition to the azimuth angle. Nevertheless, this model is not applicable to HAP-based systems. In particular, this model assumes that the distance between the user and the scatterers in the azimuth plane is constant. Moreover, the derivation of this model and its statistical properties was ground on the simplified assumption that the maximum elevation angle of arrival of the scattered waves is smaller than 20° , which typically represents terrestrial mobile-to-mobile systems (e.g., two cars driving through streets) [190]. If “above rooftop” propagation is present as in HAP-based systems, the maximum elevation angle approximates 90° [191]. Hence, other channel modeling approaches are necessary.

In Chapters 3 and 4, 3-D reference and simulation models for HAP-MIMO multipath fading channels have been proposed. The realization of these models is limited to narrowband, i.e., frequency-nonselctive, communications. In particular, it was assumed that the propagation delays of all incoming scattered waves are approximately equal and small in comparison to the data symbol duration. In wideband communications, the data symbol duration is small and multipath delay spread may be introduced. Therefore, the propagation delay differences cannot be neglected. In this chapter, the 3-D reference model for narrowband HAP-MIMO channels is extended with respect to frequency-selectivity and a 3-D reference model for wideband HAP-MIMO channels is derived. The proposed model utilizes carrier frequencies well below 10 GHz. Hence, both LoS and NLoS links should be considered, while rain effects are insignificant [1]. To describe the reference model, a 3-D geometrical model for wideband HAP-MIMO channels is introduced, referred to as the “two concentric-cylinders” model. This model is a modified version of the cylinder model for narrowband HAP-MIMO channels in Chapter 3. Several critical parameters are considered, e.g., the elevation angle of the platform, the array configuration, the Doppler and delay spread, and the distribution of the scatterers. Based on the reference model, the space-time-frequency correlation function (STFCF), the space-Doppler power spectrum (SDPS), and the power space-delay

spectrum (PSDS) are derived for a 3-D non-isotropic scattering environment. Numerical results demonstrate the theoretical derivations. This reference wideband model assumes an infinite number of scatterers, which prevents practical implementation. Thus, 3-D deterministic and statistical SoS simulation models for wideband HAP-MIMO channels are proposed and their statistical properties are verified by simulations.

The remainder of this chapter is organized as follows. Section 5.2 presents the wideband HAP-MIMO system model, while Section 5.3 proposes the 3-D reference model for wideband HAP-MIMO channels and constructs the corresponding input delay-spread and time-variant transfer functions. Section 5.4 studies the statistical properties of this reference model and presents numerical results. Section 5.5 details the simulation models and provides simulation results to verify their accuracy and efficiency. Finally, Section 5.6 summarizes this chapter.

5.2 The Wideband HAP-MIMO System Model

This chapter considers a downlink wideband HAP-MIMO communication channel with n_T transmit at the SBS and n_R receive antenna elements at the TMS. All antennas are fixed, omni-directional, and are numbered as $1 \leq p \leq q \leq n_T$ and $1 \leq l \leq m \leq n_R$, respectively. The complex low-pass equivalent time-variant channel response between SBS and TMS is given by $h_{pl}(t, \tau)$, and the complex low-pass equivalent input-output relation for the frequency selective HAP-MIMO fading channel is given by

$$\mathbf{r}(t) = \mathbf{H}(t, \tau) * \mathbf{s}(t) + \mathbf{n}(t), \quad (95)$$

where $\mathbf{H}(t, \tau) = [h_{p,l}(t, \tau)]_{n_R \times n_T} \in \mathbb{C}^{n_R \times n_T}$ is the matrix of the input delay-spread functions [160], $\mathbf{s}(t) \in \mathbb{C}^{n_T \times 1}$ is the transmitted signal vector, $\mathbf{r}(t) \in \mathbb{C}^{n_R \times 1}$ is the received signal vector, $\mathbf{n}(t) \in \mathbb{C}^{n_R \times 1}$ is the noise vector, which denotes the AWGN

at the receiver branches, and $(*)$ denotes convolution. The entries of the noise vector are i.i.d. complex Gaussian random variables with zero-mean and variance N_0 , where N_0 is the noise PSD.

5.3 A Reference Model for Wideband HAP-MIMO Channels

In this section, a 3-D GBSB reference model for wideband HAP-MIMO channels is introduced and its geometrical characteristics are described. Then, the input delay-spread and time-variant transfer functions are derived as a superposition of the LoS and NLoS rays.

The geometrical model proposed in Chapter 3 considers that the waves emitted from the SBS antenna elements travel over paths with different lengths and impinge the TMS array elements from different directions due to the scattering conditions within a cylinder. This section proposes a modified “two concentric-cylinders” version of this geometry [192]. The geometrical characteristics of the proposed model and the definition of the Cartesian coordinate system are discussed in Figs. 66-69 for a 2×2 HAP-MIMO channel, which is the basis to study ULAs with arbitrary number of antennas. Fig. 66 shows the LoS paths of the 3-D geometrical model, while Fig. 67 presents the projection of this model to the x - y plane. Figs. 68 and 69 show the NLoS paths for the channel in Figs. 66 and 67. For ease of reference, the parameters of the proposed reference model for wideband HAP-MIMO channels are summarized in Table 11.

The proposed reference model for wideband HAP-MIMO channels assumes that $N \rightarrow \infty$ fixed effective local scatterers surround the TMS. Then, the n^{th} scatterer is designated by $S^{(n)}$ and its projection to the x - y plane is denoted by $\tilde{S}^{(n)}$. The height of $S^{(n)}$ is $d(\tilde{S}^{(n)}, S^{(n)}) = H_S^{(n)} \in [H_{S,\min}, H_{S,\max}]$, and the distance between $\tilde{S}^{(n)}$ and O' is $d(\tilde{S}^{(n)}, O') = R_S^{(n)} \in [R_{S,\min}, R_{S,\max}]$, where $H_{S,\min} = \min\{H_S^{(n)}\}$, $H_{S,\max} = \max\{H_S^{(n)}\}$, $R_{S,\min} = \min\{R_S^{(n)}\}$, and $R_{S,\max} = \max\{R_S^{(n)}\}$.

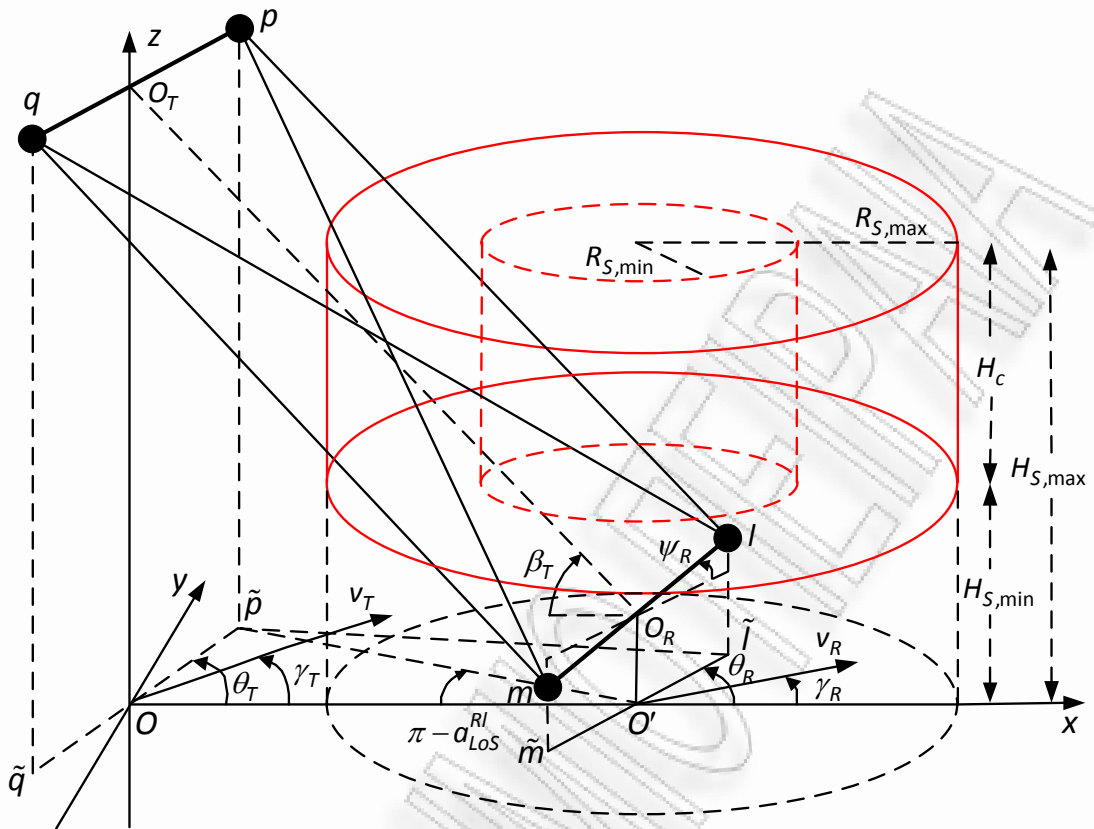


Figure 66: The LoS paths of the 3-D geometrical wideband model for a 2×2 HAP-MIMO channel.

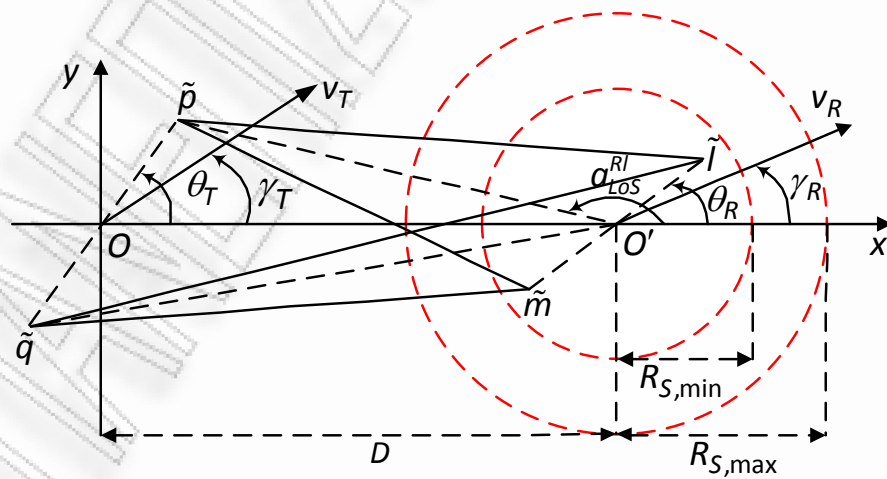


Figure 67: The LoS paths of the projection of the 3-D geometrical wideband model for a 2×2 HAP-MIMO channel.

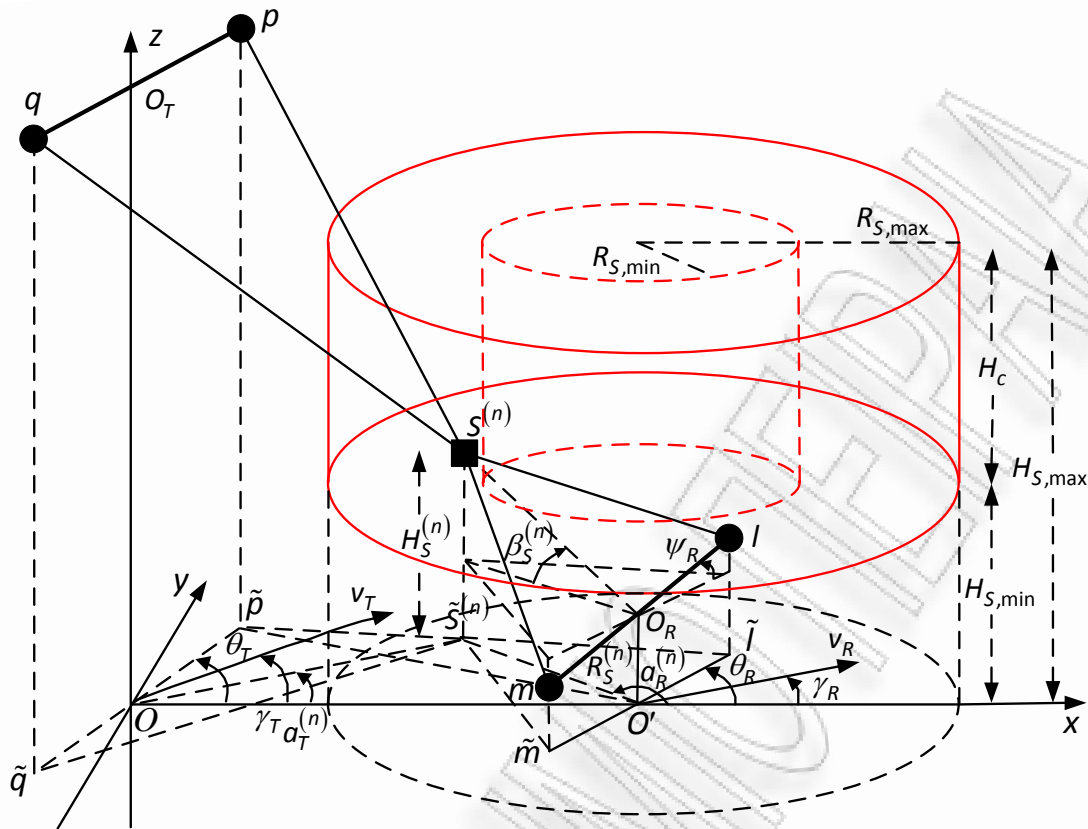


Figure 68: The NLoS paths of the 3-D geometrical wideband model for a 2x2 HAP-MIMO channel.

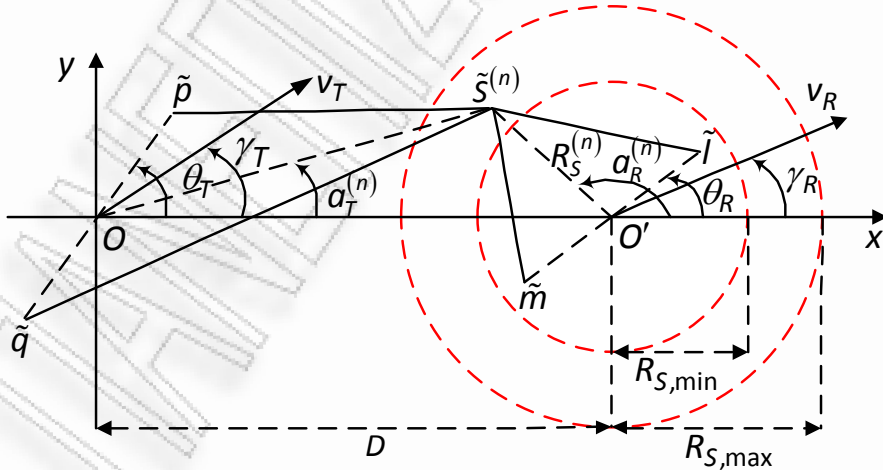


Figure 69: The NLoS paths of the projection of the 3-D geometrical wideband model for a 2x2 HAP-MIMO channel.

TABLE 11
DEFINITION OF THE PARAMETERS USED IN THE REFERENCE WIDEBAND MODEL

D	The distance between the centre O of the projections of the SBS antenna elements to the x - y plane and the lower centre O' of the cylinder.
$R_{S,\max}, H_{S,\max}$	The maximum distance between O' and $\tilde{\zeta}^{(n)}$, and the maximum height of the scatterers, respectively.
$R_{S,\min}, H_{S,\min}$	The minimum distance between O' and $\tilde{\zeta}^{(n)}$, and the minimum height of the scatterers, respectively.
δ_T, δ_R	The spacing between two adjacent antenna elements at the SBS and TMS, respectively.
θ_T, θ_R	The orientation of the SBS and TMS antenna array in the x - y plane (relative to the x -axis), respectively.
ψ_T, ψ_R	The elevation angle of the p^{th} SBS and l^{th} TMS antenna element, relative to the x - y plane, respectively.
v_T, v_R	The velocities of the SBS and TMS, respectively.
γ_T, γ_R	The moving directions of the SBS and TMS, respectively.
$f_{T,\max}, f_{R,\max}$	The maximum Doppler frequency shift of the SBS and TMS, respectively.
β_T	The elevation angle of the SBS relative to O_R .
$H_T, H_R, H_S^{(n)}$	The height of the SBS, the TMS, and the n^{th} scatterer, respectively.
a_{LoS}^R	The azimuth angle of arrival of the LoS paths.
$a_T^{(n)}, a_R^{(n)}$	The azimuth angle of arrival and the azimuth angle of departure at/from the n^{th} scatterer, respectively.
$R_S^{(n)}$	The distance between O' and $\tilde{\zeta}^{(n)}$.
$\beta_S^{(n)}$	The elevation angle of the n^{th} scatterer relative to O_R .
$\beta_{S,\min}, \beta_{S,\max}$	The minimum and maximum elevation angle of the n^{th} scatterer relative to O_R .
$\varphi^{(n)}, g^{(n)}$	The random phase and the amplitude introduced by the n^{th} scatterer, respectively.
μ, k	The mean azimuth angle at which the scatterers are distributed in the x - y plane and the spread of the scatterers around this angle, respectively.
a	The spread of the scatterers around the TMS.
$H_{S,\text{mean}}, \sigma$	The mean and standard deviation of scatterer's height, respectively.

Based on the modified model geometry, the scatterers occupy the volume between two concentric-cylinders with height $H_c = H_{S,\max} - H_{S,\min}$ and radius $R_{S,\min}$ and $R_{S,\max}$, respectively. This new geometry degrades to the corresponding one of the narrowband channel model in Chapter 3, when $H_{S,\min} = R_{S,\min} = 0$. Thus, the geometry of the narrowband model is a special case of the geometry of the wideband one. Using (13), this new geometry enables the determination of the minimum $\beta_{S,\min}$ and the maximum $\beta_{S,\max}$ values of $\beta_S^{(n)}$ as follows

$$\beta_{S,\min} = \arctan(H_{S,\min} / R_{S,\max}), \quad (96)$$

$$\beta_{S,\max} = \arctan(H_{S,\max} / R_{S,\min}). \quad (97)$$

Note that shadowing within the scattering region is neglected in this model.

5.3.1 Input Delay-Spread and Time-Variant Transfer Functions

Considering Ricean fading, the input delay-spread function of the link p - l is a superposition of the LoS and NLoS rays and can be written as follows [188], [189]

$$h_{pl}(t, \tau) = h_{pl,LoS}(t, \tau) + h_{pl,NLoS}(t, \tau), \quad (98)$$

where

$$h_{pl,LoS}(t, \tau) = \sqrt{\frac{\Omega_{pl} K_{pl}}{K_{pl} + 1}} e^{-\frac{j2\pi}{\lambda} d(p,l)} e^{j2\pi t (F_{T,LoS} + F_{R,LoS})} \delta(\tau - \tau_{LoS}), \quad (99)$$

$$h_{pl,NLoS}(t, \tau) = \sqrt{\frac{\Omega_{pl}}{K_{pl} + 1}} \lim_{N \rightarrow \infty} \frac{1}{\sqrt{N}} \sum_{n=1}^N g^{(n)} e^{j\varphi^{(n)}} e^{-\frac{j2\pi}{\lambda} [d(p,s^{(n)}) + d(s^{(n)},l)]} \times e^{j2\pi t (F_{T,NLoS} + F_{R,NLoS})} \delta(\tau - \tau_{NLoS}^{(n)}), \quad (100)$$

where Ω_{pl} denotes the transmitted power of the subchannel p - l , K_{pl} denotes the Ricean factor of the subchannel p - l , $g^{(n)}$ represents the amplitude of the n^{th}

scattered wave, $\varphi^{(n)} \in [-\pi, \pi)$ is the phase introduced by the n^{th} scatterer, τ_{LoS} and $\tau_{NLoS}^{(n)}$ are the propagation delays (travel times) of the waves associated with the LoS and NLoS links, respectively, and δ denotes the Dirac delta function. In addition, the parameters $d(p, l)$, $d(p, S^{(n)})$, $d(S^{(n)}, l)$, $F_{T,LoS}$, $F_{R,LoS}$, $F_{T,NLoS}$, and $F_{R,NLoS}$ are defined in (17)-(24), (27), (28), (31), and (32), respectively.

From Fig. 66, since $H_T \gg H_R$ the propagation delay from the SBS to the TMS, i.e., the minimum propagation delay, is given by

$$\tau_{LoS} = \tau_{\min} \approx \frac{D}{c_0 \cos \beta_T}, \quad (101)$$

where c_0 is the speed of light. From Fig. 68, considering that $H_{S,\max} \ll H_T$ and $R_S^{(n)} \ll D$, and using the cosine law, the travel time of a wave originated from SBS, reflected from $S^{(n)}$ and received by TMS is given by

$$\tau_{NLoS}^{(n)} \approx \frac{\sqrt{D^2 + (R_S^{(n)})^2 - 2DR_S^{(n)} \cos(\pi - a_R^{(n)})}}{c_0 \cos \beta_T} + \frac{R_S^{(n)}}{c_0 \cos \beta_S^{(n)}}. \quad (102)$$

Using the approximation $\sqrt{1+x} \approx 1+x/2$ for small x , (102) becomes

$$\tau_{NLoS}^{(n)} \approx \tau_{LoS} + \frac{R_S^{(n)} \cos a_R^{(n)}}{c_0 \cos \beta_T} + \frac{R_S^{(n)}}{c_0 \cos \beta_S^{(n)}}. \quad (103)$$

Moreover, using (13), (103) and considering that $\cos(\arctan x) = 1/\sqrt{1+x^2}$, $\cos a_R^{(n)} = 1$, $R_S^{(n)} = R_{S,\max}$, and $H_S^{(n)} = H_{S,\max}$, the maximum possible propagation delay can be derived as follows

$$\tau_{\max} \approx \tau_{LoS} + \frac{R_{S,\max}}{c_0 \cos \beta_T} + \frac{\sqrt{R_{S,\max}^2 + H_{S,\max}^2}}{c_0}. \quad (104)$$

Note that the minimum propagation delay τ_{LoS} is common to all paths. Thus, it can be neglected, without loss of generality. Then, the relative minimum and maximum propagation delays, as well as the relative propagation delay associated with the NLoS link are given, respectively, by

$$\tau_{r,LoS} = \tau_{r,min} = 0, \quad (105)$$

$$\tau_{r,max} \approx \tau_{max} - \tau_{LoS}, \quad (106)$$

$$\tau_{r,NLoS}^{(n)} \approx \tau_{NLoS}^{(n)} - \tau_{LoS}. \quad (107)$$

From (106), $R_{S,max}$ can be easily determined, considering that $H_{S,max}$ and $\tau_{r,max}$ are known (after measurements campaigns in different propagation environments and carrier frequencies). Estimated values of $\tau_{r,max}$ achieved with conventional aircrafts are in the order of hundreds of nanoseconds, which are much smaller than the corresponding values in terrestrial systems [193]. This is possibly due to the fact that the effective scatterers in a terrestrial system might be expected to be more widely distributed than those for a flying platform system operating at high elevation angles. Using (106), Fig. 70 demonstrates $\tau_{r,max}$ for $\beta_T = 60^\circ$ and different $R_{S,max}$ and $H_{S,max}$.

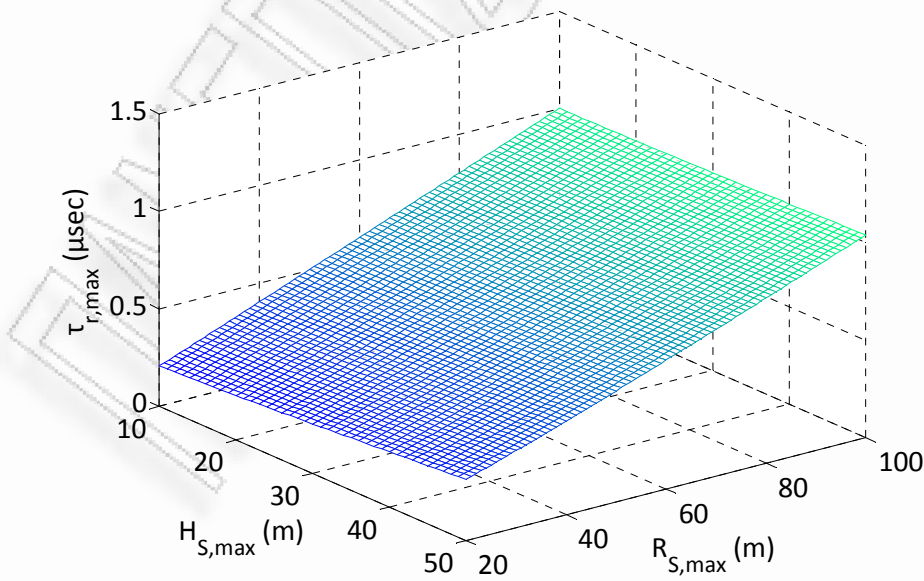


Figure 70: The relative maximum propagation delay for different maximum scatterer height and maximum distance in the azimuth plane between the TMS and the scatterers.

Finally, the time-variant transfer function is the FT of the input delay-spread function [184] and can be written as

$$T_{pl}(t, f) = \mathfrak{F}_\tau \{h_{pl}(t, \tau)\} = T_{pl,LoS}(t, f) + T_{pl,NLoS}(t, f), \quad (108)$$

where the LoS and NLoS components of the time-variant transfer function are, respectively,

$$T_{pl,LoS}(t, f) = \sqrt{\frac{\Omega_{pl}K_{pl}}{K_{pl} + 1}} e^{-\frac{j2\pi}{\lambda}d(p,l)} e^{j2\pi t(F_{T,LoS} + F_{R,LoS})} e^{-j2\pi f\tau_{LoS}}, \quad (109)$$

$$T_{pl,NLoS}(t, f) = \sqrt{\frac{\Omega_{pl}}{K_{pl} + 1}} \lim_{N \rightarrow \infty} \frac{1}{\sqrt{N}} \sum_{n=1}^N g^{(n)} e^{j\varphi^{(n)}} e^{-\frac{j2\pi}{\lambda} [d(p, s^{(n)}) + d(s^{(n)}, l)]} \\ \times e^{j2\pi t(F_{T,NLoS} + F_{R,NLoS})} e^{-j2\pi f\tau_{NLoS}^{(n)}}. \quad (110)$$

5.4 Statistical Properties of Wideband HAP-MIMO Channels

Considering a 3-D non-isotropic scattering environment, the STFCF of the complex faded envelope is derived. Then, using the STFCF, the SDPS and the PSDS are also derived.

5.4.1 Space-Time-Frequency Correlation Function

The normalized STFCF between two time-variant transfer functions $T_{pl}(t, f)$, and $T_{qm}(t, f)$ is defined as [184], [186], [194]

$$R_{pl,qm}(\delta_T, \delta_R, \Delta t, \Delta f) = \frac{\mathbb{E} [T_{pl}^*(t, f) T_{qm}(t + \Delta t, f + \Delta f)]}{\sqrt{\Omega_{pl} \Omega_{qm}}}. \quad (111)$$

Since the number of local scatterers is infinite, central limit theorem implies that both $T_{pl,NLoS}(t, f)$ and $T_{qm,NLoS}(t, f)$ are zero-mean complex Gaussian random processes, i.e., $\mathbb{E} [T_{pl,NLoS}(t, f)] = \mathbb{E} [T_{qm,NLoS}(t, f)] = 0$. Then, (111) can be written as follows (see Eq. (34) in Section 3 for a similar derivation)

$$R_{pl,qm}(\delta_T, \delta_R, \Delta t, \Delta f) = R_{pl,qm}^{LoS}(\delta_T, \delta_R, \Delta t, \Delta f) + R_{pl,qm}^{NLoS}(\delta_T, \delta_R, \Delta t, \Delta f), \quad (112)$$

where $R_{pl,qm}^{LoS}(\delta_T, \delta_R, \Delta t, \Delta f)$ and $R_{pl,qm}^{NLoS}(\delta_T, \delta_R, \Delta t, \Delta f)$ denote the STFCF of the LoS and the NLoS components, respectively. Using (17), (20), (22), (27), (28), (101), (109), and (111), and the approximate relation $a_{LoS}^{Rl} = a_{LoS}^{Rm} \approx \pi$ for $\delta_T \ll D$, the STFCF of the LoS component is derived as follows

$$\begin{aligned} & R_{pl,qm}^{LoS}(\delta_T, \delta_R, \Delta t, \Delta f) \\ & \approx \sqrt{\frac{K_{pl}K_{qm}}{(K_{pl}+1)(K_{qm}+1)}} e^{\frac{j2\pi[(q-p)\delta_T \cos \theta_T - (m-l)\delta_R \cos \theta_R \cos \psi_R]}{\lambda \cos \beta_T}} \\ & \quad \times e^{j2\pi\Delta t(f_{T,\max} \cos \gamma_T - f_{R,\max} \cos \gamma_R)} e^{-j2\pi\Delta f \frac{D}{c_0 \cos \beta_T}}. \end{aligned} \quad (113)$$

Moreover, using (13), (18)-(24), (31), (32), (110), and (111), the STFCF of the NLoS component can be written as

$$\begin{aligned} & R_{pl,qm}^{NLoS}(\delta_T, \delta_R, \Delta t, \Delta f) \\ & \approx \frac{1}{\sqrt{(K_{pl}+1)(K_{qm}+1)}} \lim_{N \rightarrow \infty} \frac{1}{N} \sum_{n=1}^N \mathbb{E} \left[\left| g^{(n)} \right|^2 e^{\frac{j2\pi(q-p)\delta_T \cos \theta_T}{\lambda \cos \beta_T}} e^{\frac{j2\pi(q-p)\delta_T \sin \theta_T R_S^{(n)} \sin a_R^{(n)}}{\lambda D \cos \beta_T}} \right. \\ & \quad \times e^{\frac{j2\pi(m-l)\delta_R \sin \psi_R \sin \left[\arctan \left(H_S^{(n)} / R_S^{(n)} \right) \right]}{\lambda}} e^{\frac{j2\pi(m-l)\delta_R \cos \theta_R \cos \psi_R \cos a_R^{(n)} \cos \left[\arctan \left(H_S^{(n)} / R_S^{(n)} \right) \right]}{\lambda}} \\ & \quad \times e^{\frac{j2\pi(m-l)\delta_R \sin \theta_R \cos \psi_R \sin a_R^{(n)} \cos \left[\arctan \left(H_S^{(n)} / R_S^{(n)} \right) \right]}{\lambda}} e^{j2\pi\Delta t f_{T,\max} \left(\frac{R_S^{(n)} \sin \gamma_T \sin a_R^{(n)}}{D} + \cos \gamma_T \right)} \\ & \quad \times e^{j2\pi\Delta t f_{R,\max} \cos \left(a_R^{(n)} - \gamma_R \right) \cos \left[\arctan \left(H_S^{(n)} / R_S^{(n)} \right) \right]} \\ & \quad \left. \times e^{-j2\pi\Delta f \left[\frac{D}{c_0 \cos \beta_T} + \frac{R_S^{(n)} \cos a_R^{(n)}}{c_0 \cos \beta_T} + \frac{R_S^{(n)}}{c_0 \cos \left[\arctan \left(H_S^{(n)} / R_S^{(n)} \right) \right]} \right]} \right]. \end{aligned} \quad (114)$$

The infinite number of local scatterers in the reference model also enables the replacement of the discrete variables $a_R^{(n)}$, $R_S^{(n)}$, and $H_S^{(n)}$ with the continuous random variables a_R , R_S , and H_S with joint pdf $f(a_R, R_S, H_S)$. According to Fig. 68,

$a_R^{(n)}$, $R_S^{(n)}$, and $H_S^{(n)}$ are independent. Thus, the joint pdf $f(a_R, R_S, \beta_S)$ can be decomposed to $f(a_R)f(R_S)f(H_S)$.

In agreement with the narrowband model in Chapter 3, the von Mises pdf in (39) is used to characterize a_R . In addition, the following truncated⁷ hyperbolic pdf is used to characterize R_S for the range $R_{S,\min} < R_S \leq R_{S,\max}$

$$f_T(R_S) = \frac{f(R_S)}{F_{R_S}(R_{S,\max}) - F_{R_S}(R_{S,\min})}, \quad (115)$$

where $f(R_S)$ and $F_{R_S}(R_S)$ are defined in (40) and (60), respectively. Furthermore, the following truncated log-normal pdf is adopted to characterize H_S for the range $H_{S,\min} < H_S \leq H_{S,\max}$

$$f_T(H_S) = \frac{f(H_S)}{F_{H_S}(H_{S,\max}) - F_{H_S}(H_{S,\min})}, \quad (116)$$

where $f(H_S)$ and $F_{H_S}(H_S)$ are defined in (41) and (63), respectively.

Finally, using the equality $\int_{-\pi}^{\pi} e^{a \sin(c) + b \cos(c)} dc = 2\pi I_0(\sqrt{a^2 + b^2})$ [161, eq.3.338-4], and (39), (115), and (116), the STFCF of the NLoS component becomes

$$R_{pl,qm}^{NLoS}(\delta_T, \delta_R, \Delta t, \Delta f) = w_1 \int_{H_{S,\min}}^{H_{S,\max}} \int_{R_{S,\min}}^{R_{S,\max}} w_2 I_0(\sqrt{w_3^2 + w_4^2}) dR_S dH_S, \quad (117)$$

where w_1 , w_2 , w_3 , and w_4 are, respectively

$$w_1 = \frac{a \left[(K_{pl} + 1)(K_{qm} + 1) \right]^{-1/2} e^{j2\pi \left(\frac{(q-p)\delta_T \cos \theta_T}{\lambda \cos \beta_T} + \Delta t f_{T,\max} \cos \gamma_T - \frac{\Delta f D}{c_0 \cos \beta_T} \right)}}{\sigma \sqrt{2\pi} I_0(k) \left[\tanh(aR_{S,\max}) - \tanh(aR_{S,\min}) \right] \left[F_{H_S}(H_{S,\max}) - F_{H_S}(H_{S,\min}) \right]}, \quad (118)$$

⁷A truncated distribution is a conditional distribution that results from restricting the domain of some other probability distribution.

$$w_2 = \frac{e^{j2\pi \left(\frac{(m-l)\delta_R \sin\psi_R \sin[\arctan(H_S/R_S)]}{\lambda} - \frac{\Delta f R_S}{c_0 \cos[\arctan(H_S/R_S)]} \right)} e^{\left[-\frac{1}{2\sigma^2} \ln^2 \left(\frac{H_S}{H_{S,\text{mean}}} \right) \right]}}{H_S \cosh^2(aR_S)}, \quad (119)$$

$$w_3 = \frac{j2\pi(q-p)\delta_T \sin\theta_T R_S}{\lambda D \cos\beta_T} + \frac{j2\pi\Delta f_{T,\text{max}} \sin\gamma_T R_S}{D} \\ + \frac{j2\pi(m-l)\delta_R \sin\theta_R \cos\psi_R \cos[\arctan(H_S/R_S)]}{\lambda} \\ + j2\pi\Delta f_{R,\text{max}} \sin\gamma_R \cos[\arctan(H_S/R_S)] + k \sin\mu, \quad (120)$$

$$w_4 = \frac{j2\pi(m-l)\delta_R \cos\theta_R \cos\psi_R \cos[\arctan(H_S/R_S)]}{\lambda} \\ + j2\pi\Delta f_{R,\text{max}} \cos\gamma_R \cos[\arctan(H_S/R_S)] \\ - j2\pi\Delta f \frac{R_S}{c_0 \cos\beta_T} + k \cos\mu. \quad (121)$$

The double integral in (117) has to be evaluated numerically, since there is no closed-form solution.

Finally, the STFCF between two time-variant transfer functions $T_{pl}(t, f)$, and $T_{qm}(t, f)$ becomes a summation of the STFCFs of the LoS and the NLoS components defined in (113) and (117)-(121), respectively.

5.4.2 Space-Doppler Power Spectrum

Considering a wide-sense stationary uncorrelated scattering (WSSUS) time-varying HAP-MIMO channel, the SDPS is derived by applying FT to the STCF, i.e., $R_{pl,qm}(\delta_T, \delta_R, \Delta t, \Delta f = 0)$, in (112). Other approaches for determining the Doppler spectrum of terrestrial and satellites systems by assuming 3-D scattering were previously proposed in [188], [189], [195]-[198].

The SDPS of the LoS component is obtained by calculating the FT of the STCF of the LoS component in (113) as follows

$$\begin{aligned}
S_{pl,qm}^{LoS}(\delta_T, \delta_R, \nu) &= \mathfrak{F}_{\Delta t} \left\{ R_{pl,qm}^{LoS}(\delta_T, \delta_R, \Delta t, \Delta f = 0) \right\} \\
&= \sqrt{\frac{K_{pl} K_{qm}}{(K_{pl} + 1)(K_{qm} + 1)}} e^{j \frac{2\pi [(q-p)\delta_T \cos \theta_T - (m-l)\delta_R \cos \theta_R \cos \psi_R]}{\lambda \cos \beta_T}} \\
&\quad \times \delta(\nu + f_{T,\max} \cos \gamma_T - f_{R,\max} \cos \gamma_R), \quad (122)
\end{aligned}$$

where ν is the Doppler frequency shift relative to the carrier frequency.

The SDPS of the NLoS component is obtained by calculating the FT of the STCF of the NLoS component in (117)-(121)

$$S_{pl,qm}^{NLoS}(\delta_T, \delta_R, \nu) = \mathfrak{F}_{\Delta t} \left\{ R_{pl,qm}^{NLoS}(\delta_T, \delta_R, \Delta t, \Delta f = 0) \right\}. \quad (123)$$

For $\Delta f = 0$, the Bessel function $I_0(\sqrt{w_3^2 + w_4^2})$ of (117) can be written as follows

$$I_0(\sqrt{w_3^2 + w_4^2})_{\Delta f=0} = J_0 \left[s_1 \sqrt{(\Delta t + s_2)^2 + s_3^2} \right], \quad (124)$$

where

$$s_1 = 2\pi f_{R,\max} \cos[\arctan(H_S / R_S)], \quad (125)$$

$$s_2 = \frac{q_1 + q_2 - q_3}{f_{R,\max} \cos[\arctan(H_S / R_S)]}, \quad (126)$$

$$s_3 = \frac{q_4 + q_5 - q_6}{f_{R,\max} \cos[\arctan(H_S / R_S)]}, \quad (127)$$

$$q_1 = \frac{(q-p)\delta_T \sin \theta_T R_S \sin \gamma_R}{\lambda D \cos \beta_T}, \quad (128)$$

$$q_2 = \frac{(m-l)\delta_R \cos \psi_R \cos(\theta_R - \gamma_R) \cos[\arctan(H_S / R_S)]}{\lambda}, \quad (129)$$

$$q_3 = \frac{jk \cos(\mu - \gamma_R)}{2\pi}, \quad (130)$$

$$q_4 = \frac{(q-p)\delta_T \sin \theta_T R_S \cos \gamma_R}{\lambda D \cos \beta_T}, \quad (131)$$

$$q_5 = \frac{(m-l)\delta_R \cos\psi_R \sin(\theta_R + \gamma_R) \cos[\arctan(H_S/R_S)]}{\lambda}, \quad (132)$$

$$q_6 = \frac{j k \sin(\mu + \gamma_R)}{2\pi}. \quad (133)$$

Using (124)-(133), the SDPS of the NLoS component becomes

$$S_{pl,qm}^{NLoS}(\delta_T, \delta_R, \nu) = \int_{H_{S,\min}}^{H_{S,\max}} \int_{R_{S,\min}}^{R_{S,\max}} A \int_{-\infty}^{\infty} e^{-j2\pi\Delta t(\nu - f_{T,\max} \cos\gamma_T)} \times J_0 \left[s_1 \sqrt{(\Delta t + s_2)^2 + s_3^2} \right] d\Delta t dR_S dH_S, \quad (134)$$

where

$$A = \frac{e^{j2\pi \left(\frac{(q-p)\delta_T \cos\theta_T}{\lambda \cos\beta_T} + \frac{(m-l)\delta_R \sin\psi_R \sin[\arctan(H_S/R_S)]}{\lambda} \right)} e^{\left[\frac{1}{2\sigma^2} \ln^2 \left(\frac{H_S}{H_{S,\text{mean}}} \right) \right]}}{H_S \cosh^2(aR_S) \sigma \sqrt{2\pi} I_0(k) \sqrt{(K_{pl}+1)(K_{qm}+1)}} \times \frac{a}{\left[F_{H_S}(H_{S,\max}) - F_{H_S}(H_{S,\min}) \right] \left[\tanh(aR_{S,\max}) - \tanh(aR_{S,\min}) \right]}. \quad (135)$$

It is well known that $e^{\pm jx} = \cos x \pm j \sin x$ (Euler's formula), the integral of the product of an odd function, i.e., $\sin x$, and an even function, i.e., $\cos x$ and $J_0(x)$, from $-\infty$ to ∞ is equal to zero, the product of two even functions is an even function, and the integral of an even function from $-\infty$ to ∞ is twice the integral from 0 to ∞ . Under these considerations and using the equality $\int_0^\infty J_0(a\sqrt{x^2+z^2}) \cos(bx) dx = \cos(z\sqrt{a^2-b^2}) / \sqrt{a^2-b^2}$ [161, eq. 6.677-3], (134) becomes

$$S_{pl,qm}^{NLoS}(\delta_T, \delta_R, \nu) = \int_{H_{S,\min}}^{H_{S,\max}} \int_{R_{S,\min}}^{R_{S,\max}} \frac{A e^{j2\pi s_2(\nu - f_{T,\max} \cos\gamma_T)}}{\pi \sqrt{f_{R,\max}^2 \cos^2[\arctan(H_S/R_S)] - (\nu - f_{T,\max} \cos\gamma_T)^2}} \times \cos \left[2\pi s_3 \sqrt{f_{R,\max}^2 \cos^2[\arctan(H_S/R_S)] - (\nu - f_{T,\max} \cos\gamma_T)^2} \right] dR_S dH_S. \quad (136)$$

The double integral in (136) has to be evaluated numerically, since there is no closed-form solution. One observes that (136) is applicable for the range

$$\begin{aligned} 0 \leq |v - f_{T,\max} \cos \gamma_T| &\leq f_{R,\max} \cos[\arctan(H_S / R_S)] \\ \Rightarrow 0 \leq |v - f_{T,\max} \cos \gamma_T| &\leq v_{\min}, \end{aligned} \quad (137)$$

where

$$\begin{aligned} v_{\min} &= \min_{H_S, R_S} \left\{ f_{R,\max} \cos[\arctan(H_S / R_S)] \right\} \\ &= f_{R,\max} \cos[\arctan(H_{S,\max} / R_{S,\min})]. \end{aligned} \quad (138)$$

However, the SDPS should be sketched for the range

$$0 \leq |v - f_{T,\max} \cos \gamma_T| \leq v_{\max}, \quad (139)$$

where

$$\begin{aligned} v_{\max} &= \max_{H_S, R_S} \left\{ f_{R,\max} \cos[\arctan(H_S / R_S)] \right\} \\ &= f_{R,\max} \cos[\arctan(H_{S,\min} / R_{S,\max})]. \end{aligned} \quad (140)$$

Hence, the following function is finally proposed as the SDPS of the NLoS component

$$\begin{aligned} S_{pl,qm}^{NLoS}(\delta_T, \delta_R, v) &= \int_{H_{S,\min}}^{x_1} \int_{x_2}^{R_{\max}} \frac{A' e^{j2\pi s_2(v - f_{T,\max} \cos \gamma_T)}}{\pi \sqrt{f_{R,\max}^2 \cos^2[\arctan(H_S / R_S)] - (v - f_{T,\max} \cos \gamma_T)^2}} \\ &\times \cos \left[2\pi s_3 \sqrt{f_{R,\max}^2 \cos^2[\arctan(H_S / R_S)] - (v - f_{T,\max} \cos \gamma_T)^2} \right] dR_S dH_S, \end{aligned} \quad (141)$$

where

$$\begin{aligned} A' &= \frac{e^{j2\pi \left(\frac{(q-p)\delta_T \cos \theta_T}{\lambda \cos \beta_T} + \frac{(m-l)\delta_R \sin \psi_R \sin[\arctan(H_S / R_S)]}{\lambda} \right)} e^{\left[-\frac{1}{2\sigma^2} \ln^2 \left(\frac{H_S}{H_{S,\text{mean}}} \right) \right]}}{H_S \cosh^2(aR_S) \sigma \sqrt{2\pi} I_0(k) \sqrt{(K_{pl} + 1)(K_{qm} + 1)}} \\ &\times \frac{a}{\left[F_{H_S}(x_1) - F_{H_S}(H_{S,\min}) \right] \left[\tanh(aR_{S,\max}) - \tanh(ax_2) \right]}, \end{aligned} \quad (142)$$

$$x_1 = \begin{cases} H_{S,\max}, & 0 \leq |v - f_{T,\max} \cos \gamma_T| \leq v_{\min} \\ R_{S,\min} B, & v_{\min} < |v - f_{T,\max} \cos \gamma_T| \leq v_{\max} \end{cases}, \quad (143)$$

$$x_2 = \begin{cases} R_{S,\min}, & 0 \leq |v - f_{T,\max} \cos \gamma_T| \leq v_{\min} \\ H_{S,\max} / B, & v_{\min} < |v - f_{T,\max} \cos \gamma_T| \leq v_{\max} \end{cases}, \quad (144)$$

$$B = \tan \left(\arccos \left(\frac{|v - f_{T,\max} \cos \gamma_T|}{f_{R,\max}} \right) \right). \quad (145)$$

5.4.3 Power Space-Delay Spectrum

Considering a WSSUS frequency-varying HAP-MIMO channel, the PSDS is derived by applying IFT to the space-frequency correlation function (SFCF) in (34) i.e., $R_{pl,qm}(\delta_T, \delta_R, \Delta t = 0, \Delta f)$. Another approach for determining the delay spectrum of terrestrial systems by assuming 3-D scattering was previously proposed in [188], [189].

The relative PSDS of the LoS component can be obtained by calculating the IFT of the SFCF of the LoS component in (113) as follows

$$\begin{aligned} P_{pl,qm}^{LoS}(\delta_T, \delta_R, \tau_r) &= \mathfrak{F}_{\Delta f}^{-1} \left\{ R_{pl,qm}^{LoS}(\delta_T, \delta_R, \Delta t = 0, \Delta f) \right\} \\ &= \sqrt{\frac{K_{pl} K_{qm}}{(K_{pl} + 1)(K_{qm} + 1)}} e^{j \frac{2\pi[(q-p)\delta_T \cos \theta_T - (m-l)\delta_R \cos \theta_R \cos \psi_R]}{\lambda \cos \beta_T}} \delta(\tau_r), \end{aligned} \quad (146)$$

where $\tau_r = \tau - \tau_{LoS} \in [0, \tau_{r,\max}]$ is the relative propagation delay.

The relative PSDS of the NLoS component can be obtained by calculating the IFT of the SFCF of the NLoS component in (117)-(121)

$$P_{pl,qm}^{NLoS}(\delta_T, \delta_R, \tau_r) = \mathfrak{F}_{\Delta f}^{-1} \left\{ R_{pl,qm}^{NLoS}(\delta_T, \delta_R, \Delta t = 0, \Delta f) \right\}. \quad (147)$$

For $\Delta t = 0$, the Bessel function $I_0(\sqrt{w_3^2 + w_4^2})$ of (117) can be written as follows

$$I_0\left(\sqrt{w_3^2 + w_4^2}\right)_{\Delta t=0} = J_0\left[2\pi\rho_1\sqrt{(\Delta f - \rho_2)^2 + \rho_3^2}\right], \quad (148)$$

where

$$\rho_1 = \frac{R_S}{c_0 \cos \beta_T}, \quad (149)$$

$$\rho_2 = \frac{(m-l)\delta_R \cos \theta_R \cos \psi_R c_0 \cos \beta_T \cos[\arctan(H_S / R_S)]}{\lambda R_S} - \frac{jkc_0 \cos \mu \cos \beta_T}{2\pi R_S}, \quad (150)$$

$$\rho_3 = \frac{(m-l)\delta_R \sin \theta_R \cos \psi_R c_0 \cos \beta_T \cos[\arctan(H_S / R_S)]}{\lambda R_S} + \frac{(q-p)\delta_T \sin \theta_T c_0}{\lambda D} - \frac{jkc_0 \sin \mu \cos \beta_T}{2\pi R_S}. \quad (151)$$

Using (148)-(151), (147) becomes

$$P_{pl,qm}^{NLoS}(\delta_T, \delta_R, \tau_r) = \int_{H_{S,\min}}^{H_{S,\max}} \int_{R_{S,\min}}^{R_{S,\max}} A \int_{-\infty}^{\infty} e^{j2\pi\Delta f(\tau_r - \rho_4)} J_0\left(2\pi\rho_1\sqrt{(\Delta f - \rho_2)^2 + \rho_3^2}\right) d\Delta f dR_S dH_S, \quad (152)$$

where

$$\rho_4 = \frac{R_S}{c_0 \cos[\arctan(H_S / R_S)]}. \quad (153)$$

Using the equality [161, eq. 6.677-3] and after extensive calculations, the relative PSDS of the NLoS component is derived as follows

$$P_{pl,qm}^{NLoS}(\delta_T, \delta_R, \tau_r) = \int_{H_{S,\min}}^{H_{S,\max}} \int_{R_{S,\min}}^{R_{S,\max}} \frac{A e^{j2\pi\rho_2(\tau_r - \rho_4)} \cos\left(2\pi\rho_3\sqrt{\rho_1^2 - (\tau_r - \rho_4)^2}\right)}{\pi\sqrt{\rho_1^2 - (\tau_r - \rho_4)^2}} dR_S dH_S. \quad (154)$$

The double integral in (154) has to be evaluated numerically, since there is no closed-form solution.

One observes that (154) is applicable for the range

$$\begin{aligned}
 & |\tau_r - \rho_4| \leq \rho_1 \\
 \Rightarrow & \rho_4 - \rho_1 \leq \tau_r \leq \rho_4 + \rho_1 \\
 \Rightarrow & \tau_1 \leq \tau_r \leq \tau_2, \tag{155}
 \end{aligned}$$

where

$$\begin{aligned}
 \tau_1 &= \max_{H_S, R_S} \{ \rho_4 - \rho_1 \} \\
 &= \frac{\sqrt{R_{S,\min}^2 + H_{S,\max}^2}}{c_0} - \frac{R_{S,\min}}{c_0 \cos \beta_T}, \tag{156}
 \end{aligned}$$

$$\begin{aligned}
 \tau_2 &= \min_{H_S, R_S} \{ \rho_4 + \rho_1 \} \\
 &= \frac{\sqrt{R_{S,\min}^2 + H_{S,\min}^2}}{c_0} + \frac{R_{S,\min}}{c_0 \cos \beta_T}. \tag{157}
 \end{aligned}$$

However, the relative PSDS should be sketched for the range

$$0 \leq \tau_r \leq \tau_{r,\max}, \tag{158}$$

where $\tau_{r,\max}$ is defined in (106). Hence, the following function is finally proposed as the relative PSDS of the NLoS component

$$P_{pl,qm}^{NLoS}(\delta_T, \delta_R, \tau_r) = \int_{y_1}^{y_2} \int_{y_3}^{R_{S,\max}} \frac{A'' e^{j2\pi\rho_2(\tau_r - \rho_4)} \cos\left(2\pi\rho_3\sqrt{\rho_1^2 - (\tau_r - \rho_4)^2}\right)}{\pi\sqrt{\rho_1^2 - (\tau_r - \rho_4)^2}} dR_S dH_S, \tag{159}$$

where

$$\begin{aligned}
 A'' &= \frac{e^{j2\pi\left(\frac{(q-\rho)\delta_T \cos \theta_T}{\lambda \cos \beta_T} + \frac{(m-l)\delta_R \sin \psi_R \sin[\arctan(H_S/R_S)]}{\lambda}\right)} e^{\left[\frac{1}{2\sigma^2} \ln^2\left(\frac{H_S}{H_{S,\text{mean}}}\right)\right]}}{H_S \cosh^2(aR_S) \sigma \sqrt{2\pi} I_0(k) \sqrt{(K_{pl} + 1)(K_{qm} + 1)}} \\
 &\quad \times \frac{a}{\left[F_{H_S}(y_2) - F_{H_S}(y_1)\right] \left[\tanh(aR_{S,\max}) - \tanh(ay_3)\right]}, \tag{160}
 \end{aligned}$$

$$y_1 = \begin{cases} H_{S,\min}, & 0 \leq \tau_r \leq \tau_2 \\ \frac{H_{S,\min}}{\sqrt{\tan^2 \beta_T R_{S,\min}^2 - 2c_0 \tau_r \sec \beta_T R_{S,\min} + c_0^2 \tau_r^2}}, & \tau_2 < \tau_r \leq \tau_{r,\max} \end{cases}, \quad (161)$$

$$y_2 = \begin{cases} \sqrt{\tan^2 \beta_T R_{S,\min}^2 + 2c_0 \tau_r \sec \beta_T R_{S,\min} + c_0^2 \tau_r^2}, & 0 \leq \tau_r < \tau_1 \\ H_{S,\max}, & \tau_1 \leq \tau_r \leq \tau_{r,\max} \end{cases}, \quad (162)$$

$$y_3 = \begin{cases} \frac{-c_0 \tau_r \sec \beta_T + \sqrt{c_0^2 \tau_r^2 + H_{S,\max}^2 \tan^2 \beta_T}}{\tan^2 \beta_T}, & 0 \leq \tau_r < \tau_1 \\ R_{S,\min}, & \tau_1 \leq \tau_r \leq \tau_2 \\ \frac{c_0 \tau_r \sec \beta_T - \sqrt{c_0^2 \tau_r^2 + H_{S,\min}^2 \tan^2 \beta_T}}{\tan^2 \beta_T}, & \tau_2 < \tau_r \leq \tau_{r,\max} \end{cases}. \quad (163)$$

5.4.4 Numerical Results

This section demonstrates the theoretical derivations described above. Figs. 71-74 depict the absolute STFCF for a 3-D non-isotropic scattering environment. Unless indicated otherwise, the values of the model parameters used to obtain the curves are $n_T = n_R = 2$, $K_{pl} = K_{qm} = 0$ for Rayleigh fading, $K_{pl} = K_{qm} = 3$ dB for Ricean fading, $H_T = 20$ km, $\beta_T = 60^\circ$, $\theta_T = 60^\circ$, $\theta_R = 30^\circ$, $\psi_R = 20^\circ$, $a = 0.01$, $R_{S,\min} = 7$ m, $R_{S,\max} = 140$ m, $H_{S,\min} = 5$ m, $H_{S,\max} = 50$ m, $H_{S,\text{mean}} = 17.6$ m, $\sigma = 0.31$, $k = 4$, $\mu = 90^\circ$, $f_{T,\max} = 300$ Hz, $f_{R,\max} = 100$ Hz, $\gamma_T = 30^\circ$, and $\gamma_R = 60^\circ$.

Fig. 71 shows the absolute frequency correlation function (FCF) $|R_{pl,qm}(\delta_T = 0, \delta_R = 0, \Delta t = 0, \Delta f)|$ of a HAP-SISO Rayleigh channel for different β_T . One observes that the correlation decreases as β_T increases. From Fig. 71, the coherence bandwidth B_c can also be estimated. Considering that the coherence bandwidth is the bandwidth over which the absolute FCF is above 0.5 [2], B_c is approximately 0.9 MHz, 0.7 MHz, and 0.4 MHz, when $\beta_T = 60^\circ$, $\beta_T = 70^\circ$, and

$\beta_T = 80^\circ$, respectively. Figs. 72 and 73 illustrate the shape of the absolute SFCFs $|R_{pl,qm}(\delta_T, \delta_R = 0, \Delta t = 0, \Delta f)|$ and $|R_{pl,qm}(\delta_T = 0, \delta_R, \Delta t = 0, \Delta f)|$ of a HAP-MIMO channel, while Fig. 74 depicts the shape of the absolute time-frequency correlation function (TFCF) $|R_{pl,qm}(\delta_T = 0, \delta_R = 0, \Delta t, \Delta f)|$ of a HAP-SISO channel. Both Rayleigh and Ricean fading conditions are considered.

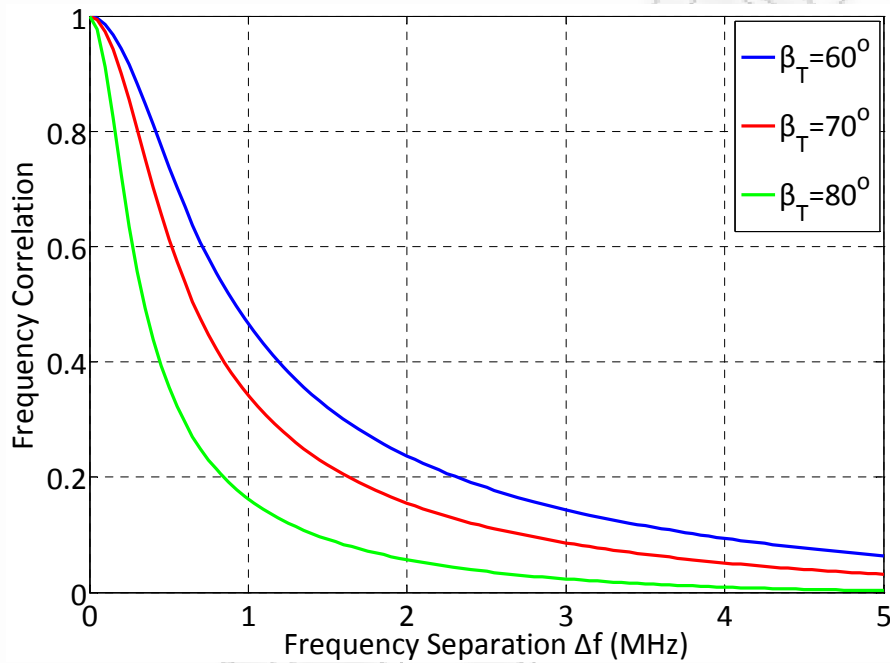


Figure 71: The FCF of a HAP-SISO Rayleigh channel for different elevation angles of the SBS.

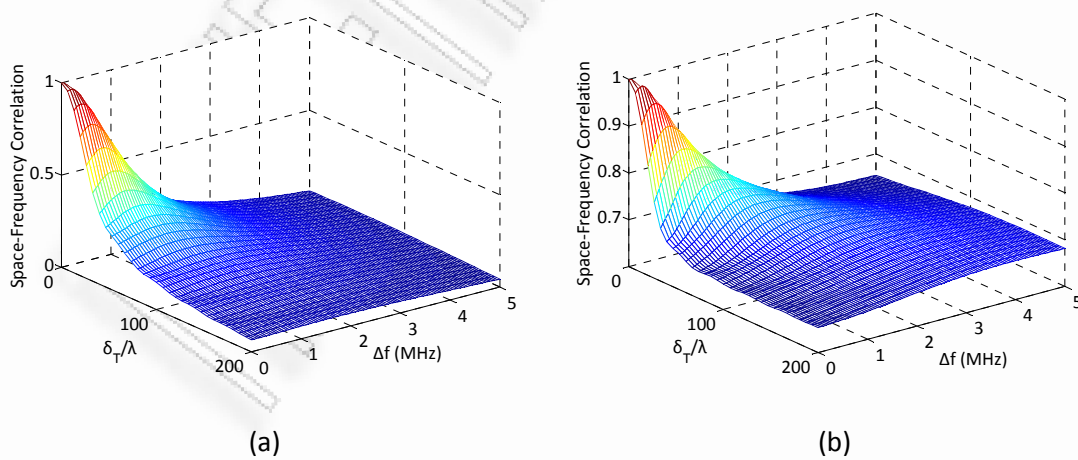


Figure 72: The transmit SFCF of a 2×2 HAP-MIMO (a) Rayleigh and (b) Ricean channel.

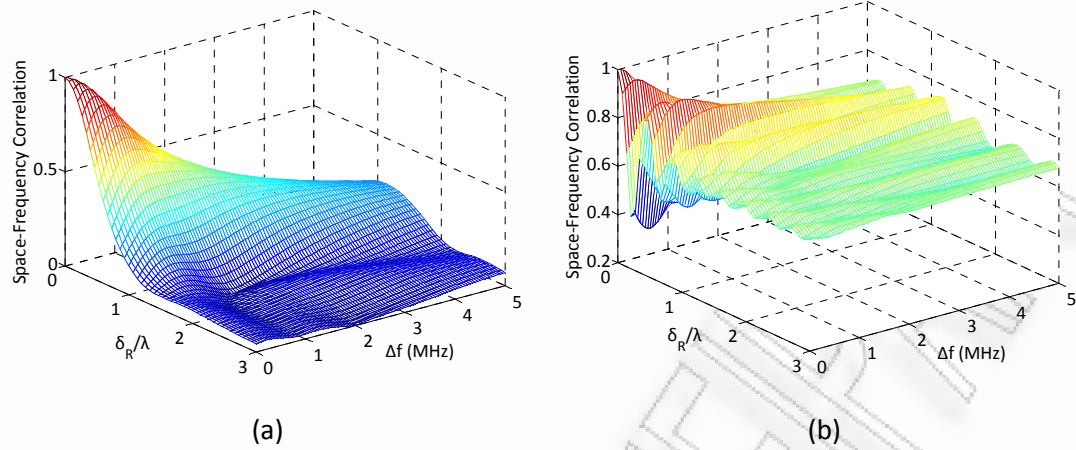


Figure 73: The receive SFCF of a 2×2 HAP-MIMO (a) Rayleigh and (b) Ricean channel.

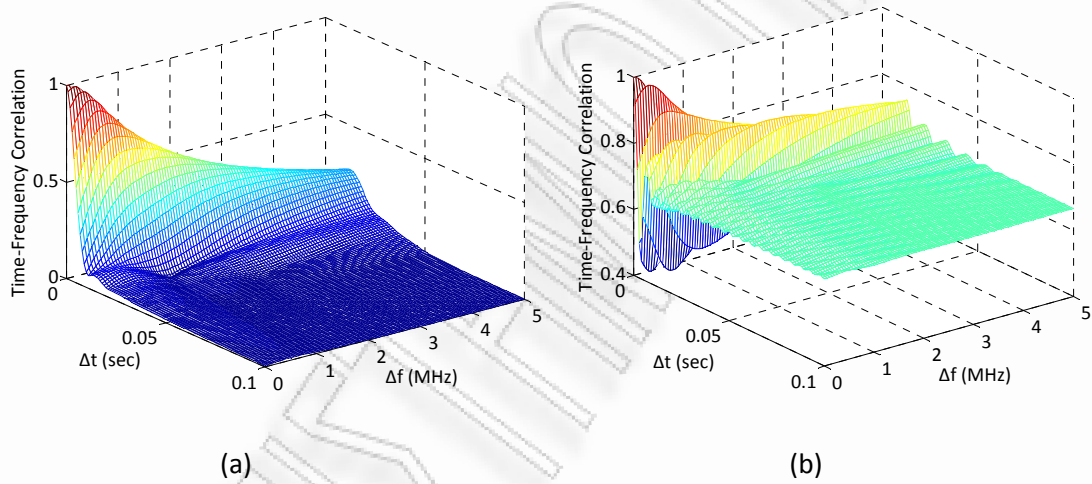


Figure 74: The TFCF of a HAP-SISO (a) Rayleigh and (b) Ricean channel.

Fig. 75 shows the SDPSs of a HAP-SISO Rayleigh channel and a 2×2 HAP-MIMO Rayleigh channel for a 3-D non-isotropic scattering environment. The values of the model parameters used are $K_{pl} = K_{qm} = 0$, $H_T = 20$ km, $\beta_T = 60^\circ$, $\delta_T = 80\lambda$, $\delta_R = \lambda$, $\theta_T = \theta_R = 45^\circ$, $\psi_R = 30^\circ$, $\alpha = 0.01$, $R_{S,\min} = 15$ m, $R_{S,\max} = 150$ m, $H_{S,\min} = 5$ m, $H_{S,\max} = 40$ m, $H_{S,\text{mean}} = 17.6$ m, $\beta_{S,\min} = \arctan(H_{S,\min} / R_{S,\max}) \approx 2^\circ$, $\beta_{S,\max} = \arctan(H_{S,\max} / R_{S,\min}) \approx 70^\circ$, $\sigma = 0.31$, $k = 3$, $\mu = 0^\circ$, $f_{T,\max} = 0$ Hz, $f_{R,\max} = 150$ Hz, and $\gamma_R = 30^\circ$. A normalized Doppler frequency $v_n = v / v_{\max}$ is used, such that $-1 \leq v_n \leq 1$. The results show that the SDPSs are similar to the

typical U-shaped spectrum of fixed-to-mobile cellular channels. These results also show that the SDPSs do not have any undesirable discontinuities⁸ and exhibit realistic finite⁹ values for the maximum Doppler frequencies.

Finally, Fig. 76 shows the relative PSDs of a HAP-SISO Rayleigh channel and a 2×2 HAP-MIMO Rayleigh channel for a 3-D non-isotropic scattering environment. The values of the model parameters used are $K_{pl} = K_{qm} = 0$, $H_T = 20$ km, $\beta_T = 60^\circ$, $\delta_T = 80\lambda$, $\delta_R = \lambda$, $\theta_T = \theta_R = 45^\circ$, $\psi_R = 10^\circ$, $a = 0.01$, $R_{S,\min} = 12$ m, $R_{S,\max} = 140$ m, $H_{S,\min} = 6$ m, $H_{S,\max} = 50$ m, $H_{S,\text{mean}} = 17.6$ m, $\sigma = 0.31$, $k = 8$, and $\mu = 90^\circ$. A normalized relative propagation delay $\tau_{r,n} = \tau_r / \tau_{r,\max}$ is used, such that $0 \leq \tau_{r,n} \leq 1$. To the author's best knowledge, there are no experimental data available in the literature to verify the theoretical results. Thus, the need for experimental verification data is pointed out to confirm the validity of this reference wideband HAP-MIMO channel model.

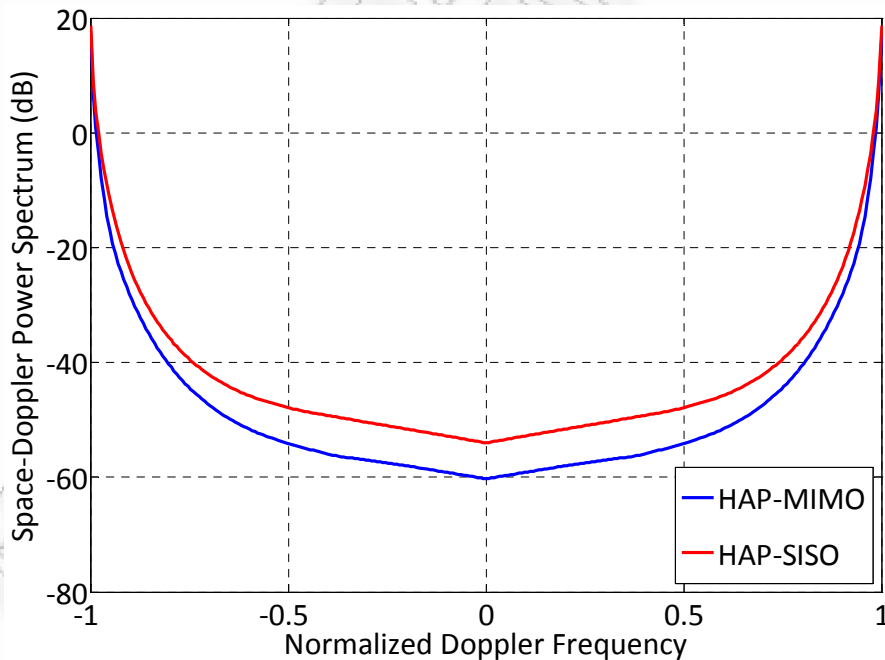


Figure 75: The SDPS of a HAP-SISO and a 2×2 HAP-MIMO Rayleigh channel.

⁸The Doppler spectrum obtained from the Aulin's 3-D model is constant for $f_{\max} \cos \beta_{\max} \leq |v| \leq f_{\max}$, where f_{\max} and β_{\max} are the maximum Doppler frequency and the maximum elevation angle of the scattered waves, respectively [195].

⁹The Doppler spectrum obtained from the Clarke's 2-D model becomes infinite at the maximum Doppler frequency [167].

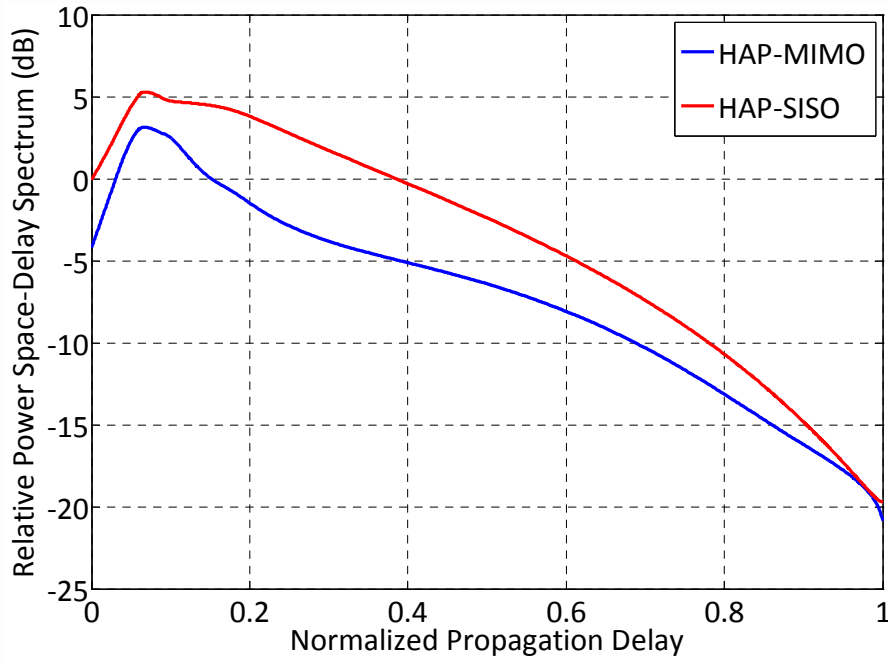


Figure 76: The relative PSDS of a HAP-SISO and a 2×2 HAP-MIMO Rayleigh channel.

5.5 Simulation Models for Wideband HAP-MIMO Channels

The reference wideband model described above assumes an infinite number of scatterers. Although this model is practically non-realizable, it can be used to derive simulation models, which have similar statistical properties as the reference model and utilize a finite (preferably small) number of scatterers. This section proposes deterministic and statistical simulation models for wideband HAP-MIMO channels.

Assuming a 3-D non-isotropic scattering environment and using the design method of HAP-MIMO simulation models described in Chapter 4, the following time-variant transfer function of the sub-channel p - l is proposed [199]

$$T'_{pl}(t, f) = T_{pl,LoS}(t, f) + T'_{pl,NLoS}(t, f), \quad (164)$$

where

$$T'_{pl,NLoS}(t, f) = \sqrt{\frac{\Omega_{pl}}{K_{pl} + 1}} \frac{1}{\sqrt{N_1 N_2 N_3}} \sum_{n_1=1}^{N_1} \sum_{n_2=1}^{N_2} \sum_{n_3=1}^{N_3} e^{j\phi^{(n_1, n_2, n_3)}} \times e^{\frac{-j2\pi}{\lambda} \left[d(p, s^{(n_1, n_2, n_3)}) + d(s^{(n_1, n_2, n_3)}, l) \right]} e^{j2\pi t (F'_{T, NLoS} + F'_{R, NLoS})} e^{-j2\pi f \tau_{NLoS}^{(n_1, n_2, n_3)}} \quad (165)$$

is the NLoS component of the time-variant transfer function, $T_{pl,LoS}(t, f)$ is defined in (109), $\varphi^{(n_1, n_2, n_3)} \in [-\pi, \pi)$ is the random phase, $d(p, S^{(n_1, n_2, n_3)})$, $d(S^{(n_1, n_2, n_3)}, l)$, $F'_{T, NLoS}$, and $F'_{R, NLoS}$ are defined in (66), (67), (68), and (69), respectively, $n_1 \in \{1, \dots, N_1\}$, $n_2 \in \{1, \dots, N_2\}$, $n_3 \in \{1, \dots, N_3\}$, the product $N_1 N_2 N_3 = N$ is the total finite number of scatterers and $\tau_{NLoS}^{(n_1, n_2, n_3)}$ is given by

$$\tau_{NLoS}^{(n_1, n_2, n_3)} \approx \tau_{LoS} + \frac{R_S^{(n_2)} \cos a_R^{(n_1)}}{c_0 \cos \beta_T} + \frac{R_S^{(n_2)}}{c_0 \cos \left[\arctan \left(H_S^{(n_3)} / R_S^{(n_2)} \right) \right]}. \quad (166)$$

Note that the input delay-spread function of the simulation models is obtained as the IFT of the time-variant transfer function in (164), i.e., $h'_{pl}(t, \tau) = \mathfrak{F}_f^{-1} \{T'_{pl}(t, f)\}$.

Providing that a sufficient number of scatterers is used, i.e., $N_1 N_2 N_3 \geq 20$, $T'_{pl, NLoS}(t, f)$ and $T'_{qm, NLoS}(t, f)$ are close to a low-pass zero-mean complex Gaussian process and the STFCF between $T'_{pl}(t, f)$, and $T'_{qm}(t, f)$ is given by (see Chapter 3)

$$R'_{pl, qm}(\delta_T, \delta_R, \Delta t, \Delta f) = R_{pl, qm}^{LoS}(\delta_T, \delta_R, \Delta t, \Delta f) + R'_{pl, qm, NLoS}(\delta_T, \delta_R, \Delta t, \Delta f), \quad (167)$$

where

$$\begin{aligned} R'_{pl, qm, NLoS}(\delta_T, \delta_R, \Delta t, \Delta f) &\approx \frac{1}{N_1 N_2 N_3 \sqrt{(K_{pl} + 1)(K_{qm} + 1)}} \sum_{n_1=1}^{N_1} \sum_{n_2=1}^{N_2} \sum_{n_3=1}^{N_3} e^{j \frac{2\pi(q-p)\delta_T \cos \theta_T}{\lambda \cos \beta_T}} \\ &\times e^{\frac{j2\pi(q-p)\delta_T \sin \theta_T R_S^{(n_2)} \sin a_R^{(n_1)}}{\lambda D \cos \beta_T}} e^{\frac{j2\pi(m-l)\delta_R \sin \nu_R \sin \left[\arctan \left(H_S^{(n_3)} / R_S^{(n_2)} \right) \right]}{\lambda}} \\ &\times e^{\frac{j2\pi(m-l)\delta_R \cos \theta_R \cos \nu_R \cos a_R^{(n_1)} \cos \left[\arctan \left(H_S^{(n_3)} / R_S^{(n_2)} \right) \right]}{\lambda}} \\ &\times e^{\frac{j2\pi(m-l)\delta_R \sin \theta_R \cos \nu_R \sin a_R^{(n_1)} \cos \left[\arctan \left(H_S^{(n_3)} / R_S^{(n_2)} \right) \right]}{\lambda}} \\ &\times e^{j2\pi\tau\Delta t (F'_{T, NLoS} + F'_{R, NLoS})} e^{-j2\pi\Delta f \left[\frac{D}{c_0 \cos \beta_T} + \frac{R_S^{(n_2)} \cos a_R^{(n_1)}}{c_0 \cos \beta_T} + \frac{R_S^{(n_2)}}{c_0 \cos \left[\arctan \left(H_S^{(n_3)} / R_S^{(n_2)} \right) \right]} \right]}. \end{aligned} \quad (168)$$

is the STFCF of the NLoS component and $R_{pl,qm}^{LoS}(\delta_T, \delta_R, \Delta t, \Delta f)$ is defined in (113).

To successfully approximate the statistical properties of the reference model, $a_R^{(n_1)}$, $R_S^{(n_2)}$, and $H_S^{(n_3)}$ must be properly determined.

First, a deterministic model is proposed. This model computes constant values for the model parameters, needs a single run to obtain the desired statistical properties and hence, preserves short simulation times. Based on the deterministic approach, $a_R^{(n_1)}$ can be generated using (72) and (75). Moreover, $R_S^{(n_2)}$ can be generated as

$$R_S^{(n_2)} = F_{T,R_S}^{-1}(\zeta'), \quad (169)$$

where

$$F_{T,R_S}(R_S) = \frac{F_{R_S}(R_S)}{F_{R_S}(R_{S,\max}) - F_{R_S}(R_{S,\min})} \quad (170)$$

is a truncated hyperbolic cdf applicable for the range $R_{S,\min} \leq R_S \leq R_{S,\max}$, $F_{R_S}(R_S)$ is defined in (60) and ζ' is defined in (76). Finally, $H_S^{(n_3)}$ can be generated as

$$H_S^{(n_3)} = F_{T,H_S}^{-1}(\xi'), \quad (171)$$

where

$$F_{T,H_S}(H_S) = \frac{F_{H_S}(H_S)}{F_{H_S}(H_{S,\max}) - F_{H_S}(H_{S,\min})} \quad (172)$$

is a truncated log-normal cdf applicable for the range $H_{S,\min} \leq H_S \leq H_{S,\max}$, $F_{H_S}(H_S)$ is defined in (63) and ξ' is defined in (77).

A statistical model is also proposed. The statistical properties of this model are stochastic for each simulation trial and converge to the theoretical statistical properties after averaging over a sufficient number of simulation trials for an arbitrary finite number of scatterers, i.e., for any $\{N_1, N_2, N_3\} \geq 1$. Considering that κ_1 , κ_2 , and κ_3 are independent random variables uniformly distributed in the

interval $[0,1)$, $a_R^{(n_1)}$ is generated using (88) and (91), while $R_S^{(n_2)}$ and $H_S^{(n_3)}$ are generated as

$$R_S^{(n_2)} = F_{T,R_S}^{-1}(\zeta^m), \quad (173)$$

$$H_S^{(n_3)} = F_{T,H_S}^{-1}(\xi^m), \quad (174)$$

where ζ^m and ξ^m are defined in (92) and (93), respectively. The STFCE of the statistical model is obtained after averaging $R'_{pl,qm}(\delta_T, \delta_R, \Delta t, \Delta f)$ over N_{trials} simulation trials

$$R''_{pl,qm}(\delta_T, \delta_R, \Delta t, \Delta f) = \frac{1}{N_{trials}} \sum_{n_{trials}=1}^{N_{trials}} R'_{pl,qm}(\delta_T, \delta_R, \Delta t, \Delta f). \quad (175)$$

It is obvious that the statistical model is more complex than the deterministic model due to the average procedure and the generation of three random variables. Hence, the number of the scatterers and the number of simulation trials should be carefully chosen to keep the complexity to a minimum.

5.5.1 Simulation Results

This subsection examines the performance of simulation models. The values of the model parameters used are $K_{pl} = K_{qm} = 0$ dB, $n_T = n_R = 2$, $\Delta f = 200$ Hz, $H_T = 20$ km, $\beta_T = 60^\circ$, $\delta_T = 60\lambda$, $\delta_R = \lambda/2$, $\theta_T = 60^\circ$, $\theta_R = 30^\circ$, $\psi_R = 20^\circ$, $k = 4$, $\mu = 90^\circ$, $\alpha = 0.01$, $R_{S,max} = 140$ m, $H_{S,max} = 60$ m, $H_{S,mean} = 17.6$ m, $\sigma = 0.31$, $f_{T,max} = 0$ Hz, $f_{R,max} = 100$ Hz, and $\gamma_R = 60^\circ$. Moreover, a normalized sampling period $f_{R,max} T_S = 0.02$ is used, where T_S is the sampling period.

Fig. 77 compares the absolute STFCEs of the reference and simulation models. One observes that the STFCE of the deterministic model closely matches the reference one for $N_1 = 30$, $N_2 = 20$, and $N_3 = 8$, while the statistical model almost perfectly reproduces the theoretical STFCE for $N_1 = 10$, $N_2 = 8$, $N_3 = 3$, and

$N_{trials} = 40$. From the results, the RMSE between the STFCFs of the deterministic and the reference model is 0.031 for $N_1 = 30$, $N_2 = 20$, and $N_3 = 8$, and 0.027 for $N_1 = 40$, $N_2 = 30$, and $N_3 = 10$. Hence, increasing the number of scatterers, enhances the performance of the deterministic model. Finally, the RMSE between the STFCFs of the statistical and the reference model is 0.019 for $N_{trials} = 40$ and 0.014 for $N_{trials} = 60$. Thus, increasing the number of trials, improves the performance of the statistical model.

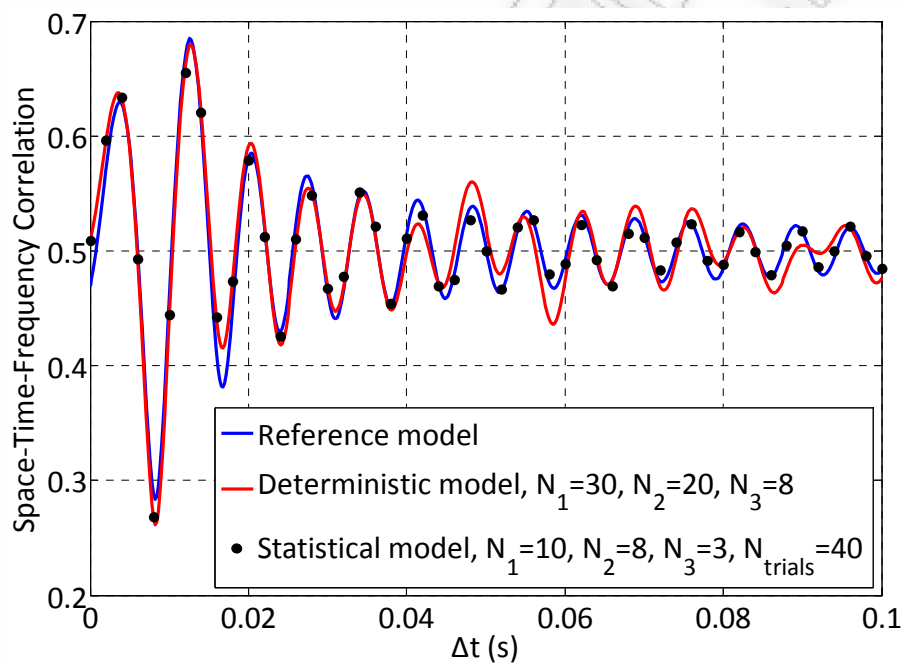


Figure 77: Comparison between the STFCFs of the reference and the simulation models.

5.6 Summary

In this chapter, a theoretical parametric model for wideband Ricean HAP-MIMO channels has been proposed to completely characterize HAP-MIMO multipath fading channels. In particular, the narrowband 3-D HAP-MIMO channel model has been extended to the wideband channel scenario with respect to frequency selectivity. Several parameters related to the physical properties of wideband stratospheric communications have been considered, in order to properly and thoroughly characterize the wideband HAP-MIMO channels. Based on the

proposed model the channel statistics have been analytically studied. Specifically, the STFCF, the SDPS, and the PSDS have been derived, under a 3-D non-isotropic scattering environment. Useful numerical results have been provided and the need for further experimental verification data has been pointed out. Future empirical results could be easily be compared with theoretical results, since the proposed model is flexible and applicable to a wide range of propagation environments, i.e., one may choose proper values for the model parameters to fit a particular environment.

The reference model assumes an infinite number of scatterers and proves to be too complex. Therefore, realizable simulation models are essential to faithfully reproduce its statistical properties. Based on the SoS principle, deterministic and statistical simulation models for wideband HAP-MIMO channels have been developed. The statistical properties of these simulation models have been verified by comparison with the corresponding statistical properties of the reference model. The results have shown that the proposed simulation model satisfactorily approximate the STFCF of the reference model and have nearly the same statistics as the reference model, while keeping the complexity to a minimum.

Overall, the proposed models are applicable to a variety of propagation environments and scenarios, and provide helpful insights and a useful framework for analyzing, designing, optimizing, and testing emerging wideband HAP-MIMO mobile communications systems, under LoS and NLoS conditions, in frequencies well below 10 GHz.

Nowadays, as the telecommunication market is driven by the increasing demand for broadcast services and high-speed ubiquitous Internet access, BFWA is gaining increased popularity. Nevertheless, frequency bandwidths wide enough to carry such services are only available at mm-wave frequency bands. MIMO technology may enhance BFWA networks, although signal propagation is severely affected by rainfall in mm-wave frequencies. Hence, Chapter 6 investigates the application of MIMO techniques to fixed HAP-based systems at Ka- and V- bands.

Chapter 6

Modeling of Line-of-Sight HAP-MIMO Channels

6.1 Introduction

Apart from providing mobile communications services, HAPs can also serve as base stations for the provision of BFWA services at the licensed Ka- and V-frequency bands. The growing exigencies for spectral efficiency and improved channel capacity have prompted the development of advanced physical layer theory and techniques. Hence, such theory and techniques should be applied, evolved and/or originated in order to construct high-performance HAP-based fixed communications systems. Previous studies investigated V-MIMO techniques based on constellations of multiple HAPs that intend to provide BFWA services at mm-wave frequency bands [200]-[202]. As MIMO technology is nowadays deemed a necessity due to its potentially high-bandwidth efficiency, whether the size of a single HAP can effectively exploit MIMO advantages at the licensed Ka- and V-frequency bands is an open research issue. Specifically, at these frequencies, the propagation characteristics are drastically different compared to those observed in frequencies well below 10 GHz, i.e., L- and S- bands. Therefore, new wireless system design approaches at the physical layer and realistic HAP-MIMO channel models are required.

As shown in Chapter 3, the MIMO gain strongly depends on the channel characteristics, which are mainly determined by the antenna configuration and the richness of scattering at frequencies well below 10 GHz. Indeed, the MIMO research has been initiated by the mathematical derivation of the MIMO channel capacity assuming Rayleigh i.i.d. fading [68], [69]. However, propagation at mm-wave bands requires a strong, dominant LoS signal for sufficient coverage due to the severe attenuation of the NLoS links [11], [37]. Conceptually, this corresponds

to a rank-deficient¹⁰ MIMO channel matrix and low spectral efficiency due to the increased spatial correlation introduced by the linear relationship of the phases of the received signals [203], [204]. Contrary to these observations, a number of studies have suggested that the LoS response is not inherently correlated and have shown the possibility of getting high MIMO gain for LoS channels by preserving the orthogonality of the received signals [205]-[208]. In detail, using specifically designed antenna arrays, i.e., placing the antenna elements in positions, where the LoS rays are orthogonal, a full-rank MIMO channel may be achieved.

In this chapter, geometrical design recommendations are introduced and the applicability of MIMO techniques to LoS-HAP channels with propagation models for the Ka- and V- frequency bands is investigated [88]. The parameters of interest are the height and the elevation angle of the platform, the carrier frequency, and the array configuration. Since rain has an important impact on the quality of the link at mm-wave frequencies [11], both clear sky and rain conditions should be considered. The results show that the proposed design method overcomes the problem of reduced capacity in LoS conditions and outperforms the conventional rank-one LoS architecture in terms of channel capacity. These results also show that the optimized scheme actually performs better than MIMO schemes based on Rayleigh i.i.d. fading. The sensitivity to possible deviation of the values of the parameters chosen to satisfy the optimal design constraints is also investigated. Thus, a deviation factor is introduced and an analysis of the sensitivity to non-optimal design with regard to channel capacity is performed.

The remainder of this chapter is organized as follows. The LoS-HAP-MIMO system model and the corresponding geometrical model are described in Section 6.2, while the maximum capacity criteria are derived in Section 6.3. Section 6.4 demonstrates the theoretical derivations by comparing the performance of different architectures, under clear sky and rain conditions, and investigating the sensitivity of the capacity performance. Finally, Section 6.5 summarizes this chapter.

¹⁰ Rank-deficient channel matrix brings correlations between MIMO subchannels and, hence, is incapable of supporting many multiple parallel data streams.

6.2 The LoS-HAP-MIMO System Model

The system model employed throughout this chapter considers a SBS and a terrestrial fixed station (TFS) utilizing ULAs with n_T transmit and n_R receive antenna elements, respectively. All antennas are fixed, highly directional¹¹ and are numbered as $1 \leq p \leq q \leq n_T$ and $1 \leq l \leq m \leq n_R$, respectively. Considering slowly varying and frequency-flat fading channels over the band of interest, the link between the SBS and TFS antenna arrays is represented using the complex baseband vector notation

$$\mathbf{r} = \sqrt{G}\mathbf{H}\mathbf{s} + \mathbf{n}, \quad (176)$$

where $\mathbf{s} \in \mathbb{C}^{n_T \times 1}$ is the transmitted signal vector, $\mathbf{r} \in \mathbb{C}^{n_R \times 1}$ is the received signal vector, $\mathbf{H} = [h_{ij}]_{n_R \times n_T} \in \mathbb{C}^{n_R \times n_T}$ is the channel matrix of complex channel gains, and $\mathbf{n} \in \mathbb{C}^{n_R \times 1}$ is the noise vector, which denotes the AWGN at the receiver branches. Moreover, G is the common power gain over the channel and is given by

$$G = G_T (\text{dBi}) + G_R (\text{dBi}) - L_f (\text{dB}) - L_r (\text{dB}), \quad (177)$$

where G_T and G_R are the transmit and receive antenna gains, respectively, L_f is the FSL, and L_r is the rain attenuation. Finally, the entries of the noise vector are i.i.d. complex Gaussian random variables with zero mean and variance N_0 , where N_0 is the noise PSD. It is assumed that all the subchannels experience the same path loss due to the significant distance between SBS and TFS. This common path loss is incorporated in the G factor.

As the propagation environment is related to BFWA in mm-wave frequencies, the multipath propagation due to local scatterers in the vicinity of TFS is neglected and \mathbf{H} corresponds to a pure LoS channel, under clear sky conditions. However, rain introduces not only severe attenuation but also a short-term variation to the

¹¹Since it is more difficult to generate power at the susceptible to propagation impairments Ka/V bands than at the lower L/S bands, omni-directional antennas are essentially not applicable. Thus, it is easier to realize highly directive antennas, which can increase the fade margin by adding more gain, and improve the link availability.

received signal. In [209], a wideband 200 MHz measurement campaign was conducted in a campus environment for short terrestrial 38-GHz BFWA links, where LoS conditions, fixed reception, high antenna directivity, and vertical polarization were maintained. An important conclusion that is drawn from this experiment was that multipath was observed even in unobstructed LoS links during rain but not observed during clear sky conditions. Hence, the MIMO channel matrix \mathbf{H} is given by

$$\mathbf{H} = \sqrt{\frac{K_r}{K_r + 1}} \mathbf{H}_{LoS} + \sqrt{\frac{1}{K_r + 1}} \mathbf{H}_{NLoS}^r, \quad (178)$$

where \mathbf{H}_{LoS} is a deterministic $n_R \times n_T$ matrix containing the non-fading LoS responses between all array elements, \mathbf{H}_{NLoS}^r is a stochastic $n_R \times n_T$ matrix containing the responses of the scattered waves due to rain, and K_r is the Ricean factor, which directly refers to the rainy conditions, i.e., it incorporates the channel dynamics as a result of radiowave propagation through the rainfall medium. Note that the channel matrix \mathbf{H} is normalized, which means that its elements have an average power of one. This normalization corresponds to a system with perfect power control [210] and makes the SNR independent of \mathbf{H} . Considering free-space propagation, the normalized matrix \mathbf{H}_{LoS} is given by

$$\mathbf{H}_{LoS} = \begin{bmatrix} h_{11,LoS} & h_{12,LoS} & \cdots & h_{1n_T,LoS} \\ h_{21,LoS} & \ddots & & \vdots \\ \vdots & & \ddots & \vdots \\ h_{n_R,1,LoS} & \cdots & & h_{n_R,n_T,LoS} \end{bmatrix} = \begin{bmatrix} e^{-j2\pi d(1,1)/\lambda} & e^{-j2\pi d(1,2)/\lambda} & \cdots & e^{-j2\pi d(1,n_T)/\lambda} \\ e^{-j2\pi d(2,1)/\lambda} & \ddots & & \vdots \\ \vdots & & \ddots & \vdots \\ e^{-j2\pi d(n_R,1)/\lambda} & \cdots & & e^{-j2\pi d(n_R,n_T)/\lambda} \end{bmatrix}, \quad (179)$$

where $h_{ij,LoS} = e^{-j2\pi d(i,j)/\lambda}$ is the complex response between the i^{th} receive and the j^{th} transmit antenna element, $d(i,j)$ is the distance between these two elements,

and λ is the carrier wavelength. Hence, the elements of \mathbf{H}_{LoS} depend only on the distances between the SBS and TFS antenna elements. These distances can be estimated by applying ray-tracing¹² techniques to the geometrical model in Fig. 75. The scattering introduced by rain can be modeled as a stochastic process [88], [208]. Therefore, the entries of \mathbf{H}'_{NLoS} are modeled as i.i.d. random variables (Rayleigh fading). Finally, the Ricean factor K_r is given by [209]

$$K_r(\text{dB}) = \begin{cases} 16.88 - 0.04R_r \text{ dB}, & R_r \neq 0 \\ \infty & \text{dB}, R_r = 0 \end{cases} \quad (180)$$

This empirical relationship between the Ricean factor K_r (in dB) and the rainfall rate R_r (in mm/h) is elevation-, frequency-, polarization-, climate-, and site-specific. Although an analytical prediction model for the CDF of the Rician factor can incorporate the mathematically intractable physical input of rain fading into the Rician channel model (see [211]) on a global scale, this chapter adopts the simplified expression in (180) to make the analysis traceable and the design less complex.

6.2.1 A Geometrical Model for LoS-HAP-MIMO Channels

The geometrical characteristics of the proposed model for a 2×2 LoS-HAP-MIMO channel with $n_T = n_R = 2$ antenna elements and the definition of the Cartesian coordinate system are discussed in Fig. 78. The x -axis is the line that connects the sub-platform point \tilde{p} and the TFS antenna element l , while the z -axis is the line that connects the sub-platform point \tilde{p} and the SBS antenna element p . The spacing between SBS and TFS antenna elements is denoted δ_T and δ_R , respectively. In addition, angles θ_T and θ_R represent the orientation of the SBS and TFS antenna arrays, respectively, while β_T , H_T , H_R , and H_r denote the elevation angle of SBS, the height of SBS, the height of TFS, and the effective rain height, respectively.

¹²Ray-tracing is based on finding the path length from each of the SBS antennas to each of the TFS antennas, and employing these path lengths to find the corresponding received phases.

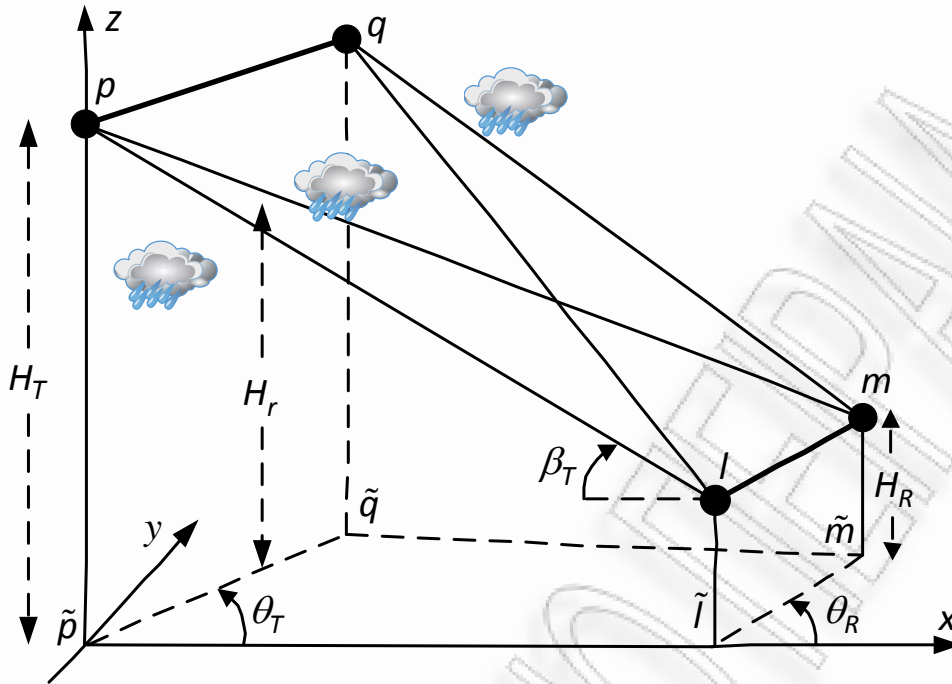


Figure 78: A geometrical model for a 2×2 LoS-HAP-MIMO channel.

6.3 Capacity Optimization Techniques

Using (179), the correlation matrix of the LoS component is equal to

$$\mathbf{H}_{LoS} \mathbf{H}_{LoS}^H = \begin{bmatrix} n_T & \dots & \sum_{j=1}^{n_t} e^{-j2\pi[d(1,j)-d(n_R,j)]/\lambda} \\ \vdots & \ddots & \vdots \\ \sum_{j=1}^{n_t} e^{-j2\pi[d(n_R,j)-d(1,j)]/\lambda} & \dots & n_T \end{bmatrix}. \quad (181)$$

Moreover, using the definition of HAP-MIMO channel capacity in (47) and considering clear sky conditions, the minimum capacity is obtained for

$$\mathbf{H}_{LoS} \mathbf{H}_{LoS}^H = n_T \mathbf{1}_{n_R}, \quad (182)$$

where $\mathbf{1}_{n_R}$ is an $n_R \times n_R$ all-ones matrix. Then, the channel matrix \mathbf{H}_{LoS} is rank-one (entirely correlated) and the capacity is equal to that of a SIMO channel [212], i.e., no multiplexing gain is obtained

$$C_{\min} = \log_2(1 + n_R \text{SNR}). \quad (183)$$

On the contrary, the maximum capacity is obtained for

$$\mathbf{H}_{LoS} \mathbf{H}_{LoS}^H = n_T \mathbf{I}_{n_R}, \quad (184)$$

where \mathbf{I}_{n_R} is an $n_R \times n_R$ identity matrix. Then, \mathbf{H}_{LoS} is full-rank and the MIMO subchannels are perfectly orthogonal. In addition, the capacity is equivalent to that of n_R independent SISO channels as follows

$$C_{\max} = n_R \log_2(1 + \text{SNR}). \quad (185)$$

Considering a 2×2 LoS-HAP-MIMO channel, the normalized channel matrix \mathbf{H}_{LoS} can be written as

$$\mathbf{H}_{LoS} = \begin{bmatrix} h_{pl,LoS} & h_{pm,LoS} \\ h_{ql,LoS} & h_{qm,LoS} \end{bmatrix}. \quad (186)$$

Then, the maximum capacity criterion is simplified as follows

$$\begin{aligned} \mathbf{H}_{LoS} \mathbf{H}_{LoS}^H &= 2\mathbf{I}_2 \\ \Rightarrow \begin{bmatrix} 2 & A_{LoS} \\ A_{LoS}^* & 2 \end{bmatrix} &= 2\mathbf{I}_2, \end{aligned} \quad (187)$$

where

$$A_{LoS} = e^{-j2\pi[d(l,p)-d(m,p)]/\lambda} + e^{-j2\pi[d(l,q)-d(m,q)]/\lambda}. \quad (188)$$

The solution to (188) can be written as [182]

$$\begin{aligned} 2\pi[d(l,p)-d(m,p)-d(l,q)+d(m,q)]/\lambda &= (2\nu+1)\pi \\ \Rightarrow d(l,p)-d(m,p)-d(l,q)+d(m,q) &= (2\nu+1)\lambda/2, \end{aligned} \quad (189)$$

where $\nu \in \mathbb{Z}$ and \mathbb{Z} represents a set of integers. As shown in Appendix B, from (189) one can easily derive the simplified 2×2 LoS-HAP-MIMO maximum capacity criterion in pure LoS as a function of δ_T , δ_R , θ_T , θ_R , β_T , H_T , and λ as follows

$$\delta_T \delta_R \approx (2\nu + 1) \frac{\lambda H_T}{2 \sin \beta_T \sin \theta_T \sin \theta_R}, \quad \{\beta_T, \theta_T, \theta_R\} \neq 0^\circ. \quad (190)$$

Physically, the approximate maximum capacity criterion corresponds to systems where the sum of the path differences is an odd integer multiple of a half wavelength. The product between δ_T and δ_R is the key design quantity on the part of maximizing the channel capacity and leads to a versatile system design, i.e., maximum capacity can be achieved using small array sizes at one end of the link and large array sizes at the other end. This product is referred to as the antenna elements spacing product (AESP). The criterion in (190) for a 2×2 LoS-HAP-MIMO channel can be extended to the case of a $n_R \times n_T$ LoS-HAP-MIMO channel with an arbitrary number of antenna elements. As shown in Appendix B, the $n_R \times n_T$ LoS-HAP-MIMO design criterion to achieve maximum channel capacity can be expressed as follows

$$\delta_T \delta_R \approx \left(\frac{1}{n_T} + \nu \right) \frac{\lambda H_T}{\sin \beta_T \sin \theta_T \sin \theta_R}, \quad \{\beta_T, \theta_T, \theta_R\} \neq 0^\circ. \quad (191)$$

From (191), one observes that the required AESP reduces with increasing n_T . Hence, high space efficiency at the SBS is obtained, i.e., smaller spacing per element at the SBS antenna array can be adjusted and a large number of elements can be accommodated. This enables the utilization of multiple antenna elements at the SBS without the problems of mutual coupling [213] and correlation [97], [98], while the performance does not depend on the existence of a rich scattering environment as in the case of the traditional MIMO. In addition, although a strong LoS signal is considered, the capacity linearly increases with increasing n_T .

6.3.1 Practical Considerations

From (190) and (191), one observes that considerable antenna spacing is needed to introduce phase differences among antennas when operating MIMO system in LoS environment. Hence, the solution corresponding to the smallest AESP is

probably the most interesting from a practical and realistic design point of view, because it requires the shortest antenna arrays. Equations (190) and (191) imply that the minimum AESP is obtained for broadside antenna array orientation, i.e., $\theta_T = \theta_R = 90^\circ$, and for location of the SBS just above TFS, i.e., $\beta_T = 90^\circ$. Note that HAPs are either airships (of about 150-200 m in length) or circling aircrafts (approximately 30 m in length) [11], [12]. Hence, based on the HAP structure used and the available HAP length, the spacing between TFS antenna elements can be ideally adjusted to satisfy (190). For instance, assuming that $\nu = 0$, $H_T = 20$ km (typical HAP height), $\beta_T = 60^\circ$ (typical value in urban environments), $\theta_T = \theta_R = 90^\circ$, and considering signal transmission at 28 GHz and 48 GHz, the required AESP is equal to approximately 124 and 72, respectively. This suggests that applying LoS-HAP-MIMO techniques to a single HAP (aircraft or airship) and a typical TFS, i.e., installing multiple antenna elements at the roof of a building, is viable. In addition, the significantly small distance between the antenna elements ensures identical atmospheric impairments for all the signals propagating to the same TFS array, i.e., the propagation is realized through the same rainfall medium for all the antenna elements at the TFS. However, as θ_T and θ_R decrease, the required AESP increases, e.g., the AESP redoubles, when $\theta_T = \theta_R = 45^\circ$. In the worst case, in which $\{\theta_T, \theta_R\} \rightarrow 0^\circ$, very large non-practical antenna spacing at the TFS and/or utilization of multiple HAPs may be required. Note that using very large antenna spacing at the SBS/TFS introduces propagation delay offsets, which may lead to synchronization problems. These problems do not occur in conventional terrestrial MIMO systems, where the multiple transmitted signals are simultaneously received [214] and the inter-element distances are usually equal to a half wavelength.

6.4 Numerical Results

This section investigates the performance of the proposed design recommendations for a 2×2 LoS-HAP-MIMO system. As mentioned in the previous

section, capacity optimized LoS-HAP-MIMO techniques are feasible in a single HAP, if the TFS antenna inter-element spacing is carefully arranged. Using (190) and considering that $\nu = 0$, $H_T = 20$ km, $\beta_T = 80^\circ$, and $\theta_T = \theta_R = 90^\circ$, the required AESP is approximately 63.4 and 108.8 for the 48 and the 28 GHz frequency band, respectively. Thus, assuming that the TFS could be a subscriber unit (SU) in an outdoor position and considering that SBS antenna inter-element spacing is fixed and equal to $\delta_T = 30$ m, the TFS antenna inter-element spacing is set $\delta_R = 2.11$ m, and $\delta_R = 3.63$ m, respectively.

Fig. 79 examines the effect of the array design on the ergodic capacity, under clear sky conditions, i.e., $R_r = 0$. In order to remove the effects of the average SNR on the channel capacity, the channel response is normalized so that the constraint in (55) is fulfilled. Specifically, the full-rank and rank-one 2×2 LoS-HAP-MIMO capacity, as well as the LoS-HAP-SISO capacity are plotted against SNR, in order to compare the performance of different architectures. Moreover, the 2×2 MIMO Rayleigh i.i.d. capacity (evaluated after a large number of channel realizations) against SNR is plotted, for reference. Note that there is a substantial gain of the full-rank 2×2 LoS-MIMO architecture over the rank-one 2×2 LoS-HAP-MIMO and LoS-HAP-SISO architectures and the capacity dramatically increases up to 8.5 and 9.5 bps/Hz, respectively. Hence, the rank-one scenario validates the common belief that a strong LoS signal results in poor capacity gain. One observes that the optimized 2×2 LoS-HAP-MIMO design can offer better performance than the Rayleigh i.i.d. 2×2 MIMO system and the capacity increases up to 1.4 bps/Hz. Hence, using multiple elements at both SBS and TFS, under LoS conditions and design constraints, can effectively boost channel capacity.

Fig. 80 shows the CCDF of the channel capacity for full-rank and rank-one LoS-HAP-MIMO architectures under the effect of rain, i.e., $R_r \neq 0$, using the propagation model described in Chapter 2 and the 28 GHz frequency band. According to (178) and (180) the channel becomes Ricean for rain rates greater than zero. In addition, the SNR depend on the rain rate. A set of realistic parameter

values are chosen to produce the results. Most of these values are found in [215] and are reproduced for convenience in Table 12 together with all the parameters employed. Considering horizontally polarized waves, the 30 GHz frequency band corresponds to $a_r = 0.187$ and $b_r = 1.021$ [82] (see Chapter 2). Then, using (7) and (180), and assuming that R_r takes values 12, 28 and 42 mm/h and the rain height is 3.5 km, the corresponding L_r and K_r approximated values are 8.3, 19.6, and 29.7 dB, and 16.4, 15.8, and 15.2 dB, respectively. Using (1)-(3), (177) the corresponding SNR values are 25.9, 14.6, and 4.5 dB, respectively. Note that increasing rain rate decreases the SNR and increases the influence of \mathbf{H}_{NLoS}^r . Since \mathbf{H}_{NLoS}^r is full-rank, increasing rain rate, degrades the capacity gain of full-rank 2×2 LoS-HAP-MIMO architecture over rank-one 2×2 LoS-HAP-MIMO architecture. Specifically, one observes that for over 50% of the channels, the capacity is greater than 16.7 and 12.7 bits/Hz for the full-rank and rank-one LoS-HAP-MIMO systems, respectively, for 12 mm/h rain rate, greater than 9.3 and 6.5 bits/Hz, respectively, for 28 mm/h rain rate, and greater than 3.6 and 2.8 bits/Hz, respectively, for 42 mm/h rain rate.

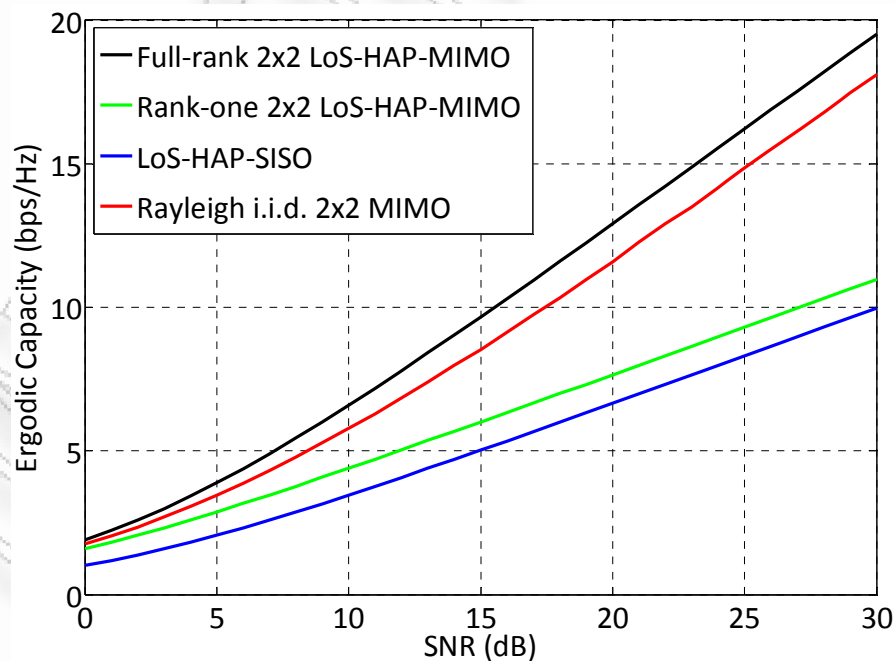


Figure 79: Comparison of the channel ergodic capacities obtained using the full-rank and rank-one 2×2 LoS-HAP-MIMO, the LoS-HAP-SISO, and the Rayleigh i.i.d. 2×2 MIMO architectures, under clear sky conditions.

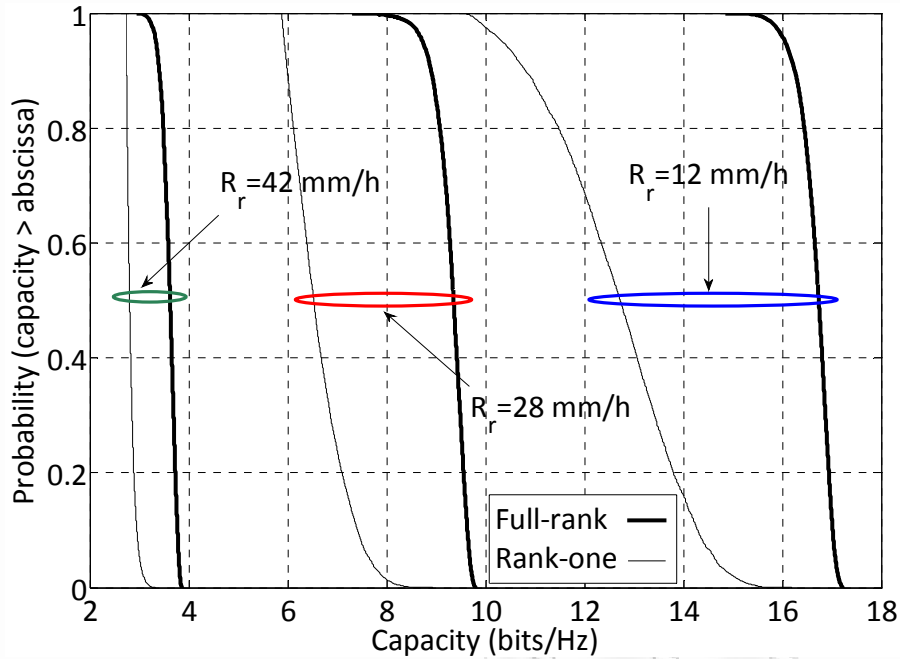


Figure 80: The complementary cumulative distribution function of the channel capacity achieved with the full-rank and rank-one 2×2 LoS-HAP-MIMO architectures for different rain rates.

TABLE 12
LINK BUDGET PARAMETERS

Frequency (f)	28 GHz	48 GHz
Free space loss (L_F)	147.4 dB	152 dB
Bandwidth (B)	20 MHz	
HAP transmit power (P_T)	-15 dBW	
HAP antenna gain (G_T)	34 dBi	
SU antenna gain (G_R)	34 dBi	
Noise Temperature (T_e)	500 K	
Noise PSD (N_0)	-201.6 dBW/Hz	
Noise power (P_N)	-128.6 dBW	

Fig. 81 shows the ergodic capacity against rain rate obtained using the optimized full-rank 2×2 LoS-HAP-MIMO architecture and compares the 28 GHz and the 48

GHz frequency bands. According to [82] and considering horizontally polarized waves, the 50 GHz frequency band corresponds to $a_r = 0.537$ and $b_r = 0.873$. One observes that the 48 GHz frequency band is more susceptible to rain attenuation, and as the rain rate increases from 0 mm/h (clear sky) to 80 mm/h, the ergodic capacity sharply degrades compared to the ergodic capacity achieved at the 28 GHz frequency band.

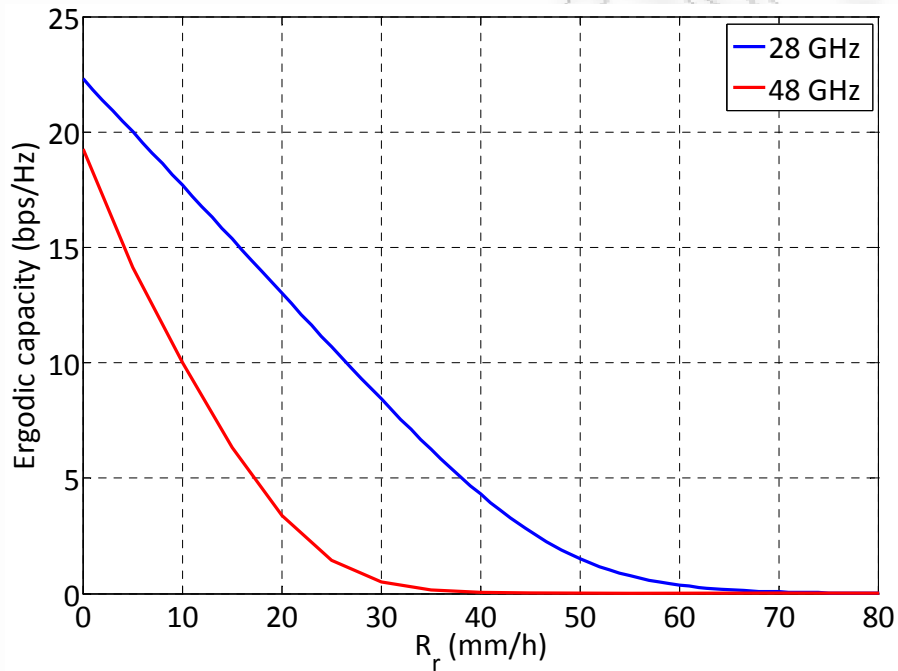


Figure 81: The ergodic capacity obtained using the full-rank 2×2 LoS-HAP-MIMO architecture as a function of the rain rate for different carrier frequency.

6.4.1 Sensitivity Study

The maximum capacity criterion corresponds to very specific array geometries fixed at optimal locations. In this section, the sensitivity of the optimized LoS-HAP-MIMO systems to deviations from the optimal AESP value in (191) is studied. For this purpose, the deviation factor η is introduced, which is defined as the ratio between the actual AESP and the optimal AESP

$$\eta \triangleq \frac{\text{AESP}_{\text{actual}}}{\text{AESP}_{\text{optimal}}} = \frac{\delta_T^{\text{actual}} \delta_R^{\text{actual}} \sin \beta_T \sin \theta_T \sin \theta_R}{(1/n_T + \nu) \lambda H_T}. \quad (192)$$

From (192), one observes that if the deviation factor is smaller than one, the actual AESP is too small compared to the optimal value, while a deviation factor larger than unity indicates that the actual AESP is too large. Indeed, the optimal AESP may be too large for practical systems. To examine this sensitivity to non-optimal design, the capacity is now evaluated in terms of the variation of the deviation factor defined in (192) for SNR = 20 dB. From Fig. 82, a large sensitivity (in terms of capacity) to the deviation factor is observed. In detail, the channel capacity is seen to vary between the minimum (7.65 bps/Hz) and the maximum (13.32 bps/Hz) values. This sensitivity needs to be taken into account in the design and fixing of LoS-HAP-MIMO communications systems.

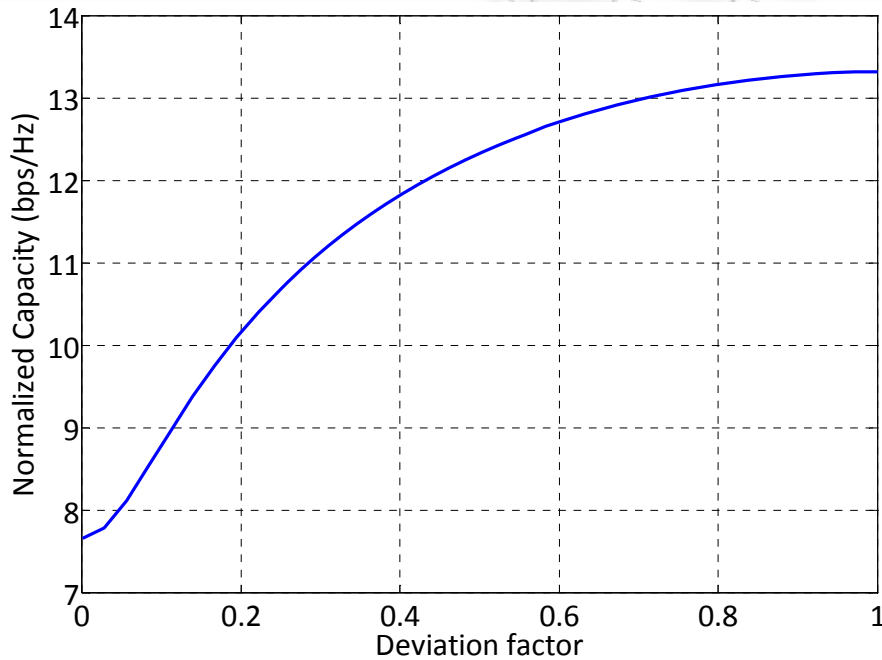


Figure 82: The normalized capacity obtained using the full-rank 2×2 LoS-HAP-MIMO architecture as a function of the deviation factor.

In practical situations, the parameters β_T , θ_T , and θ_R in (190) and (191) may be difficult to be determined with sufficient accuracy. Moreover, there is usually a need for high capacity over an area, rather than to a fixed point, while the stratospheric winds may vary the position of the platform. Hence, a compromise may be required, under more realistic deployment and propagation conditions or

imperfectly positioned arrays. The sensitivity of the performance to the orientation and positioning of the arrays is discussed and evaluated in the following figures.

Fig. 83 demonstrates the channel capacity for different orientation of the SBS antenna array. The capacity is evaluated for $\text{SNR}=20$ dB, $\beta_T = \theta_R = 90^\circ$ and $0 < \theta_T \leq 90^\circ$. According to Fig. 83, decreasing θ_T from 90° to 45° has an insignificant effect on the capacity, while a further decrease in θ_T drastically decreases the capacity. Hence, the results show a large sensitivity (in terms of capacity) to the orientation of the arrays. From (190) and (191), it is clear that the same results apply for $0 < \theta_R \leq 90^\circ$ and $0 < \beta_T \leq 90^\circ$.

Finally, Fig. 84 examines the sensitivity of the performance to SBS (or TFS) array shifting from the optimal point and demonstrates the influence of up to 20 km shifting along either x- or y-axis on the channel capacity for $\text{SNR}=20$ dB. One observes that the capacity is relatively insensitive to shifting along x- or y-axis. In particular, for a maximum shifting of 20 km, the capacity is only 3.3% and 2.2% lower than the maximum capacity, respectively.

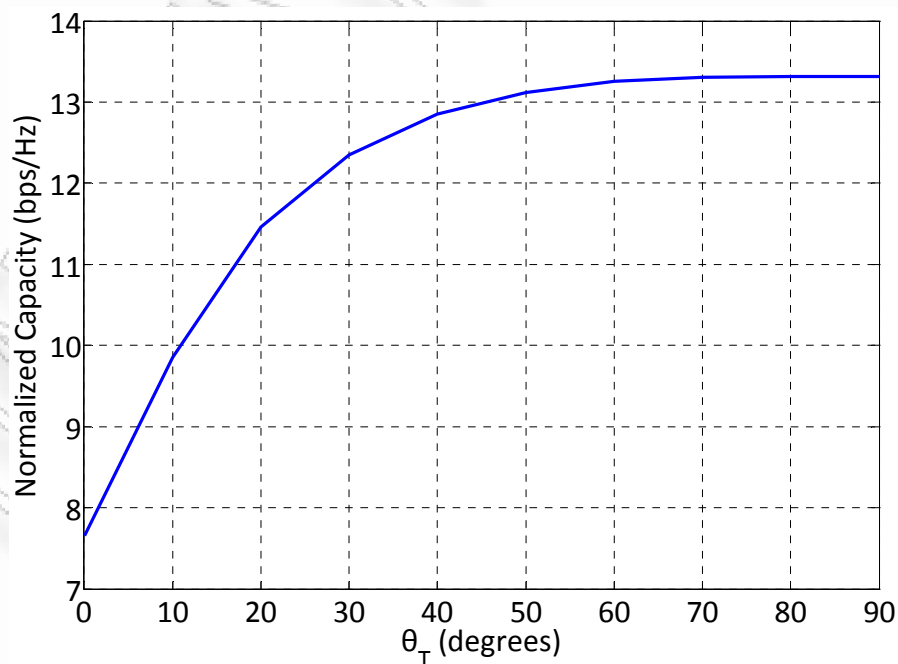


Figure 83: The normalized capacity obtained using the full-rank 2×2 LoS-HAP-MIMO architecture for different orientation of the SBS antenna array.

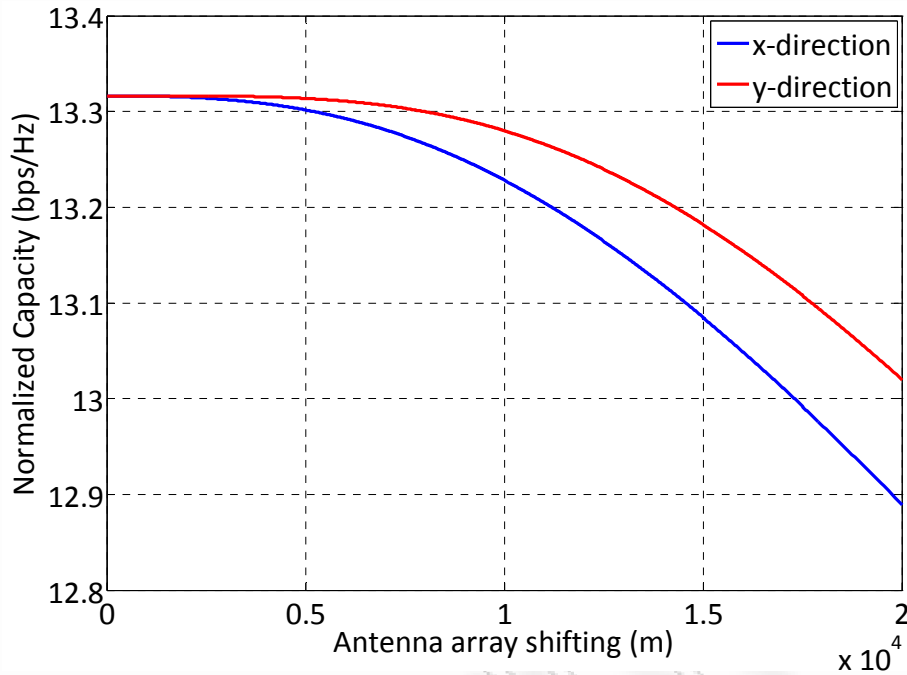


Figure 84: The normalized capacity obtained using the full-rank 2×2 LoS-HAP-MIMO architecture as a function of the antenna array shifting from the optimal point.

6.5 Summary

In this chapter, a method to achieve orthogonality between spatially multiplexed signals in LoS channels of HAP-MIMO systems employed with ULAs has been theoretically derived. In particular, antenna array design recommendations have been introduced, in order to construct a full-rank HAP-MIMO channel matrix at Ka and V frequency bands. Providing that the system parameters are carefully selected, the results have demonstrated the substantial benefits of the proposed architecture and have also illustrated the impact of real world effects, such as rain attenuation and scattering and array length constraints, on the performance. The optimized LoS-HAP-MIMO architecture outperforms the conventional rank-one LoS-HAP-MIMO and the Rayleigh i.i.d. MIMO architectures, in terms of channel capacity, under clear sky and rain conditions. However, the capacity gain is confined, as rain rate increases. The sensitivity of the performance to the positioning and orientation of the arrays has been also discussed and evaluated. Nevertheless, future experimental data are required to verify these results.

Chapter 7

Conclusions and Future Research Directions

7.1 Conclusions

The aim of this research was to quantify the benefit (if any) of applying MIMO technology to HAP-based communications systems. Since it is the channel which principally dictates any benefit, the primary focus of this thesis was to discover the nature of the HAP-MIMO radio propagation channel and develop accurate and reliable channel models that can be widely used by the research community. At the beginning of this research, a literature survey suggested that no channel model or measurement data were in existence for the HAP-MIMO channel. Furthermore, whether the size of a single HAP can effectively support multiple antennas was uncertain. Motivated by these facts, this section concludes this thesis.

In Chapter 3, the problem of modeling the narrowband HAP-MIMO channels has been addressed. A 3-D cylinder geometrical propagation model for narrowband HAP-MIMO communications has been proposed. Based on this geometrical model, a 3-D parametric reference model for narrowband HAP-MIMO Ricean fading channels has been developed. From this reference model, the STCF for a 3-D non-isotropic scattering environment has been mathematically derived. Then, the effect of the system parameters on the spatial and temporal correlation and the capacity of ULAs has been thoroughly studied. The numerical results have suggested that MIMO techniques are applicable on a single HAP, as long as the Ricean factor is sufficiently small.

To validate the accuracy of the aforementioned theoretical model, 3-D SoS-based deterministic and statistical simulation models have been developed in Chapter 4. The statistical properties of the simulation models have been derived

and verified by simulation. The simulation results have shown that the proposed simulation models are a good approximation of the reference model. Specifically, the close agreement between the theoretical-based and simulation-based channel statistics have confirmed the utility of the proposed simulation models and the method used to estimate the model parameters. These results have also evaluated the performance vs. complexity trade-offs between the statistical and deterministic simulation models. In most applications, software-based simulation is performed on a workstation or a personal computer (PC). Nevertheless, the feasibility of porting these simulation models into hardware by using digital signal processors (DSPs) is also of interest. In particular, hardware channel simulations can significantly increase the usefulness of the simulation models by enabling simulations in real-time.

Currently, a number of standardization bodies supported by industries and research institutes are trying to establish new system standards for future high-speed 4G wireless systems employing MIMO techniques. One important feature of future communications systems is that they demand considerably larger bandwidths than today's systems. In Chapter 5, the reference and simulation narrowband HAP-MIMO channel models have been extended to the corresponding frequency-selective models for high-bandwidth transmissions. In particular, a 3-D two concentric-cylinder model for wideband HAP-MIMO channels has been proposed. Based on this geometrical model, a 3-D parametric reference model for wideband HAP-MIMO Ricean fading channels has been developed. From the reference model, the STFCE has been mathematically derived for a 3-D non-isotropic scattering environment. From the STFCE, the SDPS and the PSDS have been also derived. The numerical results have demonstrated the theoretical derivations. To validate the reference wideband HAP-MIMO channel model, SoS-based deterministic and statistical simulation models for wideband HAP-MIMO Ricean fading channels have been developed and the statistics of these models have been verified by simulation. The simulation results have underlined the outstanding performance of the proposed simulation models.

Finally, the possibility of applying the MIMO technology to fixed broadband HAP-based communications systems operating at mm-wave frequencies has been explored. Although most research on MIMO technology has focused on the potential gain arising due to rich scattering environments, Chapter 6 has suggested that specifically designed antenna arrays provide a superior solution to the problem of reduced MIMO performance in LoS. In particular, maximum capacity can be reached when the relation between the antenna elements separation at both ends, the transmission distance, the wavelength, the array orientation, and the elevation angle of the platform fulfill a certain criterion. The results have demonstrated the potential channel capacity gain of the proposed optimized architecture. These results have also studied the influence of the rainfall and the deviation from the optimal relation (e.g. due to array length constraints) on the channel capacity performance.

7.2 Future Research Directions

With their unique characteristics, HAPs seem to represent an efficacious alternative infrastructure, which can revolutionize the telecommunication industry. Since MIMO architecture is the key technology, which will make 4G visions a reality, it is envisaged that HAP-MIMO systems will be potentially capable of providing and delivering a compelling range of current and next generation mobile/fixed services. Hence, HAP-MIMO research will gain much interest from academia, research centers, and industry worldwide. Although this work constitutes a robust basis for HAP-MIMO channel modeling, it could be further improved or extended into different areas. In this section, some topics that could be interesting to investigate in the future are briefly reviewed.

Measurement campaigns: Due to the lack of channel-sounding measurement campaigns, the contribution of this thesis has been limited to developing reference and simulation models for HAP-MIMO channels. However, it is important to verify these models in real-world propagation conditions. Specifically, HAPs could be

emulated by using a helicopter, a small plane or a balloon containing two or more antennas sufficiently separated. However, access to a real HAP would be even more ideal. Therefore, future research efforts may be devoted to collecting measured channel data and developing empirical models.

2nd order statistics: The first-order statistics of the channel impulse response are not sufficient to assess system characteristics such as handover, velocities of the transmitter and receiver, and fading rate. To assess the aforementioned system characteristics, accurate characterization of the second-order statistics, such as the envelope level crossing rate (LCR) and the average fade duration (AFD), is necessary. Specifically, the envelope LCR is an important statistical quantity revealing information about how fast the received signal changes with time. It is basically a measure to describe the average number of times the signal envelope crosses a certain threshold level from up to down (or from down to up) per second. Moreover, the envelope AFD is defined as the expected value of the time intervals over which the fading signal envelope remains below a certain threshold level. Based on [188], [216] and using the proposed 3-D reference model for narrowband HAP-MIMO channels, the corresponding analytical expressions for the envelope LCR and AFD can be derived for a 3-D non-isotropic scattering environment.

Other types of antenna arrays: The analysis in this thesis is restricted to HAP-MIMO systems employing ULAs at both sides of the communication link. However, the proposed channel models can be modified to employ other antenna array geometries, such as uniform planar arrays (UPAs), uniform circular arrays (UCAs), and spherical antenna arrays (SAAs), or a combination of them.

Multiple-bounce scattering: Apart from considering only single-bounce rays, this work can be extended to additionally support double-bounce or multiple-bounce rays (due to multiple scattering, reflection or diffraction of the radiated energy), that individually contribute in the total transmitted power of the link. Then, more sophisticated and realistic channel models can be obtained.

Mobile scatterers: The proposed HAP-MIMO channel models assume that all scattering objects are stationary. However, this assumption does not hold in some cases. Therefore, these models can be extended to include non-stationary scattering objects, such as vehicles and people.

Mobile applications at mm-wave bands: Although signal transmissions at mm-wave frequencies are usually associated with fixed broadband services, currently there is a clear trend to extend the applicability of these services to mobile scenarios in order to benefit from existing air interfaces and accelerate the development of new applications, such as the provision of high-speed Internet access, audio and video on demand and file transfer to vehicles, airplanes, trains and ships [217]. However, modeling the entire possible propagation effects associated with the licensed Ka and V frequency bands is an essential precondition. The propagation effects are usually classified into two main categories, the *local environment propagation effects*, e.g., multipath, shadowing, and blockage, and the *tropospheric effects*, e.g., rainfall, oxygen absorption, water vapor, clouds, and precipitation. The local environment propagation effects, which are also encountered at lower frequency bands, i.e., L and S, exist due to the local environment in the vicinity of the TMS. The atmospheric effects introduce severe attenuation to the transmitted signal in frequencies well above 10 GHz [11].

This thesis has independently treated the local environment propagation effects and the tropospheric effects depending on the operation frequency. Hence, their possible correlation has not been yet investigated. However, an accurate and realistic HAP-MIMO channel modeling of broadband mobile communications systems operating at mm-wave frequencies should treat these effects together. Under such conditions, it could be interesting to theoretically and experimentally investigate the relation between the multipath introduced by the local scatterers and the rainfall effects. The interested reader is referred to [218] for a first theoretical approach to this open research problem, where a novel statistical analysis for SISO mobile satellite systems is presented.

РАНЕЕЗНАМО ПЕРПАА

Appendix A

Derivations of Equations (17)-(19)

1. Derivation of Equation (17)

From Fig. 18, applying the cosine law to the triangles $\tilde{p}\tilde{l}O'$ and $\tilde{p}OO'$, we obtain

$$\begin{aligned} d^2(\tilde{p}, \tilde{l}) &= d^2(\tilde{p}, O') + [0.5(n_R + 1 - 2l)\delta_R]^2 - d(\tilde{p}, O')(n_R + 1 - 2l)\delta_R \cos(a_{LOS}^{Rl} - \theta_R), \end{aligned} \quad (193)$$

$$\begin{aligned} d^2(\tilde{p}, O') &= D^2 + [0.5(n_T + 1 - 2p)\delta_T]^2 - D(n_T + 1 - 2p)\delta_T \cos\theta_T. \end{aligned} \quad (194)$$

From (193) and (194), considering that $a_{LOS}^{Rl} \approx \pi$ and using the approximate relation $\sqrt{1+x} \approx 1+x/2$ for small x , we obtain

$$d(\tilde{p}, \tilde{l}) \approx d(\tilde{p}, O') + (n_R + 1 - 2l)\delta_R \cos\theta_R, \quad (195)$$

$$d(\tilde{p}, O') \approx D - (n_T + 1 - 2p)\delta_T \cos\theta_T. \quad (196)$$

Using (196), (195) becomes

$$d(\tilde{p}, \tilde{l}) \approx D - (n_T + 1 - 2p)\delta_T \cos\theta_T + (n_R + 1 - 2l)\delta_R \cos\theta_R. \quad (197)$$

Finally, from Fig. 17, since $H_T \gg H_R$, we finally obtain that

$$d(p, l) \approx [D - (n_T + 1 - 2p)\delta_T \cos\theta_T + (n_R + 1 - 2l)\delta_R \cos\theta_R \cos\psi_R] / \cos\beta_T. \quad (198)$$

2. Derivation of Equation (18)

From Fig. 20, applying the sine law to the triangle $O\tilde{S}^{(n)}O'$, we obtain

$$\frac{R_S^{(n)}}{\sin a_T^{(n)}} = \frac{d(O, \tilde{S}^{(n)})}{\sin(\pi - a_R^{(n)})} = \frac{D}{\sin[\pi - a_T^{(n)} - (\pi - a_R^{(n)})]}. \quad (199)$$

Since $R_{S,\max} \ll D$, $a_T^{(n)}$ is a small angle (see Chapter 3). Then, the approximate relations $\sin x \approx x$ and $\cos x \approx 1$ for small x can be used and (199) becomes

$$\frac{R_S^{(n)}}{a_T^{(n)}} \approx \frac{d(O, \tilde{S}^{(n)})}{\sin a_R^{(n)}} \approx \frac{D}{\sin a_R^{(n)}}. \quad (200)$$

From (200), we obtain

$$d(O, \tilde{S}^{(n)}) \approx D, \quad (201)$$

$$a_T^{(n)} \approx \sin a_R^{(n)} R_S^{(n)} / D. \quad (202)$$

From Fig. 20, applying the cosine law to the triangle $O\tilde{p}\tilde{S}^{(n)}$, we also obtain

$$\begin{aligned} d^2(\tilde{p}, \tilde{S}^{(n)}) &= d^2(O, \tilde{S}^{(n)}) + [0.5(n_T + 1 - 2p)\delta_T]^2 \\ &\quad - d(O, \tilde{S}^{(n)})(n_T + 1 - 2p)\delta_T \cos(\theta_T - a_T^{(n)}). \end{aligned} \quad (203)$$

Using (201) and the approximate relation $\sqrt{1+x} \approx 1+x/2$ for small x , (203) becomes

$$d(\tilde{p}, \tilde{S}^{(n)}) \approx D - [0.5(n_T + 1 - 2p)\delta_T] \cos(\theta_T - a_T^{(n)}). \quad (204)$$

Using (202), (204) can be written as follows

$$\begin{aligned} d(\tilde{p}, \tilde{S}^{(n)}) &\approx D - [0.5(n_T + 1 - 2p)\delta_T] \cos \theta_T \\ &\quad - [0.5(n_T + 1 - 2p)\delta_T] \sin \theta_T \sin a_R^{(n)} R_S^{(n)} / D. \end{aligned} \quad (205)$$

Finally, from Fig. 19, since $D \gg R_{S,\max}$, i.e., $D + R_{S,\max} \approx D - R_{S,\max} \approx D$, and $H_T \gg H_{S,\max}$, we finally obtain that

$$d(p, S^{(n)}) \approx d(\tilde{p}, \tilde{S}^{(n)}) / \cos \beta_T. \quad (206)$$

3. Derivation of Equation (19)

From Fig. 19, the distance $d(S^{(n)}, l)$ can be written as

$$\begin{aligned} & d^2(S^{(n)}, l) \\ & \approx d^2(\tilde{S}^{(n)}, \tilde{l}) + \left[d(O_R, S^{(n)}) \sin \beta_S^{(n)} - d(O_R, l) \sin \psi_R \right]^2 \\ \Rightarrow & d^2(S^{(n)}, l) \\ & \approx d^2(\tilde{S}^{(n)}, \tilde{l}) + d^2(O_R, S^{(n)}) \sin^2 \beta_S^{(n)} + d^2(O_R, l) \sin^2 \psi_R \\ & \quad - 2d(O_R, S^{(n)}) \sin \beta_S^{(n)} d(O_R, l) \sin \psi_R. \end{aligned} \quad (207)$$

By applying the cosine law to the triangle $O\tilde{S}^{(n)}\tilde{l}$, we obtain

$$\begin{aligned} & d^2(\tilde{S}^{(n)}, \tilde{l}) \\ & = d^2(O_R, S^{(n)}) \cos^2 \beta_S^{(n)} + d^2(O_R, l) \cos^2 \psi_R \\ & \quad - 2d(O_R, S^{(n)}) \cos \beta_S^{(n)} d(O_R, l) \cos \psi_R \cos(a_R^{(n)} - \theta_R). \end{aligned} \quad (208)$$

Using (208), (207) becomes

$$\begin{aligned} & d^2(S^{(n)}, l) \\ & \approx d^2(O_R, S^{(n)}) + d^2(O_R, l) - 2d(O_R, S^{(n)}) \sin \beta_S^{(n)} d(O_R, l) \sin \psi_R \\ & \quad - 2d(O_R, S^{(n)}) \cos \beta_S^{(n)} d(O_R, l) \cos \psi_R \cos(a_R^{(n)} - \theta_R). \end{aligned} \quad (209)$$

Using the approximate relation $\sqrt{1+x} \approx 1+x/2$ for small x , (209) finally becomes

$$\begin{aligned}
 & d(s^{(n)}, l) \\
 & \approx d(O_R, s^{(n)}) - d(O_R, l) \left[\sin \psi_R \sin \beta_S^{(n)} + \cos \psi_R \cos \beta_S^{(n)} \cos(a_R^{(n)} - \theta_R) \right]. \\
 \Rightarrow & d(s^{(n)}, l) \\
 & \approx d(O_R, s^{(n)}) - d(O_R, l) \sin \psi_R \sin \beta_S^{(n)} - d(O_R, l) \cos \beta_S^{(n)} \cos \psi_R \cos(a_R^{(n)} - \theta_R) \\
 \Rightarrow & d(s^{(n)}, l) \\
 & \approx R_S^{(n)} / \cos \beta_S^{(n)} - 0.5(n_R + 1 - 2l) \delta_R \sin \psi_R \sin \beta_S^{(n)} \\
 & \quad - 0.5(n_R + 1 - 2l) \delta_R \cos \theta_R \cos \psi_R \cos a_R^{(n)} \cos \beta_S^{(n)} \\
 & \quad - 0.5(n_R + 1 - 2l) \delta_R \sin \theta_R \cos \psi_R \sin a_R^{(n)} \cos \beta_S^{(n)}. \tag{210}
 \end{aligned}$$

Appendix B

Derivation of Equations (190) and (191)

1. Derivation of Equation (190)

From Fig. 75, considering that $H_T \gg H_R$, the Euclidean distances (path lengths) between each pair of elements are given as follows

$$d(l,p) = r \approx H_T / \sin \beta_T, \quad (211)$$

$$d(m,p) = \left[(r + \delta_R \cos \theta_R)^2 + (\delta_R \sin \theta_R)^2 \right]^{1/2}, \quad (212)$$

$$d(l,q) = \left[(r - \delta_T \cos \theta_T)^2 + (\delta_T \sin \theta_T)^2 \right]^{1/2}, \quad (213)$$

$$d(m,q) = \left[(r - \delta_T \cos \theta_T + \delta_R \cos \theta_R)^2 + (\delta_T \sin \theta_T - \delta_R \sin \theta_R)^2 \right]^{1/2}. \quad (214)$$

Equations (212)-(214) can be simplified using the following first-order Taylor series approximation

$$\left[(A+B)^2 + C^2 \right]^{1/2} = (A+B) \left[1 + \frac{C^2}{(A+B)^2} \right]^{1/2} \approx (A+B) + \frac{C^2}{2(A+B)}. \quad (215)$$

This approximation is valid for $(A+B)^2 \gg C^2$, which is a reasonable assumption for the targeted application, providing that $r \gg \{\delta_T, \delta_R\}$. Using (215), (212)-(214) are approximated as follows

$$d(m,p) \approx r + \delta_R \cos \theta_R + \frac{(\delta_R \sin \theta_R)^2}{2(r + \delta_R \cos \theta_R)}, \quad (216)$$

$$d(l,q) \approx r - \delta_T \cos \theta_T + \frac{(\delta_T \sin \theta_T)^2}{2(r - \delta_T \cos \theta_T)}, \quad (217)$$

$$d(m,q) \approx r - \delta_T \cos \theta_T + \delta_R \cos \theta_R + \frac{(\delta_T \sin \theta_T - \delta_R \sin \theta_R)^2}{2(r - \delta_T \cos \theta_T + \delta_R \cos \theta_R)}. \quad (218)$$

Since $r \gg \{\delta_T, \delta_R\}$, the denominators in equations (216)-(218) are approximately equal to $2r$, without any loss of accuracy, i.e., the error introduced by these approximations is minor for all practical systems. For instance, in a system with $r = 23$ km, $\delta_T = 30$ m, and $\delta_R = 5$ m, the maximum error, i.e., the maximum difference between (218) and (221) for all values of θ_T and θ_R is less than 10^{-3} . The error is even smaller for larger r and smaller δ_T and δ_R . Then, (216)-(218) become, respectively

$$d(m,p) \approx r + \delta_R \cos \theta_R + \frac{(\delta_R \sin \theta_R)^2}{2r}, \quad (219)$$

$$d(l,q) \approx r - \delta_T \cos \theta_T + \frac{(\delta_T \sin \theta_T)^2}{2r}, \quad (220)$$

$$d(m,q) \approx r - \delta_T \cos \theta_T + \delta_R \cos \theta_R + \frac{(\delta_T \sin \theta_T - \delta_R \sin \theta_R)^2}{2r}. \quad (221)$$

Finally, using (211) and (219)-(221), (189) becomes

$$\begin{aligned} \frac{\delta_T \delta_R \sin \theta_T \sin \theta_R}{r} &\approx (2\nu + 1) \lambda / 2 \\ \Rightarrow \delta_T \delta_R &\approx (2\nu + 1) \frac{\lambda H_T}{2 \sin \beta_T \sin \theta_T \sin \theta_R}, \quad \{\beta_T, \theta_T, \theta_R\} \neq 0^\circ, \end{aligned} \quad (222)$$

where $\nu \in \mathbb{Z}$ and \mathbb{Z} represents a set of integers.

2. Derivation of Equation (191)

The simplified maximum capacity criterion can be extended to the case of a $n_R \times n_T$ LoS-HAP-MIMO channel. It is trivial to show that (184) can be written as

$$\sum_{j=1}^{n_T} e^{-j2\pi[d(a,j)-d(b,j)]/\lambda}, \quad \forall a, b \in \{1, 2, \dots, n_R\}. \quad (223)$$

Since ULAs are used at both ends of the communication link, the phase difference $2\pi[d(a,j)-d(a,j+1)]/\lambda$ is virtually constant for all $j \in \{1, 2, \dots, n_T - 1\}$ and for all

the practical values of distance between transmitter-receiver and inter-element spacing. Therefore, $2\pi[d(a,j)-d(b,j)]/\lambda - 2\pi[d(a,j+1)-d(b,j+1)]/\lambda$ is also constant for all $j \in \{1, 2, \dots, n_T - 1\}$. Hence, the solution to (223) for $j=p$ and $j+1=q$ can be written as [206]

$$2\pi[d(a,p)-d(b,p)]/\lambda - 2\pi[d(a,q)-d(b,q)]/\lambda = \frac{2\pi}{n_T} + 2v\pi. \quad (224)$$

Since the array elements at both ends are uniformly distributed and $r \gg \{\delta_T, \delta_R\}$ the following approximation $d(a,j)-d(b,j) \approx (a-b)[d(l,j)-d(m,j)]$ can be used. Thus, (224) can be simplified to

$$2\pi[d(l,p)-d(m,p)-d(l,q)+d(m,q)]/\lambda = \frac{2\pi}{n_T} + 2v\pi \quad (225)$$

and the maximum capacity criterion can be expressed as

$$d(l,p)-d(m,p)-d(l,q)+d(m,q) = \lambda \left(\frac{1}{n_T} + v \right). \quad (226)$$

Using the derivation for the simplified 2×2 LoS-HAP-MIMO maximum capacity criterion described above, the $n_R \times n_T$ LoS-HAP-MIMO maximum capacity criterion can be written as

$$\delta_T \delta_R \approx \left(\frac{1}{n_T} + v \right) \frac{\lambda H_T}{\sin \beta_T \sin \theta_T \sin \theta_R}, \quad \{\beta_T, \theta_T, \theta_R\} \neq 0^\circ, \quad (227)$$

where $v \in \mathbb{Z}$ and \mathbb{Z} represents a set of integers.

РАНЕЕЗНАМО ПЕРПАА

REFERENCES

- [1] A. Goldsmith, *Wireless Communications*, New York, USA: Cambridge University Press, 2005.
- [2] T. S. Rappaport, *Wireless Communications: Principles and practice*, 2nd ed. Upper Saddle River, New Jersey, USA: Prentice Hall PTR, 2002.
- [3] T. Ojanpera and R. Prasad, "An Overview of Air Interface Multiple Access for IMT 2000/UMTS," *IEEE Communications Magazine*, vol. 36, no. 9, pp. 82-89, 91-5, Sep. 1998.
- [4] D. Collins and C. Smith, *3G Wireless Networks*, New York, USA: McGraw-Hill, 2001.
- [5] J. P. Castro, *The UMTS network and radio access technology: Air interface techniques for future mobile systems*, Chichester, West Sussex, England: John Wiley & Sons, 2001.
- [6] <http://www.3gpp.org/HSPA>
- [7] H. Holma and A. Toskala, *HSDPA/HSUPA for UMTS: High Speed Radio Access for Mobile Communications*, New York, USA: John Wiley & Sons, 2006.
- [8] W. Webb, "Broadband fixed wireless access as a key component of the future integrated communications environment," *IEEE Communications Magazine*, vol. 39, no. 9, pp. 115-121, Sep. 2001.
- [9] H. Bolcskel, A. J. Paulraj, K. V. S. Hari, R. U. Nabar, W. W. Lu, "Fixed broadband wireless access: state of the art, challenges, and future directions," *IEEE Communications Magazine*, vol. 39, no. 1, pp. 100-108, Jan. 2001.
- [10] H. R. Anderson, *Fixed Broadband Wireless System Design*, Chichester, West Sussex, England: John Wiley & Sons, Jan. 2003.
- [11] A. Aragón-Zavala, J. L. Cuevas-Ruiz, and J. A. Delgado-Peñín, *High-Altitude Platforms for Wireless Communications*, New York, USA: John Wiley & Sons, Dec. 2008.
- [12] S. Karapantazis and F.-N. Pavlidou, "Broadband communications via high-altitude platforms: A survey," *IEEE Communications Surveys and Tutorials*, vol. 7, no. 1, pp. 2-31, First Quarter 2005.
- [13] T. C. Tozer and D. Grace, "High-altitude platforms for wireless communications," *IEE Electronics & Communication Engineering Journal*, vol. 13, no. 3, pp. 127-137, Jun. 2001.
- [14] F.-N. Pavlidou, M. Ruggieri, M. Gerla, and R. Miura, "Communications via High Altitude Platforms: Technologies and Trials," *International Journal of Wireless Information Networks*, vol. 13, no. 1, pp. 1-4, Jan. 2006.
- [15] A. Mohammed and Z. Yang, "Broadband Communications and Applications from High Altitude Platforms," *International Journal of Recent Trends in Engineering*, vol. 1, no. 3, pp. 239-243, May 2009.
- [16] G. M. Djunnic and J. Freidenfelds, "Establishing wireless communications services via high-altitude aeronautical platforms: a concept whose time has come?," *IEEE Communications Magazine*, vol. 35, no. 9, pp. 128-135, Sep. 1997.
- [17] A. K. Widiawan and R. Tafazolli, "High Altitude Platform Station (HAPS): A Review of New Infrastructure Development for Future Wireless Communications," *Wireless Personal Communications*, vol. 42, no. 3, pp. 387-404, Aug. 2007.
- [18] N. Colella, J. Martin, and I. Akyildiz, "The HALO network," *IEEE Communications Magazine*, vol. 38, no. 6, pp. 142-148, 2000.

- [19] J. Thornton et.al., "Broadband communications from high altitude platforms – the European Helinet programme," *IEE Electronics & Communication Engineering Journal*, vol. 13, no. 3, pp. 138-144, 2001.
- [20] Y. Lee and H. Ye, "Sky station stratospheric telecommunications system, a high speed low latency switched wireless network," in *Proc. 17th AIAA International Communications Satellite Systems Conference*, pp. 25-32, 1998.
- [21] R. Tafazolli, R. Wansch, C. Plenge, J. Horwath, and U. Apel, "Stratospheric Services," *Technical Note of Stratospheric Platforms - A definition study for an ESA platform (TN1)*, 2004.
- [22] ESA-ESTEC contract 162372/02/NL/US, STRATOS: Stratospheric Platforms, a Definition Study for an ESA Platform, *Final Report*, 1-34, Sep. 2005.
- [23] Lindstrand, "ESA-HALE airship research and development program," in *Proc. 2nd stratospheric platform systems workshop (SPSW) 2000*, pp. 99-107, Tokyo, Japan, Sep. 2000.
- [24] J. Thornton and D. Grace, "Effect of Lateral Displacement of a High Altitude Platform on Cellular Interference and Handover," *IEEE Transaction on Wireless Communications*, vol. 4. no. 4, pp. 1483-1490, Jul. 2005.
- [25] D. I. Axiotis, M. E. Theologou, and E. D. Sykas, "The effect of platform instability on the system level performance of HAPS UMTS," *IEEE Communications Letters*, vol. 8, no. 2, pp. 111-113, Feb. 2004.
- [26] K. Katzis, D. A. J. Pearce, and D. Grace, "Impact of high altitude platform movements on cellular handover," in *Proc. International Workshop on High Altitude Platform Systems*, Athens, Greece, Sep. 2005.
- [27] ITU-R Recommendation V.431: Nomenclature of the frequency and wavelength bands used in telecommunications, *International Telecommunication Union*, Geneva.
- [28] IEEE Standard 521-2002: Standard Letter Designations for Radar-Frequency Bands
- [29] A. D. Panagopoulos, P.-D. M. Arapoglou, and P. G. Cottis, "Satellite communications at Ku, Ka, and V bands: Propagation impairments and mitigation techniques," *IEEE Communications Surveys and Tutorials*, vol. 6, no. 3, 3rd Quarter 2004.
- [30] J.-M. Park, B.-J. Ku, and D.-S. Oh, "Technical and Regulatory Studies on HAPS," in *Proc. International Workshop on Aerial & Space Platforms: Research, Applications, Vision of IEEE Global Communications Conference (Globecom) 2008*, pp. 1-5, New Orleans, LA, USA, Dec. 4, 2008.
- [31] B.-J. Ku, D.-S. Ahn, and N. Kim, "An Evaluation of Interference Mitigation Schemes for HAPS Systems," *EURASIP Journal on Wireless Communications and Networking*, vol. 2008, 2008.
- [32] V. F. Milas and P. Constantinou, "Interference Environment between High Altitude Platform Networks (HAPN) Geostationary (GEO) Satellite and Wireless Terrestrial Systems," *Wireless Personal Communications*, vol. 32, pp. 257-274, Feb. 2005.
- [33] RESOLUTION 122 (Rev.WRC-07), Use of the bands 47.2-47.5 GHz and 47.9-48.2 GHz by high-altitude platform stations in the fixed service and by other services, *International Telecommunication Union*, Geneva, Switzerland, 2007.
- [34] RESOLUTION 145 (Rev.WRC-07), Use of the bands 27.9-28.2 GHz and 31-31.3 GHz by high-altitude platform stations in the fixed service, *International Telecommunication Union*, Geneva, Switzerland, 2007.
- [35] RESOLUTION 221 (Rev.WRC-07), Use of high-altitude platform stations providing IMT-2000 in the bands 1885-1980 MHz, 2010-2025 MHz and 2110-2170 MHz in Regions 1 and 3 and 1885-1980 MHz and 2110-2160 MHz in Region 2, *International Telecommunication Union*, Geneva, Switzerland, 2007.

- [36] RESOLUTION 734 (Rev.WRC-07), Studies for spectrum identification for gateway links for high-altitude platform stations in the range from 5850 to 7075 MHz, *International Telecommunication Union*, Geneva, Switzerland, 2007.
- [37] D. Grace, N. E. Daly, T. C. Tozer, A. G. Burr, and D. A. J. Pearce, "Providing multimedia communications services from high altitude platforms," *International Journal of Satellite Communications*, vol. 19, no. 6, pp. 559-580, Nov. 2001.
- [38] M. Mondin, F. DAVIS, and P. Mulassano, "On the use of HALE platforms as GSM base stations," *IEEE Personal Communications*, vol. 8, no. 2, pp. 37-44, Apr. 2001.
- [39] B. T. Ahmed, M. C. Ramon, and L. H. Ariet, "On the UMTS-HSDPA in high altitude platforms (HAPs) communications," in *Proc. 3rd International Symposium on Wireless Communication Systems (ISWCS) 2006*, pp. 704-708, Valencia, Spain, Sep. 2006.
- [40] B. Taha-Ahmed, M. Calvo-Ramon, and L. de Haro-Ariet, "High altitude platforms (HAPs) W-CDMA system over cities," in *Proc. IEEE 61st Vehicular Technology Conference (VTC Spring) 2005*, vol. 4, pp. 2673-2677, Stockholm, Sweden, 30 May-1 Jun. 2005.
- [41] T. Toshiaki and H. Masatoshi, "Navigation and Positioning System Using High Altitude Platforms Systems (HAPS)," *Journal of the Japan Society for Aeronautical and Space Sciences*, vol. 52, no. 603, pp. 175-185, 2004.
- [42] K. Akalestos, T. C. Tozer, and D. Grace, "Emergency Communications from High Altitude Platforms," in *Proc. Int. Workshop on High Altitude Platform Systems*, Athens, Greece, Sep. 2005.
- [43] J. Holis and P. Pechac, "Coexistence of Terrestrial and HAP 3G Networks during Disaster Scenarios," *Radioengineering*, vol. 17, no. 4, pp. 1-7, 2008.
- [44] J. D. Deaton, "High Altitude Platforms for Disaster Recovery: Capabilities, Strategies, and Techniques for Emergency Telecommunications," *EURASIP Journal on Wireless Communications and Networking*, vol. 2008, May 2008.
- [45] M. J. H. Lum, J. Rosen, H. King, D. C.W. Friedman, G. Donlin, G. Sankaranarayanan, B. Harnett, L. Huffman, C. Doarn, T. Broderick, and B. Hannaford, "Telesurgery Via Unmanned Aerial Vehicle (UAV) with a Field Deployable Surgical Robot," *Studies in health technology and informatics*, vol. 125, pp. 313-315, 2006.
- [46] L. Jamison, G.S. Sommer, and I.R. Porche, "High-Altitude Airships for the Future Force Army," *Technical Report 234*, RAND Arroyo Center, Jan. 2005.
- [47] ITU-T, Vocabulary of terms for broadband aspects of ISDN, I.113 Recommendation, 1992.
- [48] C. Morlet, A. Bolea-Alamañac, G. Gallinaro, L. Erup, P. Takats, and A. Ginesi, "Introduction of Mobility Aspects for DVB-S2/RCS Broadband Systems," *International Journal on Space Communications*, vol. 21, no. 1-2, pp. 5-17, 2007.
- [49] J. Holis and P. Pechac, "Provision of 3G Mobile Services in Sparsely Populated Areas Using High Altitude Platforms," *Radioengineering*, vol. 17, no.1, pp. 43-49, Apr. 2008.
- [50] I. R. Palma-Lázgare, J. A. Delgado-Penín, and F. Pérez-Fontán, "An Advance in Wireless Broadband Communications based on a WiMAX-HAPS Architecture," in *Proc. 26th International Communications Satellite Systems Conference (ICSSC)*, San Diego, CA, 10-12 Jun. 2008.
- [51] J. Thornton, A. D. White, and T. C. Tozer, "A WiMAX Payload for High Altitude Platform Experimental Trials," *EURASIP Journal on Wireless Communications and Networking*, vol. 2008, May 2008.

- [52] Air Interface for Fixed and Mobile Broadband Wireless Access Systems-Amendment for Physical and Medium Access Control Layers for Combined Fixed and Mobile Operation in Licensed Band, *IEEE Std. 802.16e-2005*, 2005.
- [53] J. G. Andrews, A. Ghosh, and R. Muhamed, *Fundamentals of Wimax: Understanding Broadband Wireless Networking*, Upper Saddle River, NJ: PTR Prentice Hall, Feb. 2007.
- [54] A. Bria, M. Flament, F. Gessler, O. Queseth, R. Stridh, M. Unbehaun, J. Wu, and J. Zander, "4th Generation wireless infrastructures - scenarios & research challenges," *IEEE Personal Communications- Special Edition*, Dec. 2001.
- [55] B. G. Evans and K. Baughan, "Visions of 4G," *IEE Electronics & Communication Engineering Journal*, vol. 12, no. 6, pp. 293-303, Dec. 2000.
- [56] H.-H. Chen and M. Guizani, *Next Generation Wireless Systems and Networks*, Chichester, Hoboken, NJ: Wiley, Apr. 2006.
- [57] S. Y. Hui and K. H. Yeung, "Challenges in the Migration to 4G Mobile Systems," *IEEE Communications Magazine*, vol. 41, no. 12, pp. 54-59, Dec. 2003.
- [58] H. Ekström, A. Furuskar, J. Karlsson, M. Meyer, S. Parkvall, and J. Torsner, "Technical Solutions for the 3G Long-Term Evolution," *IEEE Communications Magazine*, vol. 44, no. 3, pp. 38-45, 2006.
- [59] S. Sesia, M. Baker, and I. Toufik, *LTE-The UMTS Long Term Evolution: From Theory to Practice*, 2nd ed. New York, USA: Wiley, Oct. 2010.
- [60] <http://www.3gpp.org/LTE-Advanced>
- [61] <http://www.wimaxforum.org/>
- [62] P. Demestichas, G. Vivier, K. El-Khazen, and M. Theologou, "Evolution in wireless systems management concepts: from composite radio to reconfigurability," *IEEE Communications Magazine*, vol. 42, no. 5, pp. 90-98, May 2004.
- [63] V. Stavroulaki, S. Buljore, P. Roux, and E. Melin, "Equipment management issues in B3G, end-to-end reconfigurable systems," *IEEE Wireless Communications*, vol. 13, no. 3, pp. 24-32, Jun. 2006.
- [64] S. Karapantazis and F.-N. Pavlidou, "The role of high altitude platforms in beyond 3G networks," *IEEE Wireless Communications*, vol. 12, no. 6, pp. 33-41, Dec. 2005.
- [65] F. Dovis, R. Fantini, M. Mondin, and P. Savi, "4G Communications Based on High Altitude Stratospheric Platforms: Channel Modeling and Performance Evaluation," in *Proc. IEEE Global Communications Conference (Globecom) 2001*, vol. 1, pp. 557-561, San Antonio, TX, USA, Nov. 2001.
- [66] D. Grace, M. Mohorcic, M. H. Capstick, M. B. Pallavicini, and M. Fitch, "Integrating users into the wider broadband network via high altitude platforms," *IEEE Transactions on Wireless Communications*, vol. 12, no. 5, pp. 98-105, Oct. 2005.
- [67] E. Falletti, M. Laddomada, M. Mondin, and F. Sellone, "Integrated services from high-altitude platforms: a flexible communication system," *IEEE Communications Magazine*, vol. 44, no. 2, pp. 85-94, Feb. 2006.
- [68] A. Paulraj, R. Nabar, and D. Gore, *Introduction to Space-Time Wireless Communications*, Cambridge, UK: Cambridge University Press, 2003.
- [69] E. Biglieri, R. Calderbank, A. Constantinides, A. Goldsmith, A. Paulraj, and H. Vincent Poor, *MIMO Wireless Communications*, Cambridge, UK: Cambridge University Press, 2007.
- [70] M. Pätzold, *Mobile Fading Channels*, Chichester, West Sussex, UK: John Wiley & Sons, Feb. 2002.
- [71] S. R. Saunders and A. Aragón-Zavala, *Antennas and Propagation for Wireless Communication Systems*, 2nd ed. Chichester, West Sussex, UK: John Wiley & Sons, 2007.

- [72] W. Pawlowski, "Radio wave propagation effects in high-altitude platform systems," in *Proc. International Conference on Microwaves, Radar and Wireless Communications (MIKON) 2000*, vol. 1, pp. 185-188, Wroclaw, Poland, May 2000.
- [73] G. Kandung, M. Mohorcic, E. Leitgeb, and T. Javornik, "Modelling of atmospheric impairments in stratospheric communications," in *Proc. 2nd WSEAS international Conference on Circuits, Systems, Signal and Telecommunications*, pp. 86-91, Acapulco, Mexico, Jan. 25 - Feb. 27 2008.
- [74] M. Smolnikar, M. Mohorcic, T. Javornik, and D. Grace, "Propagation Impairment Countermeasures in Mobile Stratospheric Operating Environment," in *Proc. IEEE 69th Vehicular Technology Conference (VTC Spring) 2009*, pp. 1-5, Barcelona, Spain, 26-29 Apr. 2009.
- [75] Q. Feng, J. McGeehan, E. K. Tameh, and A. R. Nix, "Path Loss Models for Air-to-Ground Radio Channels in Urban Environments," in *Proc. IEEE 63rd Vehicular Technology Conference (VTC Spring) 2006*, vol. 6, pp. 2901-2905, Melbourne, Australia, 7-10 May 2006.
- [76] Iskandar and S. Shimamoto, "Prediction of Propagation Path Loss for Stratospheric Platforms Mobile Communications in Urban Site LOS/NLOS Environment," in *Proc. IEEE International Conference on Communications (ICC) 2006*, vol. 12, pp. 5643-5648, Istanbul, Turkey, Jun. 2006.
- [77] C. L. Spillard, T. C. Tozer, B. Gremont, and D. Grace, "The Performance of High-Altitude Platform Networks in Rainy Conditions," in *Proc. 22nd AIAA International Communications Satellite Systems Conference*, Monterey, USA, 9-12 May 2004.
- [78] S. Zvanovec, P. Piksa, M. Mazanek, and P. Pechac, "A study of gas and rain propagation effects at 48 GHz for HAP scenarios," *EURASIP Journal on Wireless Communications and Networking*, vol. 2008, pp. 1-7, Jan. 2008.
- [79] A. Mohammed and T. Hult, "Evaluation of Depolarization Effects on the Performance of High Altitude Platforms (HAPs)," in *Proc. IEEE 67th Vehicular Technology Conference (VTC Spring) 2008*, pp. 2942-2946, Singapore, 11-14 May 2008.
- [80] S. K. Agrawal and P. Garg, "Calculation of Channel Capacity and Rician Factor in the Presence of Vegetation in Higher Altitude Platforms Communication Systems," in *Proc. 15th International Conference on Advanced Computing and Communications (ADCOM) 2007*, pp. 243-248, India, Dec. 2007.
- [81] S. K. Agrawal and P. Garg, "Effect of urban-site and vegetation on channel capacity in higher altitude platform communication system," *IET Microwaves, Antennas and Propagation*, vol. 3, no. 4, pp. 703-713, Jun. 2009.
- [82] "Specific attenuation model for rain for use in prediction methods," *International Telecommunication Union*, Geneva, Switzerland, ITU-R P.838-1, 1997.
- [83] "Characteristics of precipitation for propagation modeling," *International Telecommunication Union*, Geneva, Switzerland, ITU-R P.837-4, 2003.
- [84] A. D. Panagopoulos, E. M. Georgiadou, and J. D. Kanellopoulos, "Selection Combining Site Diversity Performance in High Altitude Platform Networks," *IEEE Communications Letters*, vol. 11, no. 10, pp.787-789, Oct. 2007.
- [85] T. Konefal, C. L. Spillard, and D. Grace, "Site diversity for high-altitude platforms: a method for the prediction of joint site attenuation statistics," *IEE Proceedings of Microwaves, Antennas and Propagation*, vol. 149, no. 2, pp. 124-128, Apr. 2002.
- [86] J. L. Cuevas-Ruiz and J. A. Delgado-Penín, "HAPS Systems Performance Using a Ka-Band Channel Model Based on a Time Series Generator," in *Proc. 15th International Conference on Electronics, Communications and Computers (CONIELECOMP) 2005*, pp. 10-15, Puebla, Mexico, Feb. 28 - 2 Mar. 2005.

- [87] C. L. Spillard, D. Grace, J. Thornton, and T. C. Tozer, "Effect of ground station antenna beamwidth on rain scatter interference in high-altitude platform links," *Electronics Letters*, vol. 38, no. 20, pp. 1211-1213, Sep. 2002.
- [88] E. T. Michailidis and A. G. Kanatas, "Capacity Optimized Line-of-Sight HAP-MIMO Channels for Fixed Wireless Access," in *Proc. International Workshop on Satellite and Space Communications (IWSSC) 2009*, pp. 73-77, Siena-Tuscany, Italy, 10-11 Sep. 2009.
- [89] J. Holis and P. Pechac, "Elevation Dependent Shadowing Model for Mobile Communications via High Altitude Platforms in Built-Up Areas," *IEEE Transactions on Antennas and Propagation*, vol. 56, no. 4, pp. 1078-1084, Apr. 2008.
- [90] M. Kong, O. Yorokinov, and S. Shimamoto, "Evaluations of Urban Shadowing Characteristics for HAPS Communications," in *Proc. IEEE 5th Consumer Communications and Networking Conference (CCNC) 2008*, pp. 555-559, Las Vegas, USA, Jan. 2008.
- [91] F. Dovis, R. Fantini, M. Mondin, and P. Savi, "Small-scale fading for high-altitude platform (HAP) propagation channels," *IEEE Journal on Selected Areas in Communications*, vol. 20, no. 3, pp. 641-647, Apr. 2002.
- [92] D. Gesbert, M. Kountouris, R. W. Heath, Jr., C.-B. Chae, and T. Salzer, "Shifting the MIMO Paradigm: From Single User to Multiuser Communications," *IEEE Signal Processing Magazine*, vol. 24, no. 5, pp. 36-46, Oct. 2007.
- [93] T. Hult, A. Mohammed, Z. Yang, and D. Grace, "Performance of a multiple HAP system employing multiple polarization," *Wireless Personal Communications*, vol. 52, no. 1, pp. 105-117, Jan. 2010.
- [94] A. Mohammed and T. Hult, "Capacity evaluation of a high altitude platform diversity system equipped with compact MIMO antennas," *International Journal of Recent Trends in Engineering*, vol. 1, no. 3, pp. 244-247, May 2009.
- [95] E. Telatar, "Capacity of multi-antenna Gaussian channels," *European Transactions on Telecommunications*, vol. 10, no. 6, pp. 585-595, 1999.
- [96] G. J. Foschini and M. J. Gans, "On limits of wireless communications in a fading environment when using multiple antennas," *Wireless Personal Communications*, vol. 6, no. 3, pp. 311-335, 1998.
- [97] J. Salz and J. H. Winters, "Effect of fading correlation on adaptive arrays in digital mobile radio," *IEEE Transactions on Vehicular Technology*, vol. 43, no. 4, pp. 1049-1057, Nov. 1994.
- [98] D.-S. Shiu, G. J. Foschini, M. J. Gans, and J.M. Kahn, "Fading correlation and its effect on the capacity of multielement antenna systems," *IEEE Transactions on Communications*, vol. 48, no. 3, pp. 502-513, Mar. 2000.
- [99] C.-N. Chuah, D. N. C. Tse, J. M. Kahn, and R. A. Valenzuela, "Capacity scaling in MIMO wireless systems under correlated fading," *IEEE Transactions on Information Theory*, vol. 48, no. 3, pp. 637-650, Mar. 2002.
- [100] J. G. Proakis and M. Salehi, *Digital Communications*, 5th ed. New York, USA: McGraw-Hill, 2008.
- [101] V. Tarokh, N. Seshadri, and A. R. Calderbank, "Space-time codes for high data rate wireless communication: Performance criterion and code construction," *IEEE Transactions on Information Theory*, vol. 44, no. 2, pp. 744-765, Mar. 1998.
- [102] A. Abdi and M. Kaveh, "A space-time correlation model for multielement antenna systems in mobile fading channels," *IEEE Journal on Selected Areas in Communications*, vol. 20, no. 3, pp. 550-560, Apr. 2002.

- [103] A. Abdi, C. Tepedelenlioglu, M. Kaveh, and G. Giannakis, "On the estimation of the K parameter for the Rice fading distribution," *IEEE Communications Letters*, vol. 5, no. 3, pp. 92-94, Mar. 2001.
- [104] A. Jahn, "Propagation considerations and fading countermeasures for mobile multimedia services," *International Journal on Satellite Communications*, vol. 19, no. 3, pp. 223-250, 2001.
- [105] Iskandar and S. Shimamoto, "Channel characterization and performance evaluation of mobile communication employing stratospheric platforms," *IEICE Transactions on Communications*, vol. E89-B, no. 3, pp. 937-944, Mar. 2006.
- [106] P.-D. Arapoglou, E. T. Michailidis, A. D. Panagopoulos, A. G. Kanatas, and R. Prieto-Cerdeira, "The Land Mobile Earth-Space Channel: SISO to MIMO Modeling from L- to Ka-Bands," *IEEE Vehicular Technology Magazine, Special Issue on Trends in Mobile Radio Channels: Modeling, Analysis, and Simulation*, vol. 6, no. 2, pp. 44-53, Jun. 2011.
- [107] M. Vázquez-Castro, F. Pérez-Fontán, B. Arbesser-Rastburg, "Channel modeling for satellite and HAPS system design," *Wireless Communications and Mobile Computing*, vol. 2, no. 3, pp. 285-300, 2002.
- [108] Y. Yang, R. Zong, X. Gao, and J. Cao, "Channel modeling for High-Altitude Platform: A review," in *Proc. International Symposium on Intelligent Signal Processing and Communication Systems (ISPACS) 2010*, pp. 1-4, Cheng Du, China, 6-8 Dec. 2010.
- [109] S. Liu, Z. Niu, and Y. Wu, "A blockage based channel model for high altitude platform communications," in *Proc. IEEE 57th IEEE Vehicular Technology Conference (VTC Spring) 2003*, vol. 2, pp. 1051-1055, Seoul, Korea, 22-25 Apr. 2003.
- [110] J. L. Cuevas-Ruiz and A. Aragón-Zavala, G. A. Medina-Acosta, and J. A. Delgado-Penín, "Multipath propagation model for High Altitude Platform (HAP) based on circular straight cone geometry," in *Proc. International Workshop on Satellite and Space Communications (IWSSC) 2009*, pp. 235-239, Siena-Tuscany, Italy, 9-11 Sep. 2009.
- [111] J. L. Cuevas-Ruiz and J. A. Delgado-Penín, "A statistical switched broadband channel model for HAPS links," in *Proc. IEEE Wireless Communications and Networking Conference (WCNC) 2004*, Atlanta, USA, Mar. 2004.
- [112] J. L. Cuevas-Ruiz and J. A. Delgado-Penín, "Channel model based on semi-Markovian processes, an approach for HAPS systems," in *Proc. XIV International Conference on Electronics, Communications, and Computers (CONIELECOMP) 2004*, Veracruz, Mexico, pp. 52-56, Feb. 2004.
- [113] E. Lutz, D. Cygan, M. Dippold, F. Dolainsky, and W. Papke, "The land mobile satellite communications channel - Recording, statistics, and channel model," *IEEE Transactions on Vehicular Technology*, vol. 40, no. 2, pp. 375-386, May 1991.
- [114] Y. Karasawa, K. Kimura, and K. Minamisono, "Analysis of availability improvements in LMSS by means of satellite diversity based on three-state propagation channel model," *IEEE Transactions on Vehicular Technology*, vol. 46, no. 4, pp. 1047-1056, Nov. 1997.
- [115] F. Perez-Fontan, J. P. González, M. J. S. Ferreiro, M. A. V. Castro, S. Buonomo, and J. P. Baptista, "Complex envelope three-state Markov model based simulator for the narrow-band LMS channel," *International Journal of Satellite Communications*, vol. 15, no. 1, pp. 1-15, Jan. 1997.
- [116] L.E. Bråten and T. Tjelta, "Semi-Markov multistate modeling of the land mobile propagation channel for geostationary satellites," *IEEE Transactions on Antennas and Propagation*, vol. 50, no. 12, pp. 1795-1802, Dec. 2002.

- [117] J. Holis and P. Pechac, "Penetration loss measurement and modeling for HAP mobile systems in urban environment," *EURASIP Journal on Wireless Communications and Networking*, 2008, vol. 2008, Jan. 2008.
- [118] F. Perez-Fontan, V. Hovinen, M. Schönhuber, R. Prieto-Cerdeira, J. A. Delgado-Penín, F. Teschl, J. Kyrölänen, and P. Valtr, "Building entry loss and delay spread measurements on a simulated HAP-to-indoor link at S-band," *EURASIP Journal on Wireless Communications and Networking*, vol. 2008, Jan. 2008.
- [119] D. I. Axiotis and M. E. Theologou, "An empirical model for predicting building penetration loss at 2 GHz for high elevation angles," *IEEE Antennas and Wireless Propagation Letters*, vol.2, no.1, pp.234-237, 2003.
- [120] T. S. Rappaport, and J. C. Liberti, "A geometrical-based model for line-of sight multipath radio channel," in *Proc. IEEE 46th Vehicular Technology Conference (VTC) 1996*, Atlanta, GA, USA, 844-848, April/May 1996.
- [121] P. Almers, E. Bonek, A. Burr, et al., "Survey of Channel and Radio Propagation Models for Wireless MIMO Systems," *EURASIP Journal on Wireless Communications and Networking*, vol. 2007, 2007.
- [122] K. Yu and B. Ottersten, "Models for MIMO propagation channels: a review," *Wireless Communications and Mobile Computing*, vol. 2, no. 7, pp. 653-666, Nov. 2002.
- [123] Iskandar, S. Shimamoto, "Ray Tracing for Urban Site Propagation in Stratospheric Platform Mobile Communications," in *Proc. Asia-Pacific Conference on Communications*, pp. 212-216, Perth, Australia, 3-5 Oct. 2005.
- [124] A. F. Molisch, M. Steinbauer, M. Toeltsch, E. Bonek, and R.S. Thoma, "Capacity of MIMO systems based on measured wireless channels," *IEEE Journal on Selected Areas in Communications*, vol. 20, no. 3, pp. 539-549, Apr. 2002.
- [125] P. R. King, *Modelling and Measurement of the Land Mobile Satellite MIMO Radio Propagation Channel*, PhD Thesis, University of Surrey, 2007.
- [126] P.-D. Arapoglou, K. Liolis, M. Bertinelli, A. Panagopoulos, P. Cottis, and R. De Gaudenzi, "MIMO over Satellite: A Review," *IEEE Communications Surveys & Tutorials*, vol. 13, no. 1, pp.27-51, First Quarter 2011.
- [127] C. Tzaras, B.G. Evans and S.R. Saunders, "Physical-statistical analysis of land mobile-satellite channel," *Electronics Letters*, vol. 34, no. 13, pp. 1355-1357, Jun. 1998.
- [128] P. R. King, B. G. Evans, and S. Stavrou, "Physical-statistical model for the land mobile-satellite channel applied to satellite/HAP MIMO," in *Proc. 11th European Wireless Conference 2005*, vol. 1, pp. 198-204, Nicosia, Cyprus, Apr. 2005.
- [129] G. Zang, B. Huang, and J. Mu, "One scheme of cooperative diversity with two satellites based on the Alamouti code," in *Proc. IET 3rd International Conference on Wireless, Mobile and Multimedia Networks (ICWMNN) 2010*, pp. 151-154, 26-29 Sept. 2010.
- [130] D. S. Ahn, S. Kim, H. W. Kim, and D.-C. Park, "A cooperative transmit diversity scheme for mobile satellite broadcasting systems," *International Journal of Satellite Communications and Networking*, vol. 28, no. 5-6, pp. 352-368, Dec. 2010.
- [131] P. Horvath and I. Frigyes, "Application of the 3D Polarization Concept in Satellite MIMO Systems," in *Proc. IEEE Global Communications Conference (Globecom) 2006*, pp. 1-5, Nov. 27 2006 - Dec. 1 2006.
- [132] K. P. Liolis, A. D. Panagopoulos, and P. G. Cottis, "Multi-satellite MIMO communications at Ku band and above: Investigations on spatial multiplexing for capacity improvement and selection diversity for interference mitigation," *EURASIP Journal on Wireless Communications and Networking*, vol. 2007, 2007.

- [133] P.-D. Arapoglou, M. Zamkotsian, and P. Cottis, "Dual polarization MIMO in LMS broadcasting systems: Possible benefits and challenges," *International Journal of Satellite Communications and Networking*, 2010,
- [134] P. Horvath, G. Karagiannidis, P.R. King, S. Stavrou, I. Frigyes, "Investigations in satellite MIMO channel modeling: Accent on polarization," *EURASIP Journal on Wireless Communications and Networking*, vol. 2007, 2007.
- [135] M. Sellathurai, P. Guinand, and J. Lodge, "Space-time coding in mobile satellite communications using dual-polarized channels," *IEEE Transactions on Vehicular Technology*, vol. 55, no. 1, pp. 188-199, Jan. 2006.
- [136] See for details of the MiLADY (Mobile satellite channel with Angle DiversitY) project: [Online]. Available: <http://telecom.esa.int/telecom/www/object/index.cfm?fobjectid=29020>
- [137] F. Lacoste, F. Carvalho, F. Perez Fontan, A. Nunez Fernandez, V. Fabro, G. Scot, "Polarization and spatial diversity measurements of the Land Mobile Satellite propagation channel at S-band," *COST Action IC0802*, 2nd MCM, ESA/ESTEC, Toulouse, France, 4-6 Nov. 2009.
- [138] K. Liolis, I. Andrikopoulos, and P. Cottis, "On statistical modeling and performance evaluation of SIMO land mobile satellite channels," in *Proc. 4th Advanced Satellite Mobile Systems (ASMS) 2008*, pp. 76-81, Bologna, 26-28 Aug. 2008.
- [139] E. T. Michailidis and A. G. Kanatas, "Three-Dimensional HAP-MIMO Channels: Modeling and Analysis of Space-Time Correlation," *IEEE Transactions on Vehicular Technology*, vol. 59, no. 5, pp. 2232-2242, Jun. 2010.
- [140] E. T. Michailidis, and A. G. Kanatas, "A Three Dimensional Model for Land Mobile-HAP-MIMO Fading Channels," in *Proc. 10th International Workshop on Signal Processing for Space Communications (SPSC) 2008*, Rhodes Island, Greece, 6-8 Oct. 2008.
- [141] E. T. Michailidis, G. Efthymoglou, and A. G. Kanatas, "Spatially Correlated 3-D HAP-MIMO Fading Channels," in *Proc. International Workshop on Aerial & Space Platforms: Research, Applications, Vision of IEEE Global Communications Conference (Globecom) 2008*, pp. 1-7, New Orleans, LA, USA, 4 Dec. 2008.
- [142] S.-Y. Leong, Y. R. Zheng, and C. Xiao, "Space-Time Fading Correlation Functions of a 3-D MIMO Channel Model," in *Proc. IEEE Wireless Communications Networking Conference (WCNC) 2004*, vol. 2, pp. 1127-1132, Atlanta, 21-25 Mar. 2004.
- [143] A. G. Zajić, and G. L. Stüber, "Three-dimensional modeling, simulation, and capacity analysis of space-time correlated mobile-to-mobile channels," *IEEE Transactions on Vehicular Technology*, vol. 57, no. 4, pp. 2042-2054, Jul. 2008.
- [144] G. L. Stüber, *Principles of Mobile Communications*, 2nd edition. Norwell, MA: Kluwer, 2001.
- [145] W. C. Jakes, Jr., "Multipath interference," in *Microwave Mobile communications*, New York, Wiley, 1974, pp. 11-78.
- [146] K. I. Pedersen, P. E. Mogensen, and B. H. Fleury, "Power azimuth spectrum in outdoor environments," *Electronics Letters*, vol. 33, no. 18, pp. 1583-1584, Aug. 1997.
- [147] A. Abdi, J. A. Barger, and M. Kaveh, "A parametric model for the distribution of the angle of arrival and the associated correlation function and power spectrum at the mobile station," *IEEE Transactions on Vehicular Technology*, vol. 51, no. 3, pp. 425-434, 2002.
- [148] R. Von Mises, "Über die "Ganzzahligkeit" der Atomgewicht und verwandte Fragen," *Physikalische Zeitschrift*, vol. 19, pp. 490-500, 1918.

- [149] K. V. Mardia and P. E. Jupp, *Directional Statistics*, New York, USA: John Wiley & Sons, 2000.
- [150] M. K. Simon, S. M. Hinedi, and W. C. Lindsey, *Digital Communication Techniques-Signal Design and Detection*, Upper Saddle River, NJ: PTR Prentice Hall, 1995.
- [151] A. J. Viterbi, "Phase-locked loop dynamics in the presence of noise by Fokker-Planck techniques," in *Proc. of the IEEE*, vol. 51, no. 12, pp. 1737-1753, Jun. 1963.
- [152] H. Leib and S. Pasupathy, "The phase of a vector perturbed by Gaussian noise and differentially coherent receivers", *IEEE Transactions on Information Theory*, vol. 34, no. 6, pp. 1491-1501, 1988.
- [153] M. D. Austin and G. L. Stuber, "Velocity adaptive handoff algorithms for microcellular systems," *IEEE Transactions on Vehicular Technology*, vol. 43, no. 3, pp. 549-561, 1994.
- [154] S. S. Mahmoud, Z. M. Hussain, and P. O'Shea, "Space-time model for mobile radio channel with hyperbolically distributed scatterers," *IEEE Antennas and Wireless Propagation Letters*, vol. 1, pp. 211-214.
- [155] S. S. Mahmoud, Z. M. Hussain, and P. O'Shea, P., "A geometrical-based microcell mobile radio channel model," *Wireless Networks*, vol. 12, no. 5, pp. 653-664, Sep. 2006.
- [156] S. S. Mahmoud, F. S. Al-Qahtani, Z. M. Hussain, and A. Gopalakrishnan, "Spatial and temporal statistics for the geometrical-based hyperbolic macrocell channel model," *Digital Signal Processing*, vol. 18, no. 2, pp. 151-167, Mar. 2008.
- [157] M.A. Vázquez-Castro, F. Perez-Fontan and S. R. Saunders, "Shadowing correlation assessment and modeling for satellite diversity in urban environments," *International Journal of Satellite Communications*, vol. 20, no. 2, March/April 2002, pp. 151-166.
- [158] M. A. Vázquez-Castro, D. Belay-Zeleke, A. Curieses-Guerrero, "Availability of systems based on satellites with spatial diversity and HAPS," *Electronics Letters*, vol. 38, no. 6, pp. 286-288, Mar. 2002.
- [159] C. Tzaras, B.G. Evans and S.R. Saunders, "Physical-statistical analysis of land mobile-satellite channel," *Electronics Letters*, vol. 34, no. 13, pp. 1355-1357, Jun. 1998.
- [160] S. R. Saunders and B. G. Evans, "Physical model of shadowing probability for land mobile satellite propagation," *Electronics Letters*, vol. 32, no. 17, pp. 1548-1549, Aug. 1996.
- [161] I. S. Gradshteyn, and I. M. Ryzhik, *Table of Integrals, Series and Products*, 5th edition, Edited by A. Jeffrey, New York, USA: Academic Press, 1994.
- [162] E. T. Michailidis and A. G. Kanatas, "On the Capacity of 3-D Space-Time Correlated HAP-MIMO Channels," in *Proc. 2nd International Conference on Advances in Satellite and Space Communications (SPACOMM) 2010*, Athens-Glyfada, Greece, 13-19 Jun. 2010.
- [163] E. T. Michailidis and A. G. Kanatas, "Capacity Analysis and Simulation of 3-D HAP-MIMO Channels," accepted for publication in *International Journal on Advances in Telecommunications*.
- [164] D. J. Young and N. C. Beaulieu, "The generation of correlated Rayleigh random variates by inverse discrete Fourier transform," *IEEE Transactions on Communications*, vol. 48, no. 7, pp. 1114-1127, Jul. 2000.
- [165] D. Verdin and T. C. Tozer, "Generating a fading process for the simulation of land-mobile radio communications," *Electronics Letters*, vol. 29, no.23, pp. 2011-2012, Nov. 1993.

- [166] S. A. Fechtel, "A novel approach to modeling and efficient simulation of frequency-selective fading radio channels," *IEEE Journal on Selected Areas in Communications*, vol. 11, no. 3, pp. 422-431, Apr. 1993.
- [167] R. H. Clarke, "A statistical theory of mobile-radio reception," *Bell Systems Technical Journal*, vol. 47, pp. 957-1000, Jul. 1968.
- [168] M. F. Pop and N. C. Beaulieu, "Limitations of sum-of-sinusoids fading channel simulators," *IEEE Transactions on Communications*, vol. 49, no. 4, pp. 699-708, Apr. 2001.
- [169] C. Xiao, Y. R. Zheng, and N. C. Beaulieu, "Novel sum-of-sinusoids simulation models for Rayleigh and Rician fading channels," *IEEE Transactions on Wireless Communications*, vol. 5, no. 12, pp. 3667-3679, Dec. 2006.
- [170] M. Pätzold, U. Killat, F. Laue, and Y. Li, "On the statistical properties of deterministic simulation models for mobile fading channels," *IEEE Transactions on Vehicular Technology*, vol. 47, no. 1, pp. 254-269, Feb. 1998.
- [171] C.-X. Wang, M. Patzold, and D. Yuan, "Accurate and efficient simulation of multiple uncorrelated Rayleigh fading waveforms," *IEEE Transactions on Wireless Communications*, vol. 6, no. 3, pp. 833-839, Mar. 2007.
- [172] C. S. Patel, G. L. Stüber, and T. G. Pratt, "Comparative analysis of statistical models for the simulation of Rayleigh faded cellular channels," *IEEE Transactions on Communications*, vol. 53, no. 6, pp. 1017-1026, Jun. 2005.
- [173] Y. R. Zheng and C. Xiao, "Simulation models with correct statistical properties for Rayleigh fading channels," *IEEE Transactions on Communications*, vol. 51, no. 6, pp. 920-928, Jun. 2003.
- [174] Y. R. Zheng and C. Xiao, "Improved models for the generation of multiple uncorrelated Rayleigh fading waveforms," *IEEE Communications Letters*, vol. 6, no. 6, pp. 256-258, Jun. 2002.
- [175] A. S. Akki and F. Haber, "A statistical model for mobile-to-mobile land communication channel," *IEEE Transactions on Vehicular Technology*, vol. 35, no. 1, pp. 2-10, Feb. 1986.
- [176] A. S. Akki, "Statistical properties of mobile-to-mobile land communication channels," *IEEE Transactions on Vehicular Technology*, vol. 43, no. 4, pp. 826-831, Nov. 1994.
- [177] C. S. Patel, G. L. Stüber, and T. G. Pratt, "Simulation of Rayleigh-faded mobile-to-mobile communication channels," *IEEE Transactions on Communications*, vol. 53, no. 11, pp. 1876-1884, Nov. 2005.
- [178] S. O. Rice, "Mathematical analysis of random noise," *Bell Systems Technical Journal*, vol. 23, pp. 282-332, Jul. 1944.
- [179] E. T. Michailidis and A. G. Kanatas, "Statistical Simulation Modeling of 3-D HAP-MIMO Channels," accepted for publication in *Wireless Personal Communications*.
- [180] M. Pätzold, B. O. Hogstad, "A space-time channel simulator for MIMO channels based on the geometrical one-ring scattering model," *Wireless Communications and Mobile Computing, Special Issue on Multiple-Input Multiple-Output (MIMO) Communications*, vol. 4, no. 7, pp. 727-737, Nov. 2004.
- [181] M. Pätzold, B. O. Hogstad, and D. Kim, "A New Design Concept for High-Performance Fading Channel Simulators Using Set Partitioning," *Wireless Personal Communications*, vol. 40, no. 2, pp. 267-279, Feb. 2007.
- [182] C. A. Gutierrez-Diaz-de-Leon, M. Patzold, "Sum-of-sinusoids-based simulation of flat fading wireless propagation channels under non-isotropic scattering conditions," in *Proc. IEEE Global Communications Conference (Globecom) 2007*, pp. 3842-3846, 26-30 Nov. 2007.

- [183] G. Ungerboeck, "Channel coding with multilevel/phase signals," *IEEE Transactions Information Theory*, vol. 28, no. 1, pp. 55-67, Jan. 1982.
- [184] P. A. Bello, "Characterization of randomly time-variant linear channels," *IEEE Transactions on Communications Systems*, vol. 11, pp. 360-393, 1963.
- [185] Z. Latinovic, A. Abdi, and Y. Bar-Ness, "A wideband space-time model for MIMO mobile fading channels," in *Proc. IEEE Wireless Communications and Networking Conference (WCNC) 2003*, pp. 338-342, New Orleans, USA, 16-20 Mar. 2003.
- [186] Z. Latinovic, A. Abdi, and Y. Bar-Ness, "On the utility of the circular ring model for wideband MIMO channels," in *Proc. IEEE 60th Vehicular Technology Conference (VTC Fall) 2004*, vol. 1, pp. 96-100, Los Angeles, USA, 26-29 Sep. 2004.
- [187] M. Yuanyuan and M. Pätzold, "A Wideband One-Ring MIMO Channel Model Under Non-Isotropic Scattering Conditions," in *Proc. IEEE Vehicular Technology Conference (VTC Spring) 2008*, pp. 424-429, Singapore, 11-14 May 2008.
- [188] A. G. Zajić, G. L. Stüber, T. G. Pratt, and S. Nguyen, "Wideband MIMO mobile-to-mobile channels: Geometry-based statistical modeling with experimental verification," *IEEE Transactions on Vehicular Technology*, vol. 58, no. , pp. 517-534, Feb. 2009.
- [189] A. G. Zajić and G. L. Stüber, "Three-dimensional modeling and simulation of wideband MIMO mobile-to-mobile channels," *IEEE Transactions on Wireless Communications*, vol. 8, no. , pp. 1260-1275, Mar. 2009.
- [190] Y. Yamada, Y. Ebine, and N. Nakajima, "Base station/vehicular antenna design techniques employed in high capacity land mobile communications system," *Review of the Electrical Communication Laboratory*, vol. 35, no. 2, pp. 115-121, 1987.
- [191] A. Kuchar, J. P. Rossi, and E. Bonek, "Directional macro-cell channel characterization from urban measurements," *IEEE Transactions on Antennas and Propagation*, vol. 48, no. 2, pp. 137-146, Feb. 2000.
- [192] E. T. Michailidis and A. G. Kanatas, "Wideband HAP-MIMO Channels: A 3-D Modeling Approach," submitted to *IEEE Transactions on Wireless Communications*.
- [193] M. Döttling, A. Jahn, J. Kunisch, and S. Buonomo, "A versatile propagation channel simulator for land mobile satellite applications," in *Proc. 48th IEEE Vehicular Technology Conference (VTC) 1998*, Ottawa, Canada, pp. 213-217, 18-21 May 1998.
- [194] B. H. Fleury, "First- and Second-order characterization of direction dispersion and space selectivity in the radio channel," *IEEE Transactions on Information Theory*, vol. 46, pp. 2027-2044, 2000.
- [195] T. Aulin, "A modified model for the fading signal at a mobile radio channel," *IEEE Transactions on Vehicular Technology*, vol. 28, no. 3, pp. 182-203, Aug. 1979.
- [196] F. Vatalaro and A. Forcella, "Doppler spectrum in mobile-to-mobile communications in the presence of three-dimensional multipath scattering," *IEEE Transactions on Vehicular Technology*, vol. 46, no. 1, pp. 213-219, Feb. 1997.
- [197] S. Qu and T. Yeap, "A three-dimensional scattering model for fading channels in land mobile environment," *IEEE Transactions on Vehicular Technology*, vol. 48, no. 3, pp. 765-781, May 1999.
- [198] C. Kasparis, P. R. King, and B. G. Evans, "Doppler spectrum of the multipath fading channel in mobile satellite systems with directional terminal antennas," *IET Communications*, vol. 1, no. 6, pp. 1089-1094, Dec. 2007.
- [199] E. T. Michailidis and A. G. Kanatas, "Modeling and Simulation of 3-D Wideband HAP-MIMO Channels," accepted for publication in *IEEE 74th Vehicular Technology Conference (VTC Fall) 2011*, San Francisco, USA, 5-8 Sep. 2011.

- [200] D. Grace, J. Thornton, C. Guanhua, G. P. White, and T. C. Tozer, "Improving the system capacity of broadband services using multiple high-altitude platforms," *IEEE Transactions on Wireless Communications*, vol. 4, no. 2, pp. 700-709, Mar. 2005.
- [201] G. Chen, D. Grace, and T. C. Tozer, "Performance of Multiple High Altitude Platforms using Directive HAP and User Antennas," *Wireless Personal Communications*, vol. 32, no. 3-4, pp. 275-299, Feb. 2005.
- [202] T. Celcer, G. Kandus, T. Javornik, M. Mohorcic, and S. Plevel, "Evaluation of diversity gain and system capacity increase in a multiple HAP system," in *Proc. International Workshop on Satellite and Space Communications (IWSSC) 2006*, pp. 114-118, Leganes-Madrid, Spain, 14-15 Sep. 2006.
- [203] L. Cottatellucci and M. Debbah, "On the capacity of MIMO rice channels," in *Proc. 42nd Allerton Conference on Communication, Control, and Computing 2004*, pp. 1506-1516, Monticello-Illinois, USA, 29 Sep. - 1 Oct. 2004.
- [204] K. Sakaguchi, H. Y. E. Chua, and K. Araki, "MIMO channel capacity in an indoor line-of-sight (LoS) environment," *IEICE Transactions on Communications*, vol. E88-B, no. 7, pp. 3010-3019, Jul. 2005.
- [205] P. F. Driessen and G. J. Foschini, "On the capacity formula for multiple input-multiple output wireless channels: A geometric interpretation," *IEEE Transactions on Communications*, vol. 47, no. 2, pp. 173-176, Feb. 1999.
- [206] I. Sarris and A. R. Nix, "Design and performance assessment of high-capacity MIMO architectures in the presence of a line-of-sight component," *IEEE Transactions on Vehicular Technology*, vol. 56, no. 4, pp. 2194-2202, Jul. 2007.
- [207] F. Bohagen, P. Orten, and G. E. Oien, "Design of Optimal High-Rank Line-of-Sight MIMO Channels," *IEEE Transactions on Wireless Communications*, vol. 6, no. 4, pp. 1420-1425, Apr. 2007.
- [208] F. Bohagen, P. Orten, and G. E. Oien, "Modeling and analysis of a 40 GHz MIMO system for fixed wireless access," in *Proc. IEEE 61st Vehicular Technology Conference (VTC Spring) 2005*, vol. 3, pp. 1691-1695, Stockholm, Sweden, 30 May - 1 Jun. 2005.
- [209] H. Xu, T. S. Rappaport, R. J. Boyle, and J. H. Schaffner, "Measurements and models for 38-GHz point-to-multipoint radiowave propagation," *IEEE Journal on Selected Areas in Communications*, vol. 18, pp. 310-321, Apr. 2000.
- [210] R. U. Nabar, Ö. Oyman, H. Bolcskei, and A. J. Paulraj, "Capacity scaling laws in MIMO wireless networks," in *Proc. 41st Allerton Conference on Communication, Control, and Computing 2003*, pp. 378-389, Monticello-Illinois, USA, Oct. 2003.
- [211] D. Panagopoulos, K. P. Liolis, and P. G. Cottis, "Rician K-Factor Distribution in Broadband Fixed Wireless Access Channels under Rain Fades," *IEEE Communications Letters*, vol. 11, no. 4, pp. 301-303, Apr. 2007.
- [212] M. A. Khalighi, J.-M. Brossier, G. Jourdain, and K. Raoof, "On capacity of Rician MIMO channels," in *Proc. IEEE 12th International Symposium on Personal, Indoor and Mobile Radio Communications (PIMRC) 2001*, vol. 1, pp. A150-A154, San Diego, USA, September 30 - October 3, 2001.
- [213] S. Lu, H. T. Hui, and M. Bialkowski, "Optimizing MIMO Channel Capacities Under the Influence of Antenna Mutual Coupling," *IEEE Antennas and Wireless Propagation Letters*, vol. 7, pp. 287-290, 2008.
- [214] D. Gesbert, M. Shafi, D.-S. Shiu, P. J. Smith, and A. Naguib, "From theory to practice: an overview of MIMO space-time coded wireless systems," *IEEE Journal on Selected Areas in Communications*, vol. 21, no. 3, pp. 281-302, Apr. 2003.

- [215] J. N. Martin and N. J. Colella, "Broadband Wireless Services from High Altitude Long Operation (HALO) Aircraft," in *Proc. SPIE International Symposium on Voice, Video, and Data Communications: Broadband Engineering for Multimedia Markets*, 1997.
- [216] A. G. Zajić, G. L. Stüber, T. G. Pratt, and S. Nguyen, "Envelope level crossing rate and average fade duration in mobile-to-mobile Ricean fading channels," in *Proc. IEEE International Conference on Communications (ICC) 2008*, pp. 4446-4450, Beijing, China, 19-23 May 2008.
- [217] C. Morlet, A. B. Alamañac, G. Gallinaro, L. Erup, P. Takats, and A. Ginesi, "Introduction of Mobility Aspects for DVB-S2/RCS Broadband Systems," *International Journal on Space Communications*, vol. 21, no. 1-2, pp. 5-17, 2007.
- [218] K. P. Liolis, A. D. Panagopoulos, and S. Scalise, "On the Combination of Tropospheric and Local Environment Propagation Effects for Mobile Satellite Systems Above 10 GHz," *IEEE Transactions on Vehicular Technology*, vol. 59, no. 3, pp. 1109-1120, Mar. 2010.

Σύντομο Βιογραφικό Σημείωμα

Ο **Εμμανουήλ Θ. Μιχαηλίδης** γεννήθηκε στην Αθήνα τον Ιούλιο του 1980. Είναι πτυχιούχος Ηλεκτρονικός Μηχανικός Τεχνολογικής Εκπαίδευσης (ΤΕ) από το τμήμα Ηλεκτρονικής του Τεχνολογικού Εκπαιδευτικού Ιδρύματος (ΤΕΙ) Πειραιώς από τον Ιούνιο του 2004. Έλαβε το Μεταπτυχιακό Δίπλωμα Ειδίκευσης (ΜΔΕ) στο αντικείμενο των Ψηφιακών Επικοινωνιών και Δικτύων από το τμήμα Ψηφιακών Συστημάτων του Πανεπιστημίου Πειραιώς το Σεπτέμβριο του 2006.

Από το Σεπτέμβρη του 2006 είναι μέλος του Εργαστηρίου Τηλεπικοινωνιακών Συστημάτων (ΕΤΣ) του τμήματος Ψηφιακών Συστημάτων του Πανεπιστημίου Πειραιώς. Από τον Ιούλιο του 2006 έως το Δεκέμβριο του 2007 συμμετείχε ενεργά στο χρηματοδοτούμενο από την Ευρωπαϊκή Ένωση ερευνητικό πρόγραμμα αριστείας “European Information Society Technologies (IST) Antenna Centre of Excellence (ACE)”. Από το 2009 συμμετέχει στην ευρωπαϊκή ερευνητική δράση COST IC0802 με τίτλο “Propagation Tools and Data for Integrated Telecommunication, Navigation and Earth Observation Systems”. Παράλληλα με την ερευνητική του δραστηριότητα είναι εργαστηριακός συνεργάτης στο Τμήμα Ηλεκτρονικής του ΤΕΙ Πειραιώς από τον Οκτώβριο του 2007 και έχει συμμετάσχει ως εισηγητής πληροφορικής σε διάφορα προγράμματα επαγγελματικής κατάρτισης από το Μάρτιο του 2007.

Τα τρέχοντα ερευνητικά του ενδιαφέροντα εστιάζονται στην ανάπτυξη νέων ψηφιακών τεχνικών για ασύρματα, δορυφορικά και στρατοσφαιρικά συστήματα επικοινωνιών, καθώς και στο χαρακτηρισμό, τη μοντελοποίηση και την προσομοίωση του ραδιοδιαύλου διάδοσης μελλοντικών ασύρματων συστημάτων επικοινωνιών.

Ο κ. Μιχαηλίδης βραβεύτηκε με τη διάκριση καλύτερης εργασίας (Best Paper Award) στο διεθνές συνέδριο “International Conference on Advances in Satellite and Space Communications (SPACOMM) 2010” και είναι μέλος του Ινστιτούτου Ηλεκτρολόγων και Ηλεκτρονικών Μηχανικών (IEEE).

РАНЕЕЗНАМО ПЕРПАА

Vita

Emmanouel T. Michailidis was born in Athens, Greece, in July 1980. He received the B.Sc. degree in Electronics Engineering in June 2004 from the Technological Educational Institute of Piraeus, Piraeus, Greece, and the M.Sc. degree in Digital Communications and Networks in September 2006 from the University of Piraeus.

Since September 2006, he has been a Graduate Research Engineer with the Telecommunications Systems Laboratory (TSL), Department of Digital Systems, University of Piraeus. From July 2006 to December 2007, he was with the European Information Society Technologies (IST)-funded research project Antenna Centre of Excellence (ACE). Since 2009, he has participated in the COST IC0802 action entitled “Propagation Tools and Data for Integrated Telecommunication, Navigation, and Earth Observation Systems”. Since 2007, he has been a Laboratory Assistant with the Department of Electronics, Technological Educational Institute of Piraeus and he has also been an informatics trainer in vocational training institutes.

His current research interests include the development of new digital techniques for wireless, satellite, and stratospheric communications systems, and the radio channel characterization, modeling, and simulation for future wireless communications systems.

Mr. Michailidis received the Best Paper Award at the “International Conference on Advances in Satellite and Space Communications (SPACOMM) 2010” and he is a member of the Institute of Electrical and Electronics Engineers (IEEE).

РАНЕЕ НЕ ПЕРПА